UNIVERSITÄT HAMBURG
DEPARTMENT PHYSIK

Search for new physics in diphoton and E_T^{miss} final states using the ATLAS detector at the LHC

Dissertation
zur Erlangung des Doktorgrades
am Fachbereich Physik
der Universität Hamburg

vorgelegt von
Diplom-Physiker Martin Wildt
aus Zweibrücken

Hamburg
2012

Gutachter der Dissertation:	Prof. Dr. Johannes Haller Prof. Dr. Peter Schleper
Gutachter der Disputation:	Prof. Dr. Johannes Haller Dr. Kerstin Tackmann
Datum der Disputation:	10. Dezember 2012
Vorsitzender des Prüfungsausschusses:	Dr. Georg Steinbrück
Vorsitzender des Promotionsausschusses:	Prof. Dr. Peter Hauschildt
Leiterin des Departments Physik:	Prof. Dr. Daniela Pfannkuche
Dekan der MIN-Fakultät:	Prof. Dr. Heinrich Graener

Abstract

A search for new physics in diphoton events with large missing transverse momentum with the ATLAS detector is presented in this thesis. The 2011 dataset of $4.8\,\mathrm{fb}^{-1}$ of proton-proton collisions provided by the LHC at a center-of-mass energy of $\sqrt{\mathrm{s}} = 7\,\mathrm{TeV}$ is analyzed.

By making use of three signal regions, an optimized sensitivity of the event selection is achieved in different parameter ranges of physics models beyond the Standard Model (SM). The SM background is estimated mainly in data control regions. No excess of events above the SM expectation is found in any signal region. Hence, 95 % confidence level (CL) exclusion limits on the production cross section and on masses of new physics particles are derived.

The results are interpreted in scenarios with gauge-mediated SUSY breaking (GMSB), namely the general gauge mediation (GGM) scenario with a bino-like lightest neutralino ($\tilde{\chi}_1^0$) and the SPS8 scenario of the (minimal) GMSB model. In the GGM scenario, gluino (squark) masses, which are required to be greater than the lightest neutralino mass, are excluded below 1.10 TeV (0.91 TeV) at 95 % CL, for masses of the lightest neutralino greater than 50 GeV. In the GMSB SPS8 scenario, masses of the lightest neutralino (chargino) are excluded at 95 % CL below 302 GeV (582 GeV) corresponding to an 95 % CL exclusion of the SUSY breaking scale $\Lambda < 208\,\mathrm{TeV}$. Furthermore, the results are interpreted in the context of universal extra dimensions (UED) with one additional space dimension. Scenarios with a compactification scale $R^{-1} < 1410\,\mathrm{GeV}$ are excluded at 95 % CL.

Zusammenfassung

In dieser Arbeit wird die Suche nach neuer Physik in Ereignissen mit zwei Photonen und großer fehlender Transversalenergie mit dem ATLAS Detektor präsentiert. Hierbei wird der 2011 bei einer Schwerpunktsenergie von $\sqrt{s} = 7\,\text{TeV}$ am LHC aufgenommene Datensatz von Proton-Proton Kollisionen analysiert, der einer integrierten Luminosität von $4.8\,\text{fb}^{-1}$ entspricht.

Durch die Verwendung von optimierten Signalregionen wird eine hohe Sensitivität der Ereignisselektion in verschiedenen Parameterbereichen unterschiedlicher Modelle jenseits des SM erreicht. Der Standardmodell-Untergrund wird größtenteils aus den Daten selbst bestimmt. In keiner Signalregion wurde ein Überschuss an Ereignissen über den Erwartungen des SM gefunden. Daher können Ausschlussgrenzen auf den Wirkungsquerschnitt und auf die Massen von neuen Teilchen gesetzt werden.

Die Ergebnisse werden in Szenarien mit *Gauge-Mediated SUSY Breaking* (GMSB), namentlich dem *General Gauge Mediation* (GGM) Modell, sowie im SPS8 Szenario des (minimalen) GMSB Modells interpretiert. Im GGM Szenario können die Massen von Gluinos (Squarks), die größer als die leichteste Neutralinomasse sind, unter 1.10 TeV (0.91 TeV) mit 95 % CL ausgeschlossen werden. Diesgilt für Massen des leichtesten Neutralinos größer als 50 GeV. Im GMSB SPS8 Szenario werden die leichtesten Neutralinos (Charginos) mit Massen unter 302 GeV (582 GeV) mit 95 % CL ausgeschlossen. Dies entspricht einer Ausschlussgrenze auf der SUSY Brechungsskala von $\Lambda < 208\,\text{TeV}$. Darüber hinaus werden die Ergebnisse im Kontext von Modellen mit *Universal Extra Dimensions* (UED) mit einer Extra-Dimension interpretiert. Szenarien mit einer Kompaktifizierungsskala von $R^{-1} < 1410\,\text{GeV}$ werden mit 95 % CL ausgeschlossen.

Contents

1 Introduction **1**

2 Standard Model, SUSY and UED **3**

2.1 The Standard Model . . . 3

2.1.1 Particles and Interactions . . . 3

2.1.2 Inadequacies and Unsolved Problems . . . 6

2.2 Supersymmetry . . . 7

2.2.1 Basic Concepts . . . 7

2.2.2 Remedies . . . 9

2.2.3 Gauge-mediated SUSY Breaking . . . 10

2.2.4 General Gauge Mediation . . . 10

2.2.5 Phenomenology . . . 11

2.3 Universal Extra Dimensions . . . 13

2.3.1 Phenomenology . . . 14

2.4 State of Knowledge . . . 14

3 LHC and ATLAS **19**

3.1 The LHC . . . 19

3.2 The ATLAS Detector . . . 20

3.2.1 The Coordinate System and Conventions . . . 21

3.2.2 The Magnet System . . . 23

3.2.3 The Inner Detector . . . 24

3.2.4 Calorimetry . . . 25

3.2.5 The Muon Spectrometer . . . 28

3.3 Trigger and DAQ . . . 28

3.3.1 The Level-1 Trigger . . . 29

3.3.2 The High Level Trigger and Data Recording . . . 30

3.3.3 Diphoton Trigger . . . 31

4 Reconstruction and Simulation **33**
4.1 Data Processing . . . 33
4.2 Generation and Simulation . . . 33
4.2.1 Event Generation . . . 34
4.2.2 MC Generators . . . 35
4.2.3 Detector Simulation and Digitization . . . 35
4.3 Reconstruction and Identification . . . 36
4.3.1 Electromagnetic Clustering . . . 36
4.3.2 Electrons . . . 37
4.3.3 Photons . . . 39
4.3.4 Jets . . . 42
4.3.5 Muons . . . 43
4.3.6 Missing Transverse Energy . . . 43
4.4 Monte Carlo Samples . . . 45
4.4.1 Background Samples . . . 45
4.4.2 GGM Samples . . . 46
4.4.3 GMSB SPS8 Samples . . . 48
4.4.4 UED Samples . . . 48
4.4.5 Benchmark Points . . . 49
4.4.6 Reweighting of MC Events . . . 49

5 Data Taking and Selection **51**
5.1 Luminosity . . . 51
5.2 Data Taking . . . 52
5.3 Object Selection . . . 53
5.3.1 Photons . . . 55
5.3.2 Electrons . . . 56
5.3.3 Jets . . . 56
5.3.4 Muons . . . 57
5.3.5 LAr Calorimeter Vetos . . . 58
5.3.6 Total Transverse Momentum H_{T} . . . 58
5.4 Signal Selection . . . 59
5.4.1 Preselection . . . 59
5.4.2 Signal Regions . . . 62

6 SM Background Measurement **71**
6.1 Instrumental $E_{\mathrm{T}}^{\mathrm{miss}}$ Background . . . 72
6.1.1 Pseudo-Photons . . . 73
6.1.2 QCD Control Samples . . . 73
6.1.3 Dielectron Control Sample . . . 77
6.1.4 Instrumental $E_{\mathrm{T}}^{\mathrm{miss}}$ Background Results . . . 78
6.2 Genuine $E_{\mathrm{T}}^{\mathrm{miss}}$ Background . . . 82

6.2.1 Electron Misidentification Probability . . . 82
6.2.2 Electron-Photon Control Sample . . . 84
6.2.3 Genuine $E_{\mathrm{T}}^{\mathrm{miss}}$ Extrapolation . . . 85
6.2.4 Genuine $E_{\mathrm{T}}^{\mathrm{miss}}$ Background Results . . . 89
6.3 Irreducible Background . . . 90
6.4 Conclusion . . . 91

7 Systematic Uncertainties **93**
7.1 Luminosity Uncertainty . . . 93
7.2 Trigger Efficiency Uncertainty . . . 93
7.3 Photon Uncertainties . . . 94
7.4 Uncertainty on the $E_{\mathrm{T}}^{\mathrm{miss}}$ Measurement . . . 94
7.5 H_{T} Uncertainty . . . 95
7.6 Pile-up Uncertainty . . . 95
7.7 MC Statistics Uncertainty . . . 96
7.8 Theory Uncertainties . . . 96
7.8.1 SUSY Scenarios . . . 96
7.8.2 UED Scenario . . . 96
7.9 Summary . . . 97

8 Interpretation of the Results **101**
8.1 Input for the Interpretation . . . 101
8.2 Limit Setting Technique . . . 104
8.2.1 The CL_{s} Method . . . 104
8.2.2 Pseudo Experiments and Test Statistic . . . 105
8.2.3 Observed and Expected Limits . . . 106
8.2.4 Limits on Model Parameters . . . 107
8.3 Limit on the Number of Signal Events . . . 107
8.4 Results of the GGM Interpretation . . . 108
8.5 Results of the GMSB SPS8 Interpretation . . . 117
8.6 Results of the UED Interpretation . . . 118

9 Conclusion **121**
9.1 Summary . . . 121
9.2 Outlook . . . 122

A MC Samples **125**

B Details on the Background Estimation **127**
B.1 Instrumental $E_{\mathrm{T}}^{\mathrm{miss}}$ Control Samples 127
B.2 SM $\gamma\gamma$ Modeling 127
B.3 Contamination with Genuine $E_{\mathrm{T}}^{\mathrm{miss}}$ 131
B.4 Contamination with BSM Signal Events 131
B.5 Details on the Electron-Photon Control Sample 133

List of Figures **137**

List of Tables **141**

Bibliography **143**

CHAPTER 1

Introduction

The elementary particles and their interactions can be described by the Standard Model (SM) of particle physics, which has been successfully tested in various experiments. However, there are still important shortcomings that motivate extensions of the SM. In this thesis, two possible theoretical concepts are considered, namely a supersymmetric (SUSY) extension of the SM, which assumes a fundamental spin symmetry, and an extension of the space time within the context of universal extra dimensions (UED). Both are promising and well motivated candidates for physics beyond the SM.

The Large Hadron Collider (LHC), a proton-proton collider at CERN, and its experiments were developed for the discovery of new particles. In order to achieve a suitable reach for new physics models, a high center-of-mass energy $\sqrt{s}$ at the TeV scale and high interaction rates are required. The ATLAS experiment at the LHC is designed to measure SM particles as well as new physics signatures. During the year 2011, a dataset at $\sqrt{s} = 7\,\text{TeV}$ corresponding to an integrated luminosity of $\sim 5\,\text{fb}^{-1}$ was recorded with the ATLAS detector.

In the SUSY models considered in this thesis, the masses of the SUSY particles are induced by the SUSY breaking mediated by gauge interactions. The lightest and the next-to-lightest SUSY particle, the LSP and the NLSP, respectively, characterize the phenomenology of the event. The NLSP decays into a SM particle and the LSP. If the so-called R-parity is assumed to be conserved, two important consequences arise: The SUSY particles are produced in pairs, and the LSP is stable.

In the UED scenario, heavier partners of the SM particles, so-called Kaluza-Klein (KK) excitations, are produced always in pairs at the LHC due to momentum conservation in the extra dimension. KK particles decay via a cascade into the next-to-lightest KK particle (NLKP), which finally decays into a SM photon and a stable graviton, the lightest KK particle (LKP).

This thesis is dedicated to the search for the signature of two high energy photons and missing transverse momentum. In SUSY and UED models, this final state can be obtained in certain parameter ranges where the NLSP or the NLKP decays into a photon and a gravitino LSP or graviton LKP respectively. The diphoton signature occurs due to the pair production of SUSY (UED) particles decaying into a photon while the missing transverse momentum arises from the gravitinos (gravitons), which escape the detector unmeasured.

The result of the search is derived from the comparison of the data with the SM expectation from background processes and the expected signal from new physics processes. If the production cross section of new physics signals is high enough, a significant excess of events over the SM background should be found in data. The event selection performed is designed to reject most of the SM background, while a high signal sensitivity is conserved. For this purpose, several signal regions are defined, which are optimized for a certain model or parameter range. The background estimation is mostly derived from real data, which is preferred compared to an estimation from simulation. The measurement is finally interpreted in the context of the new physics models and a conclusion on the validity of the models in the considered parameter ranges can be drawn.

The thesis is structured as follows: In chapter 2, the theoretical background of the SM and the new physics models is introduced. The experimental setup, namely the LHC and the ATLAS detector, is described in chapter 3. The particle reconstruction and the simulation are described in chapter 4. The data taking and the selection of events with two photons and the definition of the signal regions can be found in chapter 5. The background estimation is described in chapter 6, while the signal uncertainties are briefly specified in chapter 7. The interpretation in the context of the various scenarios is presented in chapter 8. Finally, in chapter 9, a summary and an outlook are given.

CHAPTER 2

The Standard Model, Supersymmetry and Universal Extra Dimensions

In this chapter, the Standard Model of particle physics, its supersymmetric extension and universal extra dimensions are briefly introduced. The first section describes the SM particles and their interactions including the shortcomings of the model, which motivate extensions and ideas, that go beyond the SM (BSM). The second section gives an overview of the supersymmetric concept and the mechanisms and properties of gauge-mediated supersymmetry breaking (GMSB) and general gauge mediation (GGM) are presented. The idea of universal extra dimensions, which is also a candidate for BSM physics, is discussed in the third section. The chapter concludes with the latest measurement results and the current state of knowledge in these fields.

2.1 The Standard Model

2.1.1 Particles and Interactions

The fundamental forces, the strong and the electroweak (EW) force, together with the known elementary particles are described by the SM of particle physics. The particles are represented by fermion (half-integer spin) fields and are members of the two classes of either leptons or quarks. The interactions are mediated by gauge bosons (integer spin) and can be described in the formalism of symmetry groups:

$$SU(3)_C \otimes SU(2)_L \otimes U(1)_Y, \tag{2.1}$$

where $SU(3)_C$ represents the strong interaction and $SU(2)_L \otimes U(1)_Y$ the electroweak interaction.

All fermions occur in three generations and are summarized in Table 2.1. Each particle has a corresponding anti-particle. Table 2.2 lists the gauge bosons with their masses. The particles and their particular interactions are illustrated in Fig. 2.1.

	1st generation		2nd generation		3rd generation	
	name	mass [MeV]	name	mass [MeV]	name	mass [MeV]
quarks	up (u)	1.7 - 3.1	charm (c)	$1.29 \cdot 10^3$	top (t)	$172.9 \cdot 10^3$
	down (d)	4.1-5.7	strange (s)	100	bottom (b)	$4.19 \cdot 10^3$
leptons	electron (e)	0.511	muon (μ)	105.66	tau (τ)	1776.82
	e neutrino (ν_e)	$< 2 \cdot 10^{-6}$	μ neutrino (ν_μ)	< 0.19	τ neutrino (ν_τ)	< 18.2

Table 2.1: Overview of the SM fermions with masses [1]. The c- and b-quark masses are given in the $\overline{\text{MS}}$ schema. The mass uncertainties can be found in the reference.

	mass [GeV]	charge [e]
W-boson (W)	80.40	± 1
Z-boson (Z)	91.19	0
photon (γ)	0	0
gluon (g)	0	0

Table 2.2: Overview of the SM gauge bosons with masses and electric charge [1]. The mass uncertainties and further properties can be found in the reference.

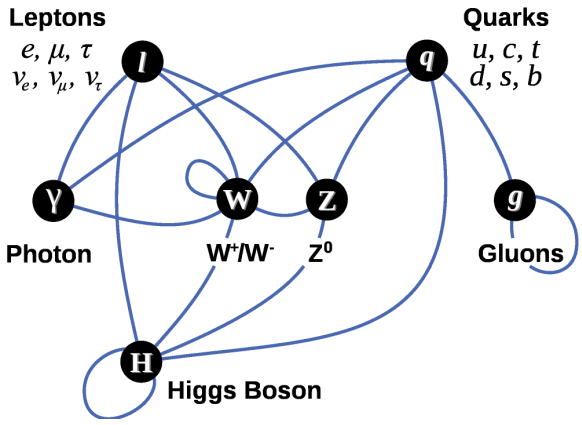

Figure 2.1: The elementary particles and interactions [2]. The first row shows the fermions, the second row the gauge bosons and the hypothetical SM Higgs boson is quoted at the bottom. The blue lines indicate the possible interactions among the particles. The neutrinos do not interact with photons.

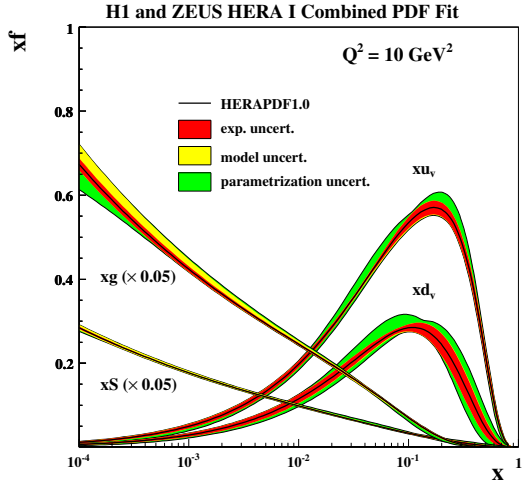

Figure 2.2: Combined PDFs extracted from H1 and Zeus measurements for different partons at $Q^2 = 10\,\text{GeV}$ [7].

Quantum Chromodynamics: The strong interaction is described in the framework of quantum chromodynamics (QCD) [1, 3–6] and it is mathematically based on the $SU(3)_C$ gauge group. The involved particles in strong interaction are the quarks (fermions) and the massless gluons (gauge bosons), which together are called partons. Both quarks and gluons carry color charge and thus gluons are self-interacting. This feature is implemented by the non-abelian property of the gauge group.

The structure of the proton consisting of quarks and gluons can be described by parton density functions (PDFs), which depend on the momentum transfer Q^2 and the parton momentum fraction x[1]. Some example PDFs of the proton are shown in Fig. 2.2 for gluons, sea quarks, up and down quarks at $Q^2 = 10\,\text{GeV}^2$. The results extracted from fits are compared. For the understanding and simulation of physical processes occurring in proton-proton collisions, a good understanding of the PDFs is required.

The coupling constant α_S depends on the momentum transfer or the distance. At low distance or high Q^2 the partons can be treated like free particles. This effect is called *asymptotic freedom*. At large distances, the *confinement* allows only bound states of quarks and gluons, while single objects are inhibited. If the potential between to quarks becomes large enough, additional quark pairs can arise and form color-neutral hadrons with the initial quarks (*hadronization*).

Electroweak Interaction The electroweak interaction [1, 8, 9] is the unification of the electromagnetic and weak interaction. From the symmetry group $SU(2)_L \otimes U(1)_Y$ four physical gauge bosons arise via mixing, namely the massless photon γ, and the massive $W^\pm$ and Z^0, which are represented by the fields A_μ, $W_\mu^\pm$ and Z_μ, respectively. Since the electroweak symmetry is broken, the $SU(2)_L$ weak eigenstates $W_\mu^{1,2,3}$ and the $U(1)_Y$ eigenstate B_μ are forming

[1]The parton momentum fraction is also referred to as *Bjorken x*.

the mass eigenstates (observable gauge bosons):

$$\begin{pmatrix} W_\mu^+ \\ W_\mu^- \end{pmatrix} = \frac{1}{\sqrt{2}} \begin{pmatrix} 1 & -i \\ 1 & i \end{pmatrix} \begin{pmatrix} W_\mu^1 \\ W_\mu^2 \end{pmatrix}, \tag{2.2}$$

and

$$\begin{pmatrix} Z_\mu \\ A_\mu \end{pmatrix} = \begin{pmatrix} \cos\theta_\mathrm{W} & \sin\theta_\mathrm{W} \\ -\sin\theta_\mathrm{W} & \cos\theta_\mathrm{W} \end{pmatrix} \begin{pmatrix} W_\mu^3 \\ B_\mu \end{pmatrix}. \tag{2.3}$$

The Weinberg angle θ_W is the mixing parameter and links furthermore the electromagnetic coupling constant α_em and the weak coupling constant α_w via

$$\alpha_\mathrm{em} = \alpha_\mathrm{w} \cdot \sin^2\theta_\mathrm{W}. \tag{2.4}$$

Higgs Mechanism The Higgs mechanism [1, 10–15] is responsible for the generation of the masses of the weak gauge bosons $W^\pm$ and Z^0 and the fermions, thus describes the breaking of the EW symmetry. The contribution to the SM Lagrangian density is given by the Yukawa-coupling to the fermion fields and the potential V of the complex scalar Higgs field ϕ:

$$V = -\mu\phi^\dagger\phi + \lambda(\phi^\dagger\phi)^2. \tag{2.5}$$

The non-zero parameters μ and λ are chosen, such that the minimum of the potential, obtained by the vacuum expectation value (VEV), is non-zero, namely

$$\nu = \sqrt{\frac{\mu^2}{\lambda}} \tag{2.6}$$

and was measured to be $\nu \approx 246\,\mathrm{GeV}$ [1].

All particle masses, including the mass of the Higgs boson H, are proportional to ν. The mass of the Higgs boson m_H is a free parameter in the SM, however masses in the area of $\simeq 100\,\mathrm{GeV}$ are favored from electroweak fits [16]. The ATLAS and the CMS collaborations observe events that agree with the assumption of a SM Higgs boson with significances of more than 5 standard deviations at a mass of $m_\mathrm{H} = 126.0 \pm 0.4\,(\mathrm{stat}) \pm 0.4\,(\mathrm{syst})\,\mathrm{GeV}$ [17] and $m_\mathrm{H} = 125.3 \pm 0.4\,(\mathrm{stat}) \pm 0.5\,(\mathrm{syst})\,\mathrm{GeV}$ [18], respectively. Figure 2.3 shows the local significance p_0 (solid curve) as a function of the Higgs mass. The dip at $m_\mathrm{H} \simeq 126\,\mathrm{GeV}$ achieves a local significance of 5.9 standard deviations corresponding to a background fluctuation probability of 1.7×10^{-9} [17]. Higgs masses in the range between approximately $111\,\mathrm{GeV} \leq m_\mathrm{H} \leq 600\,\mathrm{GeV}$ are mostly excluded at 95 % CL [19, 20]. Additional results of electroweak fits assuming a Higgs particle with a mass of $\simeq 126\,\mathrm{GeV}$ are presented in Ref. [21].

2.1.2 Inadequacies and Unsolved Problems

The SM can describe very successfully wide areas in the field of particle physics. Nevertheless, some open questions remain, which point to physics beyond the SM and makes extensions of the SM necessary. For example, the SM does not make any predictions about the neutrino

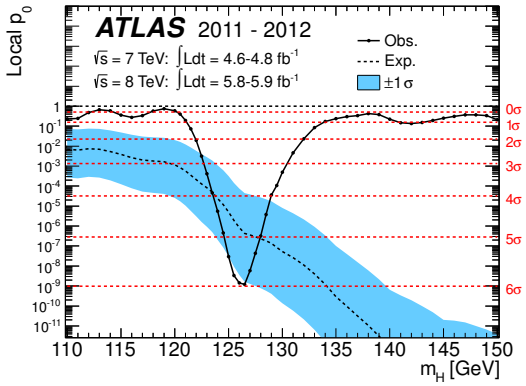

Figure 2.3: The observed (solid) local p_0 as a function of m_{H} in the low mass range. The dashed curve shows the expected local p_0 under the hypothesis of a SM Higgs boson signal at that mass with its $\pm 1\sigma$ band. The horizontal dashed lines indicate the p-values corresponding to significances of 1 to 6 sigma [17].

masses and does not include gravity. The particle masses and the coupling constants need to be measured from experiment, they are not an outcome of the model. In addition, the number of these parameters is unsatisfyingly large. The so-called *hierarchy problem* [22–26] refers to the large quantum corrections to the Higgs mass leading to a value of the order of the Planck scale and not to a value at the order of $\mathcal{O}(100\,\mathrm{GeV})$, which is constrained by the masses of the gauge bosons. An unnatural *fine-tuning* is necessary to assess the Higgs mass at this order of magnitude.

Cosmological measurements, e.g. the rotation speed of stars in galaxies, can only be consistently interpreted in the frame of the gravitational law with the help of additional invisible matter, the so-called *dark matter*. The SM describes only less than 5 % of the matter in the universe.

This collection claims not to be complete, but can certainly serve as motivation for theories beyond the SM, that can solve at least some of the problems.

2.2 Supersymmetry

2.2.1 Basic Concepts

In this section, an introduction to SUSY is given and the main aspects are discussed. It is focused on models and processes, that yield final states with photons and missing energy.

The basic concept of supersymmetry [22, 27–35] is the introduction of a symmetry between fermions and bosons generating at least twice as many particles as in the SM. The additional particles, the superpartners or *sparticles*, carry a spin different by 1/2 with respect to the corresponding SM particle, i.e. SM fermions correspond to SUSY bosons and SM bosons correspond to SUSY fermions. The minimal extension in terms of particle content of the SM is the *Minimal Supersymmetric Standard Model* (MSSM) [22, 36–40].

The following subsections give an overview of the basic concept, the particle content and the motivation for supersymmetric models. The SUSY breaking and the expected sparticle production and decays are presented in section 2.2.5. A summary of the current state of knowledge in the framework of SUSY with photon final states can be found in Section 2.4.

Particles and Eigenstates In this section, only the most important (s)particles used in this thesis are discussed. The superpartners to the fermions (spin = 1/2) are the *sfermions* (spin = 0) with the corresponding subgroups of *squarks* $\tilde{q}$ and *sleptons* $\tilde{\ell}$. The *gauginos* (spin = 1/2) are the superpartners of the gauge bosons (integer spin). The superpartners to the gauge eigenstates are referred to as *winos* ($\tilde{W}_\mu^{1,2,3}$) and *bino* ($\tilde{B}_\mu$). Their corresponding mass eigenstates are the *winos* $\tilde{W}^\pm$, *zino* $\tilde{Z}^0$, and the *photino* $\tilde{\gamma}$. The *gluino* $\tilde{g}$ is the partner of the gluon.

In broken SUSY models, the *neutralinos* ($\tilde{\chi}^0_{1,2,3,4}$) and *charginos* ($\tilde{\chi}^\pm_{1,2}$), are mixtures of the gauge eigenstates ($\tilde{B}_\mu$, $\tilde{W}^3_\mu$, $\tilde{H}^0_{\mathrm{u,d}}$) and ($\tilde{W}^{2,3}_\mu$, $\tilde{H}^+_{\mathrm{u}}$, $\tilde{H}^-_{\mathrm{d}}$), respectively, where $\tilde{H}^{\pm,0}_{\mathrm{u,d}}$ denote *higgsino* gauge eigenstates. The *gravitino* $\tilde{G}$ (spin = 3/2) superpartner corresponds to the graviton G (spin = 2).

According to supersymmetry, the masses of the sparticles are the same as the SM particle masses. However, the supersymmetry must be broken, since so far no sparticles have been observed, and the sparticle masses are large compared to the SM masses. In this thesis, the considered breaking mechanism is the gauge-mediated breaking (GMSB) [22, 41–47] (see Section 2.2.3), where the breaking is mediated by gauge interactions. Other mechanisms like gravity-mediated breaking, e.g. the minimal super gravity (mSUGRA), and anomaly-mediated breaking (AMSB) can also provide the breaking feature [22]. In the MSSM, the number of free model parameters is greater than 100, but can be reduced in the previously mentioned models to be less than 10, by e.g. assuming symmetries and implementing constraints from measurements.

In SUSY there is an additional quantum number, the R-parity R, which is defined as

$$R = (-1)^{3(B-L)+2S}, \tag{2.7}$$

where B denotes the baryon number, L the lepton number, and S the spin. SM particles carry R-parity of $+1$, whereas sparticles carry $R = -1$. Due to the assumed R-parity conservation, sparticles are produced in pairs and sparticles decays into their SM partner particle and an other sparticles. Furthermore, the lightest SUSY particle (LSP) is stable. In this thesis only scenarios with R-parity conservation are considered. Nevertheless, searches in R-parity violating scenarios are performed by many collaborations, e.g [48].

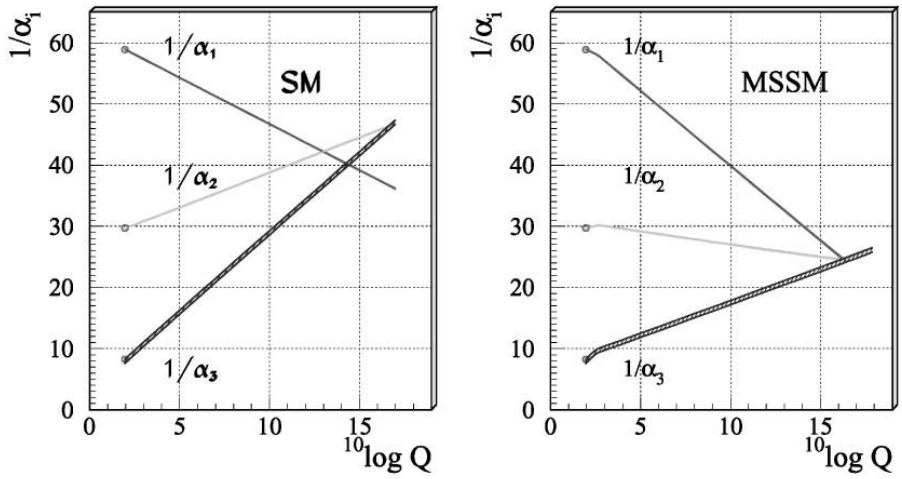

Figure 2.4: The running of the inverse coupling constants as a function of the energy scale Q (in GeV) in the SM (left) and in the MSSM (right) [49]. In the MSSM, the coupling constants unify at very high Q.

2.2.2 Remedies

As mentioned in the introduction, supersymmetry can solve a couple of shortcomings of the SM presented in Section 2.1.2, which makes SUSY an interesting theory of physics beyond the SM. In addition, SUSY is a very fundamental symmetry making it theoretically compelling.

- **Coupling constants:** The theoretically desired unification of the coupling constants at the Planck scale [22, 49–53] can be achieved in a SUSY model with masses at the TeV scale, which would be accessible at the LHC. The running of the coupling constants as a function of the energy scale Q^2 is shown in Fig. 2.4 in the SM (left) and in the MSSM (right). The unification in the MSSM takes place at the order of $Q^2 \simeq 10^{16}\,\mathrm{GeV}^2$.

- **Hierarchy problem:** [22–26] Due to the sparticles in the MSSM, the mass corrections to the Higgs mass and the Higgs mass itself are at the same order of magnitude, because in the correction terms, the ultraviolet momentum cutoff (Λ_{UV}) at the order of the Plank scale cancels out, when the masses of the SUSY particles are in the order of $\mathcal{O}$(TeV) [40, 54–58]. Hence, the hierarchy problem is solved in SUSY.

- **Dark matter:** Since dark matter (DM) is only observed via gravitational interaction, weakly interacting massive particles (WIMPs) like a stable lightest SUSY particle (in R-parity conserved models) are expedient candidates for DM [59, 60]. Note, that not in all SUSY scenarios the mass of the lightest sparticle is high enough to be consistent with DM measurements.

2.2.3 Gauge-mediated SUSY Breaking

It is assumed that in gauge-mediated breaking models, the breaking of the supersymmetry takes place at the Planck-scale in a hidden sector. The messenger particles, that transfer the breaking to the visible (MSSM) sector, are interacting with the MSSM particles via gauge bosons. The minimal[1] GMSB scenario can be described by six parameters:

- Λ: The effective SUSY breaking mass scale.
- $\tan\beta$: The ratio of the MSSM Higgs particle vacuum expectation values.
- sign(μ): The sign of the Higgs mass parameter μ.
- M_{mes}: The messenger mass.
- $N_{\text{mes}}(N_5)$: The number of messenger multiplets.
- C_{grav}: The scale factor of the $\tilde{G}$ coupling.

The masses of the sparticles can be derived from this set of parameters. Another important derived parameter is the vacuum expectation value of an auxiliary field $F = \Lambda \cdot M_{\text{mes}} \cdot C_{\text{grav}}$, which governs the coupling of the sparticles to the SM particles.

Since it is not feasible to search in a full 6-dimensional parameter space and in order to facilitate the comparison among various experiments, a particular choice of parameters, the benchmark scenario, is defined. The scenario of *snowmass points and slopes 8* (SPS8) [61] is defined by $\tan\beta = 15$, sign(μ) = +, $N_{\text{mes}} = 1$, and $C_{\text{grav}} = 1$. The model line (*slope*) is assessed by $M_{\text{mes}} = 2\Lambda$, where the effective SUSY breaking scale Λ is a free parameter. The mass spectrum of the SPS8 scenario, where the $\tilde{\chi}_1^0$ mass is chosen to be 139 GeV corresponding to $\Lambda = 100$ TeV is illustrated in Fig. 2.5. The gaugino and sleptons masses are of the same order and smaller than the squark masses. The mass of the gluino and the higgsino are in between the squark and slepton masses.

2.2.4 General Gauge Mediation

The general gauge mediation model [63–66] is a *phenomenological model* and also referred to as a *simplified model*, which embraces the physics phenomenology of several models with gauge-mediated SUSY breaking. GGM reflects the principle of model-independence. The theoretical aspects of models with gauge-mediation are reduced in a way, that the most relevant properties are conserved, but features a reduced mass spectrum and accessible particle content. Nevertheless, the GGM sfermion mass sum rules [66] need to be satisfied to avoid tachyonic particles.

In this thesis, the parameter space is given by the mass of the lightest colored sparticle and the lightest uncolored sparticle besides the gravitino, namely the masses of the gluino and the neutralino. These parameters are both detached from the other sparticle masses, which are

[1] Minimal GMSB is commonly abbreviated GMSB.

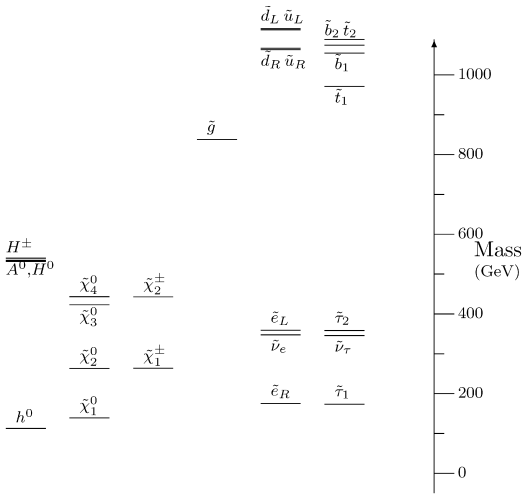

Figure 2.5: The SPS8 mass spectrum [62]. The particular choice of the model parameters is described in the text.

significantly higher (*decoupling limit*) and nearly degenerated. The 2-dimensional parameter space of the gluino mass and the neutralino mass is referred to as *mass plane* or *(mass-) grid*. The higgs sector plays a minor role in the phenomenology and the related parameters are fixed to $\tan\beta = 2$ and $\mu > 0$.

2.2.5 Phenomenology

Since there is an enormous number of different final states, that can be realized for different parameter ranges in SUSY models, only the most relevant production and decay processes, that lead to diphoton final states in the framework of gauge mediated SUSY breaking, are briefly discussed in this section.

Production In proton-proton collisions sparticles are produced in pairs via electro-weak and strong interaction:

$$q + g \rightarrow \tilde{q} + \tilde{g} \tag{2.8}$$

$$g + g \rightarrow \tilde{q} + \tilde{q} \tag{2.9}$$

$$q + \bar{q} \rightarrow \tilde{\chi}_i^0 \tilde{\chi}_j^0. \tag{2.10}$$

Some examples of Feynman diagrams are shown in Fig. 2.6. The first and the second row in the figure illustrate the squark and gluino production via strong interaction. The third row is dedicated to electroweak production. In the first row, the sparticles are produced via gluon-gluon and quark-gluon fusion, and in the second row, the sparticles are produced via quark-anti-quark annihilation. Another possible process, not listed in the figure, is quark-quark scattering. The electroweak interaction (third row) allows production of charginos, neutralinos and sleptons.

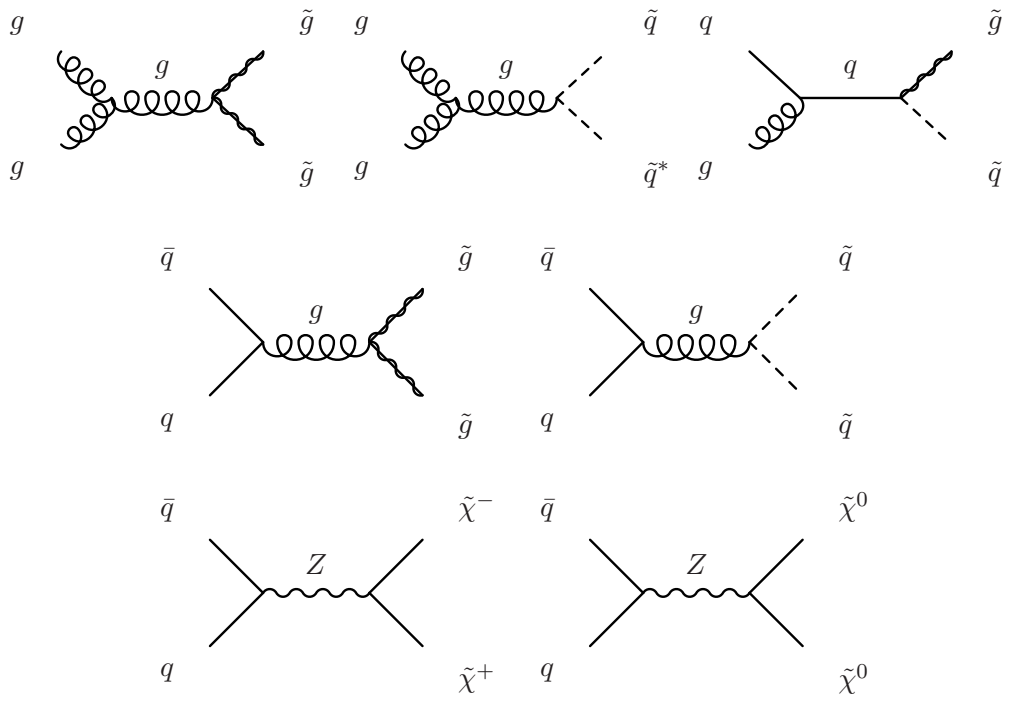

Figure 2.6: Example Feynman diagrams of sparticle production [22]. First row: Gluino and squark production via strong quark and gluon fusion. Second row: Gluino and Squark production via strong quark anti-quark annihilation. Third row: Chargino and neutralino electroweak production.

Decay The LSP in gauge-mediated scenarios is the *gravitino* $\tilde{G}$, which is stable and has a mass less than one keV. The coupling of the gravitino to all other particles is negligible, hence it escapes from the detector without being measured and appears as missing momentum in the event.

The final state is heavily depending on the parameter space configuration and the corresponding *next-to-lightest SUSY particle* (NLSP), whose decay yields a gravitino and an additional SM particle. The mixing ratio of the neutralino components determines the type of the resulting SM particle. In this thesis, only parameter space regions with neutralino NLSPs yielding a photon final state, are considered. For this reason, in the SPS8 scenario, $N_5 = 1$ and small values of $\tan\beta$ are required.

The character of the neutralino is defined by the dominant part of the mixing of gauge eigenstates: A bino-like neutralino, which has a predominant admixture of photino, decays to its SM partner, the photon, and the $\tilde{G}$ LSP as

$$\tilde{\chi}_1^0 \to \gamma\tilde{G}. \tag{2.11}$$

The lifetime τ of the NLSP is depending on the parameter C_{grav}. Only promptly decaying NLSPs corresponding to $C_{\text{grav}} \approx 1$ are considered, thus the NLSP has a decay length of $c\tau < 0.1\,\text{mm}$, where c is the speed of light.

If the $\tilde{\chi}_1^0$ is not produced directly by parton interactions, a decay cascade occurs: Gluinos

mostly decay via

$$\tilde{g} \rightarrow q\tilde{q}. \tag{2.12}$$

Squarks and sleptons can decay, if kinematically allowed, via

$$\tilde{q} \rightarrow q\tilde{g}, \tag{2.13}$$
$$\tilde{q} \rightarrow q\tilde{\chi}_i^0 \tag{2.14}$$

and

$$\tilde{l} \rightarrow l\tilde{\chi}_i^{\pm}, \tag{2.15}$$
$$\tilde{l} \rightarrow l\tilde{\chi}_i^0. \tag{2.16}$$

The decay cascade ends at the stable LSP (see also Eq. 2.11). In such decay cascades, several high energy jets are additionally produced. In summary, the final state consists of several jets, at least two photons and missing energy. The appearance of final state leptons is also possible.

2.3 Universal Extra Dimensions

A brief introduction to universal extra dimensions [67–72] is given in this section with a focus on phenomenologies that yield photons in the final state. In the UED context the SM space-time is extended by a number δ of additional spatial dimensions, where $\delta = 1$ extra dimensions (ED) is chosen in this thesis. The compactification radius R representing the size of the ED, is connected to its curvature $C = 1/R$. The ED is accessible by all particles and forces.

In order to give rise to phenomenons measurable by the LHC, several constraints have been applied: The cutoff scale Λ limits the curvature $\Lambda > C$ at the order of the electroweak scale, while the 5-dimensional Planck scale M_{D} is chosen to be $M_{\mathrm{D}} = 5\,\mathrm{TeV}$ and $\Lambda \cdot R$ is fixed to be 20. The extra dimension has a flat metric and a size of the order of TeV^{-1}. For each SM particle a Kaluza-Klein (KK) tower of excitations exists, where each excitation level represents an UED particle, which is denoted by a star (*), while the ground state is the SM particle. The masses m of the KK excitations read as

$$m^2 = m_{\mathrm{SM}}^2 + \frac{n^2}{R^2}, \tag{2.17}$$

where m_{SM} is the SM particle mass and n the integer level of the KK excitation. Without taking into account radiative correction, the mass spectrum would be degenerated, because the SM mass is much lower than the first excitation. The radiative corrections to the mass, governed by the parameter Λ, depend on the particle type and vary between less than 10 % and 20 % and result in a mass splitting. The Higgs mass is supposed to be $m_{\mathrm{H}} \lesssim 250\,\mathrm{GeV}$ to avoid a diverging Higgs quartic coupling λ_{H} in perturbative calculations. No mixing occurs because of momentum conservation of the fermion KK excitations. An example of a mass spectrum is illustrated in Fig. 2.7 [72]. The *lightest Kaluza-Klein particle* (LKP) is the first level excitation ($n = 1$) γ^* of the photon.

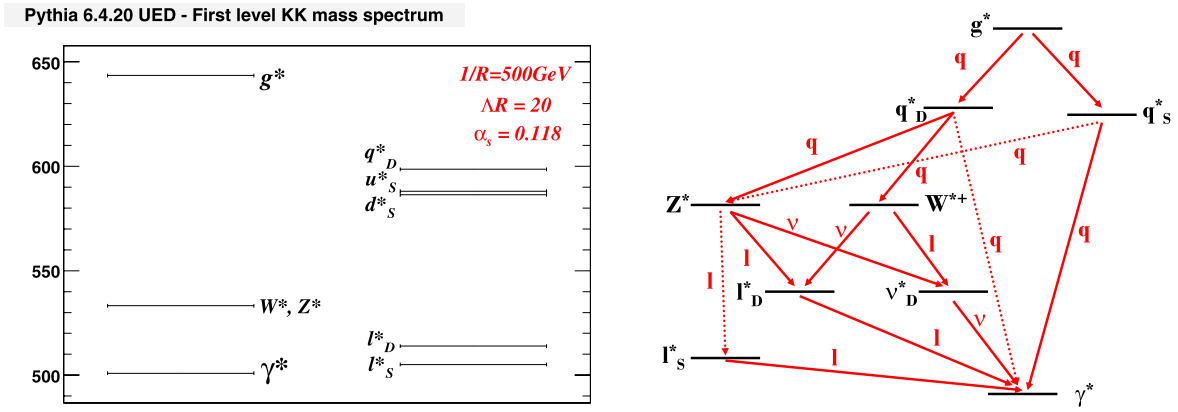

Figure 2.7: The UED mass spectrum (left) and decays (right) [72].

2.3.1 Phenomenology

Because of the momentum conservation in the extra dimension, only pairs of KK excitations are produced, for instance

$$qq \rightarrow q^* q^*. \tag{2.18}$$

The effect is also known as the KK number conservation or KK parity conservation. Although the KK excitation production amplitude is the same as for SM particles, the production cross section is smaller because of their higher masses. Both KK quarks and gluons decay in cascades to the LKPs by yielding jets and leptons. The excitations have the same spin as their SM partners. An example spectrum with possible decays is shown in Fig. 2.7 (right) [72].

Each γ^* LKP can decay finally to a high momentum photon and a non-measurable graviton G, i.e

$$\gamma^* \rightarrow \gamma + G, \tag{2.19}$$

and they create together a $\gamma\gamma + E_{\mathrm{T}}^{\mathrm{miss}}$ signature. The decay is only possible in a KK parity violating scenario: A space-time with N eV^{-1} sized (large) extra dimensions only accessible to gravity embraces the (4+1)-dimensional space-time described before. The KK parity violation is mediated by gravity and allows direct decays of each KK particle to its SM partner and a gravition inducing an overall branching ratio (BR) of less than 100 % to a diphoton final state. In the case of $N = 6$ extra dimensions, the branching ratio for several processes as a function of $1/R$ is depicted in Fig. 2.8.

2.4 State of Knowledge

In the field of GMSB and GGM, as well as in UED models, multiple searches with photon final states have been performed, which do not observe any deviation from the SM expectations. The

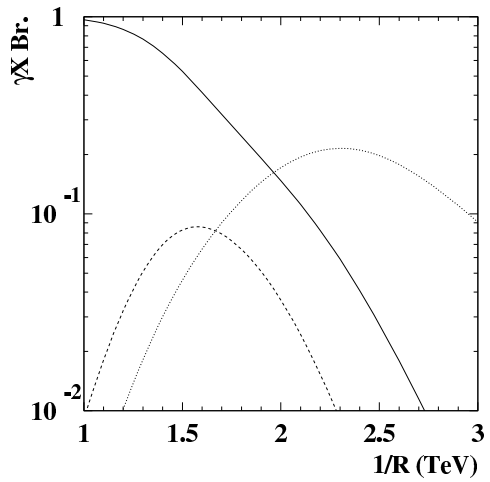

Figure 2.8: The UED branching ratios to $\gamma\gamma$ (solid line), γ + jet (dotted line) and $\gamma + l$ (dashed line) final states as a function of the inverse compactification radius [71]. The underlying model parameters are described in the text.

following searches represent the latest results from the Tevatron[1] experiments: The particular parameter values and choices can be found in the respective references [73–79].

- SPS8 scenario (D0 [73], CDF [74]): Below 149 GeV, promptly decaying $\tilde{\chi}_1^0$ are excluded at 95 % CL. The upper limit (UL) on the breaking scale is determined to be $\Lambda = 124$ TeV.
- UED scenario (D0 [73]): The UL on the compactification radius R in a UED scenario is $1/R > 447$ GeV at 95 % CL.

The following results are based on datasets of $\sqrt{s} = 7$ TeV pp-collisions corresponding to an integrated luminosity of 4.8 fb^{-1} and 4.7 fb^{-1} for ATLAS and CMS, respectively. Some selected contours are illustrated in Fig. 2.9.

- GGM scenario (ATLAS), Fig. 2.9(a): Gluino (squark) masses are excluded below 1.07 TeV (0.87 TeV) at 95 % CL for $\tilde{\chi}_1^0$ masses greater than 50 GeV [75].
- GGM scenario (CMS), Fig. 2.9(b) Gluino masses are excluded below ~ 1020 GeV at 95 % CL for $\tilde{\chi}_1^0$ masses greater than 200 GeV [76]
- SPS8 scenario (ATLAS), Fig. 2.9(c): A 95 % CL exclusion limit of $\Lambda < 196$ TeV is set on the breaking scale Λ [75].
- UED scenario (ATLAS), Fig. 2.9(d): The inverse compactification radius R^{-1} is excluded below $R^{-1} < 1.4$ TeV at 95 % CL [75].

[1] The Tevatron was a hadron collider at the Fermi National Accelerator Laboratory (Fermilab) near Chicago, USA.

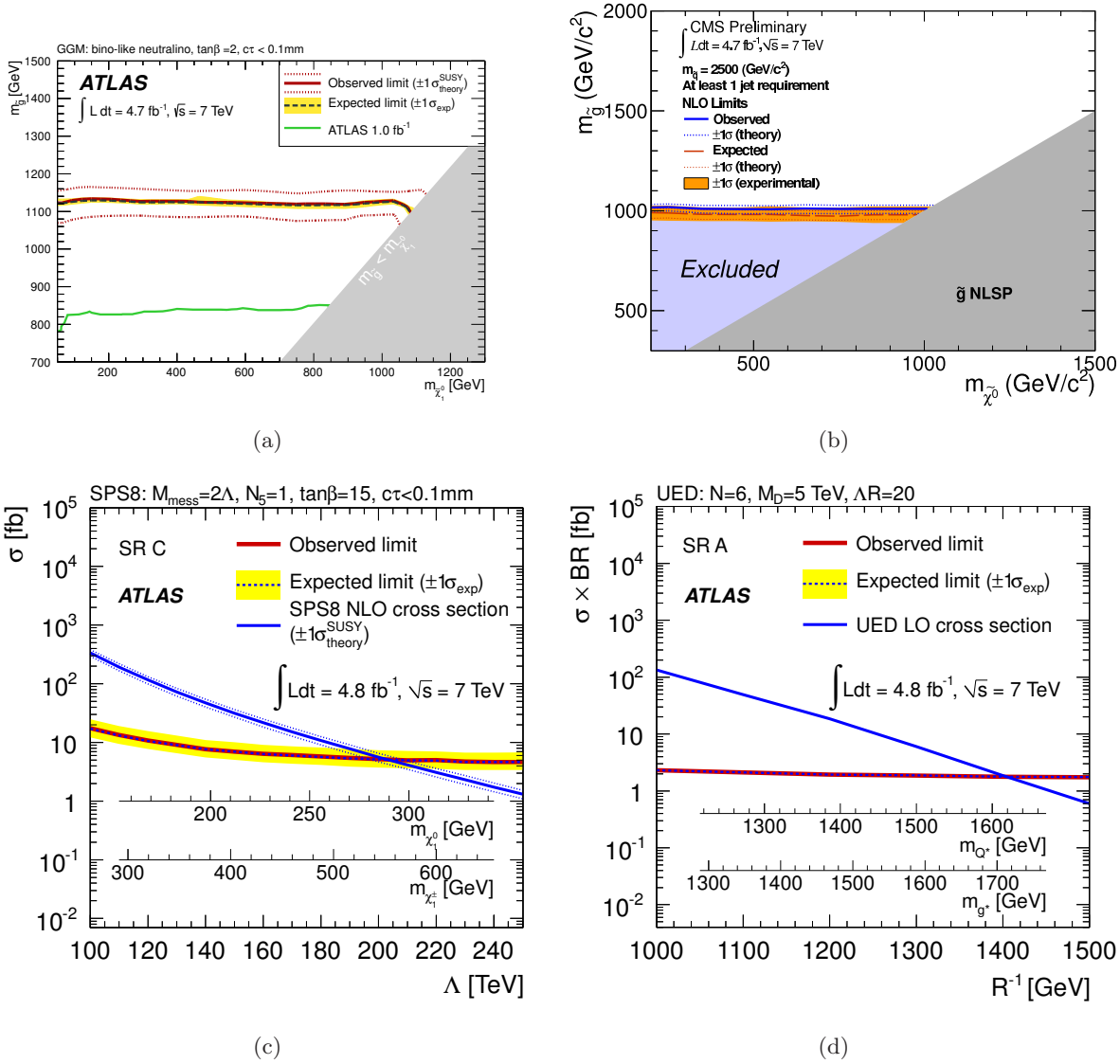

(a) (b)

(c) (d)

Figure 2.9: The 95 % CL exclusion contours for several models: The GGM gluino-bino mass plane from ATLAS determined with an integrated luminosity L = 4.8 fb^{-1} (a) [80]. The GGM gluino-bino mass plane (b) from CMS with L = 4.7 fb^{-1} [76]. The ATLAS SPS8 (c) and UED exclusion contour (d) are both carried out with L = 4.8 fb^{-1} [80].

- UED scenario (CMS), Fig. 2.10: The inverse compactification radius R^{-1} is excluded below $R^{-1} < 1.34$ TeV at 95 % CL [76].

The CMS collaboration has presented results of a search in events with photons and $E_{\mathrm{T}}^{\mathrm{miss}}$ performed on a dataset of $\sqrt{s} = 8$ TeV of pp-collisions corresponding to an integrated luminosity of 4.04 fb^{-1} [77]. Figure 2.10 shows the exclusion limit contour in the $m_{\tilde{q}} - m_{\tilde{g}}$-plane for a bino-like neutralino as an example. Further results of the CMS collaboration of searches in events with photons and $E_{\mathrm{T}}^{\mathrm{miss}}$ can be found in Ref. [78, 79].

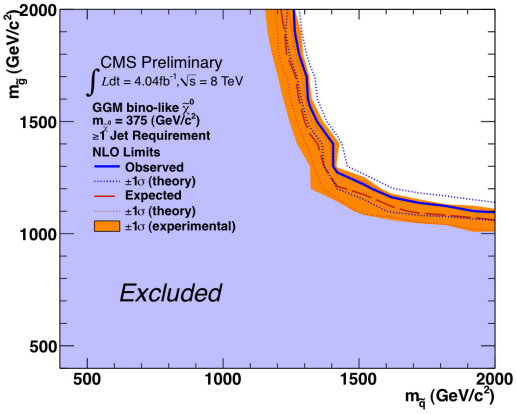

Figure 2.10: A 95 % CL exclusion contour in the $m_{\tilde{q}} - m_{\tilde{g}}$-plane [77]. The center-of-mass energy is $\sqrt{s} = 8\,\text{TeV}$.

CHAPTER 3

The LHC and the ATLAS Detector

In this chapter, the Large Hadron Collider (LHC) and the ATLAS (**A** **T**oroidal **L**HC **A**pparatu**S**) experiment are introduced. The ATLAS detector measures the products of the proton collisions provided by the LHC. The properties and the physics at the LHC as well as the design and the components of the ATLAS detector are described. The first section is dedicated to the LHC and its major technical features are outline. The ATLAS detector and its components are introduced in the second chapter. The trigger is described as a part of the ATLAS detector.

3.1 The LHC

The Large Hadron Collider [81, 82] is a ring accelerator located at CERN[1], the European organization for nuclear research, near Geneva in Switzerland. It uses the underground infrastructure of the LEP[2], closed in the year 2000.

Proton-proton (pp) collisions take place at four interaction points along this ring with a circumference f about 27 km. The protons are accelerated in two diametrical beam pipes to a beam energy up to 3.5 TeV each. This corresponds to a center-of-mass energy of $\sqrt{s} = 7\,\text{TeV}$. The design center-of-mass energy is 14 TeV, which is planned to be reached in 2014. Since the interesting processes are expected to have low cross sections, a high instantaneous luminosity $\mathcal{L}$ is required. In 2011, the peak luminosity reached a value of approx. $3.5 \cdot 10^{33}\,\text{cm}^{-2}\text{s}^{-1}$ [83], while the design value of $\mathcal{L} = 10^{34}\,\text{cm}^{-2}\text{s}^{-1}$ is planed to be achieved in the future.

In order to control the beam at these energies and particle densities, a high vacuum of less than 10^{-10} Torr and superconductive magnets are needed to provide the necessary magnetic field. The magnets can produce dipole fields above 8 T and additional magnets with higher multipole fields are installed. The two beam pipes, the magnets and the cryostat are arranged within one mechanical structure.

Besides the ATLAS experiment, that is considered in this thesis, there are additional major experiments, where particles are brought to collision:

[1] Conseil Européenne pour la Recherche Nucléaire
[2] Large Electron Positron Collider

- CMS[1] is a multipurpose experiment with similar objectives as ATLAS, but with different detector technology.
- LHCb deals with b-meson and flavor physics.
- ALICE[2] investigates heavy-ion collisions, which can also be provided by the LHC.

Before reaching the LHC the protons are stepwise accelerated in the PS[3] and the SPS[4]. A sketch of the LHC, the accelerators and the location of the experiments is shown in Fig. 3.1.

A high luminosity and a high center-of-mass energy are the requirements to probe processes with low cross sections. The event rate [82] of a considered process $\frac{dN}{dt}$ depends on the instantaneous machine luminosity $\mathcal{L}$ and the cross section of the process σ_{process}:

$$\frac{dN}{dt} = \mathcal{L} \cdot \sigma_{\text{process}}. \tag{3.1}$$

The instantaneous machine luminosity $\mathcal{L}$ is given by

$$\mathcal{L} = \frac{N_1 N_2 k \cdot f}{A}, \tag{3.2}$$

where $N_{1,2}$ is the number of particles in a bunch, k the number of bunches in the collider , the revolution frequency f and the effective interaction surface A.

At the nominal center-of-mass energy of 14 TeV, the total cross section σ_{tot} is at the order of 100 mb and has only a weak dependence on $\sqrt{s}$ [85]. The cross sections as a function of the center-of-mass energy of selected example processes are show in Fig. 3.2. The event rate of processes related to BSM are expected to be in the same order of magnitude as the Higgs particle production rate, which is much low than those from jet and SM particle production.

3.2 The ATLAS Detector

The ATLAS detector (see Fig. 3.3) is a multipurpose detector at the LHC. The installation was finished in 2007 and its design reflects the requirements of precision measurements, the high particle density and radiation hardness. This section gives an overview over the components of the detector. A detailed description can be found in reference [81].

The detector has a cylindrical shape with a length of 45 m and diameter of 22 m. It is rotational symmetric round the beam axis z with the interaction point in the center and covers almost the full solid angle. It consists of several subcomponents, that are contained in each other. These are, outgoing from the interaction point: The tracking system (inner detector), which is embedded in a solenoidal magnet field and measures the tracks and momenta of charged particles; The electromagnetic (EM) and hadronic calorimeter, where the energy of

[1] Compact Muon Solenoid
[2] A Large Ion Collider Experiment
[3] Proton Syncrotron
[4] Super Proton Syncrotron

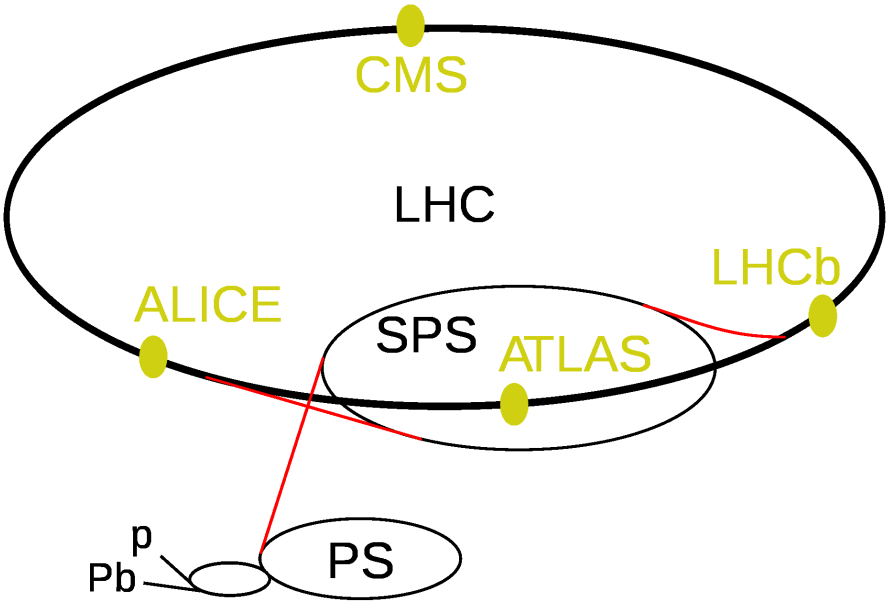

Figure 3.1: The LHC and its experiments [84]. The location of the four main experiments at the LHC and the schematic beam line is shown. Protons (p) or heavy-ions (Pb) are preaccelerated in the PS and the SPS finally injected in the LHC. The size is not to scale.

Detector component	**Required resolution**	η **coverage**	
		Measurement	Trigger
Tracking	$\sigma_{p_\mathrm{T}}/p_\mathrm{T} = 0.05\%\, p_\mathrm{T} \oplus 1\%$	± 2.5	-
EM calorimetry	$\sigma_\mathrm{E}/E = 10\%/\sqrt{E} \oplus 0.7\%$	± 3.2	± 2.5
Hadronic calorimetry (jets)			
Barrel and end-cap	$\sigma_\mathrm{E}/E = 50\%/\sqrt{E} \oplus 3\%$	± 3.2	± 3.2
Forward	$\sigma_\mathrm{E}/E = 100\%/\sqrt{E} \oplus 10\%$	$3.1 < \eta < 4.9$	$3.1 < \eta < 4.9$
Muon spectrometer	$\sigma_{p_\mathrm{T}}/p_\mathrm{T} = 10\%$ at $p_\mathrm{T} = 1$ TeV	± 2.7	± 2.4

Table 3.1: Some performance goals of the subcomponents of the ATLAS detector [81].

interacting particles is measured. Muons are detected and their momenta are measured in the muon system, which is enclosed by a toroidal magnet field.

Due to the high event rates, a high performance trigger and data acquisition (DAQ) is needed. Some important performance goals for the subsystems are summarized in Table 3.1.

3.2.1 The Coordinate System and Conventions

The ATLAS coordinate system is defined such that the z-axis is pointing counter-clockwise in the direction of the beam pipe. The positive x-axis is pointing towards the center of the LHC

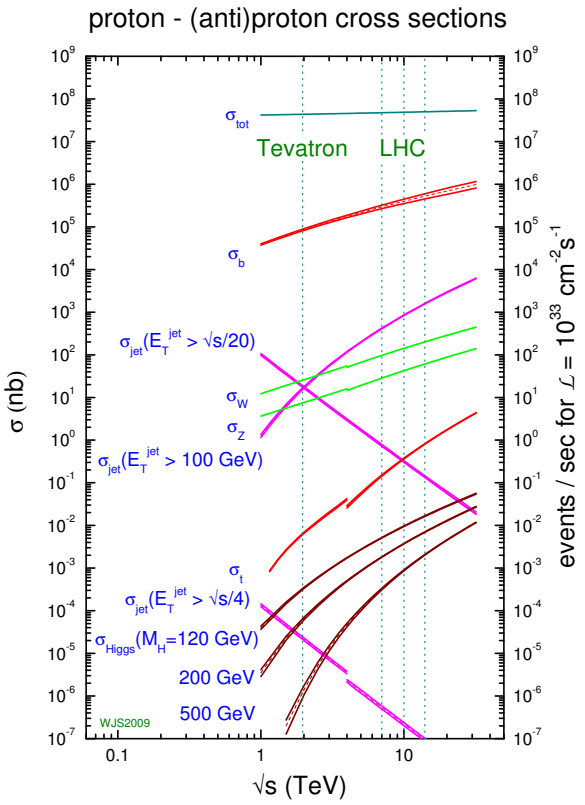

Figure 3.2: Cross sections and event rates of interesting processes as a function of the center-of-mass energy for the LHC and the Tevatron [85]. The LHC provides pp-collisions, while the Tevatron collided $p\bar{p}$.

ring and the positive y-axis to the top.

A spatial direction in the detector is described by the azimuthal angle ϕ, which indicates the direction in the transverse plane to the z-axis and the pseudo-rapidity η, which expresses the direction with respect to the beam axis. The pseudo-rapidity is defined as:

$$\eta = -\ln(\tan\left(\frac{\theta}{2}\right)), \tag{3.3}$$

where θ is the polar angle to the beam axis. The quantity η is chosen because it is more suitable in the relativistic treatment than θ.

The center-of-mass energy of the protons is known in pp-collisions, but not the energy of the interacting partons. Thus, the events can have an unknown Lorentz boost in the direction of the beam pipe. Parton momenta perpendicular to the beam axis can be considered zero before the collision. This implies the measurement of momenta in the transverse $x-y$-plane, which is defined as the Lorentz-invariant quantity

$$\begin{aligned} p_{\mathrm{T}} &= \sqrt{p_x^2 + p_y^2} \\ &= |\vec{p}| \cdot \sin\theta = \frac{|\vec{p}|}{\cosh(\eta)}. \end{aligned} \tag{3.4}$$

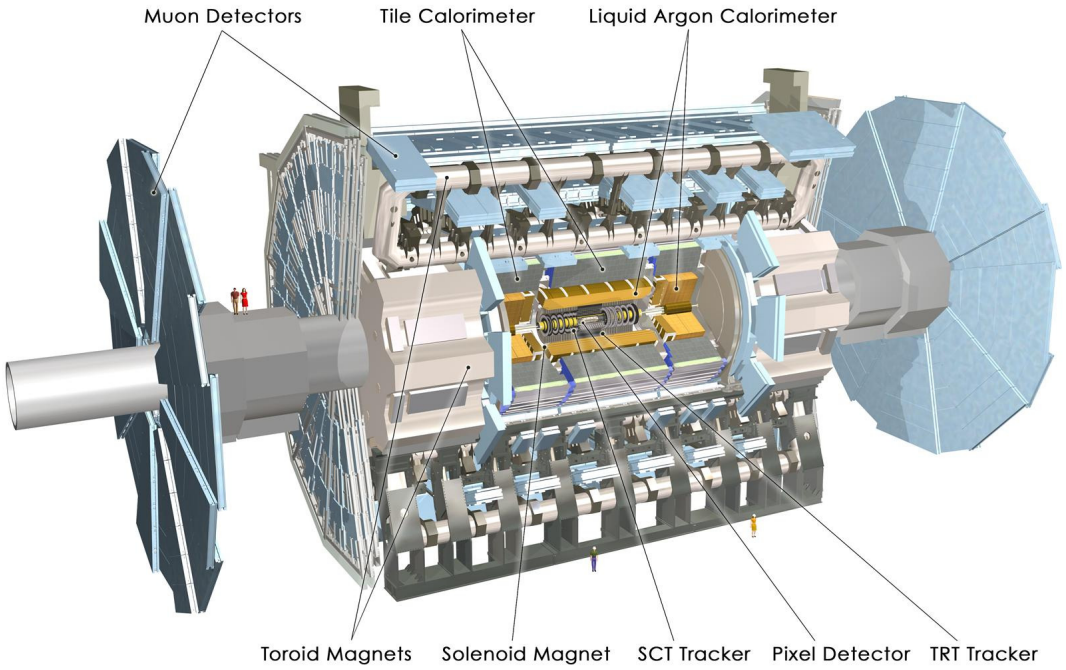

Figure 3.3: Overview of the ATLAS detector and the location of its subcomponents [81, 86].

The absolute value of the transverse momentum is p_{T}, while the x- and y-components are $p_{\mathrm{x,y}}$, and $|\vec{p}|$ is the momentum of a particle. Energies are treated in an analog way.

The distance ΔR of two objects in the $\eta - \phi$-plane given by

$$\Delta R = \sqrt{(\Delta\eta)^2 + (\Delta\phi)^2}, \tag{3.5}$$

where $\Delta\eta$ and $\Delta\phi$ are the distances in η and ϕ, respectively. The speed of light c is not explicitly indicated in most axis labels.

3.2.2 The Magnet System

To measure the momenta of charge particles, their tracks need to be bent by a magnetic field. A design goal is to use as few as possible material in order not to interfere with the measurement. The ATLAS magnet system [81] is composed of the central solenoid and the outer toroid magnets, which are subdivided in barrel and two end-cap parts, and consist of eight superconducting coils each.

The solenoid magnet provides an axial field of 2 T in the area of the inner detector, thus particles are bent in the r-ϕ-plane. The superconducting coils and the cooling infrastructure are located in the radial range between 2.46 m and 2.56 m, between the inner detector and the electromagnetic calorimeter.

The toroid magnets surround the muon system and provide a magnetic field from 0.5 to 1 T in a large area. The field has a torus shape around the beam axis, for this reason the tracks are bent in the r-z-plane. The nominal field strengths are achieved with a current of 7730 A and 20500 A for the solenoid and toroid, respectively.

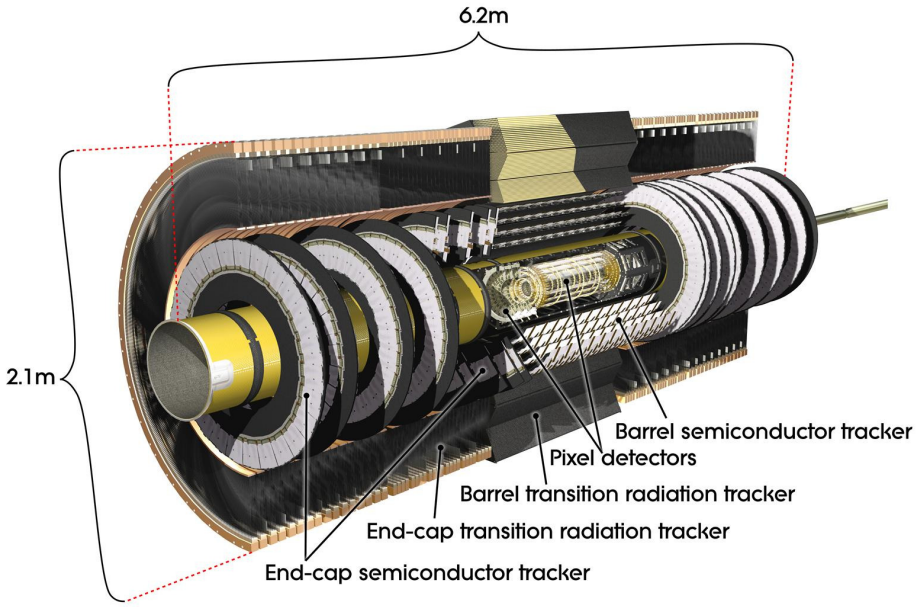

Figure 3.4: The inner detector with its subcomponents [81].

3.2.3 The Inner Detector

The *inner detector* (ID) [81], also referred to as *tracker*, (see Fig. 3.4) is arranged around the interaction point and is surrounded by the solenoid magnet (see Section 3.2.2). Its three major subsystems - the pixel detector, the semi-conductor tracker (SCT) and the transition-radiation tracker (TRT)- provide high accuracy track and vertex measurement. Charged particles leave hits in ID, which are combined to a track by software algorithms. The energy and the sign of the charge can be estimated due to the bending in the magnetic field. Furthermore, the primary interaction vertex as well as secondary vertices can be measured precisely. Photon conversions can occur due to the existing material of the inner detector and the magnet. The track and vertex information are important for the detection of converted photons, which are expected to have tracks from the emerging electron and positron pointing to one source. Nevertheless, a reliable track measurement is needed for the electron and photon discrimination.

The Pixel Detector

The pixel detector is the closest to the interaction point at a distance of 5 cm and it has an acceptance of $|\eta| < 2.5$. It consists of three layers of semiconductor wafers, structured in barrel and two end-caps[1], that need high radiation hardness due to the proximity to the interaction point. The crossing of charged particles is detected by a charge deposition in the semiconductor. The so-called *b-layer* is the innermost layer and most affected by radiation damage. Most of the individual pixel units have a size of $50\times400\,\mu\text{m}^2$, thus a precise position measurement is achieved. The intrinsic resolution of a pixel in the barrel is $10\,\mu$m in (R-ϕ)

[1]The detection layers of the end-caps are also referred to as *disks*.

and 115 μm in z direction. The pixel detector contributes with up to three space points to the track measurement.

The SCT

The SCT envelopes the pixel detector and provides four additional track space points inside the acceptance of $|\eta| < 2.5$. It consists of the three main part, namely the barrel and two end-caps. The sensors, that are aligned in layers, are made of semiconductors, that also need high radiation hardness. The detection principle is similar as in the pixel detector. The SCT sensors in the barrel have an intrinsic resolution of 17 μm in (R-ϕ) and 580 μm in z.

The TRT

Up to 36 additional space points can be measured with the TRT, which is composed of barrel and end-cap modules. Besides, electrons and hadrons, e.g pions, can be distinguished, because high-relativistic electrons produce transition radiation. The TRT is made up of gas-filled ($Xe/CO_2/O_2$) drift tubes with a diameter of 4 mm. The intrinsic resolution of a tube is 130 μm in R-ϕ within the acceptance region of $|\eta| < 2$. Since the straw tubes are aligned parallel to the beam axis (in the barrel), the z-position can not be measured in that region.

3.2.4 Calorimetry

The calorimeter system [81, 87] is used for the precise measurement of the energy and the direction of photons, electrons and jets. Furthermore, the total transverse and the missing transverse momentum (ΣE_{T} and $E_{\mathrm{T}}^{\mathrm{miss}}$) can be measured. The calorimeter system is composed of the electromagnetic (ECal) and the hadronic calorimeter (HCal), which both can be subdivided into barrel, end-cap and forward calorimeters. The layout is shown in Fig. 3.5.

The energy measurement is performed with a sampling technique: Layers of active material, where the energy is measured, and absorbers, where the showers arise due to the energy release [1], alternate.

The electromagnetic barrel and end-cap, the hadronic end-cap (HEC) and the forward calorimeter (FCal) are using liquid argon (LAr) as active material. Their absorber materials are lead, copper and tungsten-copper compounds, respectively. The hadronic barrel and extended barrel use iron as absorber and scintillator tiles as active material. The particles should deposit all their energy in the calorimeters, thus the calorimeter need to be thick enough in units of radiation length and absorption length. In order to achieve uniform energy deposition from most directions, an accordion structure was chosen. The energy loss due to material in the inner detector and the solenoid can be corrected by making use of the *presampler*, located upstream of the calorimeters inside the cryostat, in the range of $|\eta| < 1.8$.

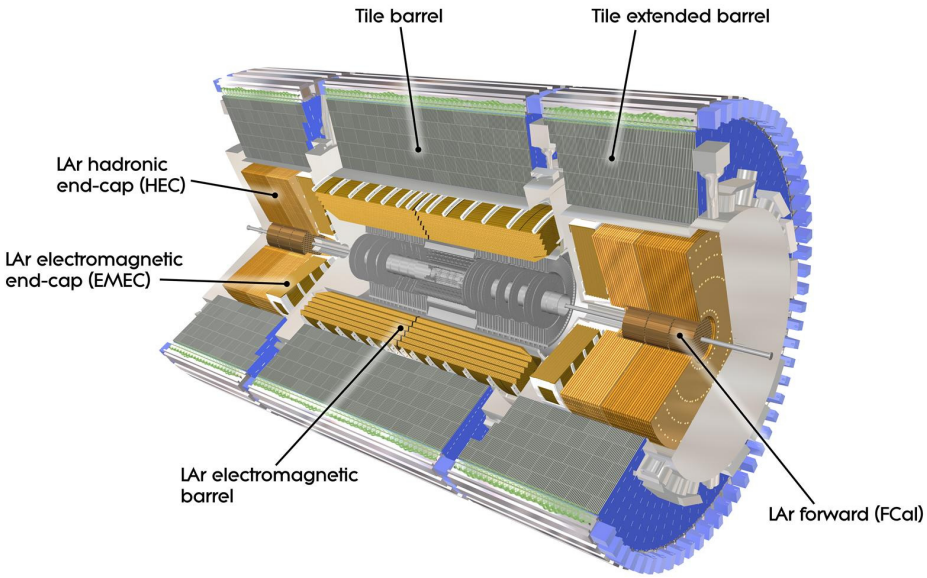

Figure 3.5: The calorimeter system [81].

The Electromagnetic Calorimeter

The electromagnetic calorimeter (ECal) [81, 88, 89] is composed of the electromagnetic barrel ($|\eta| < 1.475$) and the electromagnetic end-caps ($1.375 < |\eta| < 2.5$). In the transition region between barrel and end cap ($1.37 < |\eta| < 1.52$), referred to also as *"crack"*, where supporting infrastructure is located, no reliable measurement can be performed. The two equal parts of the barrel are joined at $|\eta| = 0$. The barrel is housed in a cryostat, that allows temperatures of 88 K in order to keep the Argon in liquid state. Together with the HEC and the FCal, the electromagnetic end-caps are housed in two other cryostats. The electromagnetic calorimeter has an inner radius of 1.25 m and an outer radius of 2.25 m, wherein three cell layers are contained, at a length of ± 4.25 m. Its thickness in units of its radiation length X_0 is 24. The segmentation of the cells of each layer declines outwards. A precise measurement of η is possible, e.g. the discrimination between $\pi^0 \to \gamma\gamma$ decays and prompt photons, due to the fine granularity of the first layer (strip layer) of $\Delta\eta = 0.025/8$ in the barrel. Most of the electromagnetic energy can be deposited in the second layer, which is the thickest in terms of radiation length, with a segmentation in $\Delta\eta \times \Delta\phi$ of (0.025×0.025). The third layer is designed to estimate the leakage of electromagnetic showers out of the EM calorimeter. A schematic view of the electromagnetic calorimeter is shown in Fig. 3.6. The nominal energy resolution $\frac{\sigma(E)}{E}$ of electron and photons is given by $\frac{\sigma(E)}{E} = \frac{10\%}{\sqrt{E}/\mathrm{GeV}} \oplus 0.7\%$. The spatial resolution is constrained by the granularity of the calorimeter cell sizes. Since the energy deposited by an electron or a photon is spread over several cells, the energy of the particle is measured from a cluster of cells, which is build by the reconstruction software (see Section 4.3).

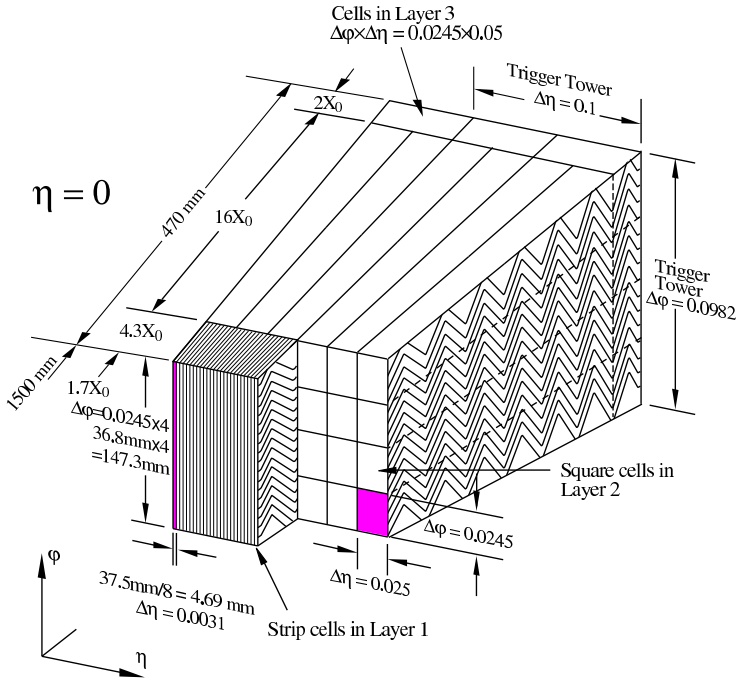

Figure 3.6: Fudge of the electromagnetic calorimeter illustrating the different layers and cell sizes [81].

The Hadronic Calorimeters

The hadronic calorimeter (HCal) [81, 87] consists of the tile calorimeter [90] and the HEC. Since the LAr technology has higher radiation hardness than the scintillator tiles, this material was chosen for the hadronic end-cap region, where higher doses are expected. The segmentation is coarser compared to the ECal, because hadronic showers have a broader spread than electromagnetic showers. In the barrel, the HCal has three layers of cells, where the first two have a granularity of (0.1×0.1) and the third of (0.2×0.1) in $\Delta\eta \times \Delta\phi$.

The Tile Calorimeter The tile calorimeter [90] (TileCal) is made up of the tile barrel ($|\eta| < 1.0$) and the tile extended barrel ($0.8 < |\eta| < 1.7$). In between, there is a gap with support structures, where the two parts overlap in η.

The signal is measured in the following way: Incoming particles excite the atoms of the scintillator, whereupon the emitted light is amplified and transformed in an electrical signal by photo multipliers (PMT).

The tile calorimeter has an inner radius of 2.28 m and an outer radius of 4.25 m at a length of ± 6.65 m and contains three cell layers. The thickness in units of radiation length and absorption length λ is $90 \cdot X_0$ and $7.5 \cdot \lambda$, respectively.

The Hadronic End-cap The hadronic end-cap [81, 87] covers a range of $1.5 < |\eta| < 3.2$, consists also of three cell layers and uses LAr as active material. The absorbers are made of copper. The readout is similar to the readout of the electromagnetic calorimeter.

The Forward Calorimeter

The FCal [81, 87] is a combination of a electromagnetic and a hadronic calorimeter and contains three layers of cells in a pseudo-rapidity range of $3.1 < |\eta| < 4.9$. The first layer can measure electromagnetic interacting particles and the two other hadronic interacting ones. Again, LAr is used due to its radiation hardness.

3.2.5 The Muon Spectrometer

The muon spectrometer, also referred to as muon system (MS) [81, 91], is the outermost subsystem of the ATLAS detector, because muons can pass through the calorimeters with minimal energy loss[1]. The momentum is determined from the bending of the trajectory, thus measured with the aid of the toroid magnet system (see Section 3.2.2). The layout of the muon system is illustrated in Fig. 3.7. It is composed of high accuracy monitored drift tubes (MDT) in the range of $|\eta| < 2.7$, which are supported by cathode strip chambers (CSC) in the forward region $2 < |\eta| < 2.7$. Resistive plate chambers (RPC) and thin gap chambers (TGC) in $|\eta| < 1.05$ and $1.05 < |\eta| < 2.4$, respectively, are used for triggering on charged tracks. The focus for MDT and CSC is a very precise measurement of muon hits, while the latter have strong requirements on the reaction time with less accuracy. MDTs and RPCs are build in three layers, the so-called *stations*.

The MDTs are drift chambers with 3 cm diameter, that are filled with Ar/CO_2 gas mixture. They provide a spatial resolution of 80 μm and a momentum resolution in the barrel region of $\sigma_{p_T}/p_T = 10\%$ at $p_T = 1$ TeV.

3.3 Trigger System and Data Acquisition

In order to select interesting physics events with a limited amount of storage space and bandwidth, ATLAS uses a three level trigger system [81, 92–94]. The nominal bunch crossing rate is 40 MHz at a luminosity of $\mathcal{L} = 10^{34}\,\mathrm{cm}^{-2}\mathrm{s}^{-1}$ which results in an event rate of approx. 1 GHz. Only event rates up to several hundreds Hz can be stored by the data acquisition (DAQ) and can be processed further, in such a way, that the event rate needs to be decreased without loosing the most interesting physics events. The schematic layout of the three trigger levels is shown in Fig. 3.8 together with the expected nominal data and event rates. The trigger system is divided into three levels: The first level (L1), the second level (L2) and the event filter (EF). The first level is operating on hardware close to the detector, where only inputs from the calorimeter and muon trigger chambers are considered. The granularity of the information is reduced in order to keep the latency low. Regions with interesting objects (RoI) are transmitted to the second level at a event rate of less than 100 kHz. The level-2 as well as the EF are software based and are running on computer farms. The first is seeded by the RoIs and the trigger decision is based on data from those regions. The output rate is less than 2 kHz. The remaining events are reconstructed with the full detector information in the event builder

[1] Muons are minimal ionizing particles (MIPs)

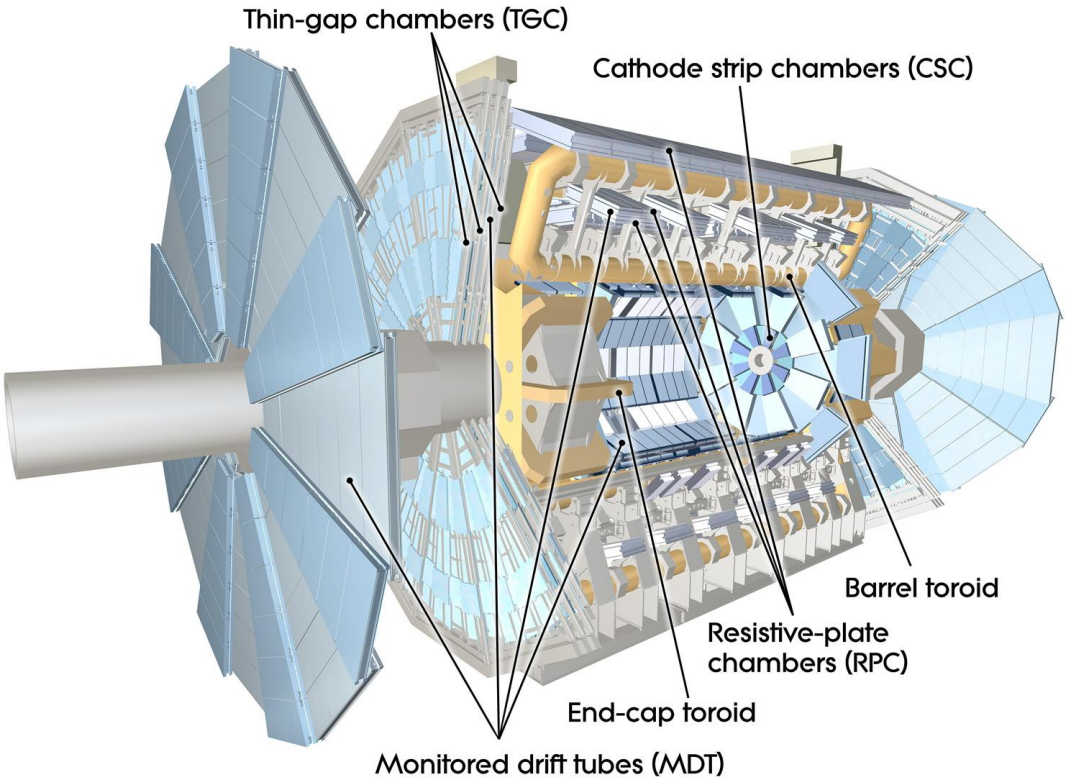

Figure 3.7: The muon system with its components [81].

and the final selection is performed by the event filter. The persistent storage takes place at ≈100 Hz which corresponds to a data rate of $\approx 150 - 300\,\mathrm{MB/s}$.

The trigger menu is the configuration of trigger elements of the different trigger levels and subsystems. Trigger elements represent physical objects with particular requirements, e.g. one photon with $p_\mathrm{T} > 15\,\mathrm{GeV}$ or two jets with $p_\mathrm{T} > 30\,\mathrm{GeV}$ and elements from the three levels are grouped together as a *trigger chain*. The menu reflects the needs of the measurements and the storage constraints and is evolving with different beam conditions.

3.3.1 The Level-1 Trigger

The Level-1 trigger (L1) [81] is in charge of the fast (latency time $< 2.5\,\mu\mathrm{s}$) selection of coarsely reconstructed objects. Objects measured by the calorimeter are treated by the Level-1 calorimeter trigger (L1Calo) subsystem, while objects coming from the muon trigger chambers are processed by the muon trigger subsystem. The input from both subsystems are processed in the central trigger processor (CTP), which performs a decision, whether the event is rejected or further processed, based on the configured trigger menu. If an event is accepted, the coordinates of the region of interest are handed over to the level-2 trigger (L2) and the event buffers of the detector subsystems are read out. Fig. 3.9 provides a sketch of the components and their relation in L1. Events containing photons are selected by L1Calo, which is explained in detail in Section 3.3.3.

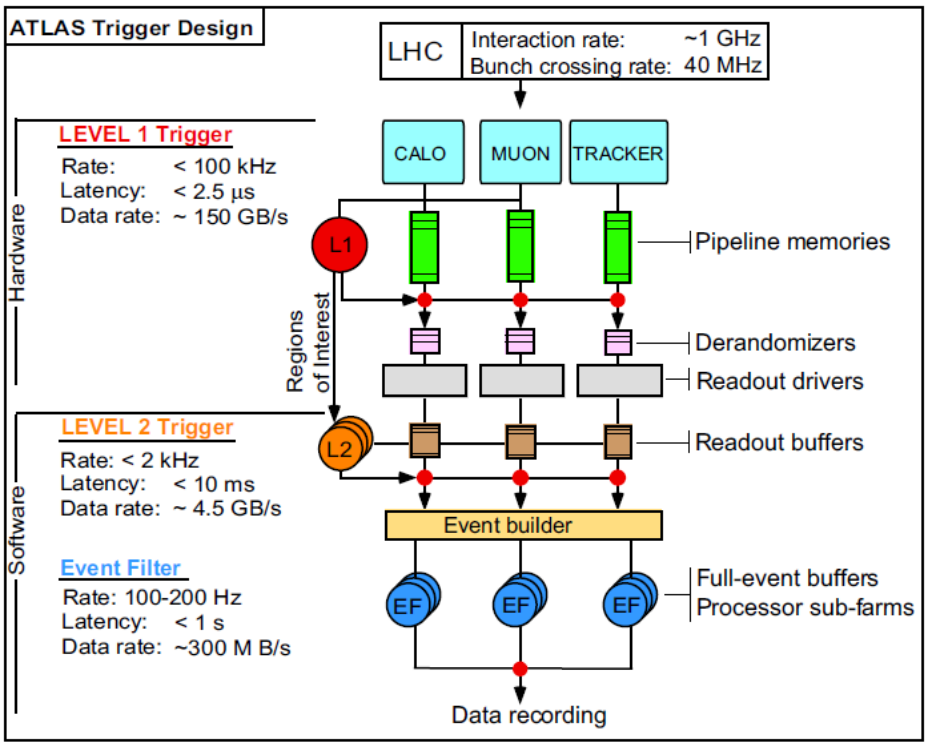

Figure 3.8: The 3-level trigger system [95]. The design event and data rates are quoted on the left.

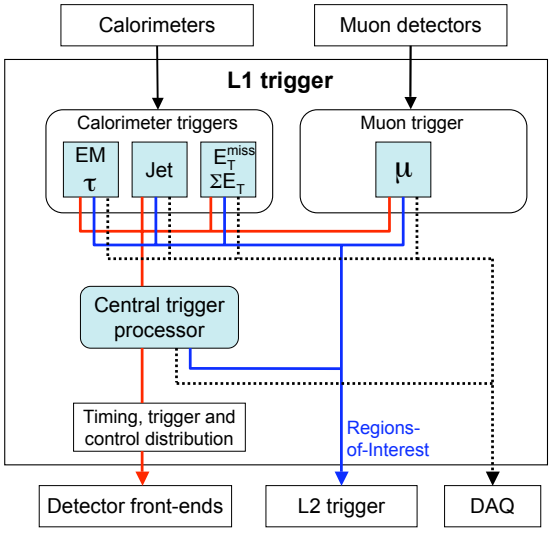

Figure 3.9: The Level-1 trigger system [81].

3.3.2 The High Level Trigger and Data Recording

The Level-2 trigger (L2) [81] and the subsequent event filter (EF) [81] are summarized as high level trigger (HLT) [81], whose software algorithms are running on processor farms. The selection criteria become more complex at higher trigger levels with respect to the level-1

trigger, while the event rate is reduced further. The level-2 trigger receives the RoI coordinates for events, that pass level-1. The L2 decision is based on the full detector information in the RoI, i.e. all detector components (including the ID) at their full granularity is used. This subset represents only 2-6% of the available data. The event data is processed stepwise, in order to minimize the amount of data transfer. The steps are configured by the steering algorithms, which optimizes the processing order for a given trigger menu. If the event does not satisfy a criterion at a certain step, it is rejected imediately. The total event rate is reduced to approximately 1 kHz at L2.

The decision of the event filter, the third trigger level, is based on the full detector information by running the offline reconstruction algorithms (event builder). The output rate of the EF is several hundreds of Hz.

If the event passes the EF, it is recorded permanently. The events are grouped into streams depending on their primary signature, e.g. events selected due to a photon go into the *EGamma stream*, which covers all events triggered by an e/γ signature. Other physics streams are for instance the *Muon* and the *Jet/Tau/Etmiss* stream.

3.3.3 Diphoton Trigger

This section is dedicated to the selection of diphoton events with the ATLAS trigger system. The expected BSM signature involving two photons and missing momentum is selected by a diphoton trigger, that requires at least two photons with a momentum $p_{\mathrm{T}} > 20\,\mathrm{GeV}$. The photons need at least to be consistent with loose identification quality (see Section 4.3.3). The trigger chain for this signature is

$$\texttt{L1\_2EM14} \rightarrow \texttt{L2\_2g20\_loose} \rightarrow \texttt{EF\_2g20\_loose}, \tag{3.6}$$

starting with two electromagnetic objects with an energy greater than 14 GeV at level-1 (`L1_2EM14`). At level-2 (`L2_2g20_loose`) and event filter (`EF_2g20_loose`), two identified photons (`2g`) satisfying loose ID criteria with a $p_{\mathrm{T}} > 20\,\mathrm{GeV}$ are required. At all levels, the chain remains unprescaled[1].

Photon Trigger at Level-1 Photons and electrons are not distinguished at L1, because the ID information is not available. The calorimeter cell energy is summed up over the layers respectively of the electromagnetic and hadronic calorimeter in coarser blocks of (0.1×0.1) in $\Delta\eta \times \Delta\phi$, the so-called *trigger towers*. The decreased granularity allows a faster calculation in the following steps. Inside the acceptance range of $|\eta| < 2.5$, the algorithm searches for energy maxima in the electromagnetic part of the trigger towers in the $(\eta \times \phi)$-plane. The criteria of selecting an electromagnetic energy deposition are

1. a local maximum in two neighboring trigger towers above a certain threshold,

[1] A prescale is the artificial reduction of the event rate by accepting only every n-th event, where n is the prescale factor.

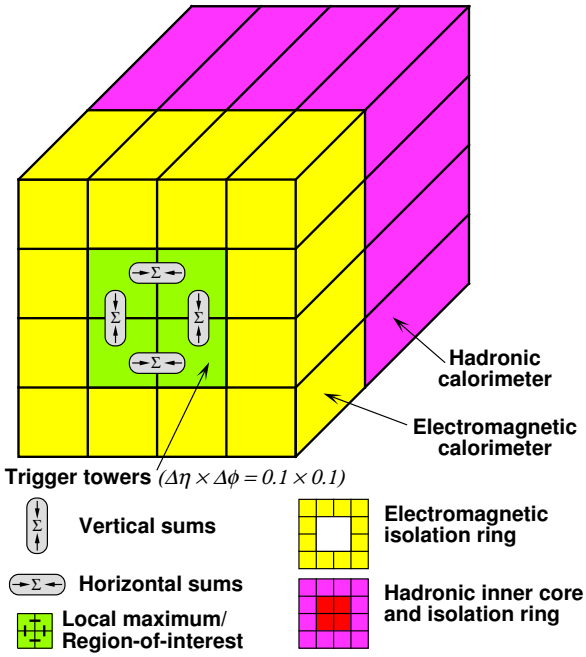

Figure 3.10: Illustration of the level-1 calorimeter cluster finding algorithm [81].

2. the energy in the isolation ring of (4×4) trigger towers is less than a certain threshold or

3. the energy in the hadronic part is less than a certain threshold.

The different thresholds are defined in the trigger menu. The isolation and the hadronic energy veto are required in order to suppress jets, which have a broader spread and a significant amount of energy in the hadronic calorimeter. Fig. 3.10 illustrates the e/γ trigger algorithm. The green area represents the center of the electromagnetic energy deposition, the yellow area the isolation ring. The hadronic trigger towers are drawn in magenta. Besides of photons, the L1Calo trigger is able to search for electrons, taus and jets with similar techniques. Furthermore, the missing energy is calculated and provided as trigger item.

The number of electromagnetic objects together with their energy is handed over to the central trigger processor, which performs the L1 trigger decision according to the implemented trigger menu, which is at least two electromagnetic object with a transverse energy at L1 greater than 14 GeV in the case of the diphoton selection in this thesis.

High Level Photon Trigger At L2, a fast identification and reconstruction of photons is performed oparating on a smaller calorimeter region (0.4×0.4 in $\Delta\eta \times \Delta\phi$) as the offline algorithm and furthermore requires only a subset of identification variables of the *loose* working point (see Section 4.3.3) [96]. The same algorithm as for the offline selection is used at the EF requiring *loose* identification criteria and a momentum threshold of $p_{\mathrm{T}} > 20\,\mathrm{GeV}$ for at least two photons. However, not the full energy corrections with respect to the offline measurement are applied at the HLT due to the necessary decision speed [96].

CHAPTER 4

Reconstruction and Simulation

Measurements with the ATLAS detector require a transformation of the hits in the ID and the energies measured in single cells of the calorimeter to a physics object. Furthermore, the simulation is crucial in many data analysis for the interpretation of the results or for optimization studies. In Section 4.1 to 4.3, the evolution of measured and simulated data to an identified particle is described. In Section 4.4, the simulated samples of SM and BSM processes are listed and described.

4.1 Data Processing

The data processing in ATLAS is centrally performed within the `ATHENA` software framework [97–99]. For simulated events the *simulation chain* is run, which includes the subsequent steps of *generation*, *detector simulation*, *digitization* explained in Section 4.2. After these steps, the simulated data has the same format as measured data from collisions. The last processing step is the *reconstruction and identification* of physics objects, e.g. photons (see Section 4.3). In further data preparation steps, the amount of data is reduced by conserving only the reconstructed physics objects and removing the corresponding calorimeter cell and track hits information.

4.2 Generation and Simulation

Simulations are a powerful tool for physics analysis. Since new physics is not yet discovered, events of such processes need to be generated and their proper detector response needs to be simulated in order to extract results. Similarly for SM processes, the simulations allow a deeper understanding of the physical processes and the detector. The statistical nature of interactions in particle physics are reflected by Monte-Carlo (MC) techniques implemented in MC generator software, which are briefly referred to as *MC generators*.

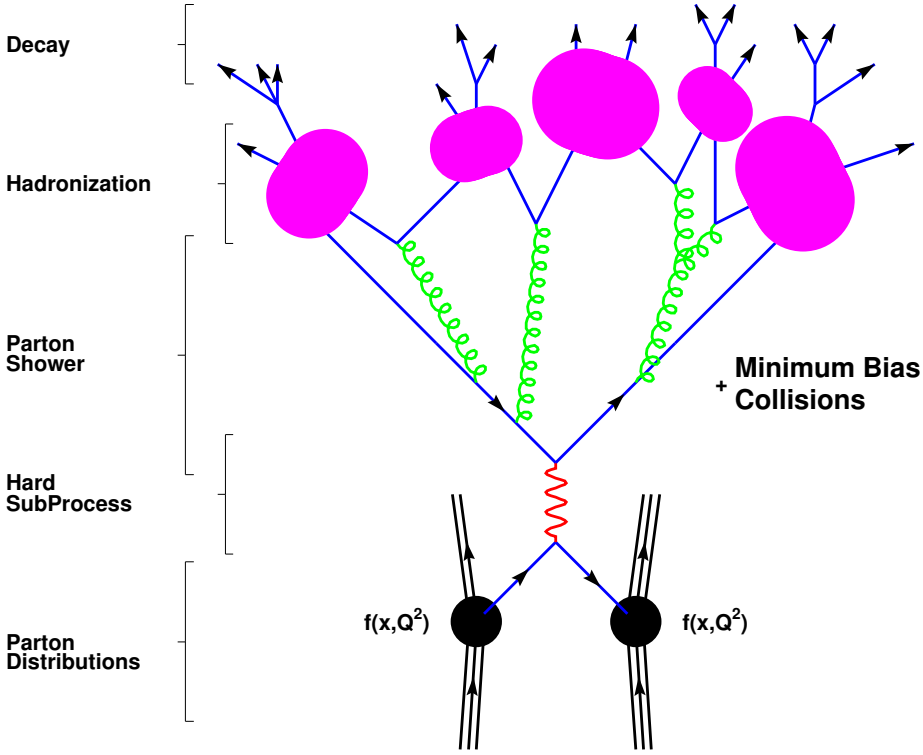

Figure 4.1: The MC event generation stages as implemented in most generators [100]. The processing starts at the bottom with incoming partons and ends up in the decay into final state particles. More information can be found in the text.

4.2.1 Event Generation

The event generation [100, 101] (see Fig. 4.1) can be divided in several stages implemented in many MC generators, e.g `PYTHIA` [102].

The partons of the incoming protons are described by the PDF (see Section 2.1.1). The matrix element of the interaction process is calculated by making use of perturbation techniques. The particles of the final state and production processes can usually be configured. Most generators are working at leading-order perturbation calculations, whereupon the higher order cross section corrections are determined in a later step, for instance with `PROSPINO` [103]. Another approach is, instead of performing higher order calculations, to use modified PDFs, that yields similar results.

The parton cascade reflects the radiative corrections, which gives rise to single partons and photons denoted as initial (ISR) and final state radiation (FSR) depending on their source. Furthermore the *beam remnants*, the colored fragments of the colliding protons are taken into account, which is also referred to as *underlying event*. Possible *multiple interactions*, where more than two initial partons interact, are computed as well.

Only uncolored particles are allowed to exist in the final state, thus the colored particle have to be hadronized. One hadronization approach is presented as example: The idea of the

Lund string model [104, 105] is to couple the color charge and the energy between partons by strings. New particle can arise when the string bursts and arrange with the initial ones to uncolored hadrons.

At the final decay stage, unstable particles decay into their stable final state.

The MC generators are usually able to generate various SM and BSM physics processes. In order to select a particular final state, e.g. at least one photon, an event filter can be imposed. The mass spectrum for BSM physics processes is often provided by external programs, like e.g. `ISAJET` [106]. The generated cross section and the filter efficiency are available after the generation procedure.

4.2.2 MC Generators

In this section, the most important MC generators used in this thesis are briefly introduced. An overview of MC generators is given in reference [100].

`HERWIG` [107, 108] and `HERWIG++` [109, 110] are generic generators with broad functionality and flexibility providing interfaces to tool kits and various inputs. The first is written in FORTRAN, while the latter is a new, improved software based on the knowledge of `HERWIG` and is realized in C++ language. Many SM and SUSY processes, based on e.g. `ISAJET` [106] mass spectra, can be generated. `HERWIG` uses `JIMMY` [111] for the calculation of the underlying event. The showering is done across a large spectrum of partonic evolution including ISR and FSR. The hadronization makes use of the *cluster hadronization model* [100, 112] and polarization effects are considered.

An other powerful generator with similar features is `PYTHIA` [102]. It provides event generation of many $2 \to n$ SM and BSM processes, e.g UED [72], including spin correlations. The showering, hadronization (explained as example in Section 4.2.1) and decay capabilities are used by multiple other generators. Generation of multiparton final states of SM model processes is a strength of the `ALPGEN` [113] generator, which can be interfaced to `PYTHIA` or `HERWIG` for the showering and the hadronization.

The hard interaction is computed at next-to-leading order (NLO) by the `MC@NLO` [114] generator. Hence, the soft parton emission and especially the first hard parton is described more accurate with respect to leading-order (LO) calculations. The showering and hadronization is carried out by `HERWIG`. `MadGraph` [115] provides an easily configurable interface for the generation of a variety of processes. `PYTHIA` is used for the showering and hadronization.

4.2.3 Detector Simulation and Digitization

The propagation of the generated particles through the detector and their interaction is simulated [97, 98] with the help of the program `GEANT4` [116]. The detector geometry, the alignment, material distribution and imperfections are an important input to the simulation. Furthermore the exact magnetic field properties need to be known. The detector simulation is constantly improved by taking information from previous measurements, e.g. test beams, 2009 data or measurement of cosmic rays. The interaction with the detector material of the initial particles

and the subsequently produced particles are propagated further and the resulting showers are computed. The interaction points with the detector (hits) and the energy loss are stored for the further processing. This computational step can be time-consuming due to a large amount of particles. The transformation of the `GEANT4` hits in electronic detector output signals is performed in the *digitization* step. Soft QCD scatterings[1] of two additional colliding protons in the same bunch crossing are referred to as *pile-up* and are superimposed according to the beam configuration.

At this stage the simulated data and the data from real collisions are in the same format and are handed over to the reconstruction (Section 4.3).

4.3 Reconstruction and Identification

For a physics analysis, the raw energy, track hits and position information from each subdetector component need to be transformed back into the underlying physics object. This is done centrally by the reconstruction and identification algorithms. The reconstruction algorithm forms a basic object, while the subsequent identification procedure provides further quality criteria and background suppression methods. Different particles are interacting differently in the subdetectors. For instance, the neutral photons do not induce hits in the tracker in contrast to charged electrons. However, both electrons and photons are electromagnetic objects, that deposit energy in the calorimeter. Hadronic jets are mostly measured by the hadronic calorimeter. Muons can be found by their tracks in the ID and the muon chambers, and are expected to not deposit energy in the calorimeters. The different signatures of these particles are exploited to measure and distinguish them from each other. In the following, the reconstruction and identification procedure of the SM particles used in this thesis are briefly explained with a focus on photons.

4.3.1 Electromagnetic Clustering

Photons and electrons deposit their energy in the electromagnetic calorimeter. Since the cell size is smaller than the expected spread of the energy deposition, the affected cells need to be clustered together to get the total energy of the particle. The clustering is performed by a *sliding-window* algorithm [117], where a rectangle of a fixed size covering multiple cells is iterating over the calorimeter cells in the $\eta \times \phi$ space in order to find a local energy maximum. The size of the rectangle depends on the position in the calorimeter and the corresponding calorimeter cell granularity. The cluster formation is performed in three steps:

- **Tower building:** The energy of all ECal layers is summed in blocks, which are denoted as towers, with a size of (0.025×0.025) in $(\Delta\eta \times \Delta\phi)$ within $|\eta| < 2.5$.
- **Seed finding:** A sliding-window is used to find a local energy maximum in the $\eta \times \phi$-space. The position of the maximum is computed as energy-weighted barycenter in the window and is used as starting point (seed) for the cluster formation.

[1] The so-called *minimum bias* events

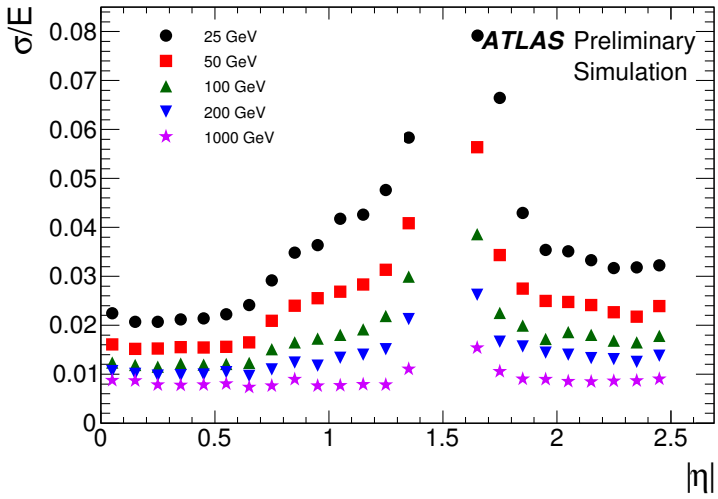

Figure 4.2: Energy resolution of electrons as a function of η for different electrons energies [121].

- **Cluster filling:** The size of the cluster and the energy calibration depends on the type of the subsequently identified object. In the barrel region, the cluster size of an electron is 3×7 cells and that of an unconverted photon is 3×5 cells.

4.3.2 Electrons

The detector signature of electrons ($|\eta| < 2.5$) is expected to consist of an electromagnetic cluster and an associated track after the reconstruction procedure. The standard algorithm [117–120] is initiated from a electromagnetic cluster, if the energy is above a certain threshold. The track matching to a calorimeter cluster is accepted if the distance of the extrapolated track is below a certain threshold. The object is considered as an electron after the matching. The shower shapes are calculated with respect to the new barycenter. In addition, the track is refitted taking Bremsstrahlung losses into account. Electrons from photon conversions are reconstructed as electrons as well, since both consist of an electromagnetic cluster and an associated track, but they can be identified by their non-prompt characteristics (see Section 4.3.3).

If enough hits in the silicon strips, which provide highest accuracy, are available, the η and ϕ direction of the electron is identified from the track parameters, otherwise the direction is measured from the cluster. The energy E is measured from the cluster. The relative energy resolution is illustrated in Fig. 4.2 as a function of η and for different electron energies. The resolution for electron at $p_{\mathrm{T}} > 25\,\mathrm{GeV}$ varies between 2 and 8 %.

The identification is performed via a set of cuts allowing a classification of electrons in three main categories, namely *loose*, *medium* and *tight*, where the subsequent categories include the requirements of the former. The identification criteria are based on shower shape variables (as a function of η and p_{T}) as well as track quality and matching requirements. The background arising from jets being misidentified as electrons, is reduced further by tightening the criteria. Signals originating from noise are reduced by requiring that the energy is distributed over several cells. Table 4.1 summarizes the identification cuts sets. The *loose* ID quality requires

Type	Description	Name
Loose selection		
Acceptance	$\|\eta\| < 2.47$	
Hadronic leakage	Ratio of E_T in the first layer of the hadronic calorimeter to E_T of the EM cluster (used over the range $\|\eta\| < 0.8$ and $\|\eta\| > 1.37$)	R_{had1}
	Ratio of E_T in the hadronic calorimeter to E_T of the EM cluster (used over the range $\|\eta\| > 0.8$ and $\|\eta\| < 1.37$)	R_{had}
Middle layer of EM calorimeter	Ratio of the energy in 3×7 cells over the energy in 7×7 cells centred at the electron cluster position	R_η
	Lateral shower width, $\sqrt{(\Sigma E_i \eta_i^2)/(\Sigma E_i) - ((\Sigma E_i \eta_i)/(\Sigma E_i))^2}$, where E_i is the energy and η_i is the pseudorapidity of cell i and the sum is calculated within a window of 3×5 cells	$w_{\eta 2}$
Medium selection (includes loose)		
Strip layer of EM calorimeter	Shower width, $\sqrt{(\Sigma E_i (i - i_{\mathrm{max}})^2)(\Sigma E_i)}$, where i runs over all strips in a window of $\Delta\eta \times \Delta\phi \approx 0.0625 \times 0.2$, corresponding typically to 20 strips in η, and i_{max} is the index of the highest-energy strip	w_{stot}
	Ratio of the energy difference between the largest and second largest energy deposits in the cluster over the sum of these energies	E_{ratio}
Track quality	Number of hits in the pixel detector (≥ 1)	n_{pixel}
	Number of total hits in the pixel and SCT detectors (≥ 7)	n_{Si}
	Transverse impact parameter ($\|d_0\|$ <5 mm)	d_0
Track–cluster matching	$\Delta\eta$ between the cluster position in the strip layer and the extrapolated track ($\|\Delta\eta\| < 0.01$)	$\Delta\eta$
Tight selection (includes medium)		
Track–cluster matching	$\Delta\phi$ between the cluster position in the middle layer and the extrapolated track ($\|\Delta\phi\| < 0.02$)	$\Delta\phi$
	Ratio of the cluster energy to the track momentum	E/p
	Tighter $\Delta\eta$ requirement ($\|\Delta\eta\| < 0.005$)	$\Delta\eta$
Track quality	Tighter transverse impact parameter requirement ($\|d_0\|$ <1 mm)	d_0
TRT	Total number of hits in the TRT	n_{TRT}
	Ratio of the number of high-threshold hits to the total number of hits in the TRT	f_{HT}
Conversions	Number of hits in the b-layer (≥ 1)	n_{BL}
	Veto electron candidates matched to reconstructed photon conversions	

Table 4.1: Summary of variables and cut thresholds for *loose*, *medium*, and *tight* identification of electrons within $|\eta| < 2.47$ [118].

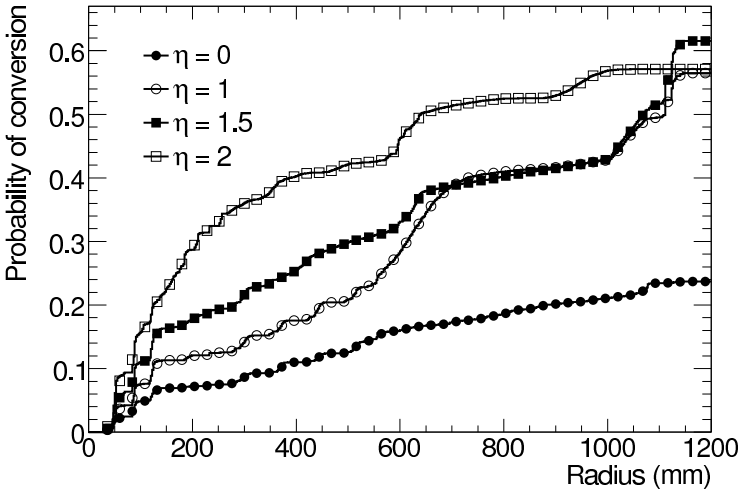

Figure 4.3: Conversion probability of a photon in dependence of the conversion radius and the pseudo-rapidity [120].

a cut against energy leakage in the hadronic calorimeter and the shower shape in the second calorimeter layer. Electrons can be distinguished from jets via the width of the shower. The *medium* ID adds cuts in the first calorimeter layer (against π^0 decays) and track quality criteria are required. The highest background suppression is achieved using the *tight* ID, where harsher requirements on the track quality including hits in the b-layer and asking for high-threshold TRT hits. Furthermore, electrons candidates consistent with electrons from photon conversions are rejected.

4.3.3 Photons

A photon can convert into a e^+e^- pair, when it is propagating through the tracker due to interactions with the detector material. Such photons are denoted *converted photons*. The space point, where the conversion takes place is the conversion vertex, where the conversion radius is the distance of the conversion vertex to the interaction point. Since the matter distribution in the tracker is not homogeneous, the conversion probability is a function of the pseudo-rapidity and increases with the traversed matter, which is demonstrated in Fig. 4.3. If the photon passes through the tracker without converting, it is called *unconverted photon*. The different possible signatures of photons in the detector as well as the ambiguity between prompt electrons and electrons from conversions need to be accounted for in the reconstruction and identification [120–124].

Unconverted Photons The reconstruction of unconverted photons ($|\eta| < 2.37$) starts from an electromagnetic cluster found by the sliding window algorithm (see Section 4.3.1). If no track can be associated to the cluster, the object is considered to be a photon candidate [120–124]. The energy of the photon is measured from the cluster energy and the position is estimated from the energy weighted barycenter of the cluster.

Category	Efficiency (%)
All photons	97.82 ± 0.03
Unconverted photons	99.83 ± 0.01
Converted photons	94.33 ± 0.09

Table 4.2: Summary of reconstruction efficiencies for different photon categories. Photons ($p_{\mathrm{T}} > 20\,\mathrm{GeV}$) within $|\eta| < 2.37$ excluding the region of $1.37 < |\eta| < 1.52$, are considered [122].

Converted photons Converted photons ($|\eta| < 2.37$) are identified by a conversion vertex in the inner detector with associated tracks pointing to a electromagnetic cluster. Details and additional information about tracking can be found in [120–124]. If two tracks are originating from the same vertex, the conversion is classified as *double-track conversion* and a combined fit is performed. If one of the conversion electrons is not reconstructed, for instance if the conversions takes place in the outer regions of the tracker, the conversion vertex is defined at the starting point of the single track and is referred to as *single-track conversion*. The final matching between cluster and vertex tracks has to pass certain thresholds. The assigned tracks are refitted under the assumption of originating from a massless photon and Bremsstrahlung losses are taken into account. Prompt electrons and electrons from conversions can be distinguished by the presence of a conversion vertex, so their ambiguity can be reduced. The converted photon energy is measured from the calorimeter cluster, while the direction is taken from the vertex.

The reconstruction efficiency of converted, unconverted, and all photons with $p_{\mathrm{T}} > 20\,\mathrm{GeV}$ in $|\eta| < 2.37$ excluding the region of $1.37 < |\eta| < 1.52$[1], is summarized in Table 4.2. It shows a high total photon reconstruction efficiency of almost 98 %, while the best reconstruction efficiency can be achieved for unconverted photons.

The relative energy resolution is illustrated in Fig. 4.4(a) for converted and in Fig. 4.4(b) for unconverted photons as a function of η and for different photon energies. The resolution for unconverted photons is better, since the resolution of the converted photons is based also on the tracking performance. Except in one η-bin, the resolution of $p_{\mathrm{T}} > 25\,\mathrm{GeV}$ photons is better than 3 % for converted and 2 % for unconverted photons.

Since possible backgrounds from $\pi^0 \to \gamma\gamma$ or QCD jets and electrons misidentified as photons need to be suppressed for physics analysis, the identification step imposes additional requirements on the photon candidates. Two set of cuts, namely *loose* and *tight*, are defined where the latter extends the first. Photons are classified according to the passed identification cut set, where the background rejection is increased with the tightness of the cuts. Table 4.3 lists the quantities on which the photon identification is based for *loose* and *tight* [120–122]. The *tight* set makes use of the full set of available variables, which are related to the hadronic calorimeter, the first or the second ECal compartment. The particular cuts on the quantities

[1]The transition region between the barrel and the end-caps of the calorimeter is excluded because of the poor measurement efficiency in that region.

Category	Description	Name	Loose	Tight
Acceptance	$\|\eta\| < 2.37$, $1.37 < \|\eta\| < 1.52$ excluded	–		✓
Hadronic leakage	Ratio of E_T in the first sampling of the hadronic calorimeter to E_T of the EM cluster (used over the range $\|\eta\| < 0.8$ and $\|\eta\| > 1.37$)	R_{had_1}	✓	✓
	Ratio of E_T in all the hadronic calorimeter to E_T of the EM cluster (used over the range $0.8 < \|\eta\| < 1.37$)	R_{had}	✓	✓
EM Middle layer	Ratio in η of cell energies in 3×7 versus 7×7 cells	R_η	✓	✓
	Lateral width of the shower	w_2	✓	✓
	Ratio in ϕ of cell energies in 3×3 and 3×7 cells	R_ϕ		✓
EM Strip layer	Shower width for three strips around maximum strip	$w_{s\,3}$		✓
	Total lateral shower width	$w_{s\,\text{tot}}$		✓
	Fraction of energy outside core of three central strips but within seven strips	F_{side}		✓
	Difference between the energy associated with the second maximum in the strip layer, and the energy reconstructed in the strip with the minimal value found between the first and second maxima	ΔE		✓
	Ratio of the energy difference associated with the largest and second largest energy deposits over the sum of these energies	E_{ratio}		✓

Table 4.3: Variables used for photon identification and their description [122].

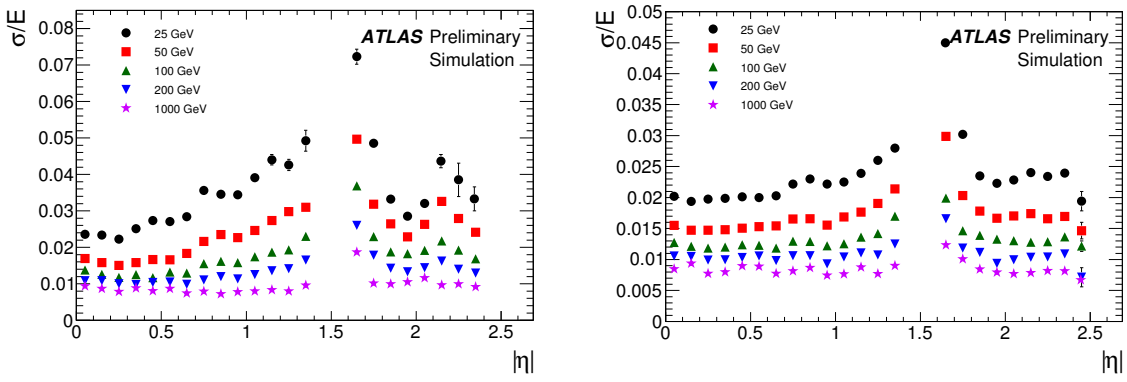

(a) (b)

Figure 4.4: Energy resolution of converted (a) and unconverted (b) photons as a function of η for different photon energies [121].

are applied depending on the η and E_{T} value. Furthermore, the difference of converted and unconverted photons is reflected in the cut thresholds. The QCD background can be suppressed by requiring only a small fraction of the cluster energy in the HCal. The jet $\rightarrow \gamma$ ($p_{\mathrm{T}} > 40\,\mathrm{GeV}$) background rejection can be improved by a factor of approximately 5 from *loose* to *tight* identification quality, resulting in a misidentification rate of a single jet of roughly 0.0002. The cuts in the second ECal layer exploit the fact, that showers of real photons have a narrower spread than QCD jets. Another important background that needs to be rejected comes from neutral pion, η or ω decays with two photons: The design of the first ECal sampling layer with its fine granularity allows the detection of the two peak structure of such backgrounds.

In addition to the *tight* requirements, the ambiguity between electrons from converted photons and prompt electrons can be further reduced by the *tightAR*[1] quality criterion, which takes dead pixels in b-layer modules into account.

The combined reconstruction and identification efficiency estimated from a simulated $H \rightarrow \gamma\gamma$ sample is (96.46±0.05) % for *loose* and (90.06±0.08) % for *tight* photons with $p_{\mathrm{T}} > 40\,\mathrm{GeV}$ [122].

4.3.4 Jets

Jets arise from hadronized partons and comprise a bunch of particles going in the direction of the initial parton. Since jets contain electromagnetic (charged and neutral) and hadronic interacting particles, the measurement includes both the hadronic and the electromagnetic calorimeter, whereupon the main fraction of particles is expected to be heavy hadrons. The spread of jets is usually broader than the one from single electromagnetic particles. The jet finding and measurement is performed by the *Anti-k_{T}* jet algorithm [120, 125, 126]. This algorithm attempts to fulfill multiple design principles, for instance infrared safety, collinear safety and high detection efficiency, which are discussed in detail in [120]. The jet algorithm operates on topological calorimeter clusters [127]. By looping over all clusters and the subsequent

[1] AR: ambiguity resolved

combination of the inverse 4-momenta ("Anti-k_T") of two objects (cluster or emerging jets) weighted by their distance, jets are formed. The distance weighting is a function of the jet cone distance parameter R. The jet energy is calibrated (referred to as *EM+JES* calibration) taking into account corrections due to pile-up, the position shift with respect to the primary vertex, the jet modeling from MC and detector quality criteria [128]. The direction of the jet is estimated from its barycenter with respect to the primary vertex.

The jet reconstruction efficiency is increasing from above 90 % for jet with $p_T = 25\,\text{GeV}$ to 99 % for jet with $p_T > 40\,\text{GeV}$. The uncertainty is approx. 2 % in the low-p_T jet region and is negligible in the high-p_T region [128]. The relative energy resolution of Anti-k_T ($R = 0.4$) jets ranges between 6 and 8 % depending on the η position ($|\eta| < 2.8$) and the momentum [126].

Since also cluster from single photons or electrons may be reconstructed as jets, an overlap removal between jets and the single objects has to be performed at the analysis level (see Section 5.3).

4.3.5 Muons

Muons can be measured in the ID and the muon system, while they traverse the calorimeters mostly with only minimal ionizing interactions in most cases [120, 129–133]. If both tracks in the ID and the MS can be matched, the object is denoted *combined* muon. If track segments (a primary stage of a full track) are found in the MS, that can be joined to an ID track, the muon is denoted *segment tagged* muon. The *staco* algorithm chain performs the corporate muon ($|\eta| < 2.5$) reconstruction by considering the ID and MS measurements as well as multiple scatterings in crossed material and the energy loss in the calorimeter in a fit. The muon 4-momentum is extracted from the fit result.

The mean corporate reconstruction efficiency [134] of combined and segment tagged muon is estimated as 0.970 ± 0.001. The relative momentum resolution varies between 5 and 23 % as a function of η and p_T [135].

4.3.6 Missing Transverse Energy

The missing transverse energy E_T^{miss} is an important quantity in many new physics signatures and represents particles, that escape from the detector without being measured. Since the transverse momentum is not balanced in case of undetected particles, such particles can only be identified by E_T^{miss}. Its determination relies on the full calorimeter cluster and muon (ID and MS) measurements, i.e. on the whole detector. In this thesis, a cell based E_T^{miss} computation (*LocHadTopo*) is used [120, 136] starting from topological cluster ($|\eta| < 4.5$) [127]. The clusters energy calibration is applied according to the shower shape based on the characterization of the cluster as either hadronic or electromagnetic, i.e for hadronic clusters, the *local hadronic* calibration is used [137]. The non-negligible energy loss in the cryostat is estimated from the energy deposition in the closest layers of the ECal and the HCal and is incorporated into the calorimeter cluster cell term (see Eq. 4.1). In addition, the energy of muons needs to be taken into account. In order to avoid double counting, the energy in the calorimeter deposited

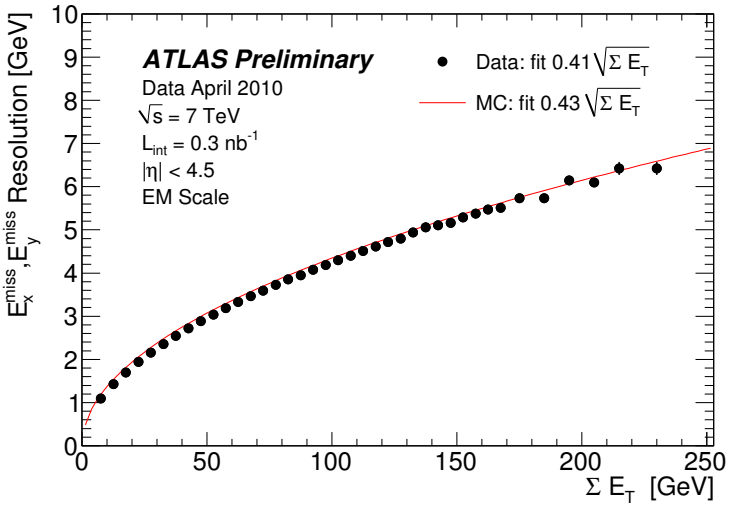

Figure 4.5: The resolution of $E_{\mathrm{x,y}}^{\mathrm{miss}}$ as a function of the total transverse energy in data and MC. A fit to MC is superimposed [138].

by muons[1] needs to be subtracted. The total missing transverse momentum is calculated as follows:

$$\begin{aligned} E_{\mathrm{T}}^{\mathrm{miss}}(x) &= -\sum_{\text{cluster cells}} E_{\mathrm{cell}} \sin\theta_{\mathrm{cell}} \sin\phi_{\mathrm{cell}} + \sum_{\text{all } \mu} p_{\mathrm{x}}^{\mu} - \sum_{\text{calo } \mu} E_{\mu} \sin\theta_{\mu} \sin\phi_{\mu}, \\ E_{\mathrm{T}}^{\mathrm{miss}}(y) &= -\sum_{\text{cluster cells}} E_{\mathrm{cell}} \sin\theta_{\mathrm{cell}} \sin\phi_{\mathrm{cell}} + \sum_{\text{all } \mu} p_{\mathrm{y}}^{\mu} - \sum_{\text{calo } \mu} E_{\mu} \sin\theta_{\mu} \sin\phi_{\mu}, \\ E_{\mathrm{T}}^{\mathrm{miss}} &= \sqrt{(E_{\mathrm{T}}^{\mathrm{miss}}(x))^2 + (E_{\mathrm{T}}^{\mathrm{miss}}(y))^2}, \end{aligned} \tag{4.1}$$

where the term $\sum_{\text{all } \mu} p^{\mu}$ denotes the contribution from reconstructed muons and the term $\sum_{\text{calo } \mu} E_{\mu} \sin\theta_{\mu} \sin\phi_{\mu}$ the energy loss of muons in the calorimeter. The total energy sum in the calorimeter $\sum E_{\mathrm{T}}$ of an event is computed by

$$\sum E_{\mathrm{T}} = \sum_{\text{cluster cells}} E_{\mathrm{cell}} \sin\theta_{\mathrm{cell}}. \tag{4.2}$$

The resolution of the x- and y component of $E_{\mathrm{T}}^{\mathrm{miss}}$ as a function of the total transverse energy is illustrated in Fig. 4.5 [138]. A good agreement between data and MC can be observed.

[1] This energy is stored in the `MET_RefMuon_Track` variable in ATLAS

4.4 Monte Carlo Samples

Samples of the expected signal in various models as well as SM background samples are needed to gain a deeper understanding of the measurement and extract results. In this section, the MC samples, used in this thesis are described.

For GGM with a bino-like $\tilde{\chi}_1^0$ two scenarios are considered and MC samples are generated accordingly: The first, in which the varying parameters are the $\tilde{g}$ and the lightest $\tilde{\chi}_1^0$ mass and the second, in which the varying parameters are the $\tilde{q}$ and the $\tilde{\chi}_1^0$ mass. The other masses are set to a higher scale. The two GGM scenarios are referred to as *GGM scenario with varying $\tilde{g}$ mass* and *GGM scenario with varying $\tilde{q}$ mass*.

Besides, MC samples are generated GMSB SPS8 scenario, where Λ is the only free parameter and the UED scenario, where R^{-1} is the only free parameter. The particular choice of model parameters and technical information on the generation procedure are described in the following sections.

The full SM background is attempted to be modeled by background samples (see Section 4.4.1), i.e. multijet, γ + jets, SM $\gamma\gamma$, and by vector boson decays with associated jets or photons, for instance $W \to e\nu$ + jets and $W(\to e\nu)$ + jets/γ, and top decays. An overview of MC generators used in this thesis is given in Section 4.2.2. The generators `PYTHIA` and `HERWIG` use the *2011 ATLAS tune* MC parameter set optimized for the 2011 data taking conditions [139, 140].

4.4.1 Background Samples

In this analysis, the SM background is mainly determined directly from data. However, for cross checks and composition studies, the SM background is modeled by several MC samples (e.g. see Section 5.4.1). Furthermore, the contamination of background control samples selected from data is probed using MC samples. The irreducible background components, i.e. background that can not be eliminated by selection cuts, needs to be fully estimated from MC since no data-driven approach is possible (see Section 6.3). Table 4.4 summarizes the SM background samples with their highest-order cross section and the used MC generator. A detailed list can be found in Table A.1 and Table A.2. The fragmentation and hadronization is performed for each sample either by `HERWIG` or `PYTHIA`. MRST PDFs are used in the generation of the QCD jet samples and prompt photon sample, while the remainder are based on CTEQ PDFs [141, 142]. The processes of $gg, q\bar{q} \to \gamma\gamma$ are represented by the prompt $\gamma\gamma$ sample (also referred to as SM $\gamma\gamma$ sample) and are collected by a filter requiring two photons ($p_{\mathrm{T}} > 50\,\mathrm{GeV}$) at generator level. The QCD γ + jets sample represents the scattering processes of $qg \to q\gamma, q\bar{q} \to g\gamma$, thus at least one photon above a subsample-dependent photon p_{T} threshold is required a generator level. These subsamples are combined to ensure adequate statistics, such that there is no overlap in terms of double counting events. Due to their genuine $E_{\mathrm{T}}^{\mathrm{miss}}$ induced by neutrinos ν the electroweak MC samples represent a major background, where the diphoton signature can arise either from true photons or fake photons coming from electrons or jets. Final states with up to five partons are simulated. A large background fraction is expected to arise from

process	cross section [pb]	generator
QCD jet	$10.5 \cdot 10^9$	PYTHIA
QCD γ + jets	$123 \cdot 10^3$	PYTHIA
prompt $\gamma\gamma$	5.27	PYTHIA
$W \to (l\nu)$ + jets	$31.4 \cdot 10^3$	ALPGEN
$W \to (l\nu)\gamma$ + jets	100.3	PYTHIAMadGraph
$W \to (l\nu)\gamma\gamma$	0.147	PYTHIAMadGraph
$Z \to (ll)$ + jets	$4.27 \cdot 10^3$	ALPGEN
$Z \to (ll)\gamma$ + jets	21.6	PYTHIAMadGraph
$Z \to (ll)\gamma\gamma$	0.014	PYTHIAMadGraph
$t\bar{t}$, single t	204.9	MC@NLOHERWIG

Table 4.4: Summary of the used background MC processes along with the highest-order cross section and the generator [143, 144]. The generators are described in Section 4.2.2.

hadronic or leptonic top decays, where electrons are misidentified as photons and $E_{\mathrm{T}}^{\mathrm{miss}}$ induced by ν. Single top events are considered as well.

4.4.2 GGM Samples

For the optimization of the selection sensitivity and the determination of the selection efficiency, signal event samples must be simulated. The GGM model has been introduced in Section 2.2.4. For the MC generation of the scenario with varying $\tilde{g}$ mass, the following parameter values are chosen: The mass of the squark and other masses are set to 2.5 TeV, $M_2 = \mu = 2.5\,\mathrm{TeV}$, $\tan\beta = 2$, and $c\tau_{\mathrm{NLSP}} < 0.1\,\mathrm{mm}$. The resulting mass spectrum is computed by SUSPECT 2.41 [145] and the decay properties are obtained from SDECAY 1.3 [146]. For the scenario with varying $\tilde{q}$ mass, the $\tilde{g}$ mass is set at $m_{\tilde{g}} = 2.5\,\mathrm{TeV}$ instead. The only available production channel is $\tilde{g}\tilde{g}$ in the scenario with varying $\tilde{g}$ mass, because the other sparticle masses are to heavy, thus they are not accessible. In the varying $\tilde{q}$ mass scenario, squark and stop production emerges. However, the stop production channel has a minor contribution to the total cross section. The generation is performed with HERWIG++ and the partons are described by MRST [147] PDFs. Figure 4.6(a) and (b) illustrate the production cross section as a function of the mass parameters.

The next-to-leading-order (NLO) corrections calculated with PROSPINO [103, 148] are applied to the cross sections and gluon radiation effects are taken into account, which is referred to as next-to-leading-logarithmic order (NLL) correction computed with NLL-fast [149–154]. In both scenarios, the cross section is independent of the $\tilde{\chi}_1^0$ mass. The corresponding $m_{\tilde{g}}$ and $m_{\tilde{q}}$ values and cross sections are listed in Table 4.5 together with the relative theoretical uncertainty, which is composed of the scale and the PDF uncertainty (see Section 7.8 for details on the uncertainty). For each parameter point a sample of 5000 events is generated.

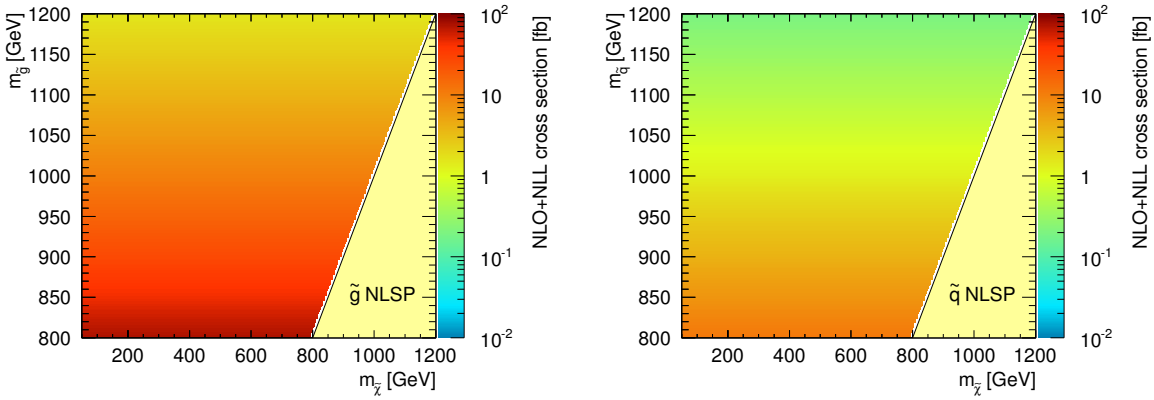

(a) (b)

Figure 4.6: Interpolated GGM NLO+NLL cross section as function of the mass parameters. In (a) and (b), the varying parameters are ($m_{\tilde{g}}$, $\tilde{\chi}_1^0$) and ($m_{\tilde{q}}$, $\tilde{\chi}_1^0$), respectively. The cross sections are taken from [143].

	varying $m_{\tilde{g}}$ scenario		varying $m_{\tilde{q}}$ scenario	
$m_{\tilde{g}}/m_{\tilde{q}}$ [GeV]	$\sigma_{\text{NLO+NLL}}$ [fb]	uncertainty [%]	$\sigma_{\text{NLO+NLL}}$ [fb]	uncertainty [%]
800	74.2	23.1	10.2	28.5
850	44.2	24.9	6.0	30.5
900	26.7	26.6	3.6	32.9
950	16.3	28.3	2.1	35.3
1000	10.0	30.0	1.3	37.8
1050	6.2	31.7	0.8	40.4
1100	3.9	33.9	0.5	43.1
1150	2.5	36.0	0.3	45.8
1200	1.6	38.6	0.2	48.6

Table 4.5: The GGM NLO+NLL cross sections $\sigma_{\text{NLO+NLL}}$ and its relative uncertainty (see Section 7.8) for different gluino masses [143]. The squark mass is fixed to 2.5 TeV, the other parameters are described in the text.

Λ [GeV]	$\sigma_{\mathrm{NLO(+NLL)}}$ [pb]	uncertainty (%)
100	0.34	6.3
110	0.19	6.7
120	0.12	7.1
130	0.073	7.4
140	0.047	7.6
150	0.032	7.4
160	0.022	7.8
170	0.015	8.0
180	0.011	8.1
190	0.0078	7.9
200	0.0056	8.1
210	0.0041	8.1
220	0.0031	8.0
230	0.0023	8.6
240	0.0017	8.4
250	0.0013	8.3

Table 4.6: The cross sections $\sigma_{\mathrm{NLO(+NLL)}}$ and its relative uncertainty (see Section 7.8) for different values of Λ [143]. The choice of the other model parameters is described in the text.

4.4.3 GMSB SPS8 Samples

The GMSB model and its SPS8 scenario are described in Section 2.2.3. The mass spectrum and the decay phenomenology induced by the parameter choice of the model parameters $\tan\beta = 15$, $\mathrm{sign}(\mu) = +$, $N_{\mathrm{mes}} = 1$ and $C_{\mathrm{grav}} = 1$ is computed with `ISAJET` [106]. The hard interaction, the showering and the hadronization are performed by `HERWIG++` working with MRST PDFs. Strong and weak production are taken into account, where the dominant production channels for $\Lambda > 100\,\mathrm{TeV}$ are $\chi_2^0\chi_1^+$ and $\chi_1^+\chi_1^-$. The total cross section (see Table 4.6) is evaluated at NLO and NLO+NLL with `PROSPINO` [103, 148] and `NLL-fast` [149–154] per process for the weak and the strong production channels, respectively, and finally integrated over all channels. The uncertainty is mostly driven by the two leading production channels and its computation is described in detail in Section 7.8.

4.4.4 UED Samples

A brief introduction to UED can be found in Section 2.3. The model parameters are fixed to $N = 6$, $M_{\mathrm{D}} = 5\,\mathrm{TeV}$ and $\Lambda \cdot R = 20$. The LO generator cross section and the branching ratio to $\gamma\gamma$ final states [71] is listed in Table 4.7. Corrections to higher order perturbation calculation are not available. The MC samples with 10000 events per parameter point are generated by `PYTHIA` using MRST PDFs.

$1/R$ [GeV]	σ_{LO} [pb]	$\gamma\gamma$ branching ratio
1000	0.133	100%
1100	0.0521	95%
1200	0.0205	90%
1250	0.0129	83%
1300	0.00813	75%
1350	0.00498	67%
1400	0.00312	60%
1500	0.00120	50%

Table 4.7: The LO generator cross sections and the $\gamma\gamma$ branching ratio [71, 143] for different values of R^{-1}. The choice of the other model parameters is described in the text.

4.4.5 Benchmark Points

In the scenarios of GGM, SPS8 and UED, the benchmark points are representatives points, that are shown in plots or tables for illustration purposes throughout this thesis. The chosen benchmark points are:

- **GGM:** $m_{\tilde{g}} = 1000\,\mathrm{GeV}$, $m_{\tilde{\chi}_1^0} = 450\,\mathrm{GeV}$,
- **SPS8:** $\Lambda = 150\,\mathrm{TeV}$,
- **UED:** $R^{-1} = 1200\,\mathrm{GeV}$.

4.4.6 Reweighting of MC Events

The beam conditions, in particular the different instantaneous luminosities and the corresponding pile-up events in the individual data taking intervals, needs to be considered in MC. MC samples are generated with four different pile-up configurations similar to those from data. Nevertheless, MC events need to be reweighted according to the mean number of pile-up events $\langle\mu\rangle$ in a time interval to describe the data [155]. The mean number of pile-up events depends on the used trigger. The MC pile-up reweighting effect is depicted in Fig. 4.7, where the data distribution is shown in yellow and the unweighted (weighted) MC distribution in red (blue). After the reweighting procedure, the MC agrees perfectly with the data distribution.

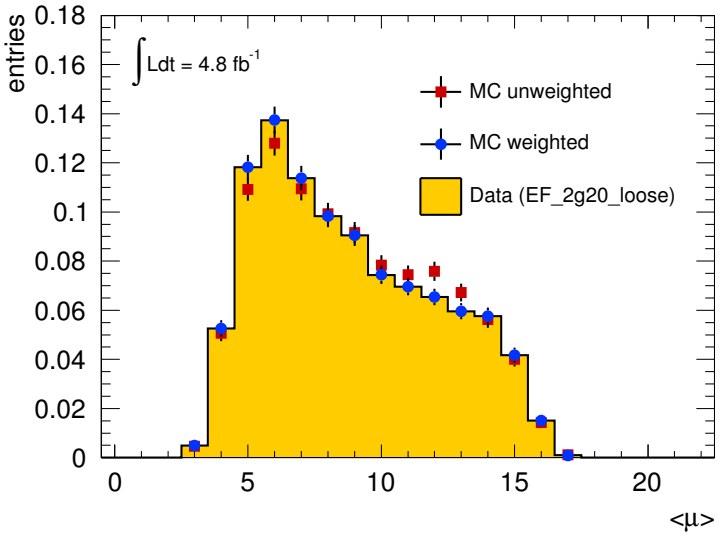

Figure 4.7: The reweighting of MC events to data due to pile-up.

CHAPTER 5

Data Taking and Selection

Aspects of the data taking and the signal candidate event selection with the $\gamma\gamma+E_{\mathrm{T}}^{\mathrm{miss}}$ signature are presented in this Section. First (see Section 5.1 and Section 5.2), the luminosity estimation and the data taking in 2011 is described. Section 5.3 is dedicated to the preselection criteria applied on reconstructed objects, like photons, electrons, muons, and jets and the requirements needed for properly measured events. The signal yield with respect to the background is maximized by using several signal regions (SR) presented in Section 5.4.2. The results of the signal event selection and the expected selection efficiencies are described in that Section as well.

5.1 Luminosity

The luminosity is determined by making use of counting methods taking into account the inputs of the BCM[1] and LUCID[2] [156–159] detectors. The event rate in a certain detector is the ratio of the number of observed events or hits and the number of bunches in a time interval. These devices are used for the event rate counting:

- BCM: The beam conditions monitor devices are placed outside of the detector on both sides of the interaction point at $|\eta| = 4.2$ [158]. It was used for luminosity estimation for the most part during data taking in 2011.
- LUCID: A Cherenkov light detector covering the range of $5.6 < |\eta| < 6.0$, which is designed for the event rate measurement [159].

The instantaneous luminosity $L = R/\sigma_{\mathrm{eff}}$ is a function of the event rate R and the effective cross section σ_{eff}, which incorporates the total inelastic cross section and the detection efficiency of the respective detector. The efficiency is referenced to the total machine luminosity, which can be extracted from machine parameters, where the beam profiles Σ_{x} and Σ_{y} in x- and y-direction are one of the key values [160, 161]: They are extracted by performing *Van-der-Meer-scans* [162], where the two beams are moved stepwise over each other. The corresponding

[1] **B**eam **C**onditions **M**onitor
[2] **Lu**minosity measurement using a **C**herenkov **I**ntegration **D**etector

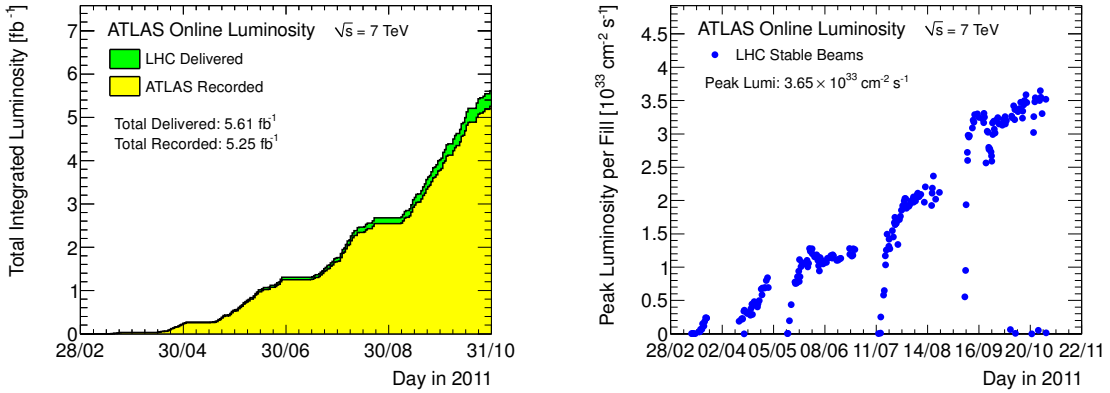

(a) (b)

Figure 5.1: Integrated luminosity (a) and peak instantaneous luminosity (b) as a function of the date in 2011 [83].

luminosity of a recorded dataset depends additionally on the trigger selection, that was used, as well as its dead-time. The smallest time unit ($\leq 2\,\text{min.}$) with stable detector conditions for which the instantaneous and integrated luminosity is measured is referred to as *luminosity block* (LB).

5.2 Data Taking

In 2011, the LHC delivered pp collision at $\sqrt{s} = 7\,\text{TeV}$ corresponding to an integrated luminosity of $5.61\,\text{fb}^{-1}$. During that data taking period, ATLAS recorded a data sample representing an integrated luminosity of $5.25\,\text{fb}^{-1}$ [83]. The evolution of the cumulative integrated luminosity as a function of the date is illustrated in Fig. 5.1(a). The corresponding peak instantaneous luminosity is increasing with time (see Fig. 5.1(b)) inducing more pile-up per event. The maximum instantaneous luminosity in 2011 was $3.65 \cdot 10^{33}\,\text{cm}^{-2}\text{s}^{-1}$. The data taking period of 2011 can be subsequently subdivided into periods, runs, and luminosity blocks. A new period, the coarsest unit, is started when the detector or beam conditions change significantly. *Runs* are data taking units usually in the order magnitude of several hours and corresponds to one fill of the LHC. In addition, it represents technical needs: For instance, if the data taking is interrupted by a malfunctioning detector component, a new run is started afterwards. A run consists of several luminosity blocks. Depending on the specific analysis and the involved physics objects, the quality of the recorded data (DQ) is evaluated for each luminosity block for the various subsystems. If a component, responsible for the measurement of physics object is not working as expected, the events belonging to that luminosity block are rejected. For instance, in this thesis, if the electromagnetic calorimeter is working fine, but not the hadronic calorimeter, photons can not be measured properly, because the hadronic leakage can not be estimated, thus the LB is marked as problematic. In this thesis, the proper measurements of photons, including the photon trigger, electrons, muons, jets, and $E_{\text{T}}^{\text{miss}}$ are required. The

ATLAS 2011 p–p run												
Inner Tracking			Calorimeters				Muon Detectors				Magnets	
Pixel	SCT	TRT	LAr EM	LAr HAD	LAr FWD	Tile	MDT	RPC	CSC	TGC	Solenoid	Toroid
99.8	99.6	99.2	97.5	99.2	99.5	99.2	99.4	98.8	99.4	99.1	99.8	99.3
Luminosity weighted relative detector uptime and good quality data delivery during 2011 stable beams in pp collisions at Vs=7 TeV between March 13th and October 30th (in %), after the summer 2011 reprocessing campaign												

Table 5.1: Luminosity weighted relative fraction of good quality data delivery by the various ATLAS subsystems during LHC fills with stable beams in pp collisions at $\sqrt{s} = 7\,\text{TeV}$, and after switching the tracking detectors on [163].

result of the DQ determination is made accessible via the *Good-Runs-List* (GRL). The luminosity weighted time fraction, where the detector subcomponents worked as expected is shown in Table 5.1 [163]. An availability of more than 97 % can be observed for all components. The photon trigger delivered good quality data at 99.3 % luminosity weighted relative fraction [163].

Events of the data sample used in this analysis are selected by a diphoton trigger. The trigger requires at least two photons with $p_{\text{T}} > 20\,\text{GeV}$ and the details of the trigger definition are given in Section 3.3.3. The recorded data sample corresponds to a total integrated luminosity of

$$\int L dt = (4.81 \pm 0.18)\,\text{fb}^{-1} \tag{5.1}$$

after the good DQ requirement have been applied with a relative uncertainty of 3.7 % [157, 164]. The data taking periods (letters), run ranges (serial number), and the corresponding integrated luminosity are listed in Table 5.2. Almost half of the data sample is collected in the last two periods (L, M). Not all runs in the run ranges have been stored. The luminosity is estimated only for good DQ luminosity blocks.

Since the instantaneous luminosity was increasing during the 2011 data taking due to the good performance of the LHC, the number of pile-up event was increasing as well. The maximum mean number of interactions per bunch crossing (BX) is shown in Fig. 5.2. The average value is computed over several LBs and varies between ∼2 and ∼17 mean interactions per BX. An high number of pile-up events induces various effects that have been taken into account in the reconstruction and the analysis.

5.3 Object Selection

For the selection of physics objects used in this work, like photons, jets, etc., a set of additional cuts on top of the identification requirements is applied to object candidates. These are based on several criteria reflecting the need for a high selection efficiency, quality improvements as well as low misidentification rates and are in agreement with the official recommendations from the ATLAS performance groups [165]. After passing the selection criteria, the objects are considered physics particles.

period	run range	luminosity [pb^{-1}]
B	178044–178109	11.7
D	179710–180481	166.7
E	180614–180776	48.8
F	182013–182519	136.1
G	182726–183462	537.5
H	183544–184169	259.5
I	185353–186493	386.2
J	186516–186755	226.4
K	186873–187815	600.1
L	188902–190343	1401.9
M	190503–191933	1037.6
Total	178044–191933	4812.3

Table 5.2: The integrated luminosity and the individual data taking periods. The luminosity is estimated from LBs, during which the detector was working as expected. The relative uncertainty is 3.7 % [157, 164].

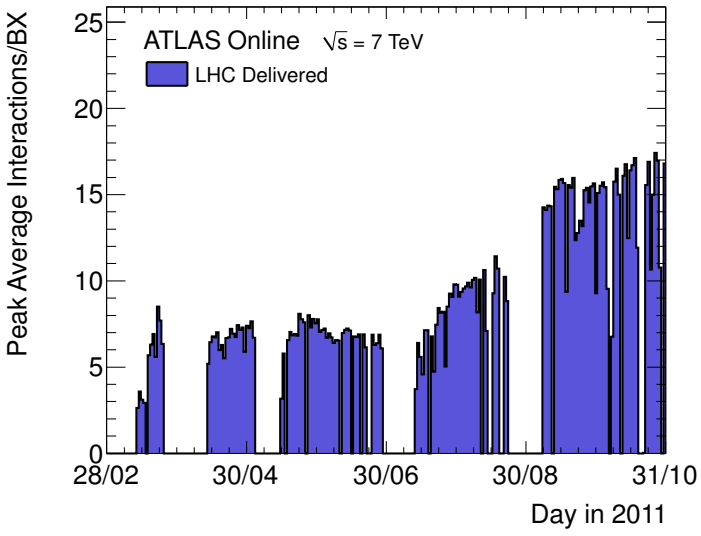

Figure 5.2: The peak average number of interactions per bunch crossing (BX) as a function of the date. [83]. The instantaneous luminosity is increasing as well during that time (see Fig. 5.1(b))

5.3.1 Photons

Reconstructed photons need to pass the *tightAR* identification quality requirement (see Section 4.3.3), which discriminates best between real photons and misidentified electrons. Since the shower shapes in simulated samples are not modeled perfectly, a correction[1] needs to be applied, followed by the rerunning of the photon identification [166, 167].

Additional quality cuts are applied for data and Monte Carlo samples: A fraction of at least 80 % of the photon energy must come from cells, that have a pulse shape as expected[2] [168, 169]. Furthermore, the energy may not be accumulated too central in the cluster, what is reflected by requirements on the shower shapes R_η or R_ϕ. The time associated to a cluster may not differ more than $10 - 12$ ns to the primary collision, whereby the time threshold is depending on the cluster energy [168, 169].

The misidentification rate especially for electrons misidentified as photons is significantly higher in the region of $|\eta| > 1.81$ due to the reduced ID coverage and due to lower calorimeter resolution in that region compared to the central region. Furthermore, signal photons are expected mainly in the central calorimeter region. Thus, the photons need to be found within $|\eta| < 1.81$, while photons in the transition between barrel and end-cap region $1.37 < |\eta| < 1.52$ are not considered due to poor measurement efficiency. The described η-acceptance ranges are referred to as *fiducial region*. The η position of the photons is taken from the η position measured in the second calorimeter layer of the cluster providing the most reliable η estimate.

An energy correction is applied for data taking into account the well known $Z \to ee$ invariant mass, while for MC an energy smearing is used to reflect the energy resolution like in data [170, 171]. At first, the corrected momentum is required to be

$$p_{\mathrm{T}}^{\gamma} > 25\,\mathrm{GeV}. \tag{5.2}$$

In order to suppress jets misidentified as photons and background from neutral hadrons, in particular π^0, which are expected to have a broader shower than photons, an isolation requirement is applied. The *isolation cone ring energy* E_{iso} is defined as the energy measured in a $\eta \times \phi$ cone of size $R < 0.2$ around the photon[3], subtracted by the cluster energy. The isolation energy is corrected for the energy leaking into the cone ring, and for the ambient energy density in the calorimeter generated by pile-up [124]. The corrected isolation energy is required to be

$$E_{\mathrm{iso}} < 5\,\mathrm{GeV} \tag{5.3}$$

for data and Monte Carlo. If a photon cluster is found within the radial distance in $(\eta \times \phi)$ $\Delta R < 0.01$ of an electron cluster, the photon is rejected to avoid misidentification. If a photon and a jet are detected within a $0.2 < \Delta R < 0.4$ cone ring, the photon is considered as a misidentified jet and is rejected.

[1] The data-MC shower shape corrections are called *photon fudge factors* in ATLAS

[2] If the measured pulse shape of a calorimeter cell deviates more than a certain threshold from the nominal shape, the measurement of the cell is considered as bad. Bad pulse shapes can occur from malfunctioning calorimeter cells or particle signals similar to the one of photons at cell level. The cell quality is expressed by the quantity Q in ATLAS.

[3] In ATLAS, the isolation cone ring energy with radius 0.2 is denoted `EtCone20`

Photon Conversion If a conversion vertex with tracks pointing to two clusters is found, the photon is designated as a converted photon, else it is considered as an unconverted photon (see Section 4.3.3). Photons with only one track assigned are classified as single track conversions. Two track conversions are defined in an analogue way. Both single and double track conversions must not have hits in the pixel detector in order to avoid the selection of prompt electrons as converted photons. No further requirements on the conversion category are applied at the object selection level.

5.3.2 Electrons

Electrons found by cluster-seeded algorithms need to pass *medium* identification criteria (see Section 4.3.2). The η position of an electrons is taken from the η position of the calorimeter cluster, if the number of track hits in the pixel detector and SCT is less than four, else it is taken from the track, which gives higher precision. The electrons need to be found within $|\eta| < 2.47$, because the misidentification rate increases above this value due to the missing coverage of the tracker.

A further quality requirement rejects electrons reconstructed from calorimeter cells with sporadic noise, voltage supply problems or being out of time [165, 172]. The energy of the electrons is measured from the cluster and is similarly recalibrated as for photons [170, 171]. The transverse momentum is required to be

$$p_{\mathrm{T}}^{\mathrm{e}} > 25\,\mathrm{GeV}. \tag{5.4}$$

If the distance between a jet and an electron is less than $\Delta R < 0.2$, the jet is rejected and the object is considered as an electron. However, if the electron is found in the cone ring of $0.2 < \Delta R < 0.4$ of a jet, the electron is removed and the object is treated as a jet.

5.3.3 Jets

Jets are reconstructed from topological clusters by the Anti-k_{T} algorithm (see section 4.3.4) with a distance parameter $R = 0.4$. The choice of the jet collection[1] is based on the expected performance in SUSY and UED events with high energetic jets at large multiplicity. The jet momentum is required to be

$$p_{\mathrm{T}}^{\mathrm{jet}} > 20\,\mathrm{GeV} \tag{5.5}$$

and it must be found within $|\eta| < 2.8$. Since badly measured jets or jets arising from instrumental effects, i.e. malfunctioning parts of the detector and electronic noise, can fake missing energy, a set of cuts[2] described below is applied to jets [173, 174]. The event is rejected, if any jet with $p_{\mathrm{T}}^{\mathrm{jet}} > 20\,\mathrm{GeV}$, that is not interpreted as a photon or an electron, fulfills at least one of the following conditions:

[1] Jets are taken from the `AntiKt4TopoNewEM` collection in this analysis.

[2] The set of cuts is referred to as *very loose* set.

- **HEC noise burst:** More than half of the jet energy is found in the HEC and more than half of the energy in the HEC is deposited in calorimeter cells of bad quality (see Section 5.3.1) and the normalized jet quality[1] is greater than 0.8 or the absolute value of the negative energy[2] in the cells associated to the jet is greater than 60 GeV.

- **EM coherent noise:** More than 95 % of the energy is found in the electromagnetic calorimeter and more than 80 % of the energy in the LAr calorimeter is deposited in bad calorimeter cells (see Section 5.3.1) and the normalized jet quality is greater than 0.8 and the jet is within $|\eta| < 2.8$.

- **Non-collision background:** This selection rejects jets reconstructed from cosmic muons or beam halo particles.

  - $|\eta| < 2$: The electromagnetic energy fraction is less than 0.05 and the energy fraction of charged particles is less than 0.05 or the energy fraction deposited in one calorimeter layer is greater than 0.99.
  - $|\eta| \geq 2$: The electromagnetic energy fraction is less than 0.05.

5.3.4 Muons

Muons are reconstructed by the *staco* algorithm chain [129–131] (see Section 4.3.5), which combines the ID and MS tracks. They need to be found within $|\eta| < 2.4$ and their momentum is required to be

$$p_{\mathrm{T}}^{\mu} > 10\,\mathrm{GeV}. \tag{5.6}$$

Furthermore, muons either have to be combined or segment-tagged muons.

Muons are rejected if they fail at least one of the following ID track requirements: A b-layer hit is expected from the ID track, but the b-layer module has none and is not dead. The track has only one pixel hit associated to the track including pixels marked as malfunctioning. The SCT hits are treated in the same way, requiring more than five hits. The sum of pixel and SCT holes associated to the track is greater than two. The track is within $|\eta| < 1.9$ while having less than six associated TRT hits or the total number of TRT hits is greater than five with more than 90 % of the total TRT hits are outliers.

If the distance between a muon and a jet is $\Delta R < 0.4$, the muon is removed from the event and the object is considered as a jet. If a selected muon has a distance with respect to the primary vertex [175] of $|z_0| > 1\,\mathrm{mm}$ or the perigee parameter[3] $|d_0| > 0.2\,\mathrm{mm}$, it is considered as a cosmic muon and the event is rejected.

[1] The normalized jet quality is defined as the fraction of the number of calorimeter cells of bad quality to the total number of calorimeter cells associated to the jet.

[2] A negative energy value can be induced by noise fluctuations below zero.

[3] The perigee parameter d_0 of a track is the shortest radial distance to the primary vertex.

5.3.5 LAr Calorimeter Vetos

If the LAr data quality is not as expected or a sporadic noise peak in LAr calorimeter cells is detected[1], the event is rejected [176].

A small part of the LAr calorimeter had temporary dead front-end boards (during period E to I), i.e. the measurement was malfunctioning in the region of $-0.1 < \eta < 1.5$ and $-0.9 < \phi < -0.5$. Photons pointing towards this region are not identified. In order to avoid mismeasured missing momentum, the event is vetoed if a jet with $p_{\mathrm{T}} > 20\,\mathrm{GeV}$ is falling in this region. Although the measurement is problematic in this region, the jet momentum can be recovered in some cases by using an averaging method[2] [177], where the measurement of well operating neighboring cells is used.

5.3.6 Total Transverse Momentum $\mathrm{H_T}$

The total transverse momentum H_{T}, also referred to as *visible energy*, is particularly interesting for BSM events with decays of heavy particles. It is the scalar sum of all visible objects, namely selected jets, electrons, muons and photons and is defined as follows,

$$H_T = \sum p_{\mathrm{T}}^{\mathrm{jets}} + \sum p_{\mathrm{T}}^{\mathrm{e}} + \sum p_{\mathrm{T}}^{\mu} + \sum p_{\mathrm{T}}^{\gamma}. \tag{5.7}$$

It represents the overall momentum in the event. $E_{\mathrm{T}}^{\mathrm{miss}}$ is not taken into account in the definition of H_{T}.

[1] This is reflected by requiring `LarError == 0` in ATLAS

[2] The method is referred to as *smart veto*.

5.4 Signal Selection

The selection of signal events is divided in two subsequent steps, the preselection and the selection in signal regions. The preselection (see Section 5.4.1) is a data preparation step, at which mainly the data quality is ensured, the objects and the basic diphoton signature is extracted. Thereafter, the splitting in several signal regions (SRs) with additional requirements allows a good sensitivity of the analysis in multiple models or parameter regions.

In the following, several control distributions are presented for the main selection variables. Note that the background is finally estimated from data, because MC is not able to model the data distributions properly[1]. However, a comparison between data and MC for cross checks and illustration purposes is performed in this section.

5.4.1 Preselection

The data is selected by a diphoton trigger (see Section 3.3.3 and Section 5.2) where both photon momenta have to pass $p_{\mathrm{T}} > 20\,\mathrm{GeV}$ at event filter level. The same requirement is applied to MC. Only events in luminosity blocks that are recorded while the necessary detector components are working properly, are taken into account (see Section 5.2). Collision candidate events are selected by requiring the primary vertex to have at least five associated tracks discriminating against cosmic muons. In addition, at least two photons

$$N_{\gamma} \geq 2 \tag{5.8}$$

with

$$p_{\mathrm{T}}^{\gamma} > 50\,\mathrm{GeV} \tag{5.9}$$

are required. The above mentioned selection steps are summarized as *preselection*[2].

The number of events after each selection step, the *cutflow*, for data and signal benchmark points (see Section 4.4.5) can be found in Table 5.3. The MC events are scaled to the integrated luminosity of $4.8\,\mathrm{fb}^{-1}$. The effect of the important quality requirements, the collision candidate vertex ("Vertex"), the jet quality and the veto against cosmic muons ("Muon veto") is small in terms of event rejection in data and MC. Since the data events are skimmed before, the trigger requirement reduces the number of events only by a small amount. The diphoton requirement has the highest impact on the number of passing events, because of the p_{T} cut and the high quality requirement. In MC, the relative reduction of events due to the diphoton requirement

[1] See Chapter 6 for the background measurement.

[2] The order of selection criteria reflects the physical, logical, as well as technical needs. The offline data selection of events recorded in the *EGamma stream* (see Section 3.3.2) technically starts with a so-called *skimming*, which requires two photons with $p_{\mathrm{T}}^{\gamma} > 23\,\mathrm{GeV}$ passing *tightAR* ID quality criterion (see Section 4.3.3). This reduces the amount of data to be processed from several millions down to $\simeq 300000$ events. The detector operational quality criterion (see Section 5.2) is satisfied by passing the GRL. The skimming and the GRL cuts are not applied in MC. Since the skimmed events are from the *EGamma stream*, where events selected by various triggers are recorded, the trigger requirement is imposed again. The object definition and the overlap removal procedure take place after the collision vertex requirement.

Selection	Data	GGM	SPS8	UED
Skimmed events	285705	128 ± 1.8	208 ± 2.1	34.2 ± 0.3
GRL	264977	128 ± 1.8	208 ± 2.1	34.2 ± 0.3
Trigger	263155	74.3 ± 1.4	154 ± 1.8	30.9 ± 0.3
Jet cleaning	261459	74.1 ± 1.4	153 ± 1.8	30.8 ± 0.3
Vertex	261742	74.2 ± 1.4	153 ± 1.8	30.9 ± 0.3
Muon veto	261438	74.0 ± 1.4	152 ± 1.8	30.8 ± 0.3
LAr veto	261216	73.5 ± 1.4	151 ± 1.8	30.7 ± 0.3
Diphoton	10451	34.3 ± 0.9	54.1 ± 1.1	15.7 ± 0.2

Table 5.3: Cutflow table of data and MC benchmark samples of BSM physics.

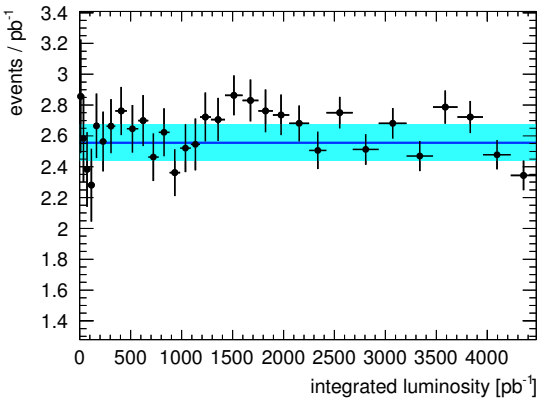

Figure 5.3: The yield of diphoton events as a function of the integrated luminosity bin. The blue line and the surrounding band illustrate the mean value with is variance.

is much smaller than for data because in the considered BSM events photons with a high p_{T} are expected. 10451 diphoton candidate events are observed in data after the preselection.

The yield of diphoton events as a function of the integrated luminosity bin (see Fig. 5.3) is uniform, which demonstrates a stable detector operation and event selection. The dark blue line with the light-blue band shows the mean event yield of $2.6 \pm 0.15\,\mathrm{events/pb^{-1}}$.

Figure 5.4 shows some control distributions of the $\Delta\phi(\gamma, E_{\mathrm{T}}^{\mathrm{miss}})$ variable (a) and the momentum of the leading photon (b) after the preselection. The total SM background is represented by a red line and the data by black dots. The total statistical uncertainty of the SM background is drawn as yellow dashed band. The individual SM background components are shown in different colors.

MC events are scaled with respect to their cross section to data luminosity of $4.8\,\mathrm{fb^{-1}}$. Since QCD multijets (white) and γ + jets (gray) event cross sections can not be estimated with high accuracy, these contributions are normalized to data events in the low $E_{\mathrm{T}}^{\mathrm{miss}}$ control region of $0 < E_{\mathrm{T}}^{\mathrm{miss}} < 30\,\mathrm{GeV}$ taking into account the contributions from the rest of the SM background. Potential missing momentum in QCD events is induced by instrumental effects of the detector. Hence, contributions mainly from QCD events (γ + jets) are expected in the low $E_{\mathrm{T}}^{\mathrm{miss}}$ control region. Moreover, this region is expected to be signal depleted.

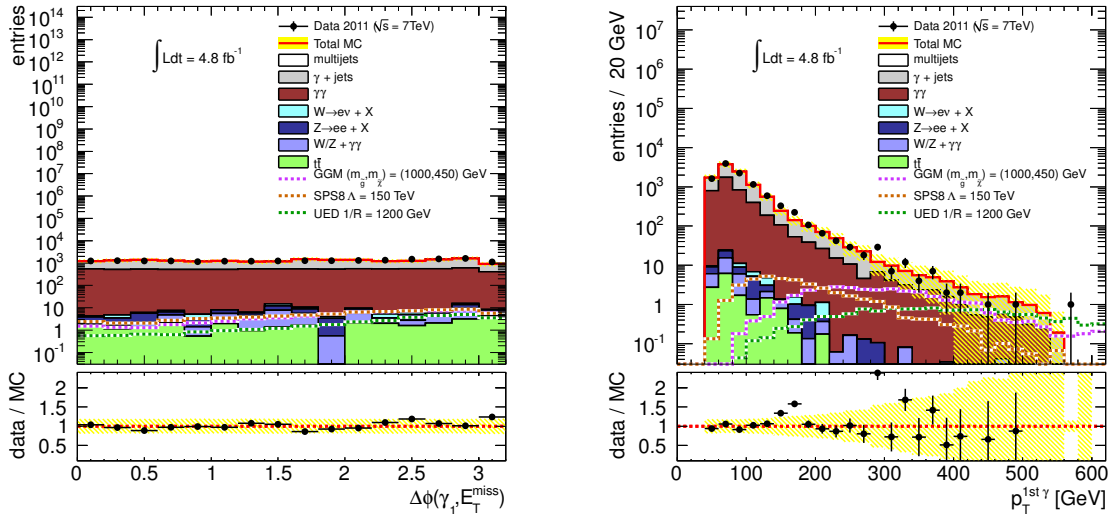

(a) (b)

Figure 5.4: Distributions of the ϕ-distance of the leading photon and $E_{\mathrm{T}}^{\mathrm{miss}}$ (a) and the momentum of the leading photon (b). The benchmark distributions of SPS8, GGM and UED are overlaid.

Events with W boson (light blue) or Z boson (dark blue) decays and QCD multijet events are mostly suppressed by requiring two high energetic photons. The expected signal histograms (dashed line) of the SPS8 (orange-white), GGM (magenta-white) and UED (green-white) benchmark points are overlaid. The SM background in the $\Delta\phi(\gamma, E_{\mathrm{T}}^{\mathrm{miss}})$ distribution has a uniform distribution, while the signal samples have an increasing shape. Thus, a $\Delta\phi(\gamma, E_{\mathrm{T}}^{\mathrm{miss}})$ requirement has a good background rejection power. For each figure, the lower plot shows the ratio of data and the total SM background in each bin and allows a better comparison of the two distributions as in the logarithmic scaled plot on top. The agreement between the data and the expected background is good. The leading photon momentum distribution agrees well between data and MC (see Fig. 5.4 (b)), and the photons with the highest momentum are mostly coming from $\gamma\gamma$ and γ + jets events.

In Fig. 5.5, distributions of $E_{\mathrm{T}}^{\mathrm{miss}}$ (a) and H_{T} (b) after the preselection can be found. In the $E_{\mathrm{T}}^{\mathrm{miss}}$ spectrum below approximately 100 GeV, the largest fraction of the SM background consists of γ + jets and $\gamma\gamma$ (dark red) events, whereas above 100 GeV contributions of top (green) and heavy boson decays with two photons (lilac-blue) become relevant. The data and MC distributions of $E_{\mathrm{T}}^{\mathrm{miss}}$ agree withing the uncertainties except in an intermediate region around 70 GeV. The absence of γ + jets events in that region can be explained by the limited statistics of the MC sample. In the high H_{T} region, the major contributions are γ + jets, $\gamma\gamma$ and top events. The underestimation of the data by MC is due to the fact, that the jet multiplicity is lower in MC than in data (see Fig. 5.7 (a)) and H_{T} heavily depends on the number of jets.

In both the $E_{\mathrm{T}}^{\mathrm{miss}}$ and the H_{T} distributions, the overlaid distributions of the GGM, SPS8 and UED benchmark points illustrate the different shape of the expected signal and point out

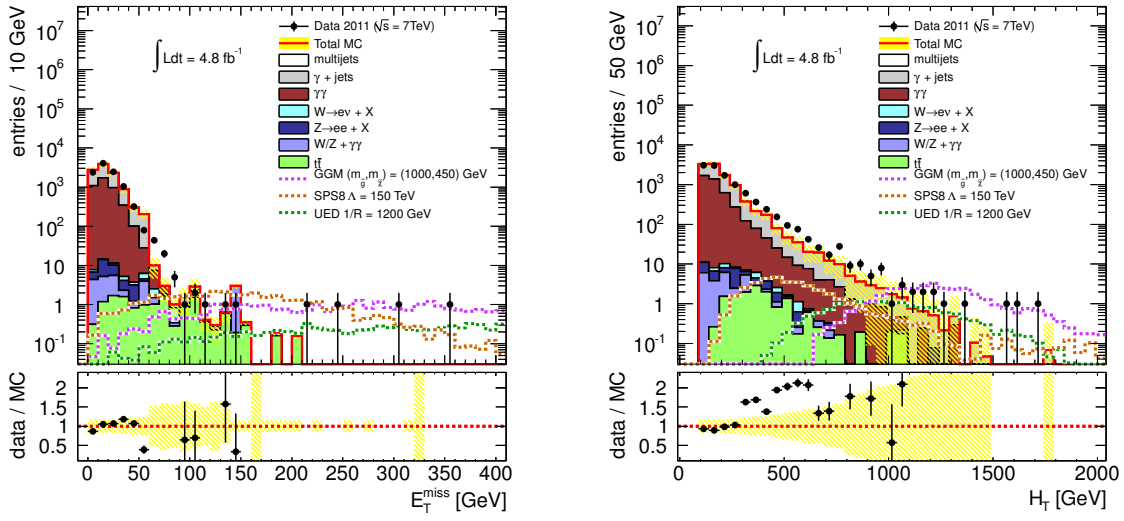

(a) (b)

Figure 5.5: Distributions of $E_{\mathrm{T}}^{\mathrm{miss}}$ (a) and H_{T} (b) for data and MC after the diphoton preselection. The distributions of SPS8, GGM and UED benchmark points are overlaid.

the separation power of the variables $E_{\mathrm{T}}^{\mathrm{miss}}$ and H_{T}.

Figure 5.6 shows some control distributions of the photon selection, namely the number of photons (a) and the momentum of the photons (b). Almost all events after the preselection are diphoton events, only two events with more than two photons are measured. The photons with the highest momentum are mostly from $\gamma\gamma$ and γ + jets events. In both distributions a good agreement between the SM background and the data is found, i.e. photon distributions are well modeled in MC.

The jet distributions (see Fig. 5.7), the number of jets (a) and the momentum of the leading jet (b), show an underestimation of the data by the MC SM background, because the simulation does not describe the number of jets precisely. Events with high jet multiplicity and high jet momentum are mostly coming from γ + jets processes. In signals from BSM physics, jets with a higher momentum and a higher jet multiplicity are expected.

A good agreement between data and MC is found in the photon distributions, while MC does not describe the jets, $E_{\mathrm{T}}^{\mathrm{miss}}$ and H_{T} distributions precisely in parts of their spectra. The background can therefore not be estimated from MC and a data-driven approach is performed, which is presented in Chapter 6. However, with the help of MC the composition of the background can be studied and illustrated.

5.4.2 Signal Regions

In order to have good sensitivity in a broad range of models with a $\gamma\gamma + E_{\mathrm{T}}^{\mathrm{miss}}$ signature, the further signal selection after the preselection is separated in three *signal regions* (SR), denoted as A, B, and C. The various sets of cuts of the individual SRs are optimized for different models or parameter regions.

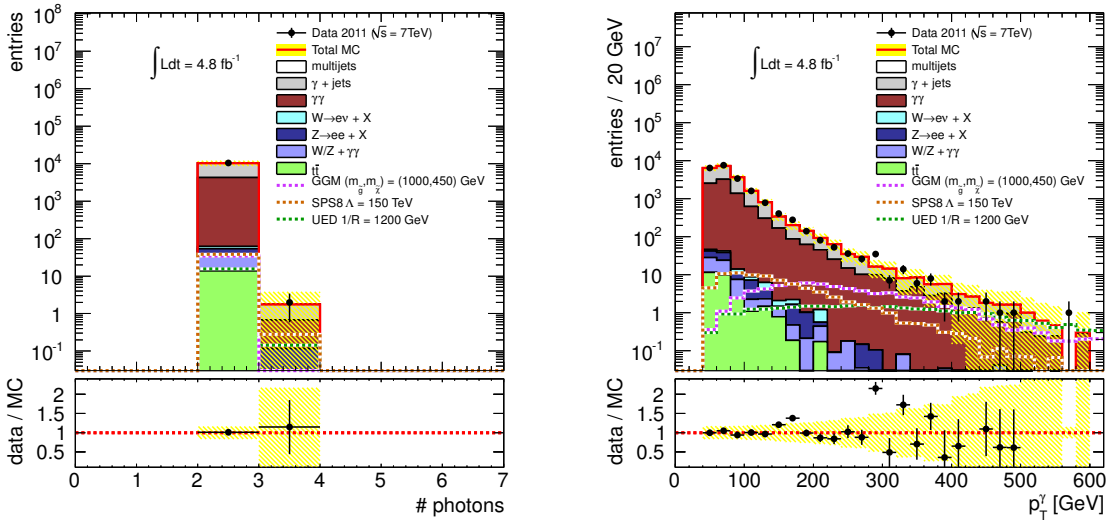

(a) (b)

Figure 5.6: Distributions of the number of photons (a) and the momentum of the photons (b) after the preselection. The distributions of SPS8, GGM and UED are overlaid.

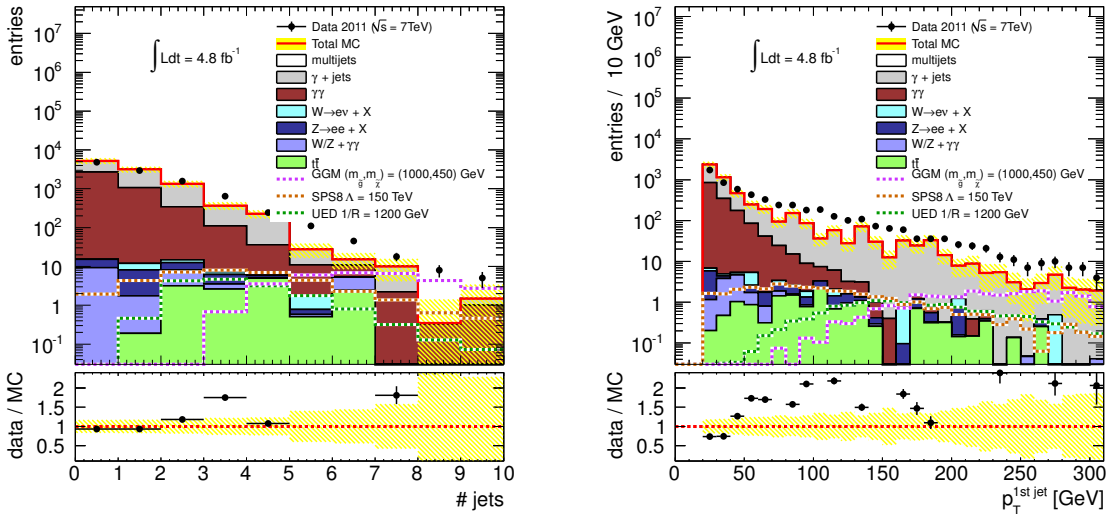

(a) (b)

Figure 5.7: Distributions of the number of jets (a) and the momentum of the leading jet (b) after the preselection. The distributions of SPS8, GGM and UED are overlaid.

The difference in polar angle $\Delta\phi(\gamma, E_{\mathrm{T}}^{\mathrm{miss}})$ between each photon and $E_{\mathrm{T}}^{\mathrm{miss}}$ is used in order to suppress events containing mismeasured $E_{\mathrm{T}}^{\mathrm{miss}}$ from jets misidentified as photons, which are arising mainly from QCD multijet events. Furthermore, in scenarios with heavy neutralinos, a good separation in $\Delta\phi(\gamma, E_{\mathrm{T}}^{\mathrm{miss}})$ between the photons and $E_{\mathrm{T}}^{\mathrm{miss}}$ is expected. Furthermore, H_{T} is expected to be greater in new physics events than in SM events due to high jet activity and high energy photons. Thus, events from BSM physics can be discriminated from SM events by an H_{T} requirement. The cut on $E_{\mathrm{T}}^{\mathrm{miss}}$ accounts for the escaping gravitinos or gravitons and has high SM background suppression power, in particular against $\gamma\gamma$ and γ + jets events, where no intrinsic $E_{\mathrm{T}}^{\mathrm{miss}}$ is expected. The explicit cuts on H_{T}, $\Delta\phi(\gamma, E_{\mathrm{T}}^{\mathrm{miss}})$ and $E_{\mathrm{T}}^{\mathrm{miss}}$ for each SR are listed in Table 5.4.

SR	$\Delta\phi(\gamma, E_{\mathrm{T}}^{\mathrm{miss}})$	H_{T} [GeV]	$E_{\mathrm{T}}^{\mathrm{miss}}$ [GeV]
A	0.5	600	200
B	0	1100	100
C	0.5	0	125

Table 5.4: Overview of the selection criteria in the different signal regions. All cuts require ">".

SR A and SR B are especially designed for the GGM parameter space. In SR A, the focus is on events with high $E_{\mathrm{T}}^{\mathrm{miss}}$ and medium H_{T}, which are expected in a high $\tilde{\chi}_1^0$ mass area resulting in high $E_{\mathrm{T}}^{\mathrm{miss}}$ and a significant separation between the photons and $E_{\mathrm{T}}^{\mathrm{miss}}$. The medium H_{T} cut helps in rejecting SM background events. The low $\tilde{\chi}_1^0$ mass region is expected to be covered by the cuts of SR B, where a relatively low $E_{\mathrm{T}}^{\mathrm{miss}}$ results from the lighter $\tilde{\chi}_1^0$. The design of SR C is reflecting the needs of the SPS8 and UED scenario. In such scenarios, the jet and lepton activity and their energy depend on the production process. Hence no global H_{T} cut is applied. The $E_{\mathrm{T}}^{\mathrm{miss}}$ selection has a high discrimination power of signal against the SM background. The optimization of the selection criteria using simulated signal samples is based on the significance $\alpha = S/\sqrt{B}$ of the number of signal events S over the number of SM background events B. Note, that no requirement on the jet multiplicity is imposed. Jets are contributing only indirectly by the H_{T} selection. In the following analysis, each SR selections is applied to all models to maximize sensitivity.

Control distributions of $E_{\mathrm{T}}^{\mathrm{miss}}$ (a) and H_{T} (b) of events passing the H_{T} requirement for SR A, SR B and SR C are presented in Figs. 5.8–5.10. For illustration purposes only, SM background from MC is shown. The scaling is done as explained in Section 5.4.1 for each SR separately. In SR A (see Fig. 5.8), the medium H_{T} cut of 600 GeV removes a big part of the γ + jets and $\gamma\gamma$ events. In the region of $E_{\mathrm{T}}^{\mathrm{miss}} > 200$ GeV only a small SM background of top events is expected. The high H_{T} requirement of $H_{\mathrm{T}} > 1100$ GeV in SR B (see Fig. 5.9) cancels almost all SM background. The remaining events are mainly from γ + jets processes. In SR C (see Fig. 5.10), no H_{T} requirement is applied. The composition of events in the SR ($E_{\mathrm{T}}^{\mathrm{miss}} > 125$ GeV) is expected to be dominated by top decays with a small admixture of $W/Z(+\gamma\gamma)$ events. A comparison after the preselection of the distributions shown in Fig. 5.4 and Fig. 5.10 (SR C) points out the impact of the $\Delta\phi(\gamma, E_{\mathrm{T}}^{\mathrm{miss}})$ requirement: Some data events

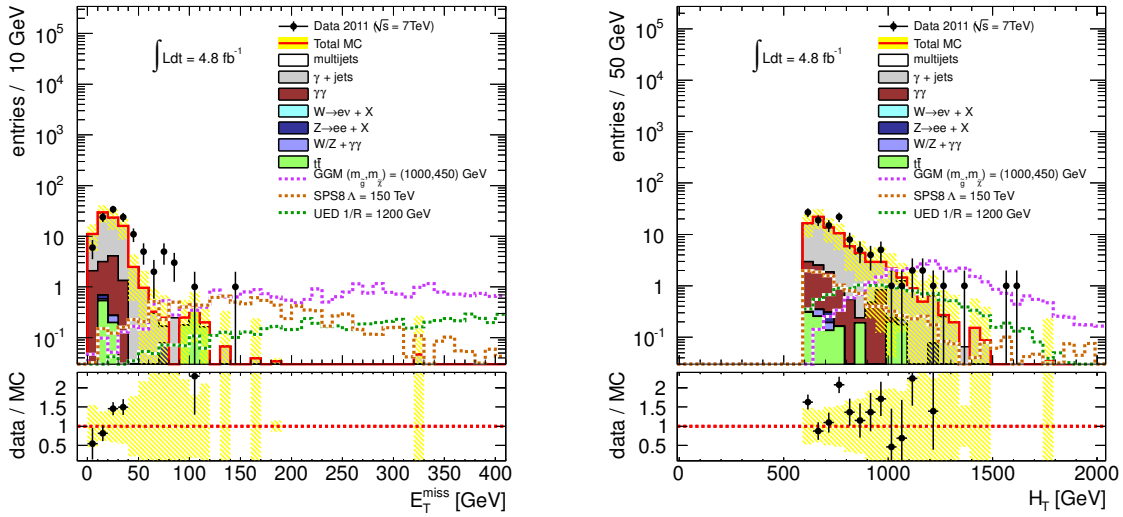

Figure 5.8: Distributions of $E_{\mathrm{T}}^{\mathrm{miss}}$ (a) and H_{T} (b) in SR A for data and MC after the H_{T} requirement. The final $E_{\mathrm{T}}^{\mathrm{miss}}$ cut is not applied. The distributions of SPS8, GGM and UED are overlaid.

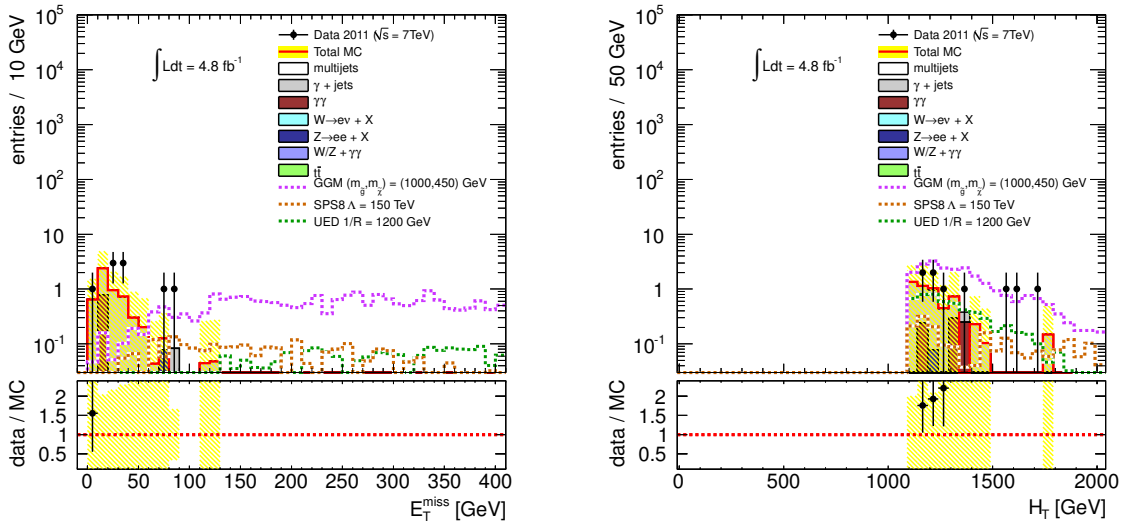

Figure 5.9: Distributions of $E_{\mathrm{T}}^{\mathrm{miss}}$ (a) and H_{T} (b) in SR B for data and MC after the H_{T} requirement. The final $E_{\mathrm{T}}^{\mathrm{miss}}$ cut is not applied. The distributions of SPS8, GGM and UED are overlaid.

in the high H_{T} (a) and high $E_{\mathrm{T}}^{\mathrm{miss}}$ (b) tail are removed, e.g. one event with $H_{\mathrm{T}} \simeq 1700\,\mathrm{GeV}$. Four events in the high $E_{\mathrm{T}}^{\mathrm{miss}}$ region seem to arise from mismeasured $E_{\mathrm{T}}^{\mathrm{miss}}$, because they are rejected by the $\Delta\phi(\gamma, E_{\mathrm{T}}^{\mathrm{miss}})$ requirement. Those high $E_{\mathrm{T}}^{\mathrm{miss}}$ events are not present in SR B, although there is no $\Delta\phi(\gamma, E_{\mathrm{T}}^{\mathrm{miss}})$ requirement.

After the preselection, 10451 diphoton events with $p_{\mathrm{T}}^{\gamma} > 50\,\mathrm{GeV}$ are found in data. The event yield after passing the cuts for the respective SR is presented in Table 5.5.

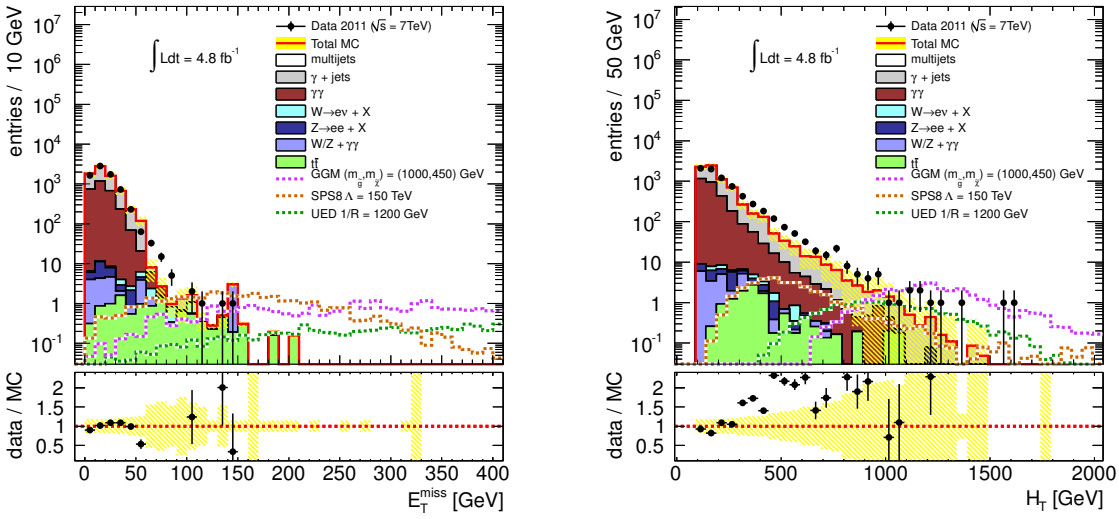

Figure 5.10: Distributions of $E_{\mathrm{T}}^{\mathrm{miss}}$ (a) and H_{T} (b) in SR C for data and MC after the H_{T} requirement. The final $E_{\mathrm{T}}^{\mathrm{miss}}$ cut is not applied. The distributions of SPS8, GGM and UED are overlaid.

The $\Delta\phi(\gamma, E_{\mathrm{T}}^{\mathrm{miss}})$ requirement reduces the number of events by approx. 30 % in data and a further reduction of the number of events is done the H_{T} and $E_{\mathrm{T}}^{\mathrm{miss}}$ requirements. The number of observed events N_{obs}, i.e. after the $E_{\mathrm{T}}^{\mathrm{miss}}$ requirement, is respectively $N_{\mathrm{obs}} = 0$ for SR A and SR B, and $N_{\mathrm{obs}} = 2$ in SR C. The event rejection is much smaller for the benchmark points, because the analysis is designed to select these events.

One of the two observed events[1] in SR C is illustrated in Fig. 5.11. It contains two unconverted photons with (p_{T}, η, ϕ) coordinates of (135 GeV, 0.14, -0.66π) and (82 GeV, 0.68,

[1]The event number in ATLAS is 33053172.

Selection	Data	GGM	SPS8	UED
SR A				
$\Delta\phi(\gamma, E_{\mathrm{T}}^{\mathrm{miss}})$	7293	30.8 ± 0.9	46.9 ± 1.0	14.3 ± 0.2
H_{T}	116	30.8 ± 0.9	13.1 ± 0.5	13.5 ± 0.2
$E_{\mathrm{T}}^{\mathrm{miss}}$	0	22.0 ± 0.8	4.03 ± 0.3	11.9 ± 0.2
SR B				
$\Delta\phi(\gamma, E_{\mathrm{T}}^{\mathrm{miss}})$	10451	34.3 ± 0.9	54.1 ± 1.1	15.7 ± 0.2
H_{T}	9	24.0 ± 0.8	4.33 ± 0.3	5.6 ± 0.1
$E_{\mathrm{T}}^{\mathrm{miss}}$	0	21.8 ± 0.7	3.39 ± 0.3	5.5 ± 0.1
SR C				
$\Delta\phi(\gamma, E_{\mathrm{T}}^{\mathrm{miss}})$	7293	30.8 ± 0.9	46.9 ± 1.0	14.3 ± 0.2
H_{T}	7293	30.8 ± 0.9	46.9 ± 1.0	14.3 ± 0.2
$E_{\mathrm{T}}^{\mathrm{miss}}$	2	27.1 ± 0.8	27.3 ± 0.8	13.5 ± 0.2

Table 5.5: Cutflow table of data and signal MC benchmark samples in SR A, B and C.

0.52π), respectively. Furthermore, $E_{\mathrm{T}}^{\mathrm{miss}}$ is measured as $140 \pm 13\,\mathrm{GeV}$. In the second event, $E_{\mathrm{T}}^{\mathrm{miss}}$ is measured as $139 \pm 11\,\mathrm{GeV}$ and an unconverted photon with (165 GeV, 1.04, -0.62π) and a converted photon with (108 GeV, 1.53, -0.76π) are found. In both events additional jets with more than 100 GeV are present.

The selection efficiency ϵ of signal events is defined in a certain SR by

$$\epsilon = \frac{\#(\text{events passing all cuts})}{\#(\text{events before cuts})}, \tag{5.10}$$

The efficiency is an ingredient for the limit calculation and depends on the model parameters, e.g. the $\tilde{g}$ and $\tilde{\chi}_1^0$ mass. The efficiencies of the GGM scenario are presented in Fig. 5.12 and 5.13 for all signal regions. In the parameter space, where the $\tilde{g}$ is the NLSP, the analysis is not sensitive. The bin size reflects the generated parameter point density. The first three Figures illustrate the $\tilde{g}$-$\tilde{\chi}_1^0$ mass plane, while the latter shows the $\tilde{q}$-$\tilde{\chi}_1^0$ mass plane. The highest efficiency in the $\tilde{g}$-$\tilde{\chi}_1^0$ plane is observed in SR A, where the $\tilde{g}$ mass is similar to the $\tilde{\chi}_1^0$ mass (close to the $\tilde{g}$ NLSP borderline), while the lowest efficiency is found for low $\tilde{\chi}_1^0$ and low $\tilde{g}$ masses. In SR B, the situation is different: The highest efficiencies can be found in the region of a high $\tilde{g}$ mass and the region of high $\tilde{g}$-$\tilde{\chi}_1^0$ mass difference. The efficiency is decreasing towards the $\tilde{g}$ NLSP region. The efficiency distribution in SR C is similar to SR A, but less dependent on the $\tilde{g}$ mass because of the missing H_{T} requirement. In all SRs, the efficiency is increasing towards the $\tilde{g}$ NLSP region up to a $\tilde{\chi}_1^0$-$\tilde{g}$ mass difference of approx. 40 GeV.

In Fig. 5.14 (a), the efficiency in the SPS8 scenario is presented, where the highest efficiency can be observed for SR C increasing from 7 to 20 % over the considered Λ range, because the $\tilde{\chi}_1^0$ mass increases simultaneously, i.e. its decay products, the photons and the gravitions, have higher energies and pass the requirements more easily. The efficiency stays below 5 % in SR B. The efficiencies of the UED scenario are presented in Fig. 5.14 (b). The efficiency in SR C is almost constant over the considered range of $1/R$, whereas the efficiencies of SR A and B are lower, but increase with smaller compactification radii. The relative statistical uncertainty in the GGM scenarios is less than 5 % in most areas of the mass planes. In regions with low $\tilde{\chi}_1^0$ mass, the relative uncertainty can be up to 15 % high. In the UED and SPS8 scenarios, the statistical uncertainty is lower than in the GGM scenarios, because of the higher number of generated events. There are 5000 events per parameter point generated in the GGM scenario and 10000 events per parameter point available for SPS8 and UED scenarios.

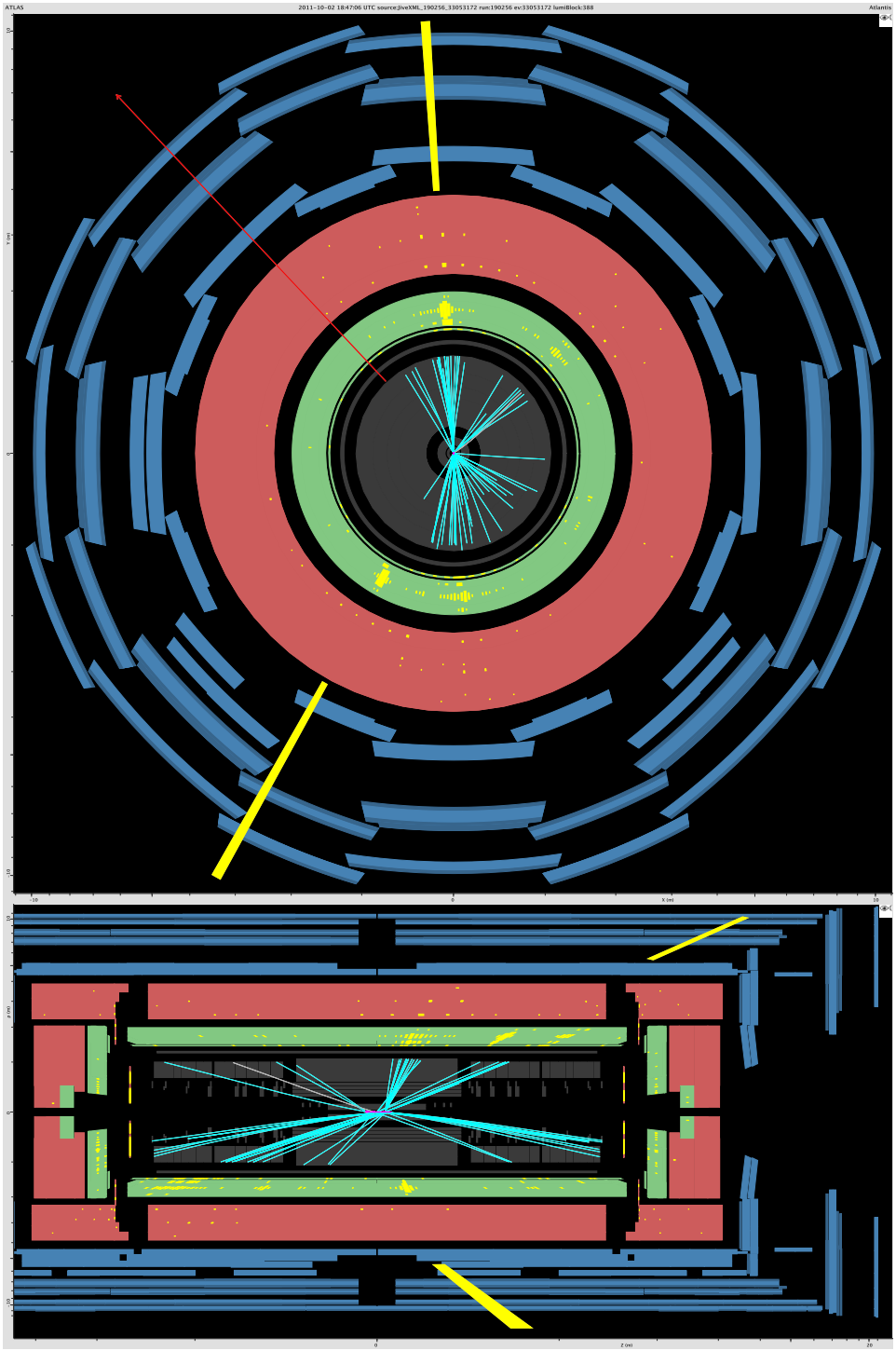

Figure 5.11: Schematic illustration of one of the events (event number 33053172) observed in SR C. The x-y view of the detector is shown on top, while the r-z projection view can be found on the bottom. The energy depositions of the two photons are indicated in yellow in the electromagnetic calorimeter (green), while the corresponding cluster energy is show as yellow tower outside the calorimeters. The red line (top) shows the ϕ direction of the missing transverse energy. Tracks are shown in cyan in the ID.

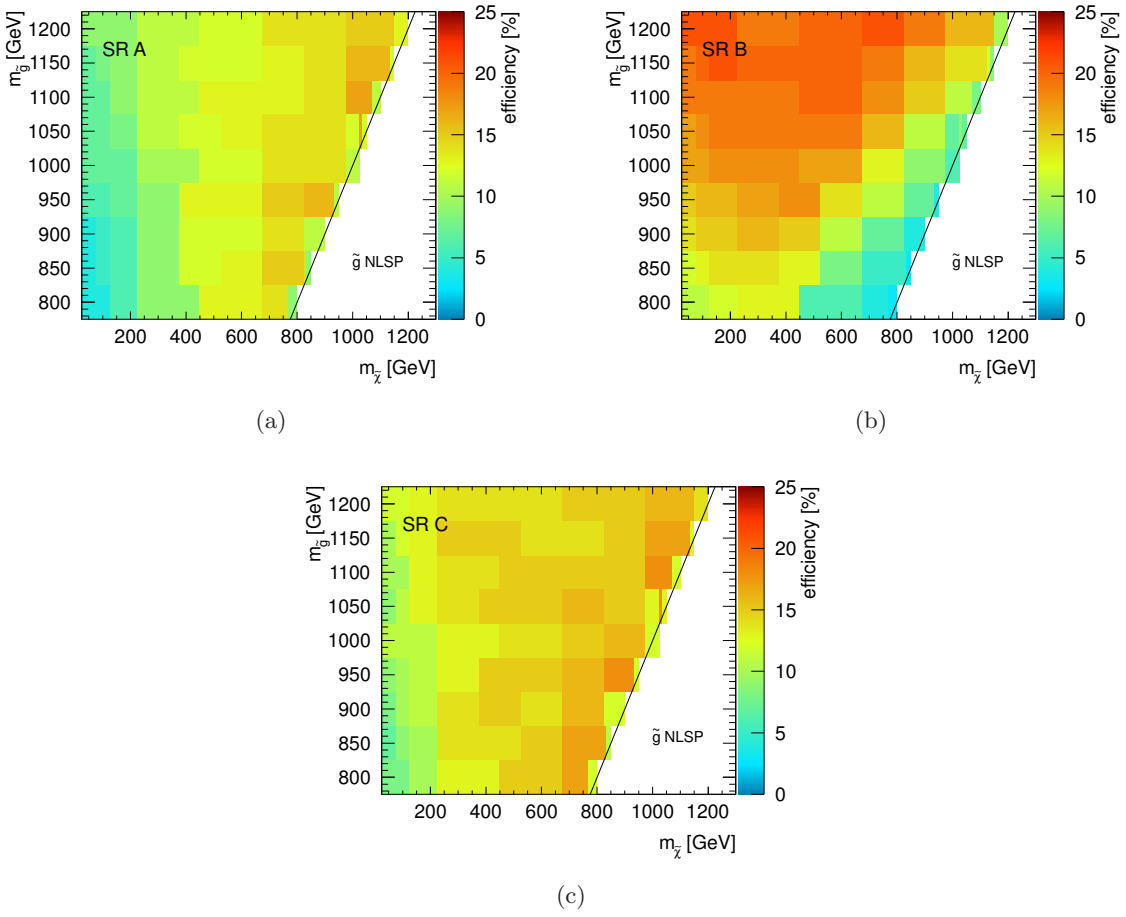

(a) (b)

(c)

Figure 5.12: Signal efficiencies of the GGM $\tilde{g}$-$\tilde{\chi}_1^0$ mass plane for SR A (a), SR B (b) and SR C (c). The $\tilde{g}$ NLSP region is not accessible by the analysis. The bin size reflects the generated parameter point density.

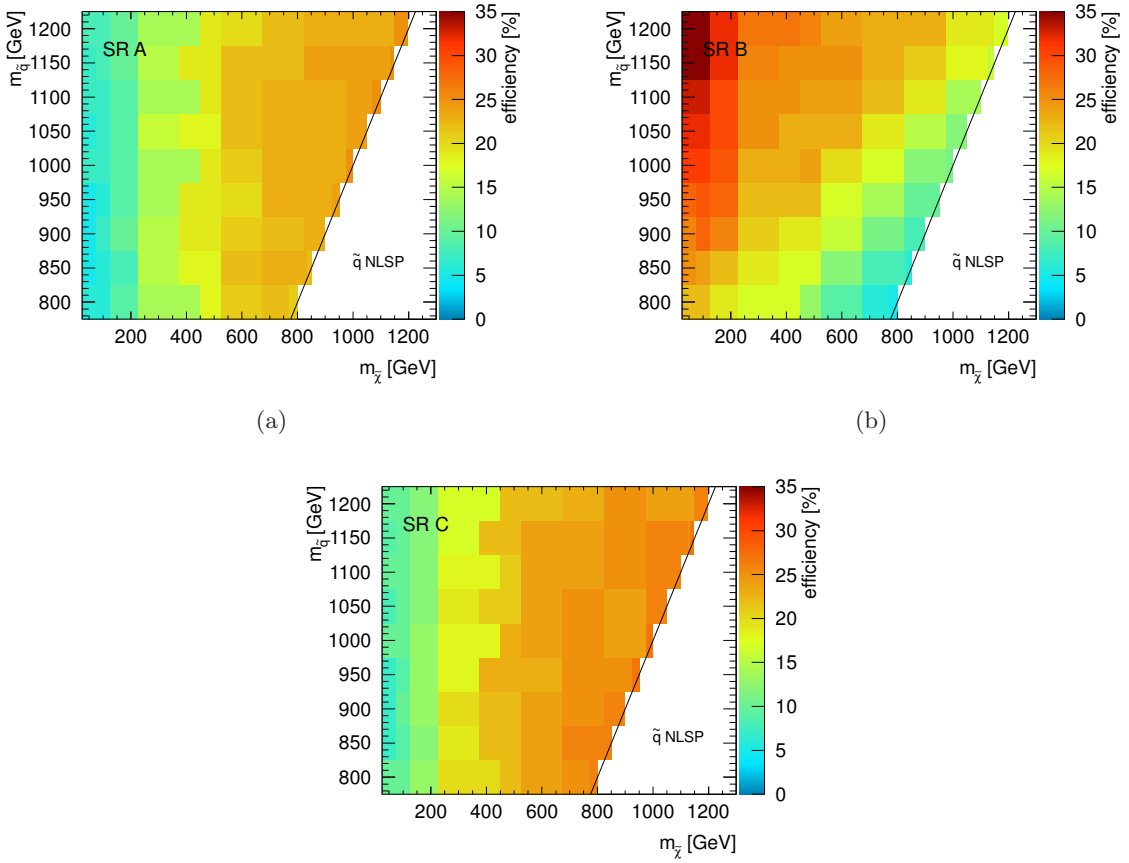

(a) (b)

(c)

Figure 5.13: Signal efficiencies of the GGM $\tilde{q}$-$\tilde{\chi}_1^0$ mass plane for SR A (a), SR B (b) and SR C (c). The $\tilde{q}$ NLSP region is not accessible by the analysis. The bin size reflects the generated parameter point density.

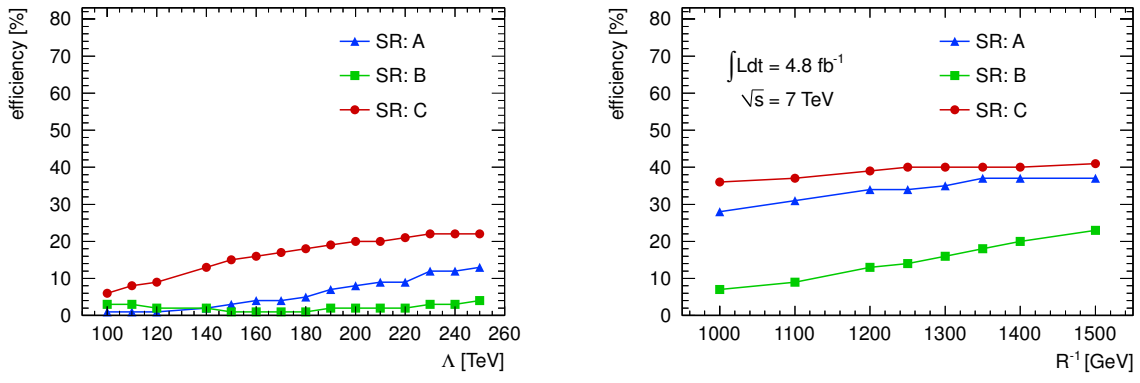

(a) (b)

Figure 5.14: Signal efficiencies of the GMSB SPS8 (a) and the UED (b) scenarios: The efficiency as a function of the parameter Λ (a) and the efficiency as a function of the inverse compactification radius (b).

CHAPTER 6

SM Background Measurement

In new physics searches, it is crucial to know how many events result from SM processes. The SM events are considered as a background for possible new physics signatures, which would appear as an excess of events over the SM background. In this section, the main background sources and their estimations in the SRs are presented. They are determined from data control samples which are enriched by different SM process categories. The Chapter concludes with the results of the SM measurement in the various SRs.

The high-p_{T} diphoton selection (see Chapter 5) in combination with the signal region cuts eliminate many background events. The remaining SM background with a $\gamma\gamma + E_{\mathrm{T}}^{\mathrm{miss}}$ signature can be classified in several categories:

- **Instrumental $E_{\mathrm{T}}^{\mathrm{miss}}$ background:** This source is related to QCD events with jets, i.e. γ + jets and multijet events, where jets are misidentified as photons and thus fake a diphoton signature. Instrumental $E_{\mathrm{T}}^{\mathrm{miss}}$ is generated by detector effects, e.g noise, dead cells or misidentified physics objects. Furthermore, SM $\gamma\gamma$ events are a background source, where $E_{\mathrm{T}}^{\mathrm{miss}}$ is also due to detector imperfections. These background sources are modeled by the QCD control sample discussed in Section 6.1. An alternative method using a dielectron sample is presented in Section 6.1.3.

- **Background with genuine $E_{\mathrm{T}}^{\mathrm{miss}}$ events:** This category contains events with genuine $E_{\mathrm{T}}^{\mathrm{miss}}$ from neutrinos, e.g. $t\bar{t}$ or W decays with one or more neutrinos. Electrons in such decays could be misidentified as photons and lead to a diphoton signature. This background is estimated from an $e\gamma$ control sample (see Section 6.2).

- **Irreducible background:** This background results from $Z(\rightarrow \nu\bar{\nu}) + \gamma\gamma$ and $W(\rightarrow \ell\nu) + \gamma\gamma$ events with two real photons involved having the same signature as potential BSM events. Hence, they can not be reduced by selection cuts without reducing signal selection efficiency at the same time.

- **Cosmic ray background:** Muons originating from cosmic rays can deposit large amounts of energy in the detector via bremsstrahlung or pair production [1]. Both processes result in high-p_{T} photons accompanied by a noticeable amount of $E_{\mathrm{T}}^{\mathrm{miss}}$ in the event. Additional

photons may be produced in the collision event. However, the background from cosmic ray is found to be negligible [143].

The background measurement procedure discussed here follows the procedure presented in [80]. All backgrounds are estimated after the H_T cut, but before the final $E_{\mathrm{T}}^{\mathrm{miss}}$ selection. The $E_{\mathrm{T}}^{\mathrm{miss}}$ spectrum can be used to define the signal region with a minimum of SM background events, as well as the background events enriched control region (CR) where only a small amount of signal events are expected. The control region is mostly used for normalization purposes.

The measurement of the amount of background of a certain source from data is preferred over the estimation from MC, hence the main sources, e.g. the contributions of instrumental and genuine $E_{\mathrm{T}}^{\mathrm{miss}}$ events are measured from data. Nevertheless, the irreducible background estimate and particular background checks can only be done using MC.

For each of the two background sources, the instrumental background and the background with genuine $E_{\mathrm{T}}^{\mathrm{miss}}$, a control sample is defined. In order to combine the different background control samples in the final result, they have to be orthogonal: An event may only appear in one sample, i.e. the samples are not overlapping. This includes also the diphoton data sample.

Furthermore, background cross checks are performed: $Z \to \nu\bar{\nu}$ + jets events contribute to the background, if the jets are misidentified as photons. In addition, if the electrons in $WW/WZ(\to e\nu e\nu/e)$ events are misidentified as photons, such events are considered as a background source. The contribution of these samples is studied.

6.1 Instrumental $\mathbf{E_T^{miss}}$ Background

Events in this background category have in common that their $E_{\mathrm{T}}^{\mathrm{miss}}$ is coming from detector artifacts or poorly measured objects. The main sources of hadronic instrumental background are γ + jets and multijet events, whereas the electromagnetic instrumental component comes from SM $\gamma\gamma$ events. Since the underlying interactions are different, two independent control samples are studied:

- QCD γ + jets and multijet events are represented by the QCD control samples, which are explained in Section 6.1.2.

- SM $\gamma\gamma$ events are attempted to be modeled by $Z \to ee$ events accumulated in the dielectron ($Z \to ee$) sample (see Section 6.1.3).

The control samples are normalized to the diphoton data such that the number of events agree in the CR of $E_{\mathrm{T}}^{\mathrm{miss}} < 20\,\mathrm{GeV}$, where background events are expected to dominate. For each SR, the determination of the control events and the normalization is done separately. Additional details can be found in Appendix B.1.

6.1.1 Pseudo-Photons

In order to obtain a control sample orthogonal to the diphoton data sample, but containing objects with similar kinematic properties and hence a compatible $E_{\mathrm{T}}^{\mathrm{miss}}$ distribution shape, the so-called *pseudo-photons* are defined. They have to pass the same selection as photons, but must fail at least one particular shower shape requirement of the *tightAR* identification criteria (see Section 4.3.3), i.e. the photon requirement is *inverted*. The inversion of the photon requirement is done by requiring the pseudo-photons to fail at least one of two first calorimeter sampling shower shape cuts [178]. These two cuts are the energy fraction of the shower core (F_{side}) and the shower width (w_{s3})[1], that have only a minimal dependence on other shower shape variables and the isolation energy. This ensures that most of the properties of the photons are conserved by making use of pseudo-photons. Nevertheless, pseudo-photons need to pass the *loose* identification quality. Kinematic distributions of the pseudo-photons and a comparison to the diphoton data are presented in Appendix B.1.

6.1.2 QCD Control Samples

The $\mathrm{QCD}_{\gamma\gamma}$ *control sample* represents background with instrumental $E_{\mathrm{T}}^{\mathrm{miss}}$ originating from hadronic events with jets. It is preselected in the same way as the diphoton data in order to have a similar kinematic distribution, i.e. pseudo-photons are also required to pass the $\Delta\phi(\gamma, E_{\mathrm{T}}^{\mathrm{miss}})$ requirement and are taken into account in the visible energy calculation. However, instead of at least two photons, at least two pseudo-photons are required covering especially the multijet background, where at least two jets are misidentified as photons. In addition, events with exactly one photon and at least one pseudo-photon go into this sample covering mainly the γ + jets contribution. Diphoton data events and events with an electron are vetoed in order to keep the sample orthogonal to other samples and because no electrons are expected in such events. The sample containing events with exactly one electron falls into the category of genuine $E_{\mathrm{T}}^{\mathrm{miss}}$ and is described in Section 6.2.

Since the statistics in the $\mathrm{QCD}_{\gamma\gamma}$ sample are limited, a control sample with looser selection criteria is constructed, denoted as QCD_{γ}. The QCD_{γ} sample is preselected in the same way as photon events, unless exactly one pseudo-photon is required, whereas photons and electrons are vetoed. So it is not overlapping in terms of events with the $\mathrm{QCD}_{\gamma\gamma}$ sample. The average yield of QCD_{γ} events per integrated luminosity bin is shown in Fig. 6.1. The mean value and its statistical uncertainty are illustrated by the blue band. The uniform distribution indicates a steady event selection rate and a stable detector operation.

An $E_{\mathrm{T}}^{\mathrm{miss}}$ shape comparison of the $\mathrm{QCD}_{\gamma\gamma}$ and the QCD_{γ} sample after the preselection is presented in Fig. 6.2. It shows significantly higher statistics in the high-$E_{\mathrm{T}}^{\mathrm{miss}}$ tail in the QCD_{γ} sample and a good agreement of both samples. Hence, the loosening of the number of pseudo-photon requirement in the QCD_{γ} sample is a valid approach to increase the statistics of the control sample. Finally, the orthogonal $\mathrm{QCD}_{\gamma\gamma}$ and QCD_{γ} samples are combined, denoted

[1] The energy fraction of the shower core and the shower width in the first calorimeter sampling layer are denoted technically `fracs1` and `weta1`, respectively.

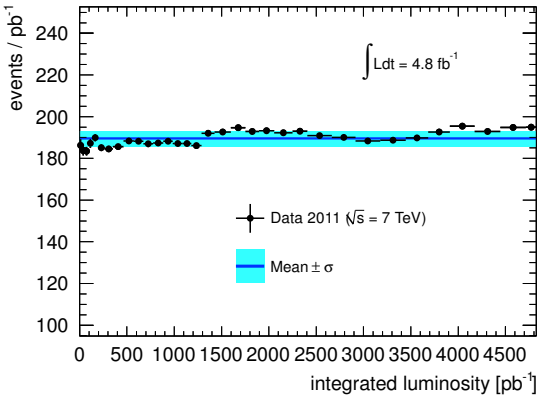

Figure 6.1: Average yield of QCD_{γ} control events per integrated luminosity bin. The blue line with the band indicates the the mean value and its statistical uncertainty.

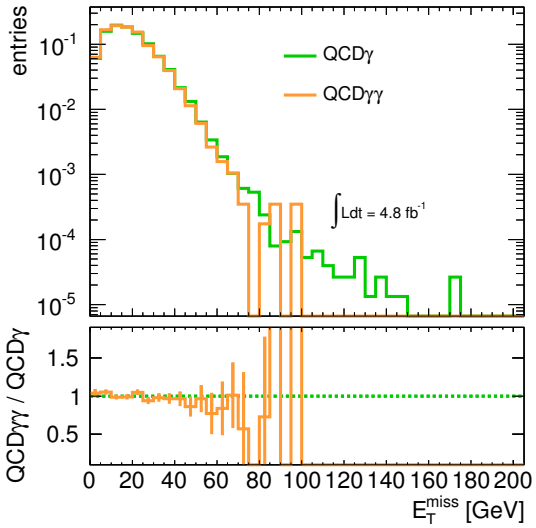

Figure 6.2: Shape comparison of $E_{\mathrm{T}}^{\mathrm{miss}}$ between the QCD_{γ} (green line) and the $\mathrm{QCD}_{\gamma\gamma}$ (orange line) sample after the preselection. The distributions are normalized to an integral of one.

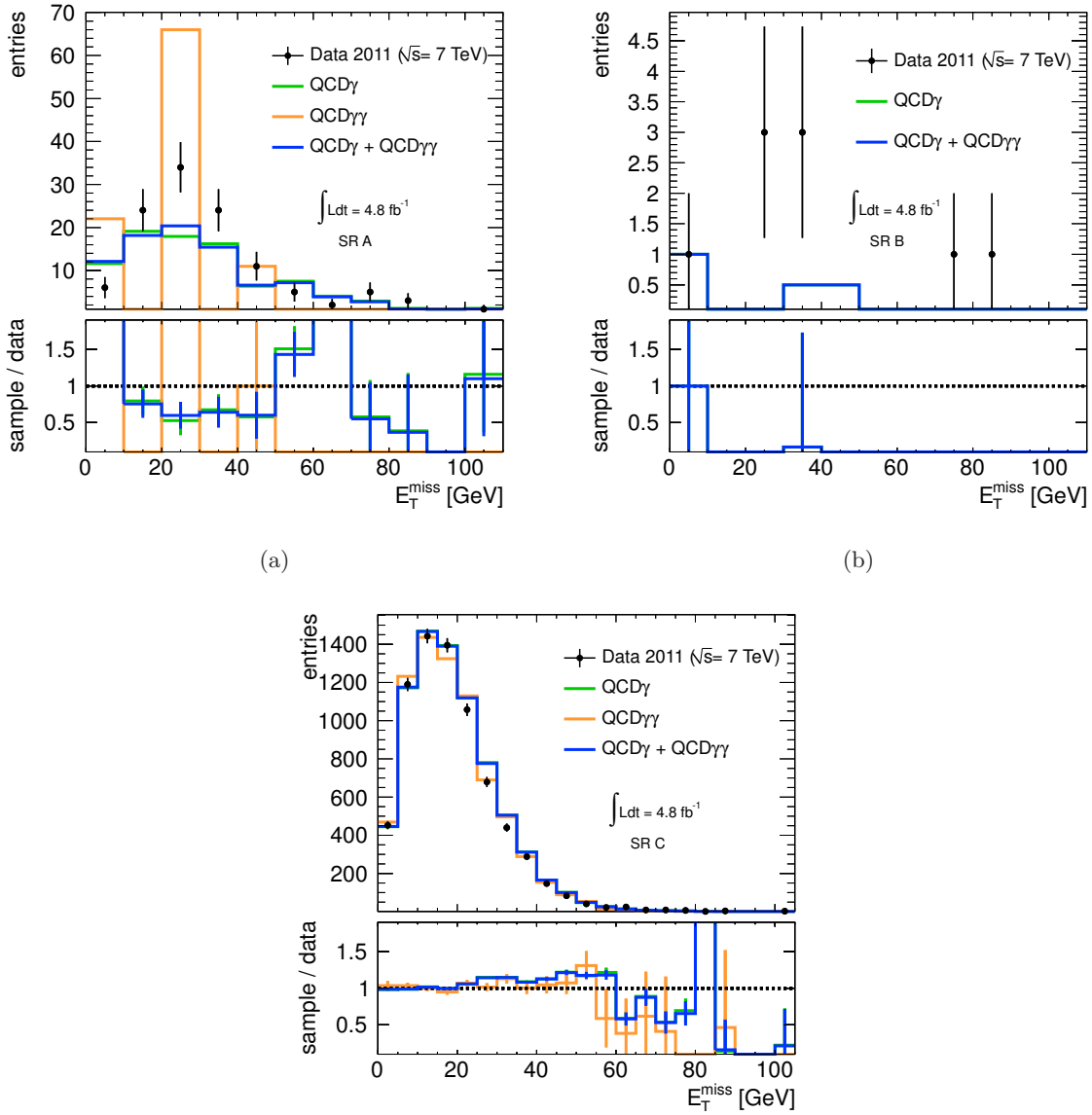

Figure 6.3: Shape comparison between diphoton data and multiple control samples as a function of $E_{\mathrm{T}}^{\mathrm{miss}}$ for SR A (a), SR B (b) and SR C (c). The QCD control samples (QCD_{γ} in green, $\mathrm{QCD}_{\gamma\gamma}$ in orange and the QCD template in blue) are normalized to data events (black dots) in the control region of $E_{\mathrm{T}}^{\mathrm{miss}} < 20\,\mathrm{GeV}$.

as *QCD template* (or "QCD_{γ} + $\mathrm{QCD}_{\gamma\gamma}$"), in order to gain the maximum statistics. The usage of the QCD template for the instrumental background estimation is discussed further in Section 6.1.4 taking into account an alternative approach with a different control sample presented in Section 6.1.3.

The modeling of the $E_{\mathrm{T}}^{\mathrm{miss}}$ distributions of the diphoton events in the three signal regions (see Section 5.4.2) is illustrated in Fig. 6.3. Data points are shown in black, the control samples, QCD_{γ}, $\mathrm{QCD}_{\gamma\gamma}$, and QCD_{γ} + $\mathrm{QCD}_{\gamma\gamma}$, are shown as green, orange, and blue curves,

(a)

sample	N events $E_{\mathrm{T}}^{\mathrm{miss}} < 20\,\mathrm{GeV}$	scale factor	N events $E_{\mathrm{T}}^{\mathrm{miss}} > 200\,\mathrm{GeV}$	N scaled events $E_{\mathrm{T}}^{\mathrm{miss}} > 200\,\mathrm{GeV}$
data $\gamma\gamma$	30 ± 5	-	0	0
QCD template	55.0 ± 7.4	0.55 ± 0.11	0	0
$Z \to ee$ (1 jet)	30.0 ± 5.5	1.0 ± 0.26	0	0

(b)

sample	N events $E_{\mathrm{T}}^{\mathrm{miss}} < 20\,\mathrm{GeV}$	scale factor	N events $E_{\mathrm{T}}^{\mathrm{miss}} > 100\,\mathrm{GeV}$	N scaled events $E_{\mathrm{T}}^{\mathrm{miss}} > 100\,\mathrm{GeV}$
data $\gamma\gamma$	1 ± 1	-	0	0
QCD template	2.0 ± 1.4	0.5 ± 0.5	0	0
$Z \to ee$ (1 jet)	0	-	1.0 ± 1.0	-

(c)

sample	N events $E_{\mathrm{T}}^{\mathrm{miss}} < 20\,\mathrm{GeV}$	scale factor	N events $E_{\mathrm{T}}^{\mathrm{miss}} > 125\,\mathrm{GeV}$	N scaled events $E_{\mathrm{T}}^{\mathrm{miss}} > 125\,\mathrm{GeV}$
data $\gamma\gamma$	4478 ± 67	-	2.0 ± 1.4	2.0 ± 1.4
QCD template	41995 ± 205	0.107 ± 0.002	8.0 ± 2.8	0.85 ± 0.30
$Z \to ee$ (1 jet)	169362 ± 412	0.0264 ± 0.0004	28.0 ± 5.3	0.74 ± 0.14

Table 6.1: Number of events N of the instrumental $E_{\mathrm{T}}^{\mathrm{miss}}$ control samples in SR A (a), SR B (b), and SR C (c). The control samples are normalized separately to data in the control region of $E_{\mathrm{T}}^{\mathrm{miss}} < 20\,\mathrm{GeV}$. The second column contains the number of unscaled events in the control region and the third column contains the scale factor used for the normalization of number of control sample events to the number of data events in the control region. In the third and forth column, the number of unscaled and scaled events of the control samples in the SR are shown, respectively.

respectively. The control samples are normalized to data events in the control region of $E_{\mathrm{T}}^{\mathrm{miss}} < 20\,\mathrm{GeV}$. The corresponding numbers of events in the control region and the SRs can be found in Table 6.1(a), (b), and (c), respectively. The scale factor used to normalize the events of each control sample to the number of diphoton data events can be found in the third column of each table. The rows with $Z \to ee$ numbers are discussed in Section 6.1.3.

For SR A, 30 diphoton data events are observed in the corresponding control region, whereas only 2 $\mathrm{QCD}_{\gamma\gamma}$ events are found. The QCD_{γ} sample contributes with 53 events, hence a significant increase in statistics by making use of both control samples is achieved. The composition of the $E_{\mathrm{T}}^{\mathrm{miss}}$ distributions of the QCD control samples in comparison to the data (see Fig. 6.3(a)) shows a slight underestimation of the data by the QCD template in the range of $10 - 50\,\mathrm{GeV}$, where the data has a sharper peak, however the statistics especially in the $\mathrm{QCD}_{\gamma\gamma}$ sample, which appears to be able to form such a peak, are very low. Since no QCD control events are found in the SR of $E_{\mathrm{T}}^{\mathrm{miss}} > 200\,\mathrm{GeV}$, the QCD background is determined to be zero.

In SR B, no events are selected in the $\mathrm{QCD}_{\gamma\gamma}$ sample. One event is observed in data and

two events are found in the QCD_{γ} sample in the control region. The QCD background is determined to be zero because of the lack of QCD control events in the SR of $E_{\mathrm{T}}^{\mathrm{miss}} > 100\,\mathrm{GeV}$. A shape modeling is impossible due to the limited statistics.

The number of diphoton data events in the control region corresponding to SR C is 4478 events and approximately 42000 events are found in the QCD template, which yields a scale factor of 0.170 ± 0.002. Eight unscaled QCD template events, representing a scaled QCD background of 0.85 ± 0.30 events are found in the SR of $E_{\mathrm{T}}^{\mathrm{miss}} > 125\,\mathrm{GeV}$. The $\mathrm{QCD}_{\gamma\gamma}$ sample is not contributing to the QCD template in this SR of $E_{\mathrm{T}}^{\mathrm{miss}} > 125\,\mathrm{GeV}$.

6.1.3 Dielectron Control Sample

Since the difference of the calorimeter signal between electrons and photons is expected to be small, an alternative to the QCD control sample, the *dielectron* ($Z \to ee$) control sample with two electrons originating from a Z boson decay, is defined to estimate the instrumental background arising mostly from SM $\gamma\gamma$ events. Furthermore, QCD events, like multijet and γ + jets events, where jets are misidentified as photons are expected to have a similar signature in the calorimeter as two electrons with an associated jet activity and thus can be described by the dielectron control sample as well. The sample is preselected like the diphoton sample, but instead of two photons, two electrons with an invariant mass m_{ee} of

$$70\,\mathrm{GeV} < m_{\mathrm{ee}} < 110\,\mathrm{GeV} \tag{6.1}$$

are required to select electrons from Z decays. Events containing photons are vetoed from that sample for reasons of orthogonality.

The capability of the $Z \to ee$ control sample to describe the SM $\gamma\gamma$ background is studied by a comparison between $Z \to ee$ MC events and SM $\gamma\gamma$ MC events (see Fig. 6.4). The number of jets and the $E_{\mathrm{T}}^{\mathrm{miss}}$ distributions are shown in (a) and (b). The jet multiplicity is higher in $Z \to ee$ MC events than in SM $\gamma\gamma$ MC events. The different kinematics is also reflected in the different $E_{\mathrm{T}}^{\mathrm{miss}}$ spectrum of the two processes (see Fig. 6.4(b)). Therefore, a study of additional jet requirements applied to the dielectron control sample is performed, in order to find the control sample with the jet activity, which describes the $E_{\mathrm{T}}^{\mathrm{miss}}$ distributions of the diphoton data best and has the highest agreement in the $E_{\mathrm{T}}^{\mathrm{miss}}$ spectrum with the SM $\gamma\gamma$ MC sample. This study is presented in Appendix B.2 and turns out that the $E_{\mathrm{T}}^{\mathrm{miss}}$ shapes are modeled best by $Z \to ee$ events measured from data with an additional requirement of exactly one jet.

A comparison of the shapes between data, the QCD template and the dielectron samples (with and without jet requirement) is presented in Fig. 6.5(a), (b) and (c) for SR A, SR B and SR C, respectively. The dielectron samples are normalized separately to the data in the control. The data is shown as black dots, the QCD template as a blue curve. The dielectron sample with jet requirement is shown as the red dashed distribution, while the dielectron sample without any jet requirement is shown as a green dashed line. The corresponding number of events can be found in Table 6.1 (a), (b), and (c) for SR A, SR B, and SR C, respectively.

In SR A, 30 dielectron with one jet events are found in the control region, but no events are found in the SR. The shape of the dielectron sample is similar to the shape of the QCD

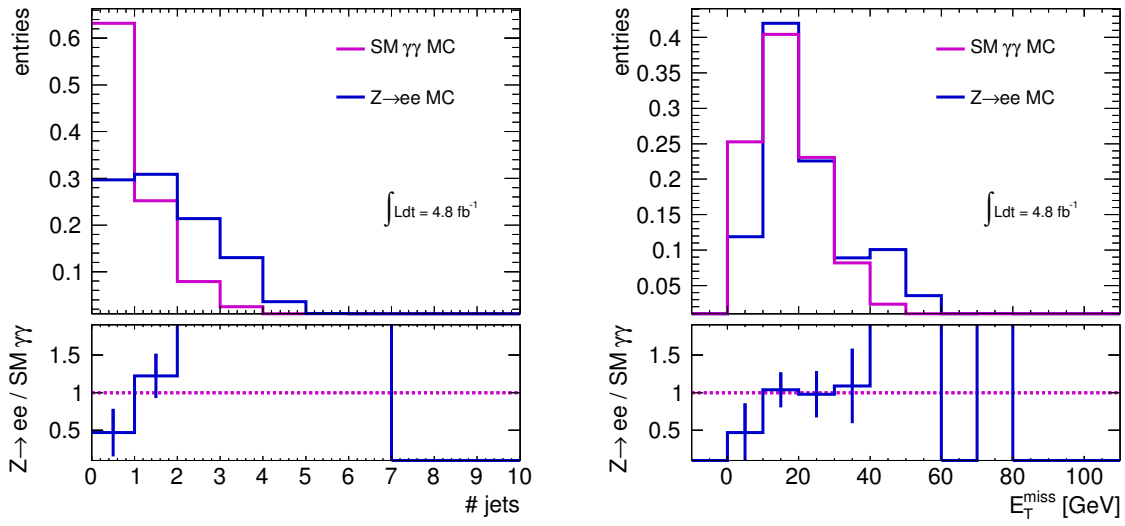

(a) (b)

Figure 6.4: Shape comparison between SM $\gamma\gamma$ MC and $Z \to ee$ MC samples as a function of the number of jets (a) and $E_{\mathrm{T}}^{\mathrm{miss}}$ (b). The distributions are normalized to unit area.

template. Since the statistics in SR B is low and no events are found in the CR, a shape modeling with the $Z \to ee$ (1 jet) sample is difficult. One event is observed in the SR, but due to the lack of a normalization factor, the background is considered to be zero. In SR C, the shape of the data is well described by the dielectron sample in the low-$E_{\mathrm{T}}^{\mathrm{miss}}$ region. In the control region, almost 170000 events are found yielding a scale factor of 0.0264 ± 0.0004. The number of scaled events in the SR is 0.74 ± 0.14.

The $E_{\mathrm{T}}^{\mathrm{miss}}$ shape modeling capabilities of the two control samples are similar and their statistics is in the same order of magnitude in all SRs. Both samples are therefore suitable to describe the $E_{\mathrm{T}}^{\mathrm{miss}}$ spectrum of the diphoton data.

6.1.4 Instrumental $E_{\mathrm{T}}^{\mathrm{miss}}$ Background Results

The number of events originating from instrumental effects is estimated from the QCD template, the combined control sample of the QCD_{γ} and the $\mathrm{QCD}_{\gamma\gamma}$ samples. In the control region of $E_{\mathrm{T}}^{\mathrm{miss}} < 20\,\mathrm{GeV}$, only very few events of genuine $E_{\mathrm{T}}^{\mathrm{miss}}$ and BSM signal are expected. Hence, the QCD template is normalized there to the number of diphoton data events. The contamination of the QCD control samples with genuine $E_{\mathrm{T}}^{\mathrm{miss}}$ events is studied in Appendix B.3 and in Appendix B.4.

Since no QCD template events are present in SR A and SR B because of the low statistics of the samples, an alternative method [143] must be used to estimated the instrumental background in those SRs: The H_{T} requirement is relaxed in steps for the QCD template and the diphoton data. From the results of the estimation obtained with the relaxed requirements, an extrapolation to the nominal SR is performed. The relaxed H_{T} cuts of SR A are 400, 200 and

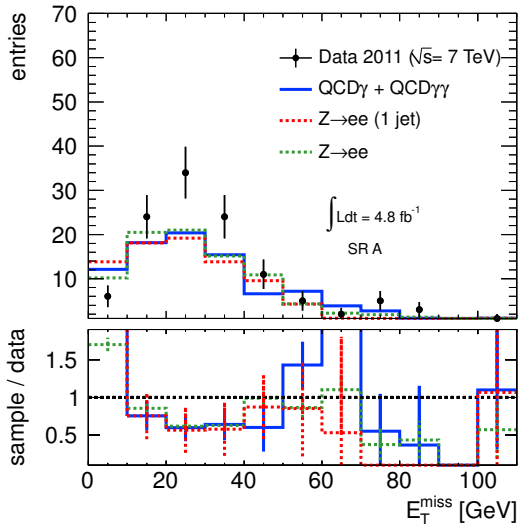

(a)

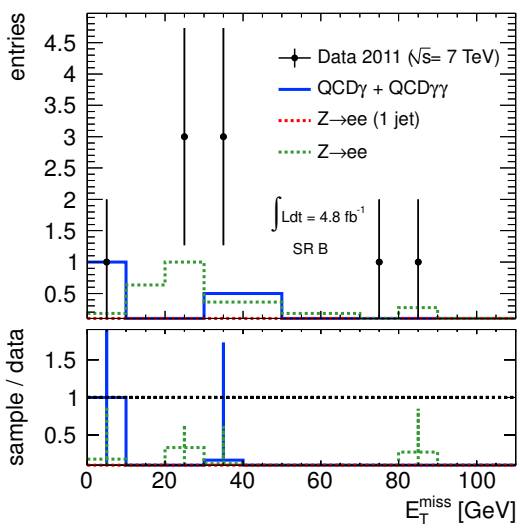

(b)

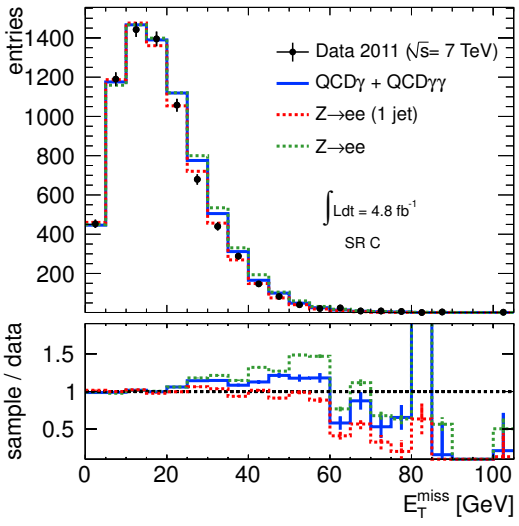

(c)

Figure 6.5: Shape comparison between diphoton data, the QCD template, and dielectron samples in SR A (a), SR B (b), and SR C (c). The control samples are normalized to diphoton data in the respective CRs.

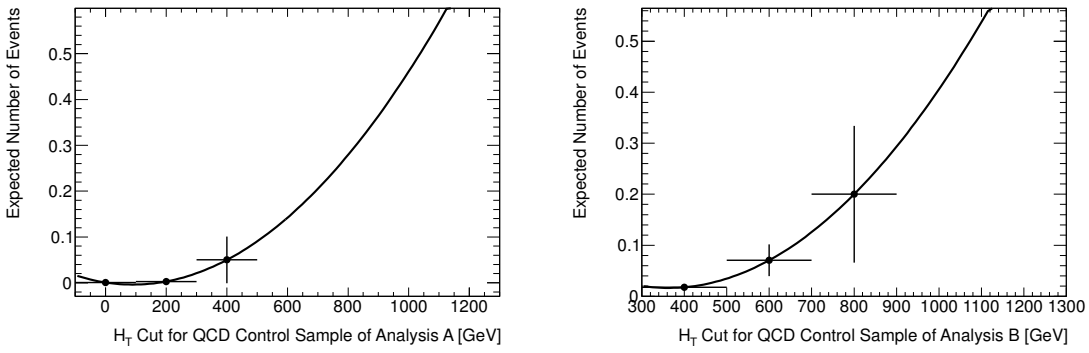

(a) (b)

Figure 6.6: The expected number of QCD background events for SR A (a) and SR B (b) as a function of the relaxed H_{T} cut placed on the QCD_{γ} + $\mathrm{QCD}_{\gamma\gamma}$ control sample [143]. The extrapolation to the nominal SR is performed via a quadratic function (black line).

0 GeV, while the cuts of SR B are 800, 600 and 400 GeV. For each step, the respective QCD template is scaled by the ratio of events in the control region of the relaxed diphoton data sample and the relaxed QCD template. By doing so, the number of events with instrumental $E_{\mathrm{T}}^{\mathrm{miss}}$ in the SR (while still using the nominal $E_{\mathrm{T}}^{\mathrm{miss}}$ requirement) is estimated. For each SR the three values are fitted with a quadratic function[1] and the value of the QCD template with the nominal H_{T} requirement is extrapolated. The extrapolated results are 0.14 and 0.54 events in SR A and SR B, respectively [143]. Figure 6.6 shows the series of H_{T} cuts with the corresponding estimates in SR A (a) and SR B (b).

The background with instrumental $E_{\mathrm{T}}^{\mathrm{miss}}$ events is expected to be between the nominal value of 0 events and the alternative result, hence the mean value is used as combined result. An uncertainty of 100 % is assigned to reflect the envelope of the two methods.

Since the relative fraction of QCD multijet, γ + jets and SM $\gamma\gamma$ events, i.e. the relative contributions of the QCD template and the dielectron control sample, is not known, the dielectron sample with one jet is used to determine the systematic uncertainty on the estimate from the QCD template. The following systematic uncertainties are considered:

- **Template difference:** The difference in number of events in the SRs between the QCD template and the dielectron (1 jet) sample is considered as a systematic uncertainty. This is relevant in particular in SR C.

- **Normalization range:** The nominal normalization range is $E_{\mathrm{T}}^{\mathrm{miss}} < 20$ GeV. In order to check the stability of the normalization factor of the QCD template under the variation of the normalization range and assign a systematic uncertainty, the lower edge of the normalization interval is increased in one GeV steps from 0 to 10 GeV, while the width of the normalization range remains constant at 20 GeV. Figure 6.7 shows the normalization factor depending on the lower edge of the normalization region. A slight instability is

[1] Other functions yield less conservative results.

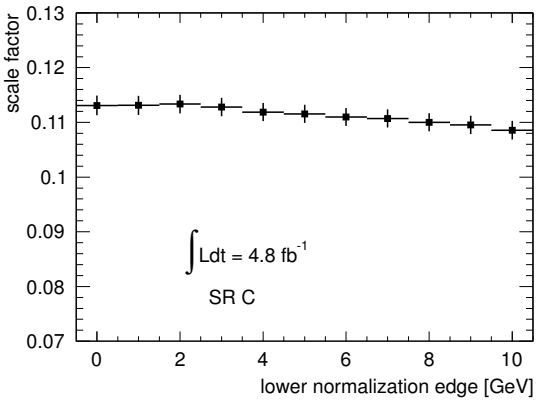

Figure 6.7: Stability of the QCD control sample normalization. The lower edge of the normalization interval is shown in the x-axis.

observed and yields a small systematic uncertainty on the scale factor 0.113 ± 0.002. The relative uncertainty is less than 2 % and can be neglected when considering the template difference systematic uncertainty. For SR A and B, the assigned systematic uncertainty is taken to be zero because no QCD control events are found in these SRs.

The systematic uncertainties in SR A and B finally result from the extrapolation and the averaging described above.

The result of the instrumental $E_{\mathrm{T}}^{\mathrm{miss}}$ background estimation is summarized in Table 6.2. In SR A (SR B), $0.07 \pm 0.00 \pm 0.07$ ($0.27 \pm 0.00 \pm 0.27$) events are found, which are the mean

	Instrumental $E_{\mathrm{T}}^{\mathrm{miss}}$ background
SR A	$0.07 \pm 0.00 \pm 0.07$
SR B	$0.27 \pm 0.00 \pm 0.27$
SR C	$0.85 \pm 0.30 \pm 0.16$

Table 6.2: Summary of the instrumental $E_{\mathrm{T}}^{\mathrm{miss}}$ background estimation. The first uncertainty is statistical, the second is the systematic uncertainty.

values of 0.0 events of the nominal estimation and of the result of the extrapolation of 0.14 (0.54) events. In SR C, the background is estimated to be $0.85 \pm 0.30 \pm 0.16$ events. The first uncertainty is statistical, whereas the second is the systematic uncertainty.

$Z(\rightarrow \nu\nu)$ + jets events can end up in the QCD control sample, if both jets are misidentified as photons. No events are observed in MC in all SRs, hence this background contribution is negligible.

6.2 Genuine E_T^{miss} Background

One of the important backgrounds to diphoton events are SM events with genuine E_T^{miss}. The diphoton signature could be created by a combination of electrons that are misidentified as photons and real photons. Typically, W and Z boson decays as well as $t\bar{t}$ events are contributing to this background, where neutrinos give rise to real E_T^{miss}. This background is estimated from the *electron-photon* ($e\gamma$) control sample, which is taken from data. In order to have a diphoton signature, the electron-photon sample has to be scaled by the misidentification rate of photons to be real electrons. The scaling and the sample definition are described in Section 6.2.1 and 6.2.2, respectively.

6.2.1 Electron Misidentification Probability

The rate of electrons misidentified as photons (scale factor) is used to calculate the diphoton contribution from electron-photon events, which contain genuine E_T^{miss}. Since the misidentification rate depends on the detector region in η, it is evaluated in several η-bins, which embodies a compromise between a granulation as fine as possible with a flat η dependence and enough statistics in each bin. This calculation is based on the full data set available and is done at preselection level. The scale factor s is defined as

$$s = \frac{N_{e\gamma}}{N_{ee}}, \tag{6.2}$$

where $N_{e\gamma}$ is the number of $Z \to e\gamma$ event candidates and N_{ee} is the number of $Z \to ee$ candidate events. The $Z \to e\gamma$ and $Z \to ee$ candidate events are selected from data by a tag-and-probe method. The tag electron is required to pass *tight* identification criteria (see Section 4.3.2), in addition to the basic cuts described in Section 5.3.2. The probe particle is either a standard photon or a standard electron. In order to ensure particles coming from Z boson decays, the invariant mass m of the tag and the probe object is required to be

$$60\,\text{GeV} < m < 120\,\text{GeV}. \tag{6.3}$$

The distributions of the invariant masses of $Z \to ee$ and $Z \to e\gamma$ tag-and-probe events of the full η range together with a signal and background fit is presented in Fig. 6.8. The overlaid fit curves are for illustration purposes and show that the peak shape is consistent with the one expected from $Z \to ee$ decays including background. The invariant mass peak is modeled by the convolution of a Breit-Wigner function and a Crystal-ball function with a background described by a Landau function. A noticeable background is found, which needs to be subtracted.

Possible background events in the invariant mass distribution are measured by a side-band method [179] instead of using a fit as it is more robust than a fit in case of low statistics. The bands are defined as intervals in the invariant mass distribution, L $= 60 - 70\,$GeV, M $= 70 - 110\,$GeV, U $= 110 - 120\,$GeV, where L and U are the lower and upper side-band

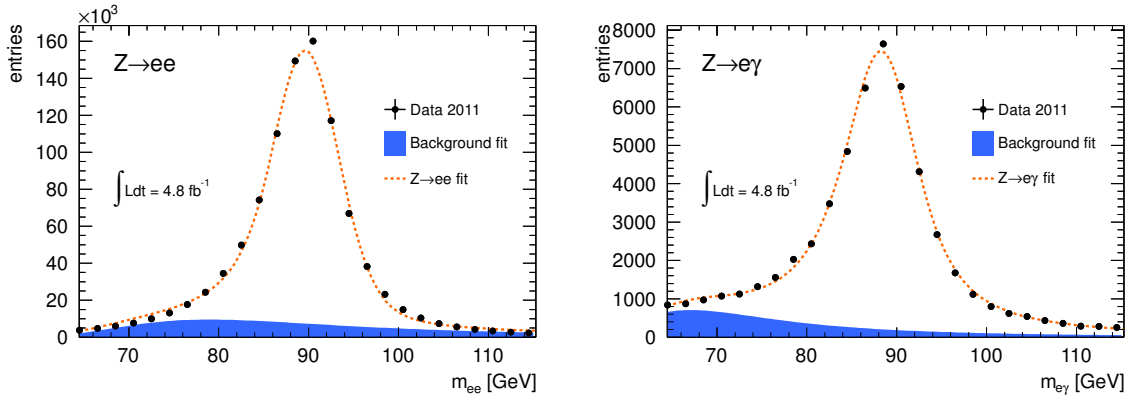

(a) (b)

Figure 6.8: Invariant mass distributions of dielectron (a) and electron-photon events (b) selected by a tag-and-probe method. A fit of the background (blue) and the signal + background (dashed orange) is overlaid.

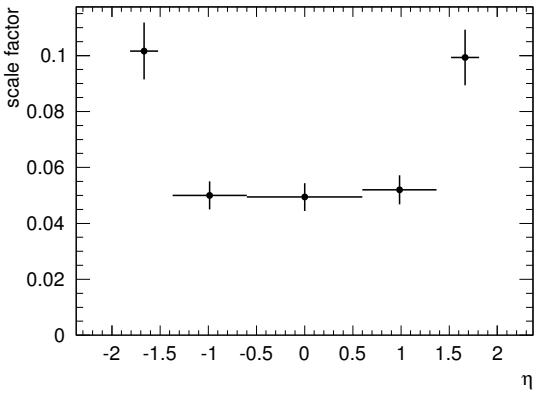

Figure 6.9: The η dependence of the background subtracted scale factors. The transition region between the calorimeter barrel and the end-cap $1.37 < |\eta| < 1.52$ is excluded.

and M is the central region. The number of background events in the central region N_{M} is estimated from the number of events in the side bands by

$$N_{\mathrm{M}} = \left(\frac{N_{\mathrm{U}}}{W_{\mathrm{U}}} - \frac{N_{\mathrm{L}}}{W_{\mathrm{L}}}\right) \frac{W_{\mathrm{M}}^2 + W_{\mathrm{L}} W_{\mathrm{M}}}{W_{\mathrm{L}} + 2W_{\mathrm{M}} + W_{\mathrm{U}}} + \frac{N_{\mathrm{L}} W_{\mathrm{M}}}{W_{\mathrm{M}}}, \tag{6.4}$$

where W_{x} is the width of the band in GeV [179]. The scale factor is estimated from the central interval. The numbers are presented in Fig. 6.9.

The background subtracted scale factors are approx. 0.05 in the central region and are rising up to 0.16 in the outermost η region. In the end-caps, a measurement of electrons and photons as precise as in the central regions is not possible due to the coarser calorimeter cell size.

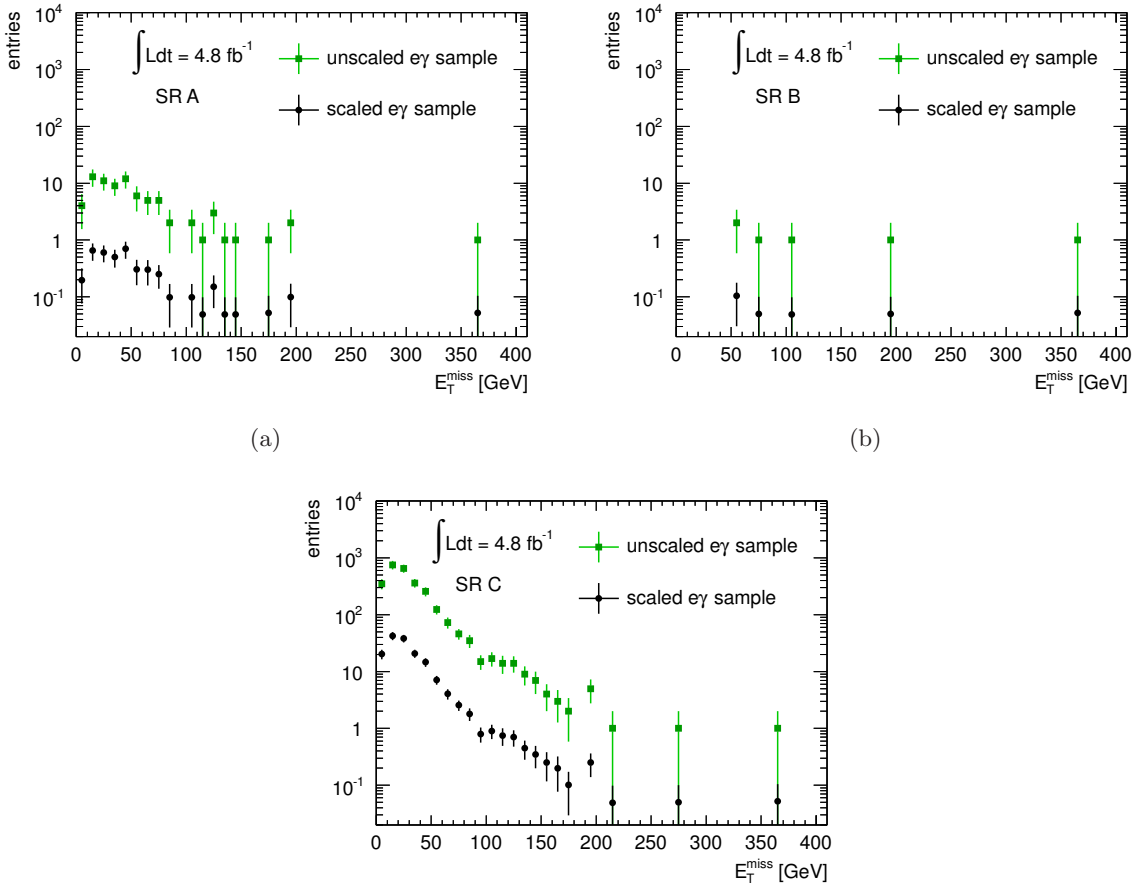

Figure 6.10: Unscaled (green) and scaled (black) $E_{\mathrm{T}}^{\mathrm{miss}}$ distributions of the $e\gamma$ control sample in SR A (a), SR B (b) and SR C (c). The scaling is done using the background subtracted $e\gamma$ scale factor.

6.2.2 Electron-Photon Control Sample

The electron-photon control sample is selected from data in the same way as the diphoton data. Events containing exactly one photon and at least one electron are required. The genuine $E_{\mathrm{T}}^{\mathrm{miss}}$ is expected to arise from neutrinos of W boson and top decays. In order to model the $E_{\mathrm{T}}^{\mathrm{miss}}$ distribution of the data, the diphoton signature is emulated from the $e\gamma$ sample by scaling each event of the sample by the scale factor, i.e. by the probability that an electron is misidentified as a photon depending on the η bin (see Section 6.2.1).

Details on the $e\gamma$ control sample can be found in Appendix B.5. The $E_{\mathrm{T}}^{\mathrm{miss}}$ distribution of the $e\gamma$ control samples integrated over all η bins in SR A, SR B and SR C are shown in Fig. 6.10(a)–(c). The green points show the unscaled distribution, while the black points show the distribution after the application of the scale factors. The shape does not change significantly by the scaling. In SR C, the $E_{\mathrm{T}}^{\mathrm{miss}}$ distribution has a steeply falling shape, whereas in SR A the shape is rather flat. The statistics are low in SR B due to the tight H_{T} requirement.

Since the $e\gamma$ sample may have some contamination from events with instrumental $E_{\mathrm{T}}^{\mathrm{miss}}$, these events have to be treated by the QCD sample. As described in Section 6.1.2, the instrumental $E_{\mathrm{T}}^{\mathrm{miss}}$ background is modeled by the QCD template. This template is used to describe the contamination in the $e\gamma$ control sample and is scaled to the $e\gamma$ control sample in the region of $E_{\mathrm{T}}^{\mathrm{miss}} < 20\,\mathrm{GeV}$. As a cross check, the dielectron sample with exactly one jet is overlaid. In the low $E_{\mathrm{T}}^{\mathrm{miss}}$ region, the $e\gamma$ control sample is strongly contaminated with events with instrumental $E_{\mathrm{T}}^{\mathrm{miss}}$. The contributions from these samples are illustrated in Fig. 6.11(a)–(c) for SR A, SR B and SR C. Since the $e\gamma$ control sample contains a significant contamination with events with instrumental $E_{\mathrm{T}}^{\mathrm{miss}}$, these events are subtracted to obtain background estimation from events with genuine $E_{\mathrm{T}}^{\mathrm{miss}}$. In SR B, the QCD template can not be scaled due to the lack of events in the normalization region. Since no events in the SR are found in the QCD template in SR A and SR B, the SR content including the $E_{\mathrm{T}}^{\mathrm{miss}}$ requirement of the $e\gamma$ control sample is determined to be purely from events with genuine $E_{\mathrm{T}}^{\mathrm{miss}}$. In SR C, the scaled QCD template yields 0.012 ± 0.004 events, which are subtracted from the result estimated from the $e\gamma$ control sample.

6.2.3 Genuine $E_{\mathrm{T}}^{\mathrm{miss}}$ Extrapolation

The modeling of the genuine $E_{\mathrm{T}}^{\mathrm{miss}}$ spectrum by MC is studied in this section. The relevant processes are $W \to e\nu + \text{jets}$, $W \to e\nu\gamma$ and $t\bar{t} \to e\nu + \mathrm{X}$. In particular in the low $E_{\mathrm{T}}^{\mathrm{miss}}$ region, the contribution of events with instrumental $E_{\mathrm{T}}^{\mathrm{miss}}$ described by the QCD template (see Section 6.1.2) needs to be taken into account. The QCD template is normalized to the $e\gamma$ sample in the low $E_{\mathrm{T}}^{\mathrm{miss}}$ CR. The MC samples are normalized to the number of $e\gamma$ events in the region of $E_{\mathrm{T}}^{\mathrm{miss}} > 50\,\mathrm{GeV}$, where only small contributions of events with instrumental $E_{\mathrm{T}}^{\mathrm{miss}}$ are expected. Four scenarios are studied: The extra cases of the extrapolation with only one of the three genuine $E_{\mathrm{T}}^{\mathrm{miss}}$ MC samples to study extremal cases and the extrapolation with the combined MC sample, where the relative fraction of a sample is determined by the cross section (see Section 4.4.1).

In Fig. 6.12, the shape extrapolations in the four scenarios in SR A are presented. The shape of the combined sample is shown in (a), the extrapolation with $W \to e\nu + \text{jets}$ events (green) in (b), the extrapolation with $W \to e\nu\gamma$ events (yellow) in (c) and the extrapolation with top events (red) in (d). In all scenarios, the QCD and $Z \to ee$ contribution is shown in blue. Figure 6.13 shows the same set of plots for SR C. The number of events estimated by the extrapolations in the SRs are listed in Table 6.3. Since the statistics are low in SR B, only the estimated values, and not the modeling of the $E_{\mathrm{T}}^{\mathrm{miss}}$ spectrum, are presented. No $W \to e\nu\gamma$ events pass the selection in SR A and B. The quoted uncertainties are statistical. The extrapolation with the $W \to e\nu + \text{jets}$ sample matches the number of events in the $e\gamma$ sample in all SRs but has poor statistics. The agreement between the combined sample and the $e\gamma$ control sample is good within the uncertainties, which are lower due to the higher number of events in that sample. Thus, the combined MC sample is able to describe the number of events in the high $E_{\mathrm{T}}^{\mathrm{miss}}$ region of the genuine $E_{\mathrm{T}}^{\mathrm{miss}}$ control sample. The single MC sample extrapolations yield consistent results as well. Finally, a systematic uncertainty due to the MC

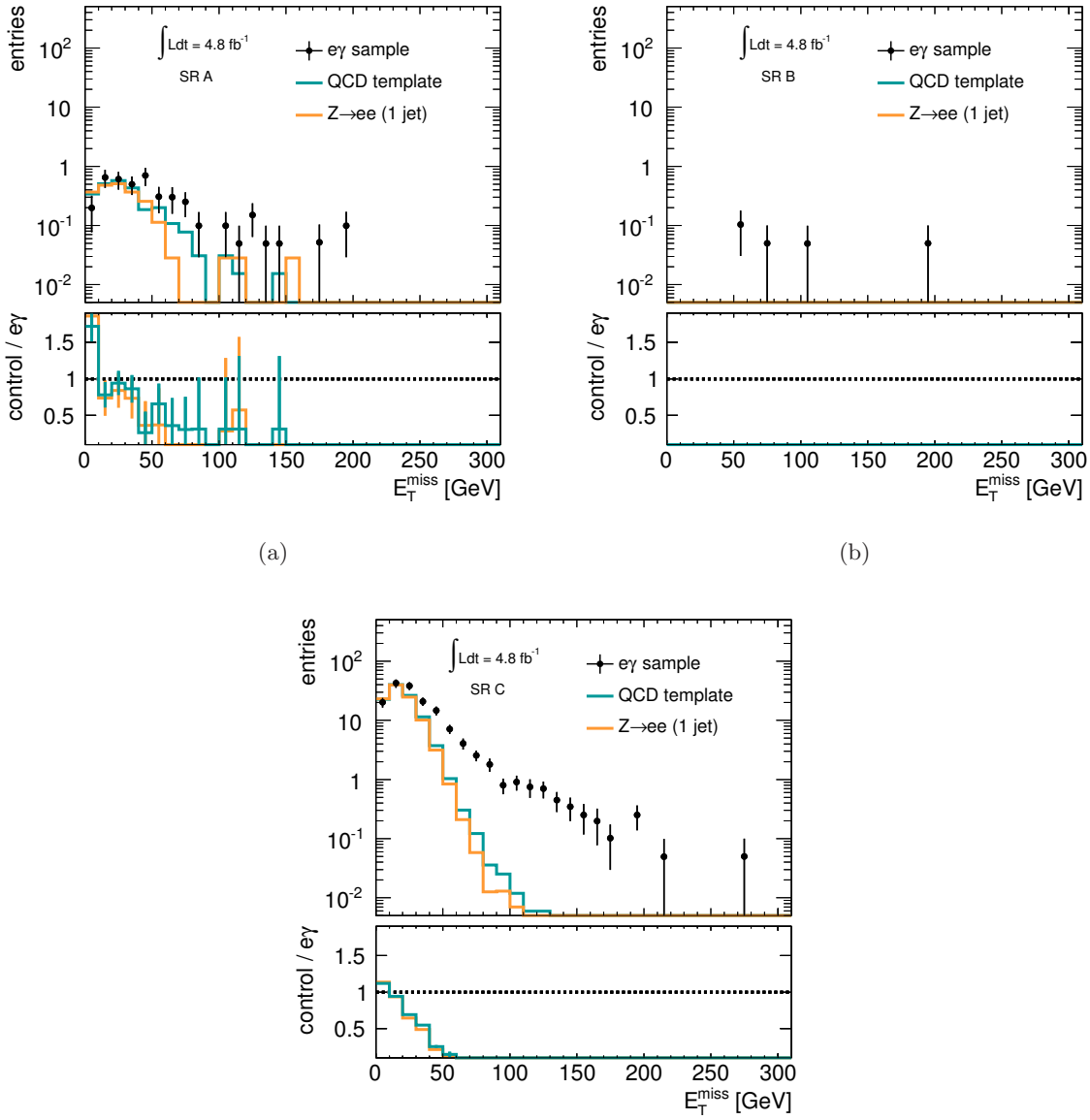

Figure 6.11: Contributions from events with instrumental $E_{\mathrm{T}}^{\mathrm{miss}}$ in the $e\gamma$ sample in SR A (a), SR B (b), and SR C (c). The QCD template (blue) and the $Z \to ee + 1$ jet control sample are normalized to the $e\gamma$ sample in the control region of $E_{\mathrm{T}}^{\mathrm{miss}} < 20\,\mathrm{GeV}$.

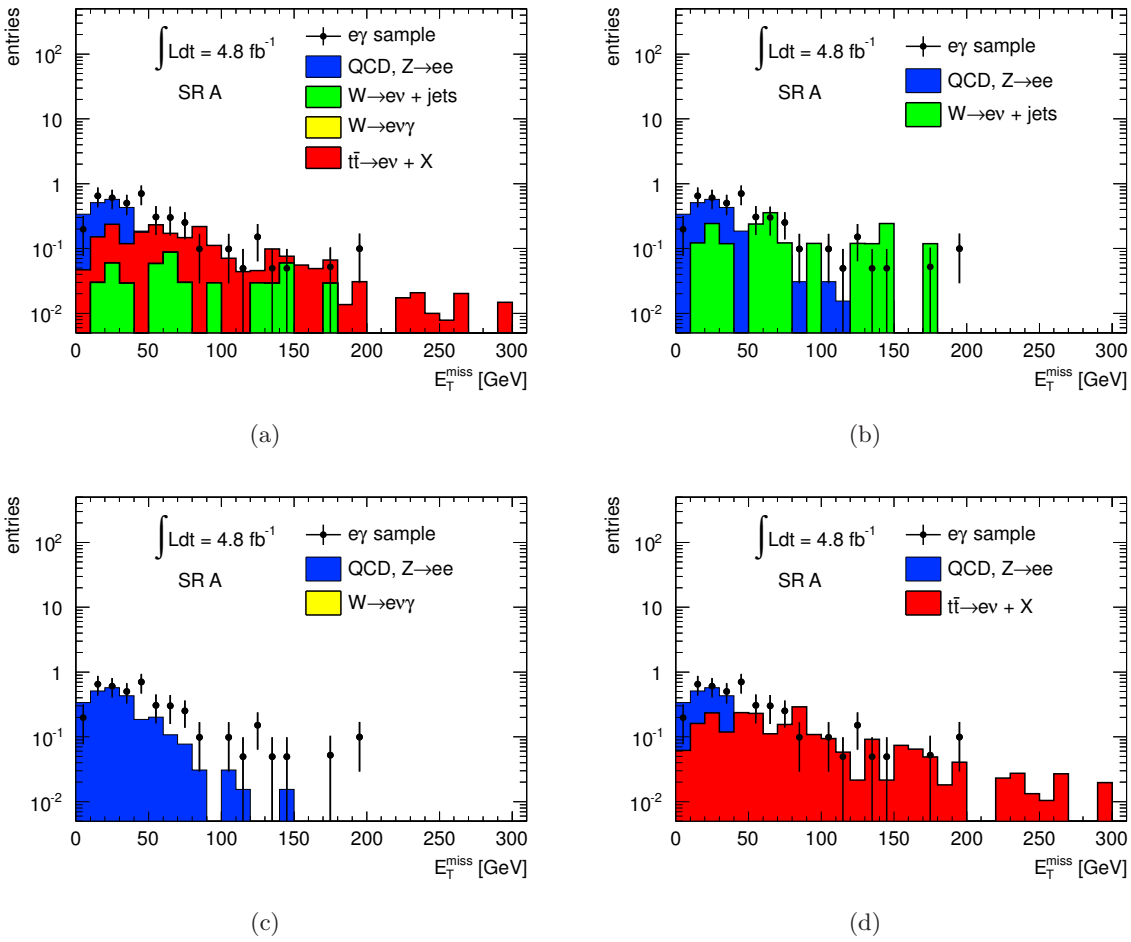

Figure 6.12: Extrapolation from MC in SR A. The extrapolations with the combined, the $W \to e\nu + \text{jets}$, the $W \to e\nu\gamma$ and the $t\bar{t} \to e\nu + \text{X}$ samples are shown in (a)–(d), respectively. The QCD and $Z \to ee$ contributions are modeled by the QCD template. More description can be found in the text.

sample	SR A	SR B	SR C
$e\gamma$ control sample	0.06 ± 0.06	0.16 ± 0.09	2.1 ± 0.4
$W \to e\nu + \text{jets}$	0.12 ± 0.12	0.34 ± 0.34	1.9 ± 0.4
$W \to e\nu\gamma$	-	-	3.4 ± 2.0
$t\bar{t} \to e\nu + \text{X}$	0.13 ± 0.06	0.36 ± 0.22	3.4 ± 0.4
Combined	0.13 ± 0.05	0.36 ± 0.18	2.42 ± 0.26

Table 6.3: Results of the extrapolation of the $E_{\mathrm{T}}^{\mathrm{miss}}$ tail of the $e\gamma$ control sample by using MC. The MC samples are normalized separately to the $e\gamma$ control sample in the region of $E_{\mathrm{T}}^{\mathrm{miss}} > 50\,\mathrm{GeV}$. The relative contribution in the combined sample ($W \to e\nu + \text{jets}$, $W \to e\nu\gamma$, $t\bar{t} \to e\nu + \text{X}$) is determined by the cross section of the process.

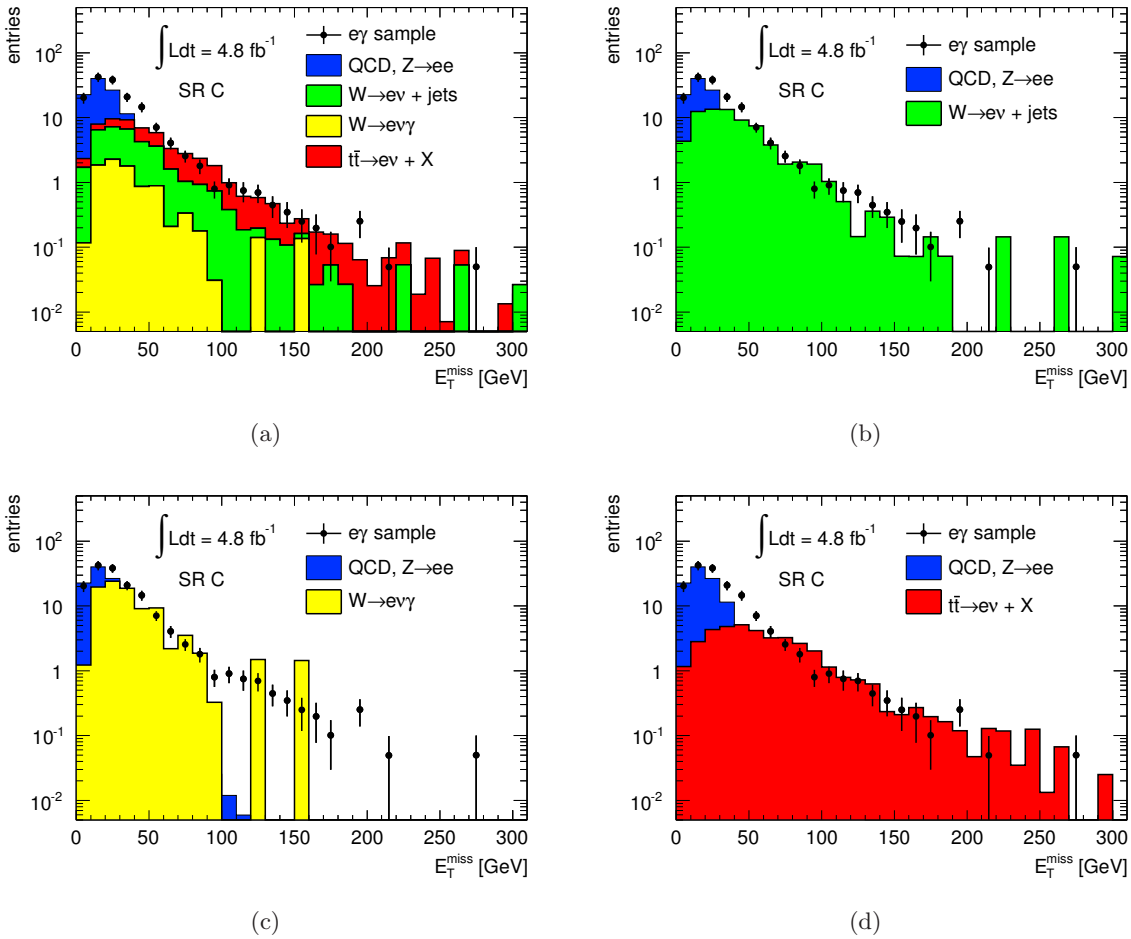

Figure 6.13: Extrapolation from MC in SR C. The extrapolations with the combined, the $W \to e\nu + \text{jets}$, the $W \to e\nu\gamma$ and the $t\bar{t} \to e\nu + \text{X}$ samples are shown in (a)–(d), respectively. The QCD and $Z \to ee$ contributions are modeled by the QCD template. More description can be found in the text.

SR	Events with genuine $E_{\mathrm{T}}^{\mathrm{miss}}$
A	$0.05 \pm 0.05 \pm 0.07$
B	$0.15 \pm 0.09 \pm 0.17$
C	$2.08 \pm 0.37 \pm 0.13$

Table 6.4: Summary of the genuine $E_{\mathrm{T}}^{\mathrm{miss}}$ background estimation. The first uncertainty is statistical, the second is the systematic uncertainty.

extrapolation difference between the $e\gamma$ sample and the combined MC sample is assigned to the genuine $E_{\mathrm{T}}^{\mathrm{miss}}$ background, as discussed in Section 6.2.4.

Background events from diboson production like $WW(\rightarrow e\nu e\nu)$ and $WZ(\rightarrow eee\nu)$ with genuine $E_{\mathrm{T}}^{\mathrm{miss}}$ and electrons misidentified as photons are taken from MC and are found to be negligible [143].

6.2.4 Genuine $\mathbf{E_{T}^{miss}}$ Background Results

The number of genuine $E_{\mathrm{T}}^{\mathrm{miss}}$ events in each SR is estimated by subtracting the number of events of the normalized QCD template from the number of events in the scaled $e\gamma$ sample. This is done for each SR separately. Several sources of systematic uncertainties related to the background with genuine $E_{\mathrm{T}}^{\mathrm{miss}}$ are taken into account.

- **MC modeling:** The modeling of the genuine $E_{\mathrm{T}}^{\mathrm{miss}}$ shape by MC is described in more detail in Section 6.2.3. The difference between the number of events computed from the combined MC sample and the estimation from the $e\gamma$ control sample is considered as a systematic uncertainty.
- **Scale factor:** A uncertainty due to the scaling factor of 2 % is derived from the fluctuation of the scale factor as a function of ϕ [179].
- **QCD template:** Instead of the QCD template, the dielectron template is subtracted from the $e\gamma$ sample. The difference to the number of events calculated with the QCD template is assigned as a systematic uncertainty.

All systematic uncertainties described above are added quadratically and yield a total systematic uncertainty of ± 0.07 events in SR A, ± 0.17 events in SR B and ± 0.13 events in SR C. The results of the background from events with genuine $E_{\mathrm{T}}^{\mathrm{miss}}$ are listed in Table 6.4.

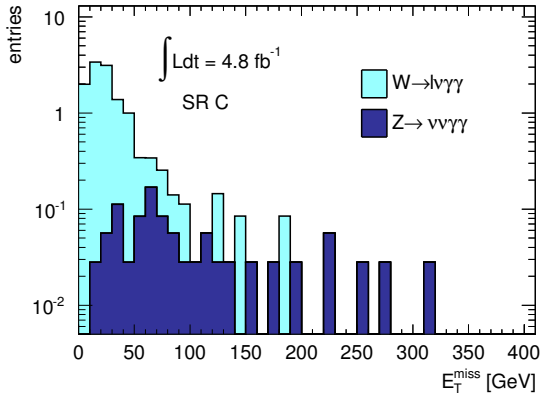

Figure 6.14: $E_{\mathrm{T}}^{\mathrm{miss}}$ distribution of the irreducible background of $Z(\to \nu\bar{\nu}) + \gamma\gamma$ and $W(\to \ell\nu) + \gamma\gamma$ events in SR C.

	$Z(\to \nu\bar{\nu}) + \gamma\gamma$	$W(\to \ell\nu) + \gamma\gamma$	total
$E_{\mathrm{T}}^{\mathrm{miss}} > 0\,\mathrm{GeV}$	1.00 ± 0.17	11.6 ± 1.0	12.6 ± 1.0
$E_{\mathrm{T}}^{\mathrm{miss}} > 125\,\mathrm{GeV}$	0.25 ± 0.08	0.18 ± 0.13	0.42 ± 0.15

Table 6.5: Irreducible background split into W and Z components in SR C. The total number of events is the sum of the second and third column. The uncertainties are statistical

6.3 Irreducible Background

SM $Z(\to \nu\bar{\nu}) + \gamma\gamma$ and $W(\to \ell\nu) + \gamma\gamma$ processes are an irreducible background, i.e. they have the same signature as the signal and can not be reduced by selection cuts without reducing the signal efficiency. Therefore, this background can only be determined from MC. Figure 6.14 illustrates the $E_{\mathrm{T}}^{\mathrm{miss}}$ distribution of the irreducible background in SR C. Corresponding values are listed in Table 6.5. Most of the events before the final $E_{\mathrm{T}}^{\mathrm{miss}}$ requirement are from the $W(\to \ell\nu) + \gamma\gamma$ process. In SR C ($E_{\mathrm{T}}^{\mathrm{miss}} > 125\,\mathrm{GeV}$), $Z(\to \nu\bar{\nu}) + \gamma\gamma$ events contribute with 0.25 ± 0.08 events and $W(\to \ell\nu) + \gamma\gamma$ with 0.18 ± 0.13 events to a total irreducible background of 0.43 ± 0.15. The quoted uncertainties are statistical. In SR A and B, no irreducible events pass the selection, thus the irreducible background is estimated to be zero. The following systematic uncertainties are assigned to the irreducible background estimate:

- **K-factors:** The NLO K-factors are 2 ± 0.3 and 3 ± 3 for Z and W events with two photons, respectively [180, 181], and are computed with the `VBFNLO` program package [182]. The K-factor uncertainty is taken into account as a systematic uncertainty.

- **Scale uncertainty:** A uncertainty due to the variation of the renormalization scale of 7.5 % is associated to the $Z(\to \nu\bar{\nu}) + \gamma\gamma$ process [180].

These systematic uncertainties are added quadratically. The total number of irreducible background events in the signal regions is summarized in Table 6.6.

SR	Irreducible background events
A	< 0.01
B	< 0.01
C	$0.42 \pm 0.15 \pm 0.26$

Table 6.6: Irreducible background results in the various SR. The first uncertainty is statistical, the second is systematic

6.4 Conclusion

In this chapter, the measurement of the SM background arising from three main sources has been discussed. The total results of the background estimation, i.e. the combination of the sources and the shape modeling of the diphoton data, is presented in Section 8.1. Furthermore, the comparison between the estimated background events and the number of observed events in data is performed in order to check for possible new physics.

CHAPTER 7

Systematic Uncertainties

This chapter is dedicated to the description of the systematic uncertainties and summarizes the studies performed in [143]. The systematic uncertainties are assigned as to the signal selection efficiency. The uncertainties related to the background estimation have been described already in Chapter 6. Signal point dependent uncertainties, e.g. the $E_{\mathrm{T}}^{\mathrm{miss}}$ systematic uncertainty, are evaluated for each generated point separately.

7.1 Luminosity Uncertainty

The measurement of the luminosity is described in Section 5.1. A relative uncertainty of 3.7 % is assigned to the total integrated luminosity of $4.8\,\mathrm{fb}^{-1}$ [157]. Since the number of signal events expected from MC is a function of the luminosity, this uncertinty is considered as a signal uncertainties. The luminosity uncertainty is not assigned to the background estimate to avoid a double-counting.

7.2 Trigger Efficiency Uncertainty

The estimation of the uncertainty of the trigger efficiency with respect to the offline selection is described in detail in [143]. The trigger chain used is `EF_2g20_loose`, which is described in Section 3.3.3. The trigger efficiency of the diphoton trigger chain is assumed to be the squared efficiency of the corresponding single photon trigger chain `EF_g20_loose`.

In data, the efficiency measurement of the `EF_2g20_loose` chain is performed by a data-driven *bootstrap method* and found to be greater than $99.7^{+0.3}_{-0.8}$ % [143]. In signal MC, the efficiency is estimated by using MC generator information and found to be within $99.8 - 100$ % with absolute uncertainties of the order of 0.1 % [143]. The difference between the efficiencies found in data and MC is considered as a systematic uncertainty. In addition, since the purity of the data is not known, a conservative diphoton trigger efficiency uncertainty of 0.5 % is used [143].

7.3 Photon Uncertainties

The following systematic uncertainties related to the photon selection are considered [143]:

- **Shower shapes:** The identification of photons is based on shower shape variables (see Section 4.3.3). The difference in selection efficiency between a data-driven method, the so-called *matrix method*, and the shifting of shower shape variables in MC to match the ones in data (see Section 5.3.1) is considered as systematic uncertainty of 4 % [143].

- **Conversions:** Photons are identified according to their conversion category (see Section 4.3.3). The classification of photons in the wrong conversion category induces a systematic uncertainty of 1.8 % [143, 183], since the subsequent identification is different for converted or unconverted photons, which results in different selection efficiencies in these cases.

- **Isolation:** The calorimeter isolation energy is measured in a cone ring around the calorimeter cluster of a photon (see Section 5.3.1). The average difference of the mean energy between data and signal MC in the isolation cone ring is found to be 0.4 GeV [143]. Hence the selection criterion on the energy is relaxed by that value and the selection efficiency is estimated. The difference in selection efficiency between the relaxed and the nominal cut threshold is assigned as uncertainty, which is 0.9 %, 0.2 %, and 0.4 % for the GGM scenarios, the GMSB SPS8 scenario, and the UED scenario, respectivly [143].

- **Object quality:** Although, detector regions, which are not working as expected (see Section 5.3.5), are attempted to be simulated in the MC, a corresponding systematic uncertainty needs to be assigned. For a signal photon, a difference in selection efficiency of 0.1 % [143] due to badly working detector regions is found between data and MC. Hence an uncertainty of 0.2 % [143] for two photons is considered.

- **Energy correction:** The energy of the calorimeter cluster is corrected in data taking into account the well known $Z \to ee$ invariant mass peak (see Section 5.3.1). The impact of the energy correction on the selection efficiency is studied by shifting the energy scale by $\pm$ one standard deviation. Since the momentum of the photons in the BSM scenarios is mostly far above the selection threshold, this uncertainty is negligible [143].

7.4 Uncertainty on the E_T^{miss} Measurement

The E_T^{miss} is calculated from topological calorimeter clusters including corrections arising from muons (see Section 4.3.6). The measurement of E_T^{miss} suffers from two major uncertainties which are the topological cluster energy scale uncertainty and the E_T^{miss} resolution uncertainty [143].

The uncertainty of the topological cluster energy scale is evaluated as a function of p_T and η of the clusters and propagated to the E_T^{miss}. The resulting differences in the selection

efficiencies are calculated for each signal point and all SRs. In the GGM scenario, the selection efficiency uncertainty varies between $0.4 - 16\,\%$ in SR A, between $0.1 - 4.9\,\%$ in SR B, and between $0.1 - 9.2\,\%$ in SR C [143]. The largest uncertainties are found in regions with a low $\tilde{\chi}_1^0$ mass, i.e. with low missing energy, because small variations in the selection threshold yield a significant impact on the selection efficiency. In regions with high $\tilde{\chi}_1^0$ mass, i.e. with high $E_{\mathrm{T}}^{\mathrm{miss}}$, the $E_{\mathrm{T}}^{\mathrm{miss}}$ of the event is often above the selection threshold. Thus, the uncertainty is small. In the GMSB SPS8 scenario uncertainties of up to 30 %, 9 %, and 14 % are estimated for SR A, B and C, respectively [143]. The uncertainty is driven by the mass of the $\tilde{\chi}_1^0$, hence, it is a function of Λ. The uncertainties in the UED scenario are not greater than 2 % in all SRs, whereupon the highest values are found in SR A [143].

The uncertainty due to the $E_{\mathrm{T}}^{\mathrm{miss}}$ resolution is estimated from a comparison of the $E_{\mathrm{T}}^{\mathrm{miss}}$ resolutions in data and signal MC. The resulting uncertainties are less than 14 % in the GGM and the GMSB SPS8 scenario, while in the UED scenario, it is smaller than 3 % over all SRs.

The uncertainty due to the muon corrections is found to be negligible [143]. The total $E_{\mathrm{T}}^{\mathrm{miss}}$ uncertainty is evaluated at each parameter point and for each SR separately from the quadratic combination of the resolution uncertainty and the cluster energy uncertainty, where the latter provides the dominant fraction of the $E_{\mathrm{T}}^{\mathrm{miss}}$ uncertainty.

7.5 H_{T} Uncertainty

The total visible energy H_{T} is the sum of the $|\vec{p}_{\mathrm{T}}|$ of jets, photons, electrons, and muons (see Section 5.3.6). The momentum uncertainties are determined for all particles separately and combined quadratically to form the H_{T} uncertainty. The uncertainty is evaluated depending on the parameter point and SR, where no uncertainty is assigned in SR C due to the absence of the H_{T} requirement. In the varying $m_{\tilde{g}}$ ($m_{\tilde{q}}$) GGM scenario, the uncertainty is found to be less than 7.3 % (4.4 %) [143]. Since the mass of the gluino sets the scale for H_{T}, the uncertainty becomes greater with ingreasing $m_{\tilde{g}}$. The uncertainties are smaller in SR A with respect to SR B because of the smaller H_{T} requirement. For the GMSB SPS8 scenario and the UED scenario, the uncertainty is less than 9 % and less than 1 %, respectively [143]. Since H_{T} and $E_{\mathrm{T}}^{\mathrm{miss}}$ are correlated in the event due to the decay kinematics, the two corresponding uncertainties are considered fully correlated.

7.6 Pile-up Uncertainty

Although the MC samples are generated attempting to reflect the beam conditions during the data taking, and a reweighting according to the number of pile-up events $\langle\mu\rangle$ is performed to model the data conditions (see Section 4.4.6). An uncertainty of 0.8 %, 0.5 %, and 0.5 % arising from a 10 % variation of $\langle\mu\rangle$ is assigned in the GGM scenarios, the GMSB SPS8, and the UED scenario, respectively [143].

7.7 MC Statistics Uncertainty

The uncertainty due to the limited MC sample size is evaluated for each grid point and each SR separately. In the GGM scenarios, the uncertainty ranges between 2.2 % and 12.9 %, while in the GMSB SPS8 scenario, the uncertainty is between 1.9 % and 27.8 %. The large uncertainties of the latter scenario are found in SR A and SR B, where only a few events pass the final selection and lead to a high relative uncertainty. In the UED scenario, the uncertainty stays below 1.6 % in SR A.

7.8 Theory Uncertainties

7.8.1 SUSY Scenarios

The cross sections of the GGM and the GMSB SPS8 scenarios are discussed in Section 4.4.2 and Section 4.4.3. The cross section uncertainties [143] of the SUSY scenarios are derived from several sources, where the cross section is recomputed separately for each source described below. The largest difference between the nominal cross section and extremal cross sections arsing from the variations is considered as theoretical uncertainty. The following source of uncertainties, which are assumed to be uncorrelated, are considered [143]:

- **PDF uncertainty:** The extremal PDF uncertainty is obtained by varying the PDF parameters within the 68 % CL ranges of the error PDF sets of the `CTEQ6.6` [142] and the `MSTW2008 NLO` [184] PDF sets.

- **Scale uncertainty:** The cross section variations, induced by up and down scaling of the factorization and the renormalization scales by a factor of two, are referred to as scale uncertainty. The maximum difference of the `CTEQ6.6` and the `MSTW2008 NLO` PDF sets with respect to the nominal cross section is taken as uncertainty.

- α_S **uncertainty:** The cross section deviations due to variations of the coupling constant α_S are calculated with the help of a special `CTEQ6.6` PDF set, which incorporates α_S variations. Due to the lack of a similar PDF set in the group of `MSTW2008 NLO` PDF sets, no uncertainty evaluation is performed in the latter case.

7.8.2 UED Scenario

The cross section uncertainty is evaluated in the UED scenario (see Section 4.4.4) by taking PDF variations into account [143]. The uncertainty due to scale variations play a minor role, since the calculations are performed at LO. For the generation of the UED samples and the nominal cross section calculation, a modified LO PDF (`MRST2007lomod` [147]) is used. Since no error sets are available for this PDF, the `MSTW2008lo90cl` error sets [184] are used instead. The difference of 4 % [143] between the cross sections obtained from the PDF error sets and the nominal cross section is taken as uncertainty.

Systematic error source		scenario		
		GGM ($\tilde{g}$, $\tilde{\chi}_1^0$)	GGM ($\tilde{q}$, $\tilde{\chi}_1^0$)	GMSB SPS8
Luminosity		3.7 %		
Trigger		0.5 %		
Shower shape		4.0 %		
Conversions		1.8 %		
Photon quality		0.2 %		
Sum photon		4.4 %		
Photon isolation		0.9 %	0.9 %	0.2 %
Pile-up		0.8 %	0.8 %	0.5 %
$\boldsymbol{E_{\mathrm{T}}^{\mathrm{miss}}}$	SR A	0.4 – 17.0 %	0.2 – 8.3 %	4.1 – 30.8 %
	SR B	0.1 – 4.9 %	0.2 – 1.6 %	1.0 – 9.4 %
	SR C	0.1 – 9.3 %	0.2 – 3.8 %	1.6 – 14.0 %
$\boldsymbol{H_{\mathrm{T}}}$	SR A	0.0 – 0.8 %	0.0 – 0.4 %	0.0 – 4.3 %
	SR B	0.0 – 7.3 %	0.0 – 4.4 %	1.6 – 9.0 %
MC statistics	SR A	2.4 – 12.9 %	2.2 – 7.8 %	2.6 – 27.8 %
	SR B	2.4 – 8.3 %	2.2 – 6.2 %	4.9 – 19.0 %
	SR C	2.3 – 8.3 %	2.2 – 5.5 %	1.9 – 11.3 %
PDF/Scale		23 – 39 %	29 – 49 %	6.3 – 8.3 %
Total (w/o PDF/scale)	SR A	8 – 21 %	7 – 11 %	9 – 45 %
	SR B	8 – 12 %	7 – 8 %	10 – 27 %
	SR C	8 – 14 %	7 – 8 %	8 – 19 %
Total (with PDF/scale)	SR A	24 – 44 %	30 – 50 %	11 – 48 %
	SR B	25 – 43 %	30 – 50 %	12 – 28 %
	SR C	24 – 44 %	30 – 50 %	9 – 20 %

Table 7.1: Systematic uncertainties in the GGM and GMSB SPS8 scenarios [143].

7.9 Summary

Table 7.1 shows the systematic uncertainties for the different SUSY scenarios, namely the GGM with varying $\tilde{g}$ mass scenario, the GGM with varying $\tilde{q}$ mass scenario and the GMSB SPS8 scenario [143]. The values are relative uncertainties, which are assigned to the selection efficiency. If the uncertainties depend on the kinematic properties of the event, i.e. they depend on the SR and the parameter point, a range of uncertainties is quoted. The theoretical uncertainties are summarized and denoted as PDF/Scale uncertainties. The total uncertainty is quoted with and without theoretical uncertainties, whereas the first is used as the final result for the interpretation (see Section 8). The latter represents the uncertainties from the measurement (and the MC generation statistics). The distribution of the total uncertainty including theoretical

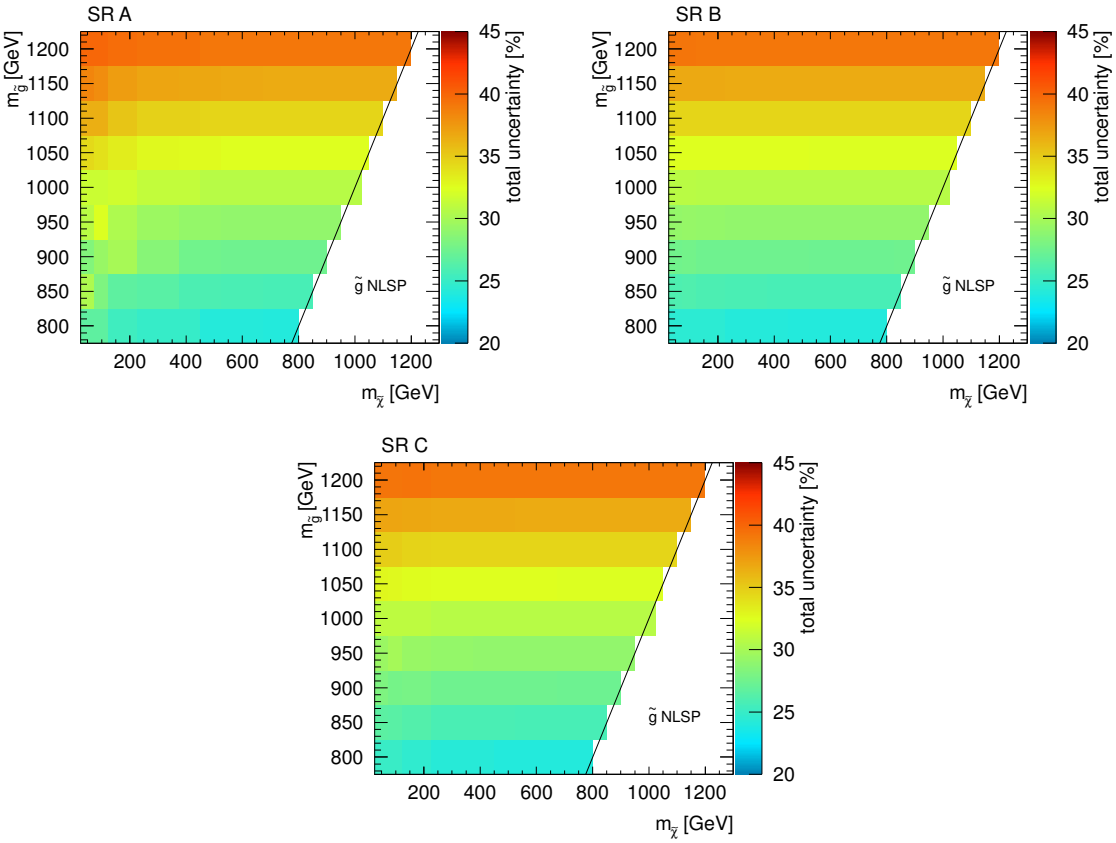

Figure 7.1: The total uncertainty including theoretical uncertainties in the GGM scenario with varying gluino mass.

uncertainties of the GGM scenario with varying $\tilde{g}$ mass is shown in Fig. 7.1(a)–(c) for the three SRs. In the GGM scenarios, the theoretical uncertainties are the dominant source of the total uncertainty, while in the GMSB SPS8 scenario, the $E_{\mathrm{T}}^{\mathrm{miss}}$ and MC statistics uncertainties are at a comparable scale. Since in the GGM scenarios the sparticles arise via strong production the theoretical uncertainties are greater than in the GMSB SPS8 scenario where the production via weak interaction is dominant and therefore the NLO corrections and the uncertainties are smaller. Since the uncertainty distribution over the mass plane is similar in the two GGM scenarios, the one with varying $\tilde{q}$ mass is not shown.

The systematic uncertainties in the UED scenario are listed in Table 7.2 as a function of R^{-1}. Since the final interpretation is performed with the results obtained in SR A (see Section 8.6), only the results of this SR are quoted.

Systematic error source	R^{-1} **[GeV]**					
	1000	1100	1200	1300	1400	1500
Luminosity	3.7 %					
Trigger	0.5 %					
Shower shape	4.0 %					
Conversions	1.8 %					
Photon quality	0.2 %					
Sum photon	4.4 %					
Photon isolation	0.4%					
Pile-up	0.5%					
$\boldsymbol{E}_{\mathbf{T}}^{\mathbf{miss}}$	2.0 %	1.9 %	1.4 %	1.5 %	1.1 %	1.0 %
$\boldsymbol{H}_{\mathbf{T}}$	1.1 %	0.6 %	0.4 %	0.4 %	0.3 %	0.1 %
MC statistics	1.6 %	1.5 %	1.4 %	1.4 %	1.3 %	1.3 %
Total	6.5 %	6.3 %	6.1 %	6.2 %	6.1 %	6.1 %
PDF uncertainty	4.0 %					

Table 7.2: Systematic uncertainties in the UED scenario in SR A [143].

CHAPTER 8

Interpretation of the Results

In this chapter, the predictions of the GGM, GMSB SPS8, and UED models are compared to the background estimation and the measurement. Conclusions on the validity of the models can be drawn in the considered parameter spaces by making use of statistical tools.

The chapter starts with a summary of the inputs (see Section 8.1), which are needed for the interpretation. In Section 8.2, the statistical method used for the interpretation is introduced while the limit on signal events is discussed in Section 8.3. The results of the statistical evaluation in each SR and the unification by best sensitivity of the SRs is performed in order to draw the most powerful conclusion. The Sections 8.4, 8.5, and 8.6 summarize the individual results for GGM, GMSB SPS8, and UED, respectively.

8.1 Input for the Interpretation

For the interpretation of the measurement in the context of the considered models, the following input quantities are needed for each of the individual SRs:

- The result of the background estimation, i.e. the number of background events,
- the number of observed events,
- the signal selection efficiency ϵ,
- the uncertainties on the signal efficiency and the background estimation, and
- the production cross section $\sigma \times BR$ of the models and the total luminosity L.

The number of background events in the various signal regions is composed of contributions from the background with instrumental and genuine $E_{\mathrm{T}}^{\mathrm{miss}}$ and the irreducible background events. The total number of background events is the sum of the three background sources. The quoted total statistic and systematic uncertainties are added quadratically from their subcomponents in the respective category.

In SR A, the total background is $0.12 \pm 0.05 \pm 0.10$ events. The $E_{\mathrm{T}}^{\mathrm{miss}}$ distribution of the background components can be found in Fig. 8.1. The instrumental background is shown in

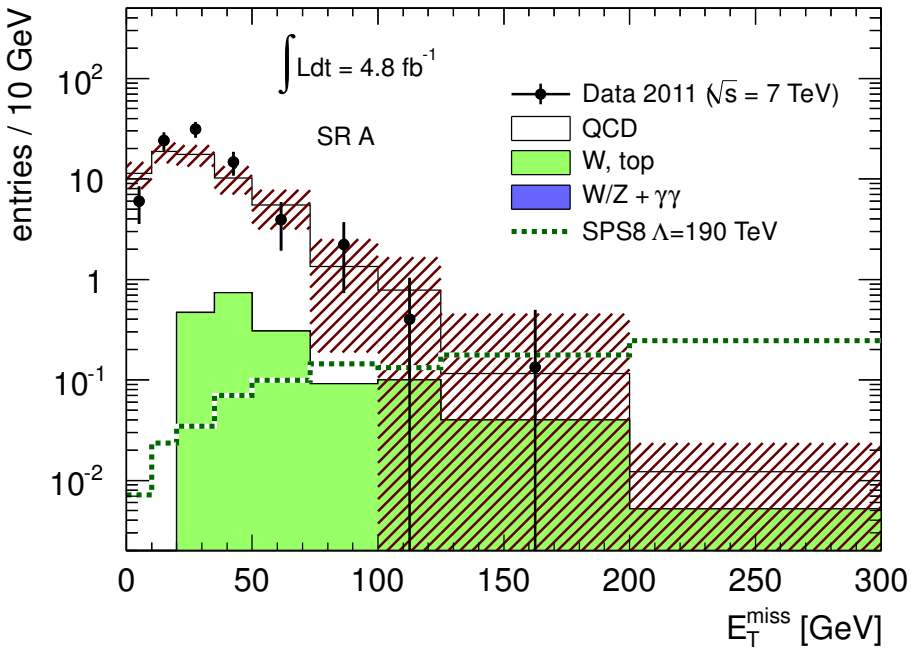

Figure 8.1: Diphoton data and total background in SR A (without $E_{\mathrm{T}}^{\mathrm{miss}}$ requirement).

white, the genuine $E_{\mathrm{T}}^{\mathrm{miss}}$ background in green and the irreducible background is shown in blue. The total uncertainty is shown by the dashed band. For illustration, the distribution of the GMSB SPS8 signal point with $\Lambda = 190\,\mathrm{TeV}$ is overlaid.

In SR B, the total background is $0.42 \pm 0.09 \pm 0.31$ events and the distributions are illustrated in Fig. 8.2. The distributions suffer from low statistics. In SR A and SR B, the $E_{\mathrm{T}}^{\mathrm{miss}}$ distribution of the nominal QCD template is used for the instrumental background modeling. In the last bin, i.e. in the SR, the combined estimate from the extrapolation (see Section 6.1.4) is taken. The background control samples are able to describe the $E_{\mathrm{T}}^{\mathrm{miss}}$ distribution of the diphoton data within the uncertainties.

The background in SR C is determined to be $3.36 \pm 0.40 \pm 0.42$ events, with contributions from all three background sources. The full $E_{\mathrm{T}}^{\mathrm{miss}}$ spectrum is well modeled by the background components (see Fig. 8.3). The results of the measurements and the background estimations are summarized in Table 8.1.

No excess of events above the SM background is observed. Hence, exclusion limits can be set on models predicting a significant amount of additional signal events. Since not all events corresponding to the production cross section are selected, the selection efficiency has to be taken into account. The production cross section of the models, the selection efficiency, and its uncertainty for the individual SR are discussed in Section 4.4, Section 5.4.2, and Chapter 7, respectively. The number of signal events in the signal region N_{s} can be expressed as $N_{\mathrm{s}} = \sigma \times BR \cdot L \cdot \epsilon$. Furthermore, the exclusion power depends on the signal and background uncertainties. In the next section, the statistical method used for the interpretation is described.

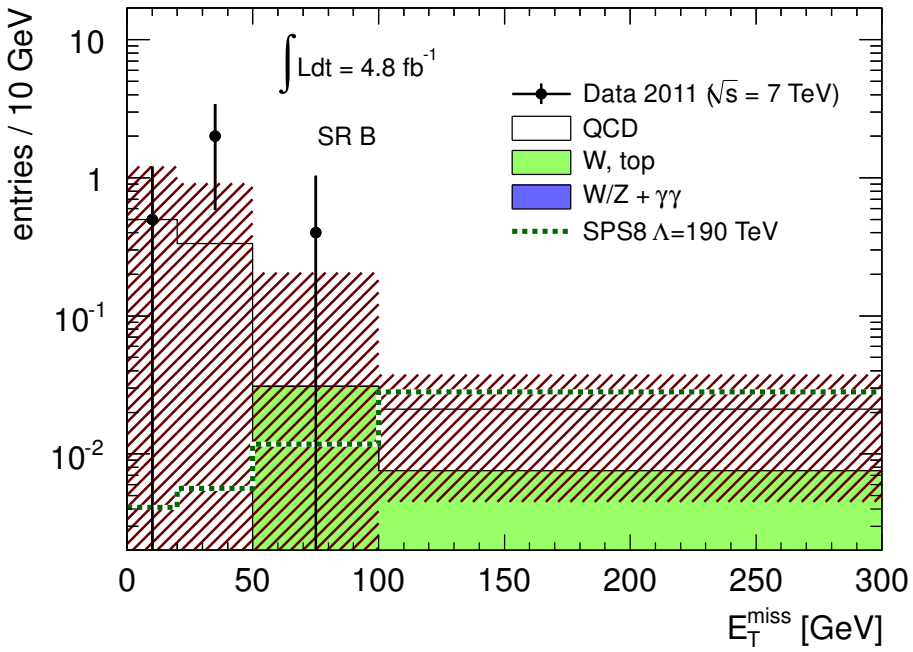

Figure 8.2: Diphoton data and total background in SR B (without $E_{\mathrm{T}}^{\mathrm{miss}}$ requirement).

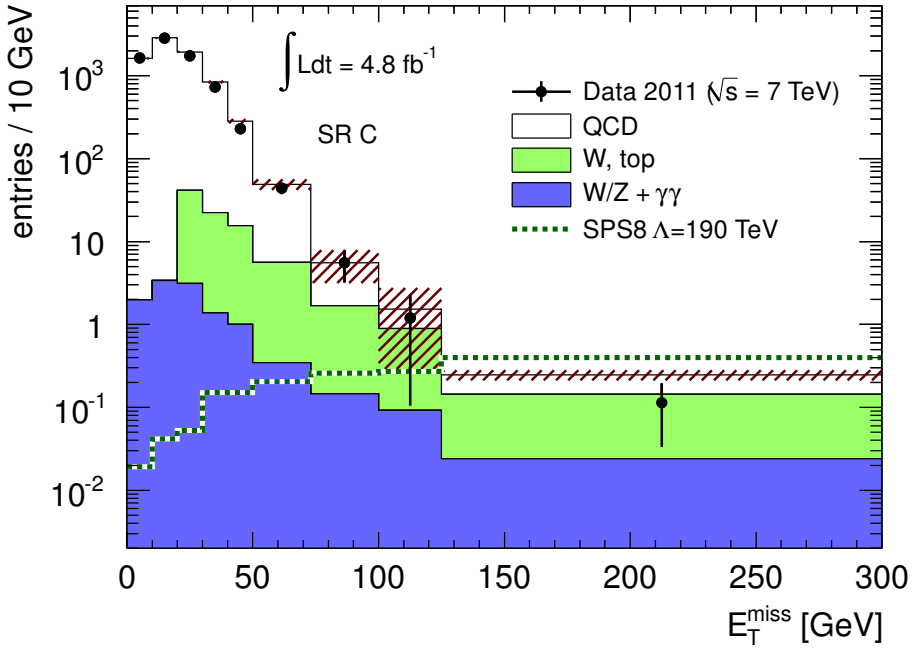

Figure 8.3: Diphoton data and total background in SR C (without $E_{\mathrm{T}}^{\mathrm{miss}}$ requirement).

SR	A	B	C
Events with instrumental $E_{\mathrm{T}}^{\mathrm{miss}}$	$0.07 \pm 0.00 \pm 0.07$	$0.27 \pm 0.00 \pm 0.27$	$0.85 \pm 0.30 \pm 0.16$
Events with genuine $E_{\mathrm{T}}^{\mathrm{miss}}$	$0.05 \pm 0.05 \pm 0.07$	$0.15 \pm 0.09 \pm 0.17$	$2.08 \pm 0.37 \pm 0.13$
Irreducible background events	< 0.01	< 0.01	$0.42 \pm 0.15 \pm 0.26$
Total background events	$0.12 \pm 0.05 \pm 0.10$	$0.42 \pm 0.09 \pm 0.31$	$3.36 \pm 0.40 \pm 0.42$
Observed events	0	0	2

Table 8.1: Total number of background events in the various SRs. The first uncertainty is statistical, the second is systematic. The contributions from different background sources are quoted in rows 2 – 4. The number of observed events is shown in the last row.

8.2 Limit Setting Technique

The results of the comparison of the number of signal, background and observed events[1] are interpreted by making use of a frequentist method referred to as CL_s technique [1, 185, 186] and has been used in many publications, e.g. [80, 187]. Since no excess of events over the SM background is observed in our case, only the exclusion of certain parameter ranges of models is considered[2].

The idea of the frequentist approach is to extract a probability of an outcome of an experiment from the infinite repetition of the experiment. As in reality, it is not possible to infinitely repeat an experiment, but a sufficiently large number of outcomes can be computed, where a single outcome is a so-called *toy (experiment)* or *pseudo experiment* (see Section 8.2.2).

For a given background, an exclusion of a certain fixed signal assumption can be finally extracted from the comparison between the measured outcome and the outcome of many pseudo experiments performed with the signal and background parameter. For instance, a certain signal hypothesis is tested, whether it is consistent with the measured data. The result of such a test is described by the *p-value* (*significance*), that represents the probability to reject a hypothesis, although it is correct. Thus, the p-value needs to be small for the exclusion of a certain model. A common choice is, that the p-value has to be smaller than $\alpha = 0.05$ to quote a statistically significant exclusion of a hypothesis. The corresponding *confidence level* CL is defined as

$$CL = 1 - p. \tag{8.1}$$

Hence, if the CL is greater than 95 %, the hypothesis is considered excluded.

8.2.1 The $\mathrm{CL_s}$ Method

The CL_{s} method is designed to have a protection against fluctuations of the background in analysis, which are not sensitive for the signal. It is defined as

$$CL_{\mathrm{s}} = \frac{CL_{\mathrm{s+b}}}{CL_{\mathrm{b}}}, \tag{8.2}$$

[1] A comparison of only single number of events are often referred to as *one bin counting experiment*

[2] The statistical treatment of discoveries is slightly different.

where the nominator is the p-value of the signal s plus background b hypothesis test $CL_{\mathrm{s+b}}$ and the denominator is the result of the background-only (CL_{b}) test[1]. Therefore, the CL_{s} method gives a more conservative result than the pure $CL_{\mathrm{s+b}}$ method because the result of the $s+b$ hypothesis test is normalized to the result of the agreement test between the observed events and the background. For instance, if the number of observed events is above the background, CL_{b} would be small since the rejection of the background-only hypothesis is likely not wrong in terms of the corresponding α. Hence, CL_{s} gets a greater value and the exclusion power decreases.

8.2.2 Pseudo Experiments and Test Statistic

In order to test a hypothesis one needs a *test statistic*, that numerically quantifies the test outcome of the real experiment and the test outcome of the pseudo experiments. For a pseudo experiment, in the case of the one bin counting experiment, the necessary input quantities are the number of observed events in a SR, the number of background events, and the number of expected signal events. In addition, systematic uncertainties need to be assigned to the signal and the background.

A pseudo experiment is performed by generating random numbers for the number of observed events according to the Poisson distribution defined by the expectation value of signal plus background events. The values of the systematic uncertainties are randomly generated according to their (Gaussian) distributions. The new value of the systematic uncertainty is used as a central value in the further calculations. This way, a *profiled* measurement with a different pseudo-observation is generated [186, 188]. In order to define the test statistic a likelihood function L is constructed as the product of a Poisson distribution P and two Gaussian distributions G:

$$L(n, \lambda(\mu, s, b, \theta_{\mathrm{s}}, \theta_{\mathrm{b}}), \theta_{\mathrm{s}}^{0}, \sigma_{\mathrm{s}}, \theta_{b}^{0}, \sigma_{\mathrm{b}},) = P(n, \lambda(\mu, s, b, \theta_{\mathrm{s}}, \theta_{\mathrm{b}})) \cdot G_{\mathrm{s}}(\theta_{\mathrm{s}}, \theta_{\mathrm{s}}^{0}, \sigma_{\mathrm{s}}) \cdot G_{\mathrm{b}}(\theta_{\mathrm{b}}, \theta_{\mathrm{b}}^{0}, \sigma_{\mathrm{b}}), \quad (8.3)$$

where the parameters and functions are defined as follows:

- n: The number of observed events in data.
- s: The number of expected signal events.
- b: The number of background events.
- μ: The so-called *signal strength* which scales the number of signal events s. It is the *parameter of interest* and can either be fixed or be a varying parameter in the range between 0 and 1.
- $\theta_{\mathrm{s,b}}$: The nuisance parameters for signal and background, denoted by the indices s and b, establish a connection between the systematic uncertainties and the number of signal and background events.

[1] For simplification, the CL_{s} value is referred to as a p-value in the following, although it is strictly speaking a ratio of p-values with some inoffensive mathematical differences to a p-value. $CL_{\mathrm{s+b}}$ and CL_{b} are p-values (not confidence levels).

- $P(n, \lambda)$: The Poisson distribution describing the probability to measure n events for a given expected value $\lambda = \mu \cdot s(1 + \theta_{\mathrm{s}}) + b(1 + \theta_{\mathrm{b}})$.

- $G_{\mathrm{s,b}}(\theta_{\mathrm{s,b}}, \theta^0_{\mathrm{s,b}}, \sigma_{\mathrm{s,b}})$: The Gaussian distributions are used to constrain the nuisance parameters which are needed in the subsequent fit. Their nominal central value is zero and the width is the value of the systematic uncertainty. The central value can be shifted by the profiling.

The test statistic $\Lambda(\mu)$ of the *logarithmic likelihood ratio* (LLR) test [1, 186, 188, 189] reads as follows

$$\Lambda(\mu) = -2\left(\ln L(n, \mu, s, \hat{\hat{b}}, \hat{\hat{\theta}}_{\mathrm{s}}, \hat{\hat{\theta}}_{\mathrm{b}})) - \ln L(n, \hat{\mu}, s, \hat{b}, \hat{\theta}_{\mathrm{s}}, \hat{\theta}_{\mathrm{b}})\right). \tag{8.4}$$

The parameters, that maximize the likelihood functions separately for the nominator and the denominator, are marked with a "$\hat{}$" or "$\hat{\hat{}}$", respectively. The number of observed events n and the signal events s are fixed parameters during the fit, while the number of background events is a free parameter. In the first term of Eq. 8.4, the signal strength is fixed to $\mu = 1$ ($\mu = 0$) during the $CL_{\mathrm{s+b}}$ (CL_{b}) test. Hence, in the first case the nominal signal is considered in the maximization. In the second term, μ is floating and therefore the signal $\mu \cdot s$ is optimized in the fit. The nuisance parameters are floating as well but they are constrained by their Gaussian functions. Since the number of events are con trained to be greater than or equal to zero, a one-sided p-value q is computed. This evaluation is performed for each pseudo experiment. The distribution of the q values of all pseudo experiments is denoted $f(q)$. A p-value of a particular outcome q', for instance the observed result, can be estimated from the distribution of the toys' q-values by

$$p(q') = \int_0^{q'} f(q)dq. \tag{8.5}$$

To obtain the result of CL_{s}, this procedure has to be carried out twice, first with the full signal strength ($CL_{\mathrm{s+b}}$) and second with the signal ($\mu = 0$) turned off (CL_{b}).

8.2.3 Observed and Expected Limits

The *observed limit* is found by integrating over the q-value distribution of the pseudo experiments: $p(q_{\mathrm{obs}}) = \int_0^{q_{\mathrm{obs}}} f(q)dq$, where q_{obs} is the single evaluation of the test statistic for the observed results.

The *(median) expected limit* represents the exclusion power without taking into account the observation, i.e. only the background estimation is considered. It is constructed in two steps. First, the 50 % quantile (median) of $f_{\mathrm{b}}(q)$ under the background-only assumption is calculated. This value is used then as a limit in the integration of $f_{\mathrm{s+b}}(q)$ with signal and background assumption. Due to the median, the observed limit has the same likelihood to be greater or smaller than the expected limit. The expected $\pm 1\sigma$ and $\pm 2\sigma$ limits are computed by using the (31.7 %, 68.3 %) and (4.5 %, 95.5 %) quantiles, respectively. The $\pm\sigma$ limits express the uncertainties and can be used to probe possible fluctuations by comparing them to the observed limit. The uncertainties are included in the observed and expected limits as well.

8.2.4 Limits on Model Parameters

The result of the above described limit setting procedure at a parameter point with a certain signal expectation is a single p-value. The p-values of all (discrete) parameter points are interpolated and a contour is formed where the interpolated p-values are at $p = 0.05$.

The *limit on the number of signal events* N_{s} can not be estimated directly from a single p-value, since the number of signal events s is a fixed input to the limit setting. So, an iteration on s is performed and the resulting p-values are interpolated and the number of signal events that corresponds to a p-value of $p = 0.05$ is extracted as result. The background and the relative uncertainties are the same in all iteration steps.

The *limit on the production cross section* $\sigma \times BR$ is calculated by

$$\sigma \times BR = L \cdot \frac{N_{\mathrm{s}}}{\epsilon}, \tag{8.6}$$

where L is the total integrated luminosity, ϵ the selection efficiency, and N_{s} the 95 % CL on the number of signal events in the SR. The expected limit on the production cross section determines the sensitivity of an analysis in a certain model or scenario. The production cross section itself is not an input parameter, but in order to retrieve limits on the model parameters a comparison between the theoretical production cross section and the 95 % CL on the cross section is performed.

The results obtained in the different SR can be unified such that the expected p-value with the highest exclusion power is chosen. The resulting limit is referred to as *unified limit*. The expected p-value is used for the unification to not be biased by signal uncertainties, so the unification is performed on results from the SM measurement only.

8.3 Limit on the Number of Signal Events

As a first step towards the interpretation of the measured results in the context of certain models, the 95 % CL exclusion limit on the number of signal events (see Section 8.2.4) is calculated[1]. The computation is based on the performed measurements in order to investigate the exclusion power of the different SRs and to study the impact of systematic uncertainties.

Table 8.2 (columns 3 and 4) lists the 95 % CL limit on the number of signal events in the different SRs. Several values of the systematic uncertainties including the expected signal uncertainties of the various models, are studied. Models predicting more events than the limit on the number of observed events $N_{\mathrm{s}}^{\mathrm{obs}}$ are excluded at 95 % CL. The limits on the number of signal events become weaker with increasing uncertainties. The lowest limits on signal events are found in SR A and SR B, because of the small background and no observed events. Since two events are observed in SR C and the background is $3.36 \pm 0.40 \pm 0.42$ events, the limit on the signal events is larger than in SR A and SR B. Note, that these limits on the number of signal events are computed for the SRs, thus selection efficiencies are considered to be $\epsilon = 1$.

[1] The statistical computations are performed with the help of the `Combination package` [190].

N_s^{obs} (N_s^{exp})	signal uncertainty		
	none	10 %	40 %
SR A	3.1 (3.1)	3.1 (3.1)	3.3 (3.3)
SR B	3.1 (3.1)	3.1 (3.1)	3.5 (3.8)
SR C	4.2 (5.4)	4.3 (5.4)	5.9 (8.2)

Table 8.2: The observed (expected) 95 % CL exclusion limit on the number of signal events N_s^{obs} (N_s^{exp}) in the different SR and for different values of the signal uncertainty. The model-independent exclusion limits can be found in the column with no signal uncertainty applied.

Although the limit on the number of signal events is weakest in SR C, a high selection efficiency could lead to high exclusion power.

The *model-independent limit* on the number of signal events, i.e. a limit on the number of signal events without taking signal uncertainties and selection efficiencies into account (see second column of Table 8.2), represents the exclusion power only due to the SM background measurement. In this case, the most powerful exclusions are expected in SR A and SR B which have an observed (expected) 95 % CL limit on signal events of 3.1 (3.1). The small differences in the background results between SR A and SR B do not lead to a significant difference in the exclusion limit. In SR C the observed (expected) 95 % CL limit on the number of signal events is 4.2 (5.4). The model-independent exclusion power expected only from the SM measurements in SR C is hence lower than in SR A and SR B.

8.4 Results of the GGM Interpretation

The results of the measurement are interpreted in the context of the GGM model (see Section 2.2.4) for two scenarios: One, where the $\tilde{g}$ mass is a varying parameter and second, where the $\tilde{q}$ mass is a varying parameter. For each generated parameter point and each SR, the CL_s observed and expected (with its $\pm 1\sigma$ deviations) p-values are computed taking into account all systematic uncertainties including theoretical uncertainties at that parameter point. The model parameters are fixed to $M_2 = 2.5\,\text{TeV}$, $\mu = 2.5\,\text{TeV}$, $\tan\beta = 2$, and $c\tau_{\text{NLSP}} < 0.1\,\text{mm}$, while the other masses are set to a value of 2.5 TeV (see Section 4.4.2). Some selected expected and observed contours of CL_s values are illustrated in Fig. 8.4 and Fig. 8.5 for SR A–C (a)–(c) for the $m_{\tilde{g}}$-$m_{\tilde{\chi}_1^0}$-plane and the $m_{\tilde{q}}$-$m_{\tilde{\chi}_1^0}$-plane, respectively. The analysis is not sensitive in the gray area, where the $\tilde{g}$ is the NLSP. The distributions of the p-values reflect on the one hand the distribution of the selection efficiency (see Section 5.4.2), which is mainly responsible for the distribution towards the higher $\tilde{\chi}_1^0$ and higher $\tilde{g}$ masses. On the other hand, the decreasing cross section with increasing $\tilde{g}$ ($\tilde{q}$) mass increases the overall scale of the p-values simultaneously. In addition, the distribution of the total uncertainty (see Section 7.9) affects the sensitivity. The p-values of the GGM scenario with varying $\tilde{g}$ mass are in general lower than those of the GGM scenario with varying $\tilde{q}$ mass due to the higher cross section in the first scenario. The observed and the expected contours are similar for both scenarios is SR A and SR B, because

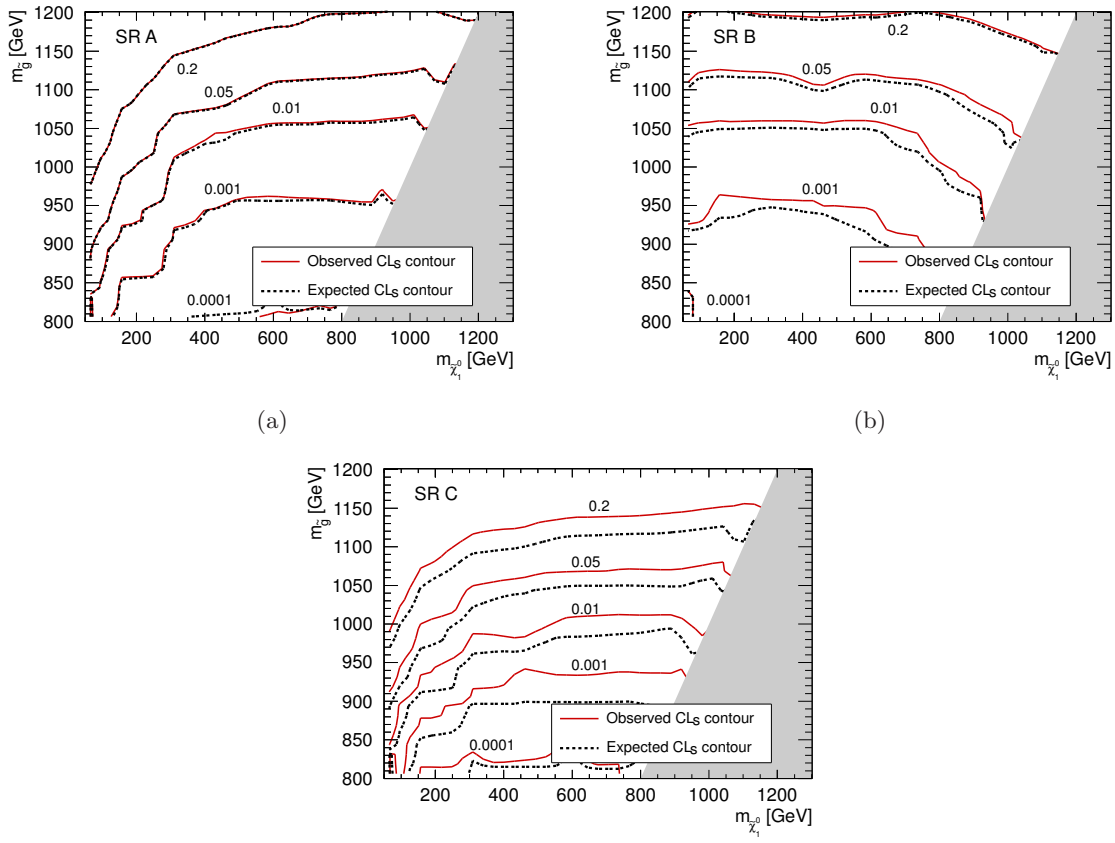

Figure 8.4: Selected expected and observed CL_s values in SR A–C (a)–(c) in the $m_{\tilde{g}}$-$m_{\tilde{\chi}_1^0}$ plane of the GGM model. The model parameters are fixed to $M_2 = 2.5\,\text{TeV}$, $\mu = 2.5\,\text{TeV}$, $\tan\beta = 2$, and $c\tau_{\text{NLSP}} < 0.1\,\text{mm}$, while the other masses are set to a value of 2.5 TeV.

the difference between the number of background events and the number of observed events is small. In SR C, the larger difference between the observed and the expected contour compared to SR A and SR B reflects the larger difference between the number of background events and the number of observed events with respect to SR A and SR B.

Parameter points with a p-value below 0.05 are excluded at 95 % CL. The 95 % CL limit contour represents the intersection line, where the p-value distribution crosses the surface of $p = 0.05$. Hence, parameter points below the observed contour are excluded. Figure 8.6 shows the observed (red line) and expected (black dashed line) limit contours with the overlaid $\pm 1\sigma$ band (filled green area) for SR A–C (a)–(c). Since the number of observed events and the number of background events agree well the observed and the expected contour match for SR A and SR B. Since the background is minimal in SR A and SR B and values below zero are not considered, possible fluctuations of the observed limit are mainly towards higher background values, i.e towards lower limits. This feature is indicated by the asymmetric green band. In SR A, the green band is smaller due to the smaller background uncertainties with respect to SR B. In SR C, the observed limit is slightly higher than the expected limit, because less events

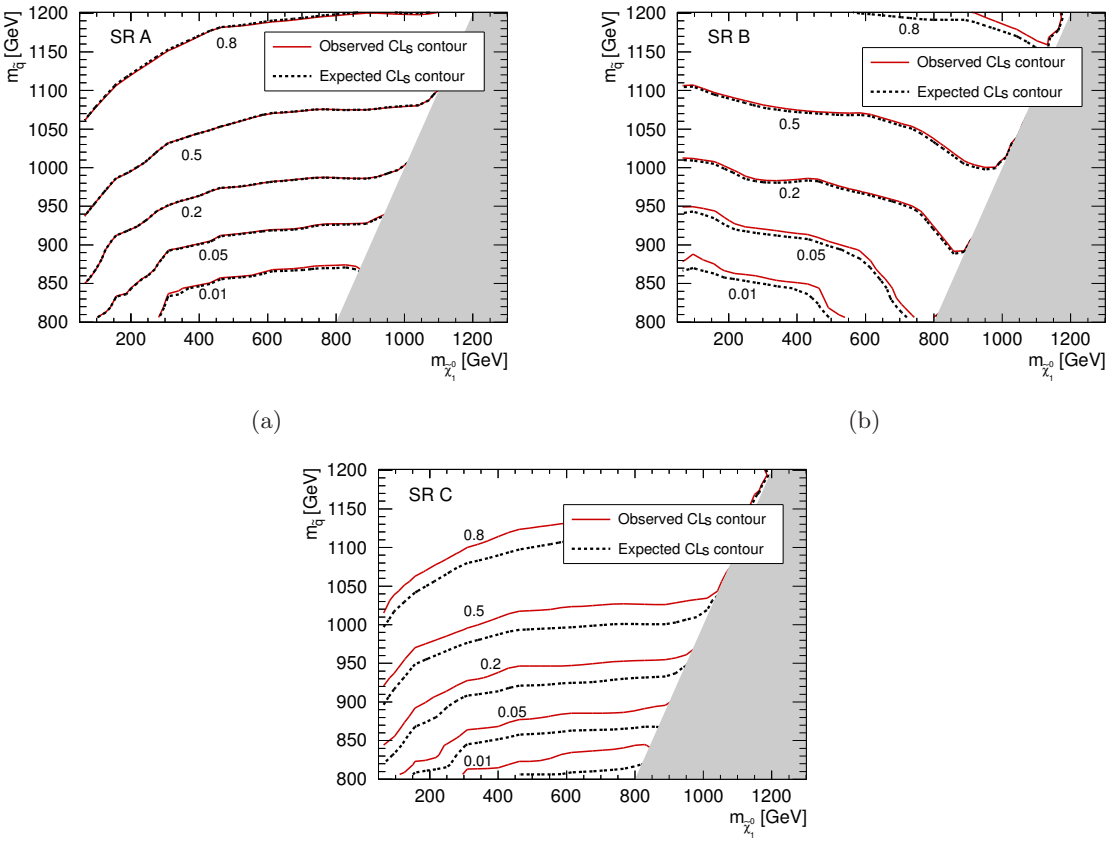

Figure 8.5: Selected expected and observed CL_s values in SR A–C (a)–(c) in the $m_{\tilde{q}}$-$m_{\tilde{\chi}_1^0}$ plane of the GGM model. The model parameters are fixed to $M_2 = 2.5\,\text{TeV}$, $\mu = 2.5\,\text{TeV}$, $\tan\beta = 2$, and $c\tau_{\text{NLSP}} < 0.1\,\text{mm}$, while the other masses are set to a value of 2.5 TeV.

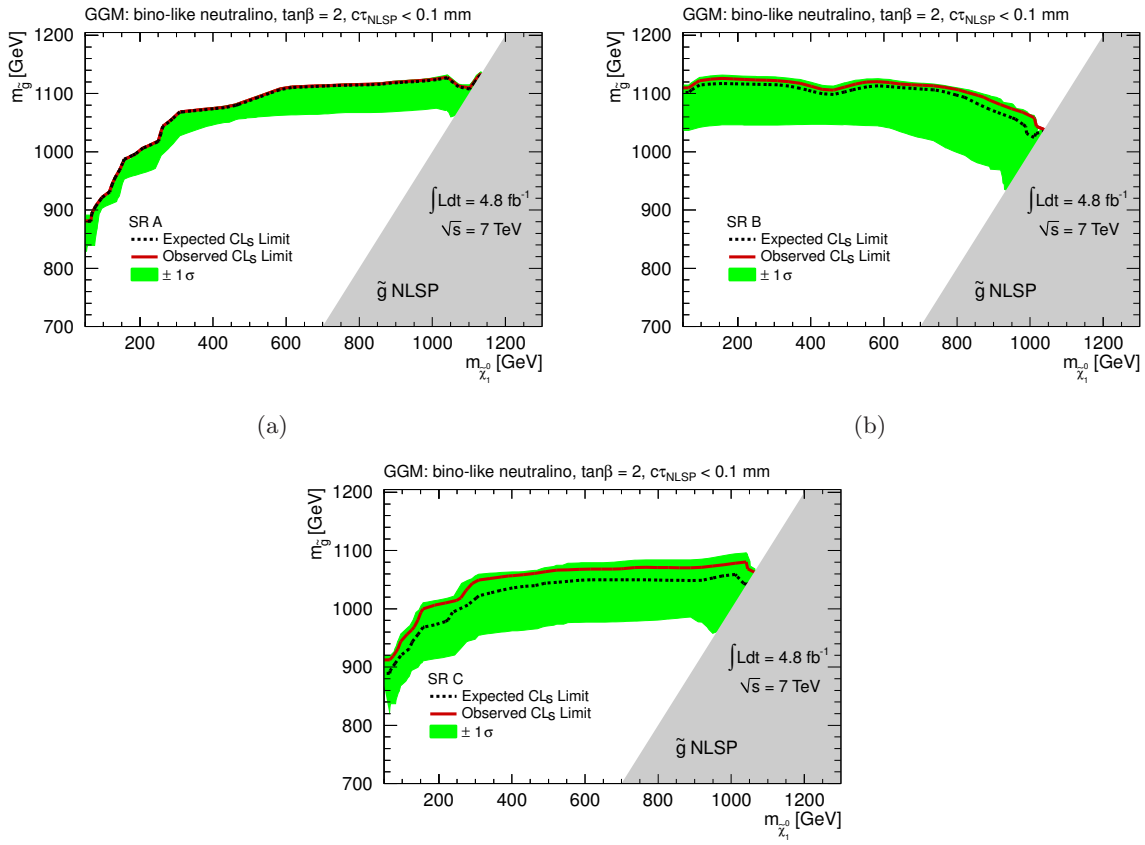

Figure 8.6: 95 % CL mass limit contours obtained using the CL_s method in SR A–C (a)–(c) in the $m_{\tilde{g}}$-$m_{\tilde{\chi}_1^0}$ plane of the GGM model. The model parameters are fixed to $M_2 = 2.5\,\text{TeV}$, $\mu = 2.5\,\text{TeV}$, $\tan\beta = 2$, and $c\tau_{\text{NLSP}} < 0.1\,\text{mm}$, while the other masses are set to a value of 2.5 TeV.

are observed than expected from the background estimation. The 95 % CL exclusion limit on the $\tilde{g}$ mass is the lowest value of the observed contour over the considered $\tilde{\chi}_1^0$ mass range ($m_{\tilde{\chi}_1^0} > 50\,\text{GeV}$ and $m_{\tilde{\chi}_1^0} < m_{\tilde{g}}$). In SR A–C, the obtained limits on the $\tilde{g}$ mass are 881 GeV, 1034 GeV, and 912 GeV, respectively.

The limit contours in SR A–C for the varying $\tilde{q}$ mass GGM scenario are presented in Fig. 8.7(a)–(c), respectively. The corresponding shapes of the mass contours in the varying $m_{\tilde{q}}$ and varying $m_{\tilde{g}}$ mass planes are similar due to the similar decay cascades and similar resulting selection efficiencies. Despite the slightly higher selection efficiencies in the varying $\tilde{q}$ mass scenario with respect to the varying $\tilde{g}$ mass scenario, the corresponding mass limit is lower because of the significantly lower production cross section ($\sim$ one order of magnitude) in the $m_{\tilde{q}}$ case.

The 95 % CL limits on the production cross section of the varying $m_{\tilde{g}}$ (varying $m_{\tilde{q}}$) scenario are illustrated in Fig. 8.8 (Fig. 8.9). The diagrams (a), (b) and (c) correspond to the results in SR A, SR B, and SR C, respectively in both scenarios. The limit on the production cross section is a function of the selection efficiency (see Eq. 8.6). The resulting limits on the production

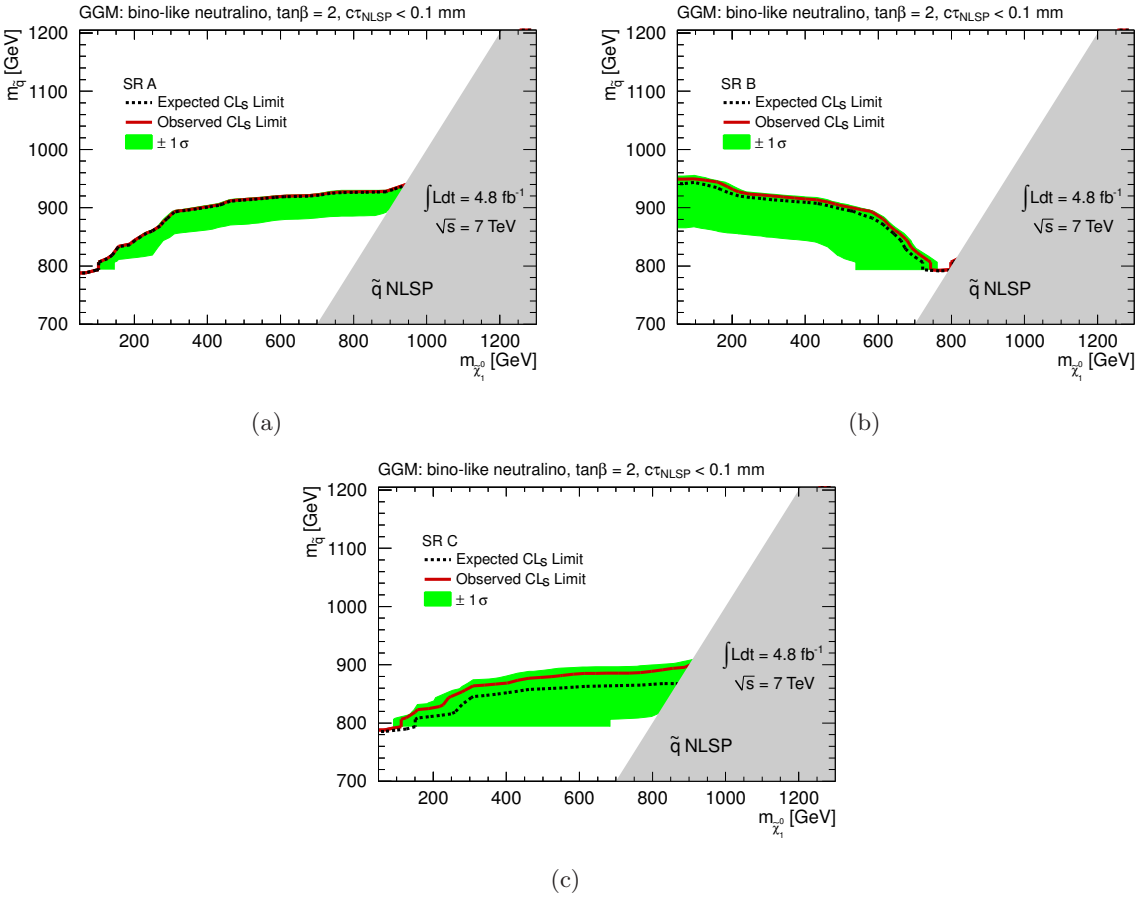

Figure 8.7: 95 % CL mass limit contours obtained using the CL_s method in SR A–C (a)–(c) in the $m_{\tilde{q}}$-$m_{\tilde{\chi}_1^0}$ plane of the GGM model. The model parameters are fixed to $M_2 = 2.5\,\text{TeV}$, $\mu = 2.5\,\text{TeV}$, $\tan\beta = 2$ and $c\tau_{\text{NLSP}} < 0.1\,\text{mm}$, while the other masses are set at a value of 2.5 TeV.

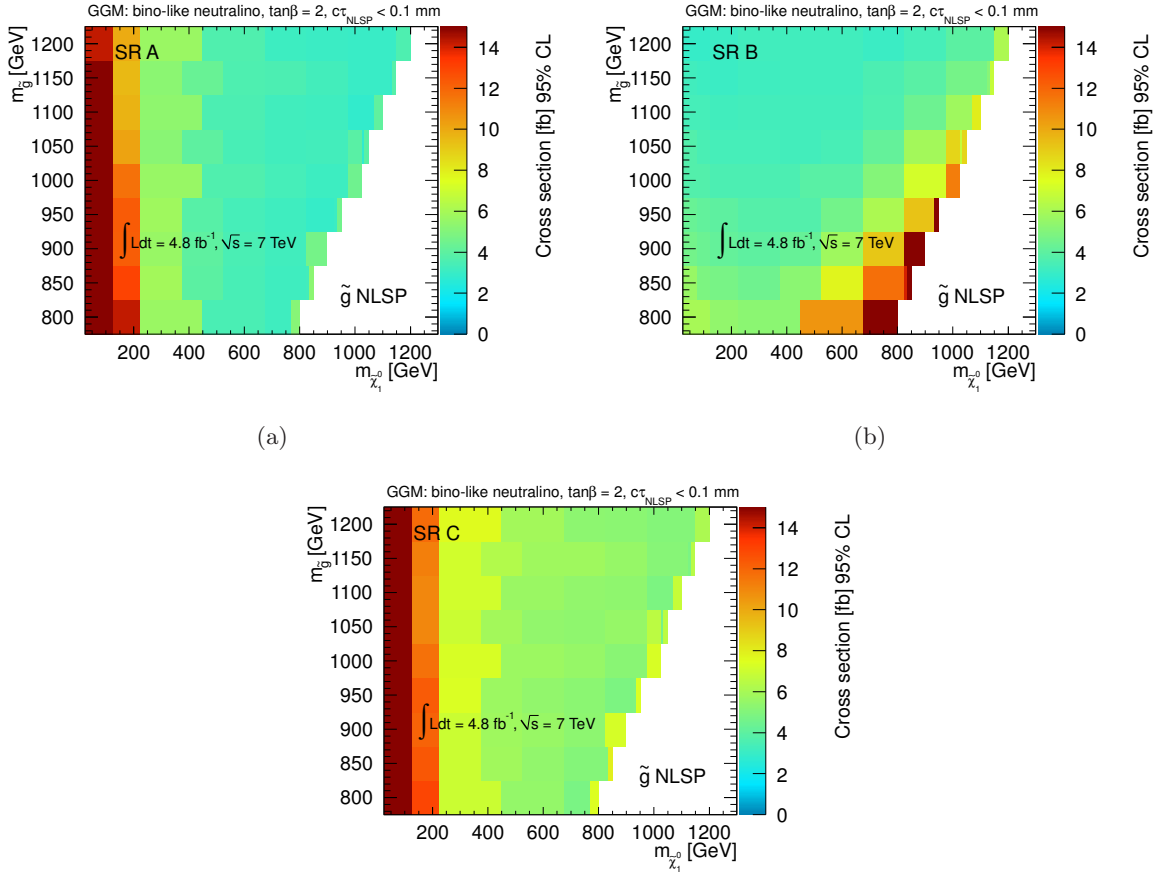

Figure 8.8: 95 % CL production cross section limit obtained using the CL_s method in SR A–C (a)–(c) in the $m_{\tilde{g}}$-$m_{\tilde{\chi}_1^0}$ plane of the GGM model. The model parameters are fixed to $M_2 = 2.5\,\text{TeV}$, $\mu = 2.5\,\text{TeV}$, $\tan\beta = 2$, and $c\tau_{\text{NLSP}} < 0.1\,\text{mm}$, while the other masses are set to a value of 2.5 TeV.

cross section are given in Table 8.3 for the whole mass plane and for a gluino mass range with fixed neutralino mass of $m_{\tilde{\chi}_1^0} = 150\,\text{GeV}$. The latter case with fixed neutralino mass is not affected by selection efficiency variations as a function of the neutralino mass. The limit on the production cross section is hence directly comparable to the production cross section, which is a function of $m_{\tilde{g}}$ only. The high values of the cross section limit are due to low selection efficiencies in some regions of the mass planes. For instance, for the gluino or squark masses above 1100 GeV, the cross section limit is higher than the production cross section, therefore these points can not be excluded.

Unification by Best Sensitivity To exploit the exclusion power of each signal region for different parameter ranges the statistical results are unified such that the strongest exclusion is obtained. Hence, for each parameter point, the lowest expected p-value of the three SR is chosen.

In Fig. 8.10, the SR with the best sensitivity is indicated by its letter for the varying $m_{\tilde{g}}$

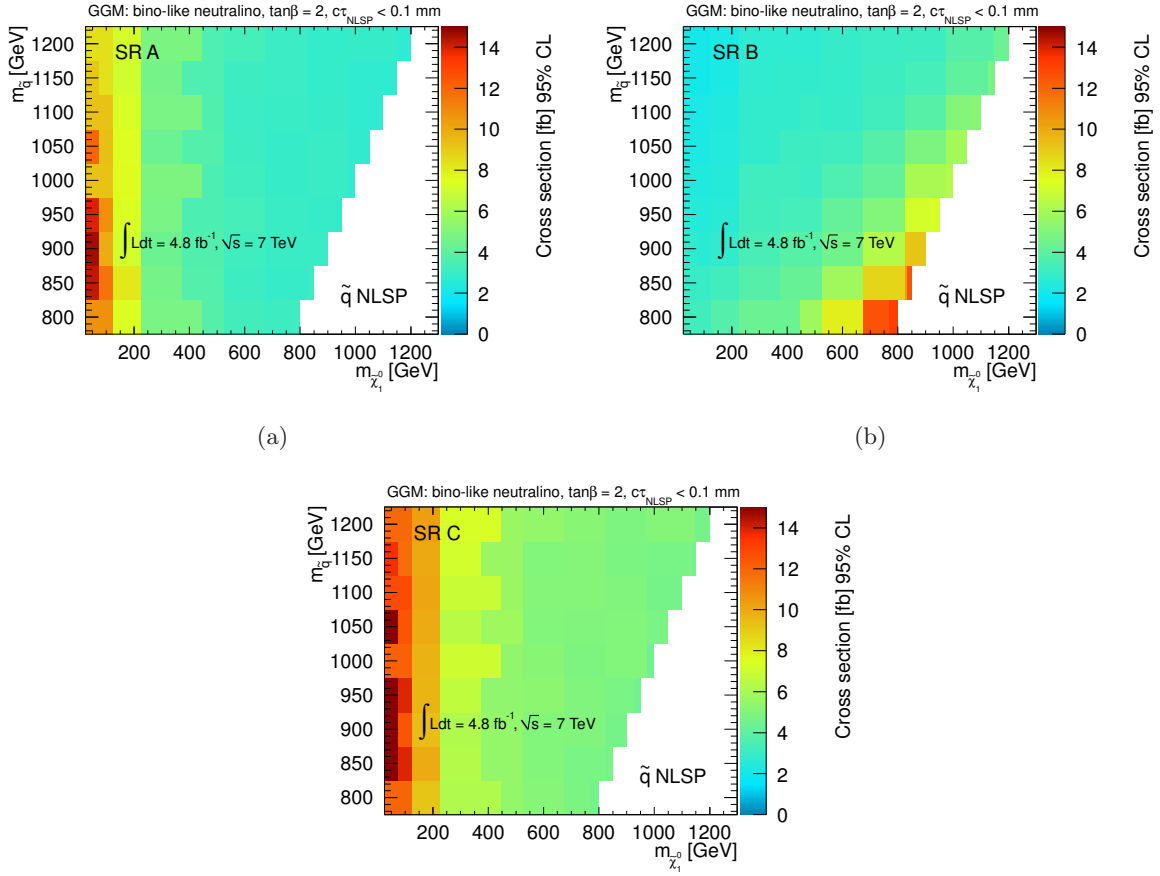

Figure 8.9: 95 % CL production cross section limit obtained using the CL_s method in SR A–C (a)–(c) in the $m_{\tilde{q}}$-$m_{\tilde{\chi}_1^0}$ plane of the GGM model. The model parameters are fixed to $M_2 = 2.5\,\text{TeV}$, $\mu = 2.5\,\text{TeV}$, $\tan\beta = 2$, and $c\tau_{\text{NLSP}} < 0.1\,\text{mm}$, while the other masses are set to a value of 2.5 TeV.

	$m_{\tilde{g}}$-$\tilde{\chi}_1^0$-plane		$m_{\tilde{q}}$-$\tilde{\chi}_1^0$-plane	
	-	$m_{\tilde{\chi}_1^0} = 150\,\text{GeV}$	-	$m_{\tilde{\chi}_1^0} = 150\,\text{GeV}$
SR A	$2.8 - 45.3\,\text{fb}$	$9.1 - 14.2\,\text{fb}$	$2.7 - 14.5\,\text{fb}$	$8.2 - 7.0\,\text{fb}$
SR B	$2.9 - 25.7\,\text{fb}$	$5.4 - 2.9\,\text{fb}$	$2.0 - 13.2\,\text{fb}$	$2.2 - 3.7\,\text{fb}$
SR C	$4.7 - 35.8\,\text{fb}$	$10.8 - 12.9\,\text{fb}$	$4.5 - 18.0\,\text{fb}$	$9.2 - 11.4\,\text{fb}$

Table 8.3: 95 % CL limit ranges on the production cross section over the mass planes of the GGM scenarios for different signal regions. The ranges of the mass parameters and the choice of model parameters can be found in Fig. 8.6 and Fig. 8.7

(a) and the varying $m_{\tilde{q}}$ scenario (b). SR C does not have a good sensitivity in those scenarios due to its design and its optimization for the GMSB SPS8 scenario. For both GGM scenarios, SR B covers the low $\tilde{\chi}_1^0$/high $\tilde{g}$ mass region and accordingly low $\tilde{\chi}_1^0$/high $\tilde{q}$ mass region, for which it was designed. In the region of higher $\tilde{\chi}_1^0$ mass values, the best expected limit is found

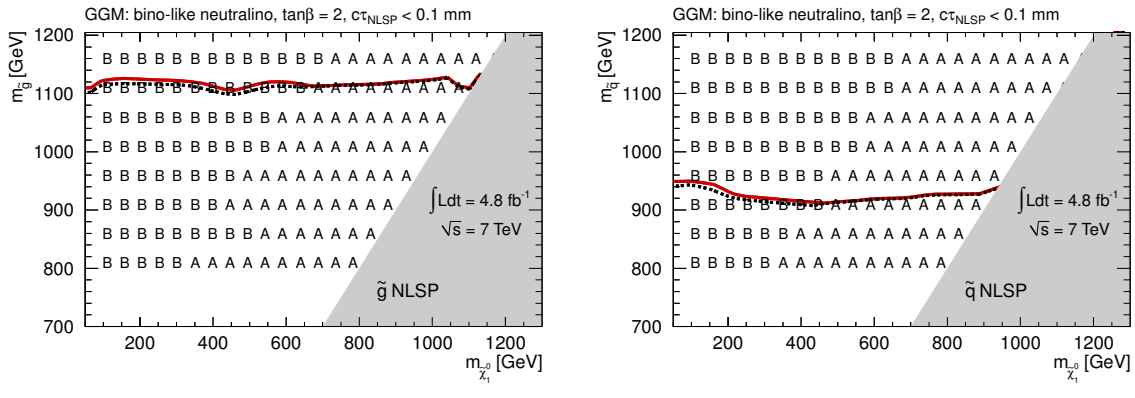

(a) (b)

Figure 8.10: Unification by the expected limit of the SRs for the varying $m_{\tilde{g}}$ (a) and varying $m_{\tilde{q}}$ scenario (b) of the GGM model. The SR, that has the strongest exclusion is indicated by its letter. The unified expected and observed limit contours is drawn on top. The model parameters are fixed to $M_2 = 2.5\,\text{TeV}$, $\mu = 2.5\,\text{TeV}$, $\tan\beta = 2$, and $c\tau_{\text{NLSP}} < 0.1\,\text{mm}$, while the other masses are set to a value of 2.5 TeV.

in SR A. The unified contours of the expected and the observed 95 % CL are drawn in addition showing a rather flat shape. The decreasing exclusion limit with increasing $\tilde{\chi}_1^0$ mass in SR B is recovered by SR A and vice verse. The transition along the limit contour between the two SRs occurs at $m_{\tilde{\chi}_1^0} \simeq 675\,\text{GeV}$ ($m_{\tilde{\chi}_1^0} \simeq 475\,\text{GeV}$) for the varying $m_{\tilde{g}}$ ($m_{\tilde{q}}$) scenario.

The unified mass limit contours with the $\pm 1\sigma$ band for the $m_{\tilde{g}}$-$m_{\tilde{\chi}_1^0}$-plane (a) and the $m_{\tilde{q}}$-$m_{\tilde{\chi}_1^0}$-plane (b) are shown in (Fig. 8.11). The width of the $\pm 1\sigma$ band varies with the underlying SR, which have different uncertainties. Gluino masses $m_{\tilde{g}} < 1.10\,\text{TeV}$ and squark masses $m_{\tilde{q}} < 0.91\,\text{TeV}$ are excluded at 95 % CL for $m_{\tilde{\chi}_1^0} > 50\,\text{GeV}$ and $m_{\tilde{\chi}_1^0} < m_{\tilde{g}}$ respectively $m_{\tilde{\chi}_1^0} < m_{\tilde{q}}$.

The unified production cross section limit is illustrated in Fig. 8.12 for the varying $m_{\tilde{g}}$ scenario (a) and the varying $\tilde{q}$ scenario (b). Production cross sections $\sigma > 2.8 - 6.0\,\text{fb}$ are excluded at 95 % CL in the varying $m_{\tilde{g}}$ scenario for $m_{\tilde{\chi}_1^0} > 50\,\text{GeV}$ and $m_{\tilde{\chi}_1^0} < m_{\tilde{g}}$. For the particular choice of $m_{\tilde{\chi}_1^0} = 150\,\text{GeV}$, the 95 % CL production cross section limit is $2.9 - 5.4\,\text{fb}$.

In the case of the varying $\tilde{q}$ mass scenario with $m_{\tilde{\chi}_1^0} > 50\,\text{GeV}$ and $m_{\tilde{\chi}_1^0} < m_{\tilde{q}}$, the production cross section is excluded at 95 % CL above $2.0 - 4.4\,\text{fb}$, while for $m_{\tilde{\chi}_1^0} = 150\,\text{GeV}$, production cross sections $\sigma > 2.2 - 3.7\,\text{fb}$ are excluded at 95 % CL.

The limit on the production cross section, which is independent of the production cross section, is a bit lower in the varying $\tilde{q}$ mass scenario than in the varying $m_{\tilde{g}}$ mass scenario because of the slightly higher selection efficiency in the first. Nevertheless, the analysis shows a similar exclusion power in both scenarios because the cross section limits are in the same order of magnitude.

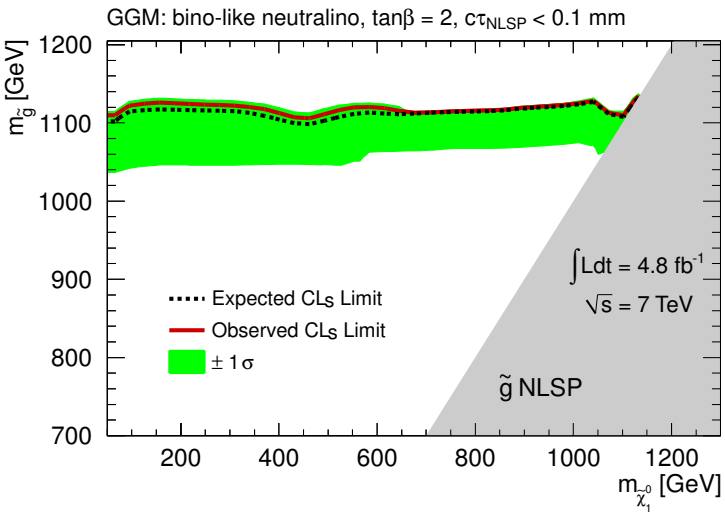

(a)

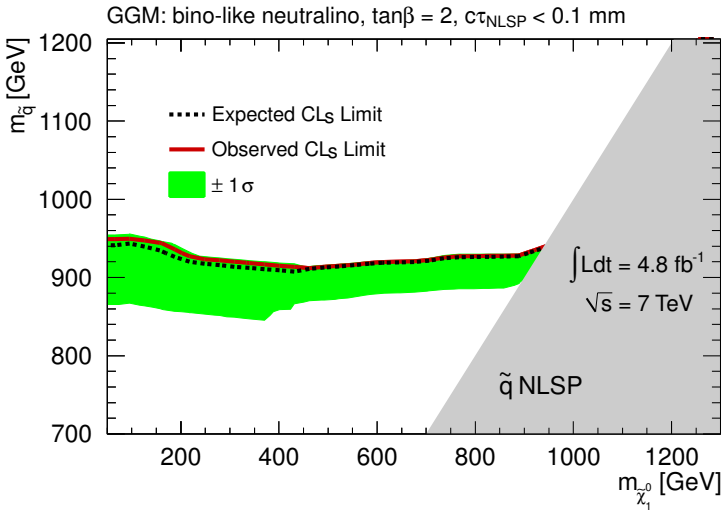

(b)

Figure 8.11: Unified observed and expected 95 % CL mass limit contours for the varying $m_{\tilde{g}}$ (a) and varying $m_{\tilde{q}}$ scenario (b) of the GGM model. The model parameters are fixed to $M_2 = 2.5\,\text{TeV}$, $\mu = 2.5\,\text{TeV}$, $\tan\beta = 2$, and $c\tau_{\text{NLSP}} < 0.1\,\text{mm}$, while the other masses are set to a value of 2.5 TeV.

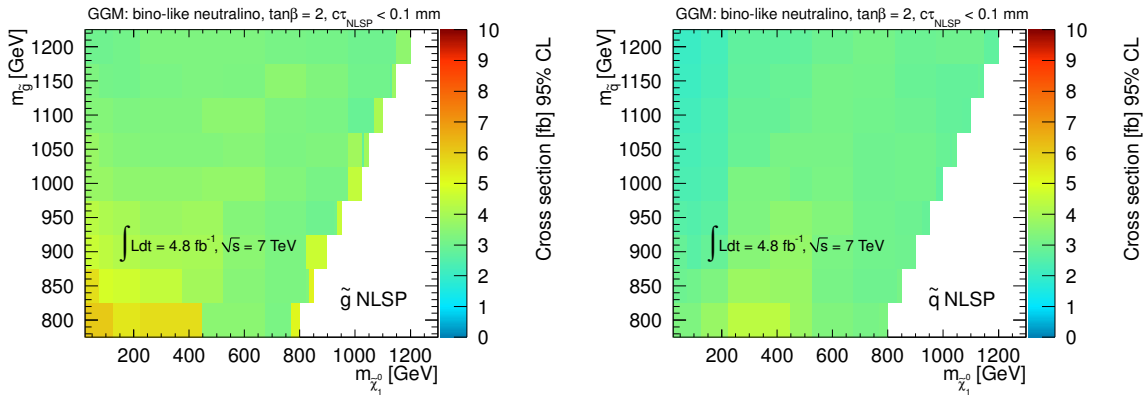

(a) (b)

Figure 8.12: Observed 95 % CL production cross section limit (unified) for the varying $m_{\tilde{g}}$ (a) and varying $m_{\tilde{q}}$ scenario (b) of the GGM model. The model parameters are fixed to $M_2 = 2.5\,\text{TeV}$, $\mu = 2.5\,\text{TeV}$, $\tan\beta = 2$, and $c\tau_{\text{NLSP}} < 0.1\,\text{mm}$, while the other masses are set to a value of 2.5 TeV.

8.5 Results of the GMSB SPS8 Interpretation

The measurements are also interpreted in the GMSB model, namely in the SPS8 scenario (see Section 2.2.3), and the results are presented in this section. The 95 % CL limit on the production cross section is computed for each generated parameter point and compared to the NLO production cross section. Figure 8.13 shows the 95 % CL observed (black solid line) and the expected (black dotted line) production cross section limit as a function of the parameter Λ in SR A (a) and SR B (b). Furthermore, the $\pm1\sigma$ (green) and $\pm2\sigma$ (yellow) bands are drawn. The NLO production cross section is shown as a blue solid line. Axes showing the $\tilde{\chi}_1^0$ and $\tilde{\chi}_1^\pm$ masses corresponding to the parameter Λ are added. This way, the result can be expressed in terms of limits on sparticles masses. The observed and the expected contours overlap, because the observed events and the background measurements agree well. In Fig. 8.13(a) the $\pm1\sigma$ band is not visible due to the small background uncertainties. The shapes of the limit contours are mainly dominated by the selection efficiencies. In SR A, the production cross section limit decreases with increasing Λ, because the efficiency grows in the considered interval of $\Lambda = 100 - 250\,\text{TeV}$. The slight bump in the shape of the limit contours in SR B around $\Lambda = 160\,\text{GeV}$ is related to the dip in the selection efficiency distribution at that position. The impact of the increasing uncertainty with increasing Λ is a less dominant effect. The limit on Λ is obtained at the intersection of the production cross section line and the 95 % CL limit contour. In SR A, $\Lambda < 170\,\text{TeV}$ is excluded at 95 % CL, while in SR B, $\Lambda < 143\,\text{TeV}$ is excluded at 95 % CL. Figure 8.14 presents the 95 % CL limits as a function of the Λ parameter in SR C. The parameter Λ is excluded at 95 % CL below 208 TeV. Thus, SR C has the highest exclusion power, which is expected, since this SR was optimized for the GMSB SPS8 scenario. The masses of the $\tilde{\chi}_1^0$ and the $\tilde{\chi}_1^\pm$ are excluded at 95 % CL below $m_{\tilde{\chi}_1^0} < 302\,\text{GeV}$ and $m_{\tilde{\chi}_1^\pm} < 582\,\text{GeV}$, respectively. The other model parameters are fixed to $M_{\text{mess}} = 2\Lambda$, $N = 1$, $\tan\beta = 15$,

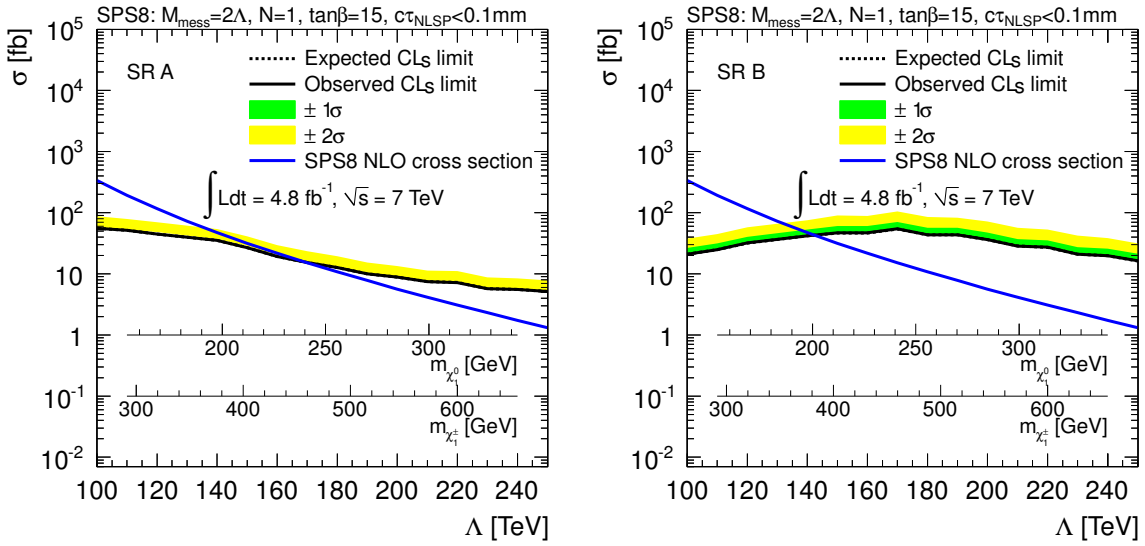

(a) (b)

Figure 8.13: The production cross section as well as the observed and expected 95 % CL limit on the production cross section as a function of Λ of the GMSB SPS8 scenario in SR A (a) and SR B (b). The other model parameters are fixed to $M_{\text{mess}} = 2\Lambda$, $N = 1$, $\tan\beta = 15$, and $c\tau_{\text{NLSP}} < 0.1\,\text{mm}$.

and $c\tau_{\text{NLSP}} < 0.1\,\text{mm}$. The 95 % CL limit on the production cross section is in the range of $4.2 - 15.6\,\text{fb}$ for $100\,\text{GeV} < \Lambda < 250\,\text{GeV}$.

8.6 Results of the UED Interpretation

The interpretation of the measured results in the context of the UED model (see Section 2.3) is performed in this section. The 95 % CL observed and expected limit on the production cross section including the $\gamma\gamma$ branching ratio $\sigma\times$ BR as a function of R^{-1} is shown in Fig. 8.15 for SR A (a), SR B (b), and SR C in (c). The LO production cross section times BR is overlaid. The inverse compactification radius is excluded in SR A, SR B, and SR C below $R^{-1} < 1410\,\text{GeV}$, $R^{-1} < 1356\,\text{GeV}$, and $R^{-1} < 1391\,\text{GeV}$, respectively. The corresponding 95 % CL limits on the masses of the KK quarks (KK gluons) are $m_{q^*} < 1625\,\text{GeV}$ ($m_{g^*} < 1720\,\text{GeV}$), $m_{q^*} < 1564\,\text{GeV}$ ($m_{g^*} < 1655\,\text{GeV}$), and $m_{q^*} < 1604\,\text{GeV}$ ($m_{g^*} < 1720\,\text{GeV}$) in the various SRs, respectively. The other model parameters are fixed at $N = 6$, $M_{\text{D}} = 5\,\text{TeV}$ and $\Lambda R = 20$ (see Section 4.4.4).

The strongest exclusion is found in SR A. Although the selection efficiency is slightly greater in SR C than in SR A, the low background and its good agreement with the number of observed events in SR A lead to the strongest exclusion power in that SR. The 95 % CL limit on the cross section times branching ratio is $1.7 - 2.3\,\text{fb}$, which has only small variations due to the flat shape of the efficiency distribution.

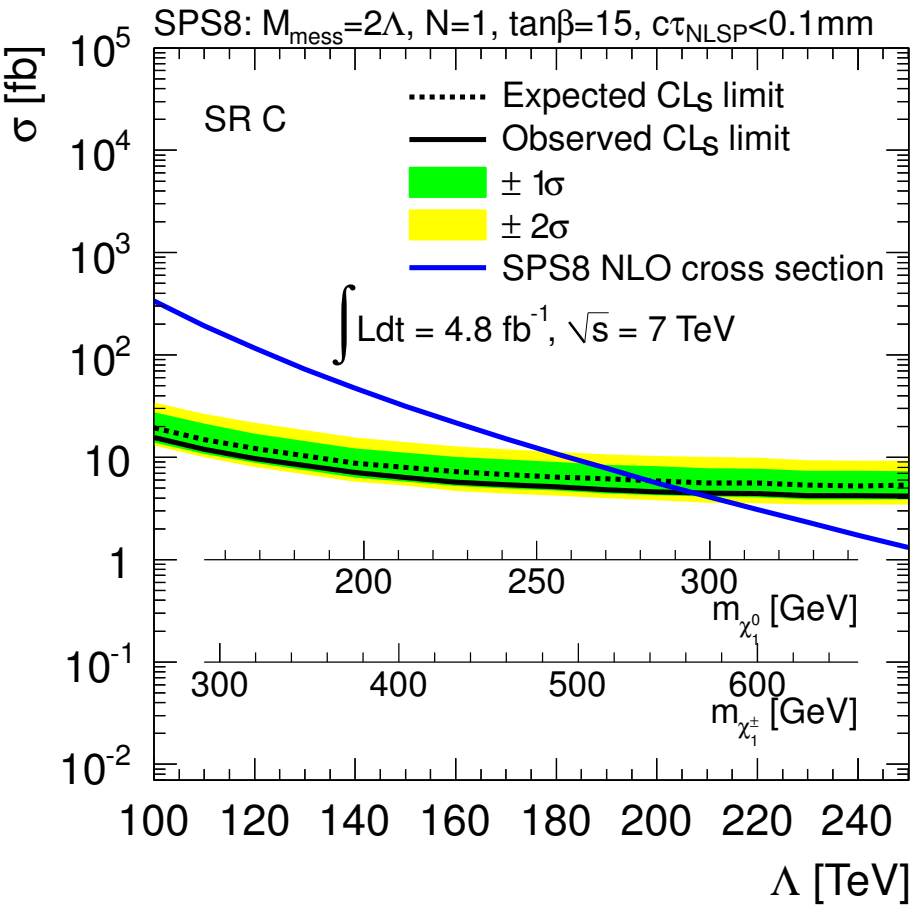

Figure 8.14: The production cross section as well as the observed and expected 95 % CL limit on the production cross section as a function of Λ of the GMSB SPS8 scenario in SR C. The other model parameters are fixed to $M_{\text{mess}} = 2\Lambda$, $N = 1$, $\tan\beta = 15$, and $c\tau_{\text{NLSP}} < 0.1\,\text{mm}$.

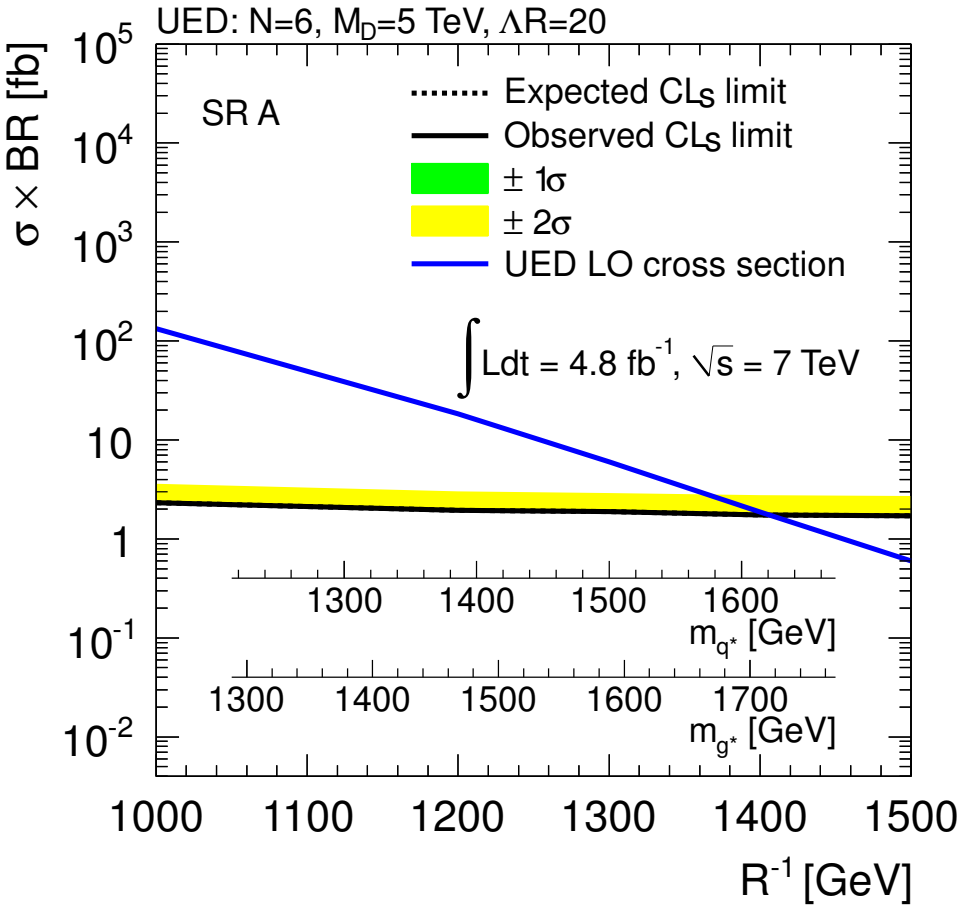

(a)

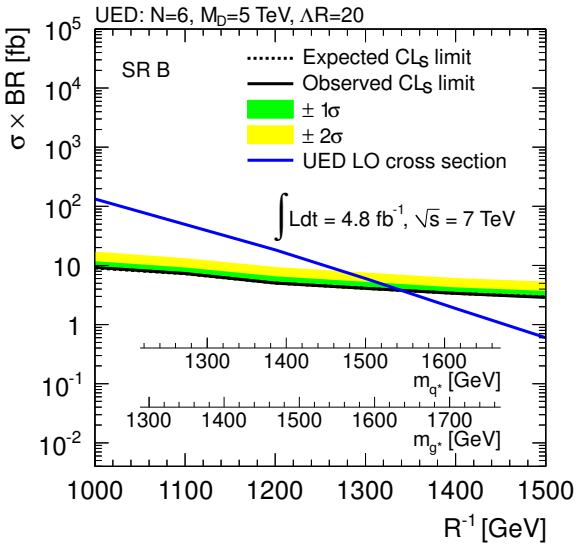

(b)

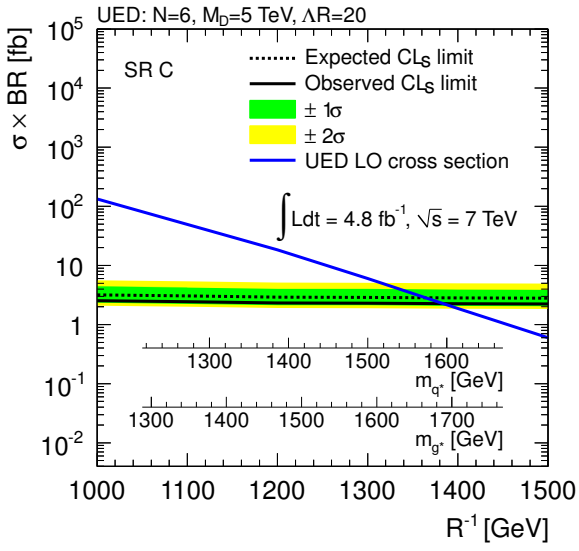

(c)

Figure 8.15: The production cross section as well as the observed and expected 95 % CL limit on the production cross section times branching ratio as a function of R^{-1} of the UED scenario in SR A (a), SR B (b) and SR C (c). The other model parameters are fixed to $N = 6$, $M_D = 5\,\text{TeV}$, and $\Lambda R = 20$.

CHAPTER 9

Conclusion

9.1 Summary

A search for physics beyond the SM using final states with at least two high energy photons and $E_{\mathrm{T}}^{\mathrm{miss}}$ in a dataset corresponding to an integrated luminosity of $4.8\,\mathrm{fb}^{-1}$ of $\sqrt{\mathrm{s}} = 7\,\mathrm{TeV}$ pp-collisions recorded by the ATLAS experiment at the LHC is presented in this thesis.

In the SUSY scenarios studied, namely the GGM scenario and the GMSB SPS8 scenario, the character of the two lightest SUSY particles, the lightest neutralino and the gravitino, determine the phenomenology of the event to a large extend. Two GGM scenarios with a bino-like $\tilde{\chi}_1^0$ are considered, which are parametrized either by $(m_{\tilde{g}}, m_{\tilde{\chi}_1^0})$ or by $(m_{\tilde{q}}, m_{\tilde{\chi}_1^0})$. The mass of the $\tilde{\chi}_1^0$ is larger than 50 GeV and smaller than the $\tilde{g}$ ($\tilde{q}$) mass. The remaining masses are decoupled by setting them to 2.5 TeV. In the UED scenario, where the space time is extended by one additional space dimension, the photons arise from the decay of an excited photon to a SM photon and a graviton. In the SUSY and UED scenarios, the assumed conservation of R-parity and KK-parity[1], results in pair production of new particles leading to two photons in the final state. The gravitinos and the gravitons are not detected leading to missing energy.

10451 diphoton events, where the photons' momenta are larger than 50 GeV, are selected from the 2011 dataset. By making use of three signal regions, incorporating different set of cuts on $\Delta\phi(\gamma, E_{\mathrm{T}}^{\mathrm{miss}})$, H_{T}, and $E_{\mathrm{T}}^{\mathrm{miss}}$, the expected phenomenology of the BSM events is exploited. The SM background, except the irreducible background component, is measured from data using several control samples. Two background classes with respect to their $E_{\mathrm{T}}^{\mathrm{miss}}$ content are defined, the instrumental $E_{\mathrm{T}}^{\mathrm{miss}}$ background and the genuine $E_{\mathrm{T}}^{\mathrm{miss}}$ background. In the first case, photons jets can be misidentified as photons, whereas in the latter case, electrons can be misidentified as photons. Therefore, the electron to photon misidentification rate needs to be determined. In all signal regions, the major background are events with genuine $E_{\mathrm{T}}^{\mathrm{miss}}$, for instance coming from SM decays of top quarks or W bosons.

The main background uncertainties arise from low statistics in the data control samples and from differences compared to other control samples or to MC. The signal uncertainties are dominated by theoretical uncertainties.

[1] However, the KK-parity can be broken by gravity, allowing the final decay of the excited photon.

Good agreement between the SM background and the observed events is found in all SRs. In SR A, SR B and, SR C, 0, 0 and 2 events are observed, while $0.12 \pm 0.05 \pm 0.10$, $0.42 \pm 0.09 \pm 0.31$, and $0.12 \pm 0.05 \pm 0.10$ events are expected by the SM background, respectively. The result is interpreted in the context of several BSM physics model scenarios predicting events with a $\gamma\gamma + E_{\mathrm{T}}^{\mathrm{miss}}$ signature, and since no excess of events over the SM background is found, exclusion limits can be set.

GGM scenario: A 95 % CL production cross section limit of $2.8 - 6.0\,\mathrm{fb}$ ($2.0 - 4.4\,\mathrm{fb}$) is found in the GGM scenario with varying $\tilde{g}$ ($\tilde{q}$) mass, corresponding to an exclusion of $\tilde{g}$ ($\tilde{q}$) with masses smaller than 1.10 TeV (0.91 TeV) at 95 % CL.

GMSB SPS8 scenario: In the GMSB SPS8 scenario, the upper limit on the production cross sections is $4.2 - 15.6\,\mathrm{fb}$ in the considered range of $100\,\mathrm{TeV} < \Lambda < 250\,\mathrm{TeV}$ for the SUSY breaking scale Λ. Hence, the region of $\Lambda < 208\,\mathrm{TeV}$ can be excluded at 95 % CL. Since in this scenario, the sparticles are mainly produced by the weak interaction, 95 % CL limits of 302 GeV (582 GeV) are found for the masses of the $\tilde{\chi}_1^0$ ($\tilde{\chi}_1^{\pm}$).

UED scenario: A 95 % CL upper limit of $1.7 - 2.3\,\mathrm{fb}$ on $\sigma \times$ BR is set in the UED scenario in the parameter range of $1000\,\mathrm{GeV} < R^{-1} < 1500\,\mathrm{GeV}$. Scenarios with $R^{-1} < 1410\,\mathrm{GeV}$ are excluded at 95 % CL.

The search for $\gamma\gamma + E_{\mathrm{T}}^{\mathrm{miss}}$ final states presented in this thesis is one of the most stringent tests of BSM models at present and significantly extends previous ATLAS results [80]. The corresponding publication by the ATLAS collaboration providing similar results has been submitted to a journal [75].

9.2 Outlook

The analysis can be improved by the classification and the separate treatment of the final states by the conversion category of the photons, for instance requiring two unconverted photons, would reduce the $e \to \gamma$ misidentification rate in certain categories and thus have a higher background suppression. A reduction of the instrumental background uncertainty might be achieved by performing a reweighting procedure of the number of jets between the $Z \to ee$ control sample and the prompt $\gamma\gamma$ sample. Hence, both the QCD template and the $Z \to ee$ control sample could be used for an improved background estimation.

GGM scenarios with wino- or higgsino-like neutralinos give rise to final states with a photon and an electron or a b-jet. A signal selection adjusted to the different final states would have a broader reach in the GGM parameter space. By considering non-promptly decaying neutralinos in addition, a search considering different settings of the C_{grav} parameter would be feasible. However, the reconstruction of the resulting photons, which are not pointing directly to the interaction vertex, is difficult.

Since spring 2012, the LHC has been providing collisions at an increased center-of-mass energy of $\sqrt{s} = 8\,\text{TeV}$. After the shutdown in 2013, the LHC will provide collisions with at least $\sqrt{s} = 13\,\text{TeV}$. The production cross section of new particles increases significantly with higher center-of-mass energy. In addition, the instantaneous luminosity will be enhanced thereby extending the reach in parameter space of many models.

However, the increased pile-up poses a big challenge on the measurement, because the higher energy density in the calorimeter affects the isolation cone energy determination, for example. Furthermore, a punch-through of particles out of the calorimeters is more likely and needs to be taken into account, especially for the $E_{\text{T}}^{\text{miss}}$ measurement, where otherwise artificial tails can occur.

A possible Higgs particle at a mass of 126 GeV would reduce the parameter space of the GMSB model significantly. In simplified models, where the Higgs mass may be decoupled and the model parameters can be tuned accordingly, a search for new physics is feasible.

Searches are expected to benefit from a refined selection, from a higher center-of-mass energy, and from the increased integrated luminosity. Large unexplored regions of parameter spaces in various models will be accessible in the future.

APPENDIX A

MC Samples

Sample ID	Name	Generator	Cross section [pb]	N_{events}
105009	J0 jetjet	Pythia	$9860 \cdot 10^6$	999997
105010	J1 jetjet	Pythia	$678 \cdot 10^6$	999993
105011	J2 jetjet	Pythia	$41.0 \cdot 10^6$	999999
105012	J3 jetjet	Pythia	$2.19 \cdot 10^6$	999992
105013	J4 jetjet	Pythia	$87.7 \cdot 10^3$	989992
105014	J5 jetjet	Pythia	2350	999987
105015	J6 jetjet	Pythia	33.6	999974
105016	J7 jetjet	Pythia	0.137	998955
105017	J8 jetjet	Pythia	$6.2 \cdot 10^{-6}$	998948
115040	diphoton50	Pythia	5.27	99999
108081	PhotonJet35	Pythia	$18.5 \cdot 10^3$	999950
108082	PhotonJet70	Pythia	1628	999943
108083	PhotonJet140	Pythia	89.2	999940
108084	PhotonJet280	Pythia	3.44	999327

Table A.1: Overview of the SM multijet, SM $\gamma\gamma$ and γ + jets MC samples and cross sections [143].

Sample ID	Name	Generator	Cross section [pb]	K-factor	N_{gen}
107680	WenuNp0_pt20	Alpgen	6930.5	1.20	6952874
107681	WenuNp1_pt20	Alpgen	1305.3	1.20	4998487
107682	WenuNp2_pt20	Alpgen	378.1	1.20	3768632
107683	WenuNp3_pt20	Alpgen	101.9	1.20	1008947
107684	WenuNp4_pt20	Alpgen	25.7	1.20	250000
144018	WenuNp5_pt20	Alpgen	6.99	1.20	69999
Sum	WenuNpi_pt20	Alpgen	8748.5	1.20	-
107700	WtaunuNp0_pt20	Alpgen	6931.8	1.20	3418296
107701	WtaunuNp1_pt20	Alpgen	1304.9	1.20	2499194
107702	WtaunuNp2_pt20	Alpgen	377.9	1.20	3750986
107703	WtaunuNp3_pt20	Alpgen	102.0	1.20	1009946
107704	WtaunuNp4_pt20	Alpgen	25.7	1.20	249998
107705	WtaunuNp5_pt20	Alpgen	7.00	1.20	65000
Sum	WtaunuNpi_pt20	Alpgen	8749.3	1.20	-
117410	WgammaNp0	Alpgen	211.4		2118995
117411	WgammaNp1	Alpgen	53.1		529998
117412	WgammaNp2	Alpgen	17.5		175000
117413	WgammaNp3	Alpgen	5.3		264999
117414	WgammaNp4	Alpgen	1.4		64999
117415	WgammaNp5	Alpgen	0.4		20000
Sum	WgammaNpi	Alpgen	289.1		-
118616	W-lepgamgam	MadGraph Pythia	$2.93 \cdot 10^{-2}$	3.0	5000
118618	W+lepgamgam	MadGraph Pythia	$4.05 \cdot 10^{-2}$	3.0	5000
107650	ZeeNp0_pt20	Alpgen	668.3	1.25	6617284
107651	ZeeNp1_pt20	Alpgen	134.4	1.25	1334897
107652	ZeeNp2_pt20	Alpgen	40.54	1.25	2004195
107653	ZeeNp3_pt20	Alpgen	11.16	1.25	549949
107654	ZeeNp4_pt20	Alpgen	2.88	1.25	149948
107655	ZeeNp5_pt20	Alpgen	0.83	1.25	50000
Sum	ZeeNpi_pt20	Alpgen	858.1	1.25	-
107670	ZtautauNp0_pt20	Alpgen	668.4	1.25	10613179
107671	ZtautauNp1_pt20	Alpgen	134.8	1.25	3334137
107672	ZtautauNp2_pt20	Alpgen	40.36	1.25	1004847
107673	ZtautauNp3_pt20	Alpgen	11.25	1.25	509847
107674	ZtautauNp4_pt20	Alpgen	2.79	1.25	144999
107675	ZtautauNp5_pt20	Alpgen	0.77	1.25	45000
Sum	ZtautauNpi_pt20	Alpgen	858.4	1.25	-
108323	Zeegamma	MadGraph Pythia	8.67		50000
108324	Zmumugamma	MadGraph Pythia	8.67		49950
108325	Ztautaugamma	MadGraph Pythia	1.41		49949
118619	Znunugamgam	MadGraph Pythia	$1.46 \cdot 10^{-2}$	2.0	5000
105200	TTbar_NoAllHad	MC@NLO	79.01	1.146	14981474
105204	TTbar_FullHad	MC@NLO	66.48	1.146	1199034

Table A.2: Overview of vector boson and top MC samples [143, 144].

APPENDIX B

Details on the Background Estimation

B.1 Instrumental $E_{\mathrm{T}}^{\mathrm{miss}}$ Control Samples

In this section, kinematic distributions, like the momentum and the pseudo-rapidity of photons and pseudo-photons, of the QCD_{γ} and $\mathrm{QCD}_{\gamma\gamma}$ samples are presented and basic information are given on the instrumental $E_{\mathrm{T}}^{\mathrm{miss}}$ events after the preselection. The focus is on photons, pseudo-photons and jets. Events containing muons were also studied, but play a minor role in the instrumental background estimation. Figures B.1(a) and (b) show the distributions of the (pseudo-)photon momentum and (pseudo-)photon η, respectively. The comparison between the data and the QCD control samples in terms of number of jets, jet momentum and pseudo-rapidity of jets can be found in Fig. B.2(a)–(c), respectively. All distributions are normalized to an integral of one. The (pseudo-)photon p_{T} distributions of the QCD samples are decreasing faster than in data with increasing momentum, which is expected from γ + jets and $\gamma\gamma$ events with real photons. Regarding the (pseudo-)photons as a function of η, the pseudo-photons appear more central than the photons. The number of jets agrees quite well between the data and the $\mathrm{QCD}_{\gamma\gamma}$ sample. The shapes of the jet momentum and the jet η distributions of the data and the $\mathrm{QCD}_{\gamma\gamma}$ sample also agree in the most part of the p_{T} spectrum and over the full η acceptance. One can conclude therefore that both pseudo-photons likely represent jets.

B.2 SM $\gamma\gamma$ Modeling

The dielectron sample (see Section 6.1.3) is used to model the $E_{\mathrm{T}}^{\mathrm{miss}}$ shape of the SM $\gamma\gamma$ background with instrumental $E_{\mathrm{T}}^{\mathrm{miss}}$. Since especially the number of jets is different in $Z \to ee$ events compared to SM $\gamma\gamma$ events, inducing a different $E_{\mathrm{T}}^{\mathrm{miss}}$ distribution, the study of an additional jet requirement applied to the dielectron sample is presented in this section. The comparison at preselection level between SM $\gamma\gamma$ (MC) events and the dielectron sample with different jet requirements is shown in Fig. B.3, where (a) shows the $E_{\mathrm{T}}^{\mathrm{miss}}$ distributions with number of jets requirement in the "greater equal" condition and (b) shows the "equal" case.

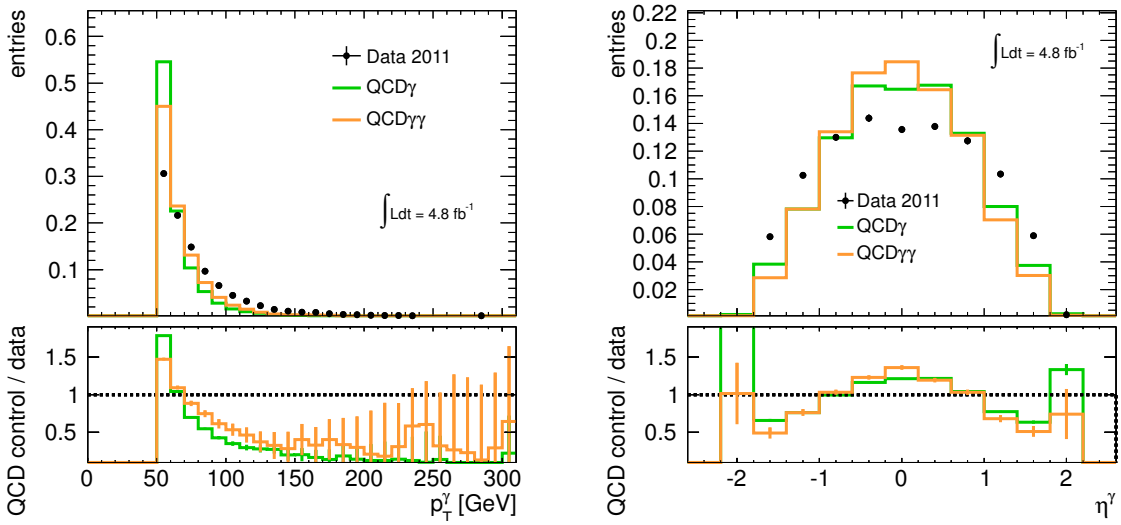

(a) (b)

Figure B.1: Kinematic distributions of (pseudo-)photons after preselection. The momentum distribution is illustrated in (a), the η distribution is shown in (b). For the data sample photons are drawn, while for the QCD control samples the properties of the pseudo-photons are taken. All distributions are normalized to an integral of one.

The number of jets is probed for 0, 1, 2 and 3 jets. The dielectron distributions are scaled to the SM $\gamma\gamma$ sample in the region of $E_{\mathrm{T}}^{\mathrm{miss}} < 20\,\mathrm{GeV}$. The requirement of $N_{\mathrm{jet}} \geq 0$ is effectively no jet requirement and represents all dielectron events. In (a), all distributions with jet requirement are shifted to higher $E_{\mathrm{T}}^{\mathrm{miss}}$ values with respect to the SM $\gamma\gamma$ shape. The higher the number of the required jets is, the greater is the shift. In Fig. B.3(b), the best agreement is shown at a requirement of exactly one jet (orange curve). The shape corresponding to the requirement of exactly zero jets (jet veto) is slightly narrower than the SM $\gamma\gamma$ shape.

The modeling $E_{\mathrm{T}}^{\mathrm{miss}}$ distribution of the diphoton data with the help of the dielectron sample is investigated and illustrated in Fig. B.4, where (a) shows the conditions of $N_{\mathrm{jet}} \geq x$, $x = 0, 1, 2, 3$ and (b) the respective "exactly equal" condition. For the $E_{\mathrm{T}}^{\mathrm{miss}}$ distribution shown in (a), the shape where no jet requirement is applied agrees best with data. For the $E_{\mathrm{T}}^{\mathrm{miss}}$ distribution shown in (b), the best agreement is observed for exactly one jet.

In conclusion, the dielectron sample with exactly one jet models the shape of the $E_{\mathrm{T}}^{\mathrm{miss}}$ distribution of the SM $\gamma\gamma$ sample and data best at preselection level. Furthermore, the full dielectron sample (without any jet requirement) needs to be considered because it models the $E_{\mathrm{T}}^{\mathrm{miss}}$ shape of the data quite well and has no explicit hadronic requirement on top of the electromagnetic processes of SM $\gamma\gamma$ and $Z \to ee$.

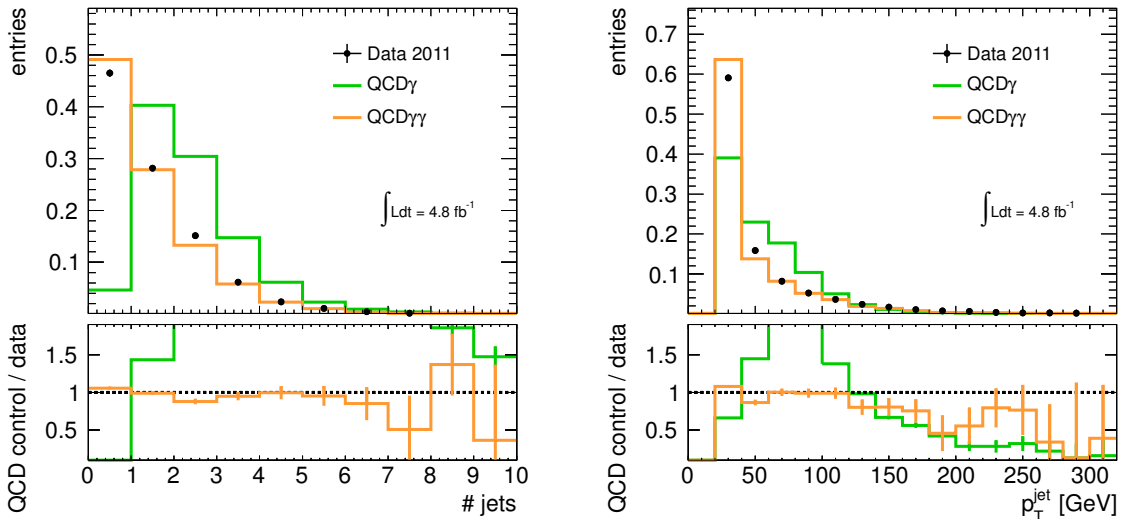

(a) (b)

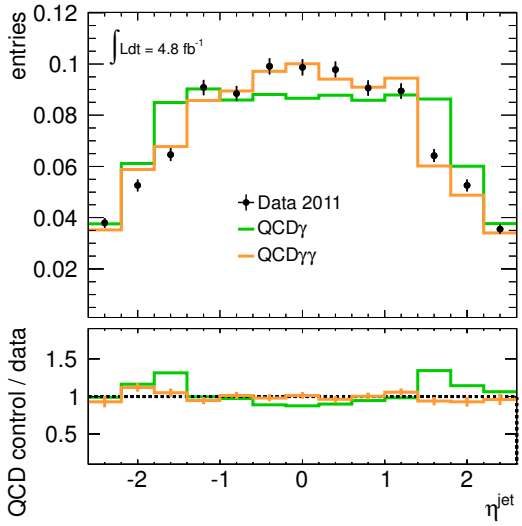

(c)

Figure B.2: Kinematic distributions of jets after preselection. The number of jets, the jet momentum and the jet η distributions are shown in (a)–(c). All distributions are normalized to an integral of one.

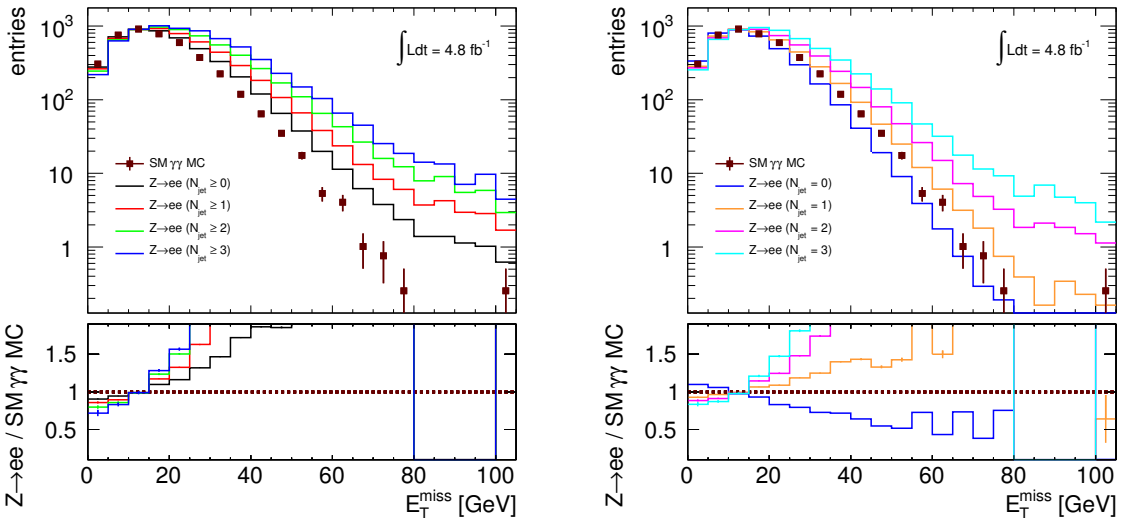

(a) (b)

Figure B.3: $E_{\mathrm{T}}^{\mathrm{miss}}$ distributions of SM $\gamma\gamma$ MC and the dielectron control sample with different jet requirements at preselection level. The requirements are $N_{\mathrm{jet}} \geq x$ in (a) and $N_{\mathrm{jet}} = x$ in (b), where $x = 0, 1, 2, 3$. The dielectron distributions are normalized to the SM $\gamma\gamma$ sample in the CR of $E_{\mathrm{T}}^{\mathrm{miss}} < 20\,\mathrm{GeV}$.

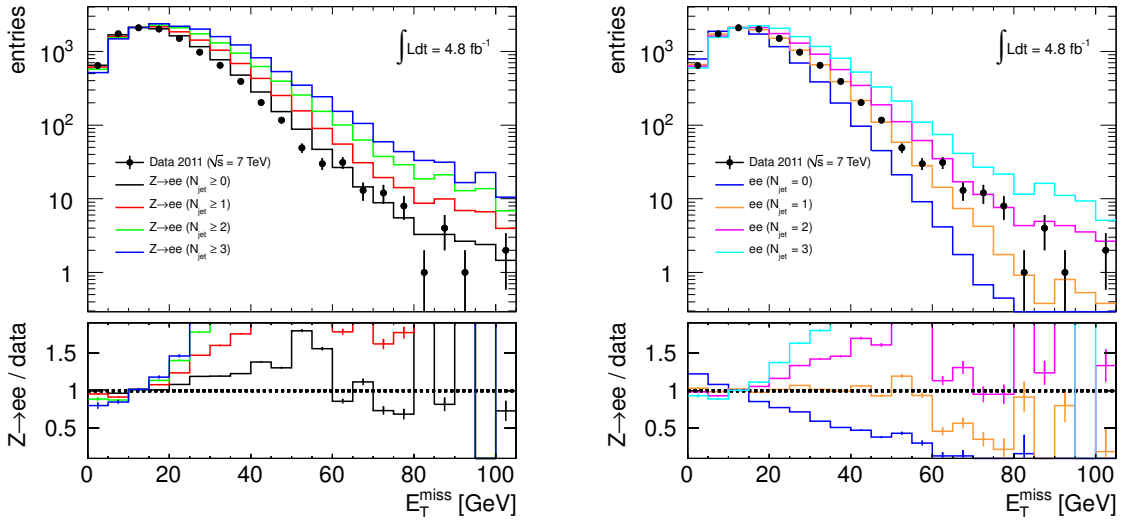

(a) (b)

Figure B.4: $E_{\mathrm{T}}^{\mathrm{miss}}$ distributions of data and $\gamma\gamma$ MC in comparison to the dielectron control sample with different jet requirements. The requirements are $N_{\mathrm{jet}} \geq x$ in (a) and $N_{\mathrm{jet}} = x$ in (b), where $x = 0, 1, 2, 3$. The dielectron distributions are normalized to the diphoton data in the CR of $E_{\mathrm{T}}^{\mathrm{miss}} < 20\,\mathrm{GeV}$

SR, QCD sample	$E_{\mathrm{T}}^{\mathrm{miss}}$ [GeV]	QCD sample	$W \to e\nu$	$W \to e\nu\gamma$	top
SR A, QCD_{γ}	0 - 20	53.0 ± 7.3	0.58 ± 0.58	0.0 ± 0.0	3.52 ± 0.81
	20 - 200	101 ± 10	0.0 ± 0.0	0.0 ± 0.0	9.2 ± 1.3
	> 200	0.0 ± 0.0	0.0 ± 0.0	0.0 ± 0.0	0.35 ± 0.26
SR C, QCD_{γ}	0 - 20	39595 ± 199	19.7 ± 3.9	0.28 ± 0.42	24.0 ± 2.1
	20 - 125	27398 ± 166	222 ± 13	4.9 ± 1.8	146 ± 5.1
	> 125	8.0 ± 2.8	11.8 ± 3.1	0.0 ± 0.0	17.2 ± 1.7

Table B.1: Genuine $E_{\mathrm{T}}^{\mathrm{miss}}$ background contamination of the QCD_{γ} control sample in SR A and C. The MC samples are normalized by their cross section (see Section 4.4.1). The uncertainties are statistical only.

B.3 Contamination with Genuine $\mathbf{E_T^{miss}}$

In this section, a study of a possible contamination of the QCD control samples is presented. In particular the contribution of events with genuine $E_{\mathrm{T}}^{\mathrm{miss}}$ needs to be investigated. The QCD control sample selection is imposed on events with genuine $E_{\mathrm{T}}^{\mathrm{miss}}$ in MC, namely $W \to e\nu$, $W \to e\nu\gamma$ and top events. The resulting distributions are illustrated in Fig. B.5. The top (bottom) row shows the result in SR A (SR C) before the $E_{\mathrm{T}}^{\mathrm{miss}}$ requirement for the QCD_{γ} sample on the left and the $\mathrm{QCD}_{\gamma\gamma}$ sample on the right. In SR B, the contamination can not be determined because no events pass the selection. The MC distributions are scaled to data luminosity and are drawn stacked. The number of events in several $E_{\mathrm{T}}^{\mathrm{miss}}$ intervals is listed in Table B.1. The interval ranges are the CR of $E_{\mathrm{T}}^{\mathrm{miss}} < 20\,\mathrm{GeV}$, the intermediate $E_{\mathrm{T}}^{\mathrm{miss}}$ interval from 20 GeV to the lower $E_{\mathrm{T}}^{\mathrm{miss}}$ edge of the SR and the $E_{\mathrm{T}}^{\mathrm{miss}}$ SR itself.

The largest contamination of the QCD_{γ} sample of SR A is due to top events and a minor contribution of W events. In the CR, the contamination is 8 %. In the SR, where no QCD_{γ} events are found, 0.35 ± 0.26 top events are expected to pass the selection indicating that any event in the QCD_{γ} SR is likely a genuine $E_{\mathrm{T}}^{\mathrm{miss}}$ event. However, the statistics are too low and the jet $\to \gamma$ misidentification rate is not well modeled in MC. No contamination is found in the $\mathrm{QCD}_{\gamma\gamma}$ sample, since no events pass the selection. In SR A, no contamination with $W \to e\nu\gamma$ is seen in the QCD control samples.

In SR C, a contamination from all three sources is observed, with a major contribution of top and $W \to e\nu$ events. The contamination is negligible in the $E_{\mathrm{T}}^{\mathrm{miss}}$ CR of the QCD_{γ} sample. In the SR, all events are expected to come from genuine $E_{\mathrm{T}}^{\mathrm{miss}}$ sources keeping in mind the poor agreement between QCD sample data and MC. In SR C, the contamination of the $\mathrm{QCD}_{\gamma\gamma}$ sample in the CR is also negligible and the events in the SR originate from top decays.

B.4 Contamination with BSM Signal Events

The contribution of new physics signal events to the QCD control samples is discussed in this section and the results of example points are presented. It is important to check the impact of BSM events in the CR, where a high contamination could lead to a mismeasurement of the

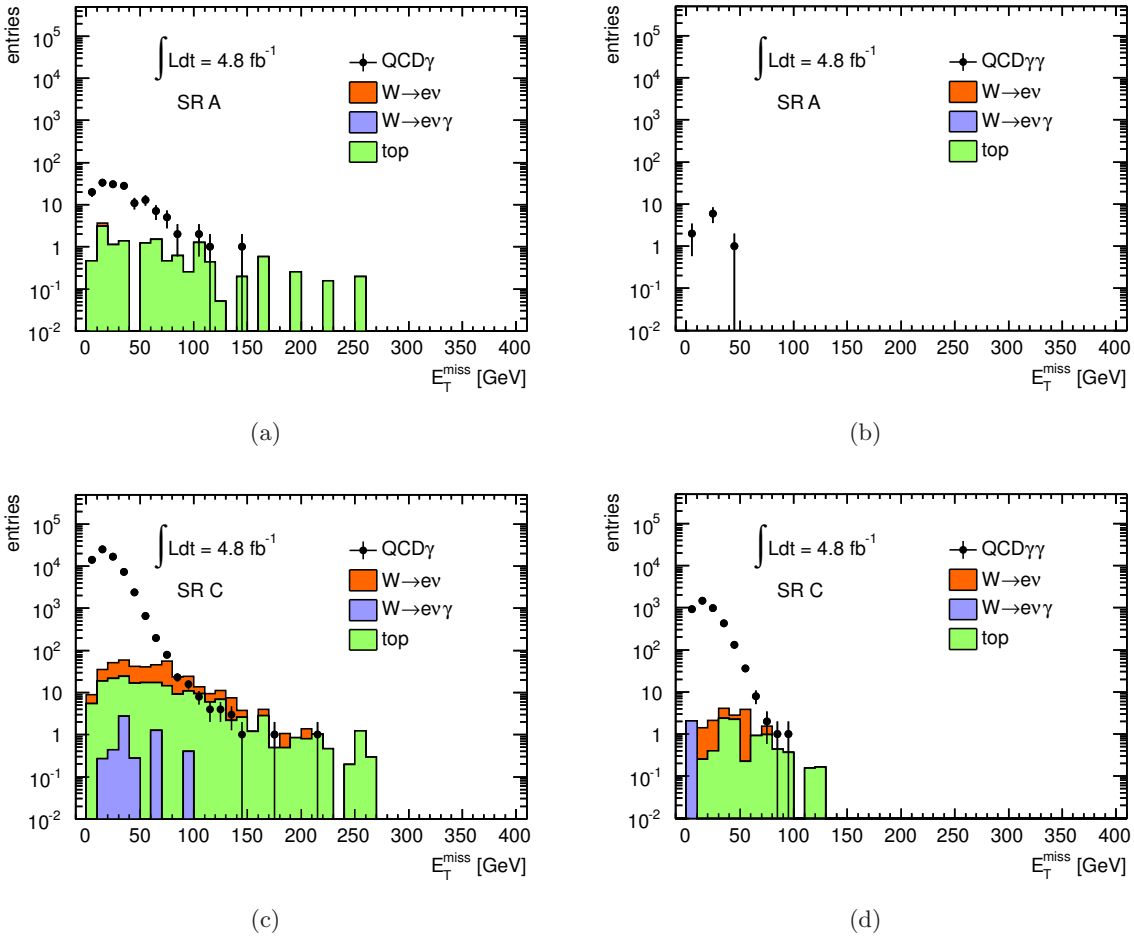

Figure B.5: Distributions illustrating the genuine $E_{\mathrm{T}}^{\mathrm{miss}}$ contribution in the QCD_{γ} (a) and (c) for SR A and SR C; The corresponding distributions of the $\mathrm{QCD}_{\gamma\gamma}$ sample selection in SR A and SR C can be found in (b) and (d). The MC samples are scaled by their production cross section (see Section 4.4.1).

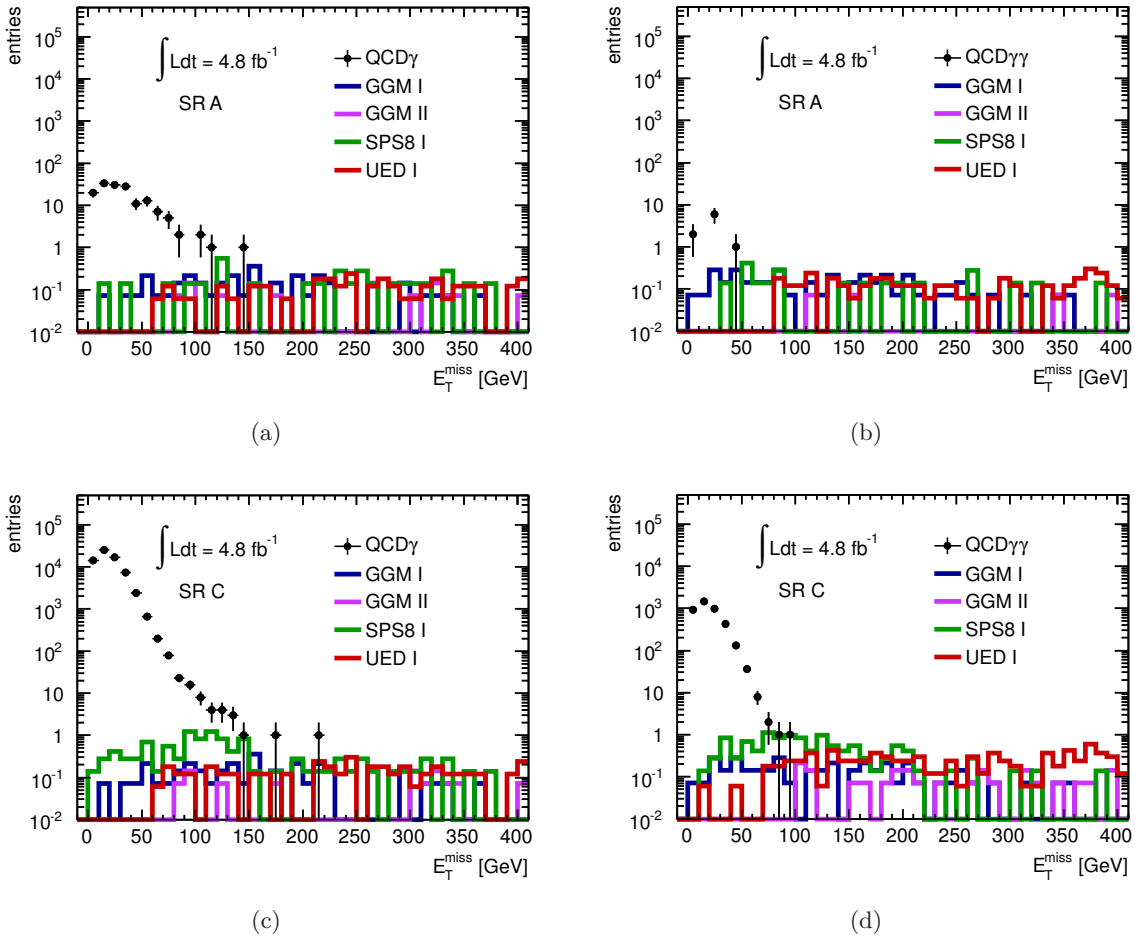

Figure B.6: Signal contamination of the QCD_{γ} (a), (c) and $\mathrm{QCD}_{\gamma\gamma}$ (b), (d) samples in SR A and SR C illustrated for example parameter points. The signal MC samples are scaled by their cross sections (see Section 4.4.1).

SM background. By design, the control region is supposed to be signal depleted. The example points (see Table B.2) are chosen, such that the parameter space of the various models is mostly covered by them and the QCD control sample selection is applied. Figure B.6 shows the $E_{\mathrm{T}}^{\mathrm{miss}}$ spectra of selected BSM signal events, that pass the QCD control sample selection. The corresponding number of events for the QCD_{γ} contamination can be found in Table B.2. In the $E_{\mathrm{T}}^{\mathrm{miss}}$ CR of SR A and SR C a negligible contamination with signal events is found. Since in SR B no QCD control events are found in the CR, the contamination study is not performed.

B.5 Details on the Electron-Photon Control Sample

The distribution of scaled $e\gamma$ control sample events as a function of η of the tag electron and $E_{\mathrm{T}}^{\mathrm{miss}}$ is presented in Fig. B.7. In SR A and SR C, all η bins contribute to the control sample, while in SR B, the two outermost bins do not have entries. One can observe, that in SR A and

signal sample	events in CR ($0 < E_{\mathrm{T}}^{\mathrm{miss}} < 20\,\mathrm{GeV}$)	
	SR A	SR C
QCD_{γ}	53.0 ± 7.28	39595 ± 199
GGM I $m_{\tilde{g}} = 800\,\mathrm{GeV}$, $m_{\tilde{\chi}_1^0} = 100\,\mathrm{GeV}$	0.0 ± 0.0	0.0 ± 0.0
GGM II $m_{\tilde{g}} = 1250\,\mathrm{GeV}$, $m_{\tilde{\chi}_1^0} = 100\,\mathrm{GeV}$	0.072 ± 0.072	0.072 ± 0.072
GGM II $m_{\tilde{g}} = 1250\,\mathrm{GeV}$, $m_{\tilde{\chi}_1^0} = 1000\,\mathrm{GeV}$	0.0 ± 0.0	0.0 ± 0.0
GGM IV $m_{\tilde{g}} = 800\,\mathrm{GeV}$, $m_{\tilde{\chi}_1^0} = 750\,\mathrm{GeV}$	0.0 ± 0.0	0.0 ± 0.0
GGM V $m_{\tilde{g}} = 1000\,\mathrm{GeV}$, $m_{\tilde{\chi}_1^0} = 450\,\mathrm{GeV}$	0.0 ± 0.0	0.0 ± 0.0
SPS I $\Lambda = 100\,\mathrm{TeV}$	0.14 ± 0.14	0.42 ± 0.24
SPS II $\Lambda = 250\,\mathrm{TeV}$	0.0 ± 0.0	0.0 ± 0.0
UED I $R^{-1} = 1000\,\mathrm{GeV}$	0.0 ± 0.0	0.0 ± 0.0
UED II $R^{-1} = 1500\,\mathrm{GeV}$	0.0 ± 0.0	0.00048 ± 0.00048

Table B.2: Signal events in the CR of the QCD control samples for SR A and SR C. The signal MC samples are scaled by their cross section (see Section 4.4).

SR C, the shape of the $E_{\mathrm{T}}^{\mathrm{miss}}$ distribution is similar over all η bins, which is expected.

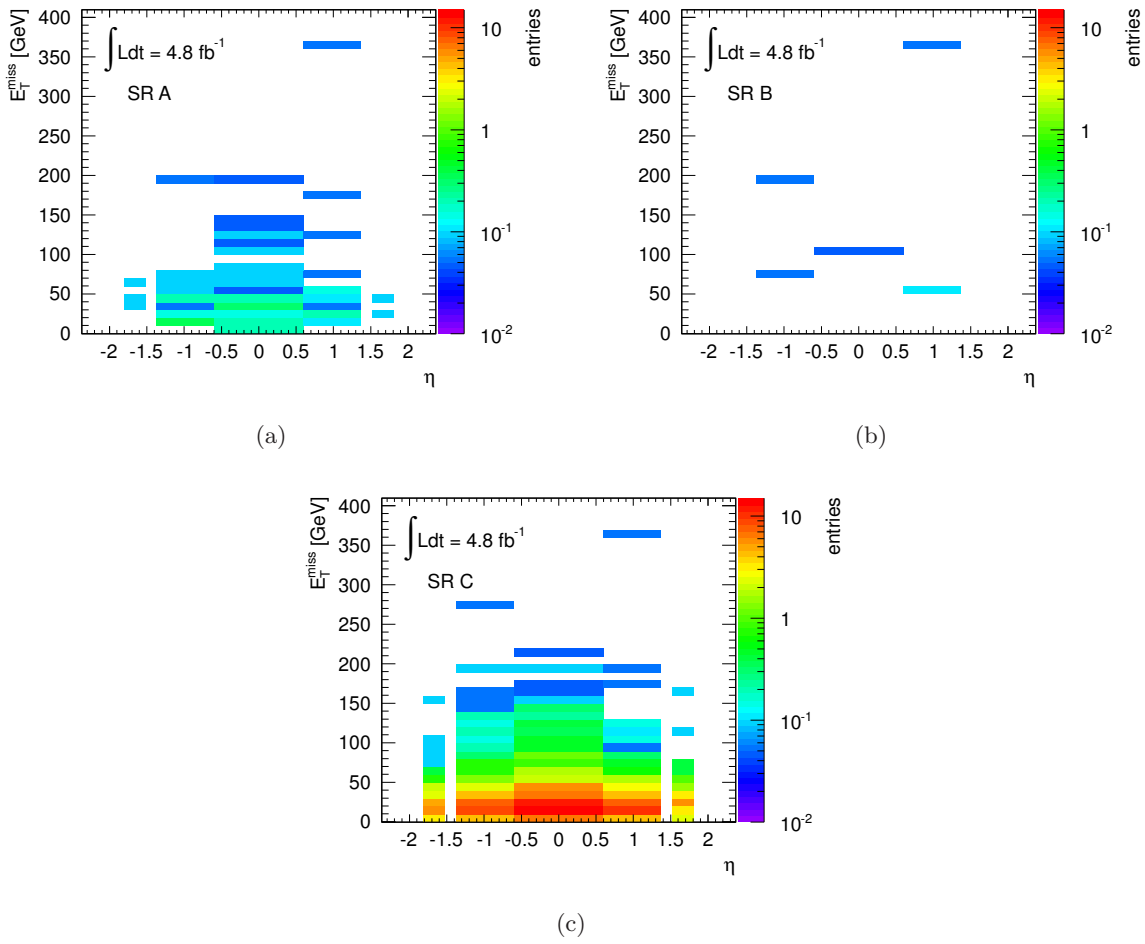

(a) (b)

(c)

Figure B.7: Scaled $e\gamma$ control sample events as a function of $E_{\mathrm{T}}^{\mathrm{miss}}$ and η of the tag electron in SR A (a), SR B (b) and SR C (c).

List of Figures

2.1 The elementary particles and interactions. 4
2.2 Combined PDFs extracted from H1 and Zeus. 5
2.3 Local p_0 as a function of m_{H} in the low mass range 7
2.4 The running of the inverse coupling constants. 9
2.5 The SPS8 mass spectrum. 11
2.6 Examples of sparticle production. 12
2.7 The UED mass spectrum and decays. 14
2.8 The UED branching ratios. 15
2.9 The 95 % CL exclusion contours for several models. 16
2.10 A 95 % CL exclusion contour in the $m_{\tilde{q}} - m_{\tilde{g}}$ plane. 17

3.1 The LHC and its experiments. 21
3.2 Cross sections as a function of the center-of-mass energy. 22
3.3 Overview of the ATLAS detector. 23
3.4 The inner detector with its subcomponents. 24
3.5 The calorimeter system 26
3.6 Fudge of the electromagnetic calorimeter. 27
3.7 The muon system. 29
3.8 The 3-level trigger system. 30
3.9 The Level-1 trigger system. 30
3.10 The level-1 calorimeter cluster finding algorithm. 32

4.1 The MC event generation stages. 34
4.2 Energy resolution of electrons. 37
4.3 Conversion probability of a photon. 39
4.4 Energy resolution of photons. 42
4.5 Resolution of $E_{\mathrm{x,y}}^{\mathrm{miss}}$. 44
4.6 GGM NLO+NLL cross section. 47
4.7 The reweighting of MC events. 50

5.1 The luminosity in 2011. 52
5.2 Average number of interactions per bunch crossing. 54
5.3 The yield of diphoton events. 60

5.4 Distributions of $\Delta\phi(\gamma, E_{\mathrm{T}}^{\mathrm{miss}})$ and the leading photon p_{T}. 61
5.5 Distributions of $E_{\mathrm{T}}^{\mathrm{miss}}$ and H_{T}. 62
5.6 Distributions of the number of photons and the photon p_{T}. 63
5.7 Distributions of the number of jets and the leading jet p_{T}. 63
5.8 Distributions of $E_{\mathrm{T}}^{\mathrm{miss}}$ and H_{T} in SR A. 65
5.9 Distributions of $E_{\mathrm{T}}^{\mathrm{miss}}$ and H_{T} in SR B. 65
5.10 Distributions of $E_{\mathrm{T}}^{\mathrm{miss}}$ and H_{T} in SR C. 66
5.11 Event display. 68
5.12 Signal efficiencies of the GGM $\tilde{g}$-$\tilde{\chi}_1^0$ mass plane. 69
5.13 Signal efficiencies of the GGM $\tilde{q}$-$\tilde{\chi}_1^0$ mass plane. 70
5.14 Signal efficiencies of the GMSB SPS8 and the UED scenarios. 70

6.1 Average yield of QCD_{γ} control events. 74
6.2 Shape comparison of $E_{\mathrm{T}}^{\mathrm{miss}}$ between the QCD_{γ} and the $\mathrm{QCD}_{\gamma\gamma}$ sample. 74
6.3 Shape comparison between diphoton data and control samples. 75
6.4 Shape comparison between SM $\gamma\gamma$ MC and $Z \to ee$ MC samples. 78
6.5 Shape comparison between diphoton data and instrumental $E_{\mathrm{T}}^{\mathrm{miss}}$ control samples. 79
6.6 Expected number of QCD background events 80
6.7 Stability of the QCD control sample normalization. 81
6.8 Invariant mass distributions. 83
6.9 The background subtracted scale factors. 83
6.10 $E_{\mathrm{T}}^{\mathrm{miss}}$ distributions of the $e\gamma$ control sample. 84
6.11 Contributions from instrumental $E_{\mathrm{T}}^{\mathrm{miss}}$ events in the $e\gamma$ sample. 86
6.12 Extrapolation from MC in SR A. 87
6.13 Extrapolation from MC in SR C. 88
6.14 $E_{\mathrm{T}}^{\mathrm{miss}}$ distribution of the irreducible background. 90

7.1 The total uncertainty in the GGM scenario. 98

8.1 Diphoton data and total background in SR A. 102
8.2 Diphoton data and total background in SR B. 103
8.3 Diphoton data and total background in SR C. 103
8.4 Expected and observed CL_{s} values of the GGM model. 109
8.5 Expected and observed CL_{s} values of the GGM model. 110
8.6 95 % CL mass limit contours in the GGM $m_{\tilde{g}}$-$m_{\tilde{\chi}_1^0}$ plane. 111
8.7 95 % CL mass limit contours in the GGM $m_{\tilde{q}}$-$m_{\tilde{\chi}_1^0}$ plane. 112
8.8 95 % CL production cross section limit in the GGM $m_{\tilde{g}}$-$m_{\tilde{\chi}_1^0}$ plane. 113
8.9 95 % CL production cross section limit in the GGM $m_{\tilde{q}}$-$m_{\tilde{\chi}_1^0}$ plane. 114
8.10 Unified expected CL_{s} of the GGM scenarios. 115
8.11 Unified 95 % CL mass limit contours in the GGM scenarios. 116
8.12 Unified 95 % CL production cross section limit in the GGM scenarios. 117
8.13 95 % CL limit on the cross section in the SPS8 scenario in SR A and SR B. . . 118

8.14 95 % CL limit on the cross section in the SPS8 scenario in SR C. 119
8.15 95 % CL limit on the cross section in the UED scenario in SR A, B and C. . . . 120

B.1 Kinematic distributions of (pseudo-)photons. 128
B.2 Kinematic distributions of jets. 129
B.3 Different jet requirements for the SM $\gamma\gamma$ MC and the dielectron control sample. 130
B.4 Distribution of data and $\gamma\gamma$ MC. 130
B.5 Contamination with genuine $E_{\mathrm{T}}^{\mathrm{miss}}$. 132
B.6 Signal contamination of the QCD_{γ} and the $\mathrm{QCD}_{\gamma\gamma}$ samples. 133
B.7 Scaled $e\gamma$ control sample events. 135

List of Tables

2.1 The SM fermions. . . . 4
2.2 The SM gauge bosons. . . . 4

3.1 Performance goals of the ATLAS detector. . . . 21

4.1 Electron identification variables. . . . 38
4.2 Summary of reconstruction efficiencies for photons. . . . 40
4.3 Photon identification variables. . . . 41
4.4 Background MC samples. . . . 46
4.5 GGM NLO+NLL cross sections. . . . 47
4.6 GMSB SPS8 NLO+NLL cross sections. . . . 48
4.7 UED cross sections. . . . 49

5.1 ATLAS subsystems data quality. . . . 53
5.2 Integrated luminosity and data taking periods. . . . 54
5.3 Cutflow of preselection. . . . 60
5.4 Selection criteria in the different signal regions. . . . 64
5.5 Cutflow in signal regions. . . . 66

6.1 Number of events of the instrumental $E_{\mathrm{T}}^{\mathrm{miss}}$ control samples in SR A. . . . 76
6.2 Summary of the instrumental $E_{\mathrm{T}}^{\mathrm{miss}}$ background estimation. . . . 81
6.3 Results of the extrapolation from MC. . . . 87
6.4 Summary of the genuine $E_{\mathrm{T}}^{\mathrm{miss}}$ background estimation. . . . 89
6.5 Irreducible background split into W and Z components in SR C. . . . 90
6.6 Irreducible background results. . . . 91

7.1 The GGM and GMSB SPS8 systematic uncertainties. . . . 97
7.2 The UED systematic uncertainties. . . . 99

8.1 Total number of background events in the various SRs. . . . 104
8.2 95 % CL exclusion limit on the number of signal events. . . . 108
8.3 95 % CL limits on the production cross section of the GGM scenarios. . . . 114

A.1 Background MC samples (A). . . . 125

A.2 Background MC samples (B). 126

B.1 Contamination with genuine $E_{\mathrm{T}}^{\mathrm{miss}}$ 131
B.2 Signal events in the CR of the QCD control samples. 134

Bibliography

[1] Particle Data Group, K. N. *et al.*, Review of particle physics, Journal of Physics G: Nuclear and Particle Physics **37**, 075021 (2010), and 2011 partial update for the 2012 edition (URL: `http://pdg.lbl.gov`).

[2] Wikipedia, TriTertButoxy, Elementary particle interactions, January, 2012, `http://upload.wikimedia.org/wikipedia/commons/4/4c/Elementary_particle_interactions.svg`.

[3] H. Fritzsch, M. Gell-Mann, and H. Leutwyler, Advantages of the Color Octet Gluon Picture, Phys.Lett. **B47**, 365 (1973), Introduces the term 'color'.

[4] I. Ivanov, Perturbative QCD, Phys.Part.Nucl.Lett. **8**, 651 (2011).

[5] P. Skands, QCD for Collider Physics, (2011), `1104.2863`.

[6] B. R. W. R. Keith Ellis, W. J. Stirling, *Qcd and Collider Physics* (Cambridge Monographs on Particle Physics, Nuclear Physics and Cosmology, 1996).

[7] H1 and ZEUS Collaborations, F. D. Aaron *et al.*, Combined Measurement and QCD Analysis of the Inclusive *ep* Scattering Cross Sections at HERA, JHEP **01**, 109 (2010), `0911.0884`.

[8] S. Weinberg, A Model of Leptons, Phys. Rev. Lett. **19**, 1264 (1967).

[9] M. Peskin and M. Schroeder, *An Introduction to Quantum Field Theory* (Addison Wesley, 1997).

[10] F. Englert and R. Brout, Broken symmetry and the mass of gauge vector mesons, Phys. Rev. Lett. **13**, 321 (1964).

[11] P. W. Higgs, Broken symmetries, massless particles and gauge fields, Phys. Lett. **12**, 132 (1964).

[12] P. W. Higgs, Broken symmetries and the masses of gauge bosons, Phys. Rev. Lett. **13**, 508 (1964).

[13] G. Guralnik, C. Hagen, and T. Kibble, Global conservation laws and massless particles, Phys. Rev. Lett. **13**, 585 (1964).

[14] P. W. Higgs, Spontaneous symmetry breakdown without massless bosons, Phys. Rev. **145**, 1156 (1966).

[15] T. Kibble, Symmetry breaking in non-Abelian gauge theories, Phys. Rev. **155**, 1554 (1967).

[16] M. Baak *et al.*, Updated Status of the Global Electroweak Fit and Constraints on New Physics, (2011), 1107.0975.

[17] ATLAS Collaboration, G. Aad *et al.*, Observation of a new particle in the search for the Standard Model Higgs boson with the ATLAS detector at the LHC, Phys.Lett.B (2012), 1207.7214.

[18] CMS Collaboration, S. Chatrchyan *et al.*, Observation of a new boson at a mass of 125 GeV with the CMS experiment at the LHC, Phys.Lett.B (2012), 1207.7235.

[19] ATLAS Collaboration, G. Aad *et al.*, Combined search for the Standard Model Higgs boson in pp collisions at $\sqrt{s} = 7$ TeV with the ATLAS detector, Phys.Rev. **D86**, 032003 (2012), 1207.0319.

[20] CMS Collaboration, S. Chatrchyan *et al.*, Combined results of searches for the standard model Higgs boson in pp collisions at $\sqrt{s} = 7$ TeV, Phys.Lett. **B710**, 26 (2012), 1202.1488.

[21] M. Baak *et al.*, The Electroweak Fit of the Standard Model after the Discovery of a New Boson at the LHC, (2012), 1209.2716.

[22] S. P. Martin, A Supersymmetry primer, (1997), hep-ph/9709356.

[23] S. Weinberg, Implications of Dynamical Symmetry Breaking, Phys. Rev. **D13**, 974 (1976).

[24] E. Gildener, Gauge Symmetry Hierarchies, Phys. Rev. **D14**, 1667 (1976).

[25] S. Weinberg, Implications of Dynamical Symmetry Breaking: An Addendum, Phys. Rev. **D19**, 1277 (1979).

[26] L. Susskind, Dynamics of Spontaneous Symmetry Breaking in the Weinberg- Salam Theory, Phys. Rev. **D20**, 2619 (1979).

[27] H. Miyazawa, Baryon Number Changing Currents, Prog. Theor. Phys. **36 (6)**, 1266 (1966).

[28] P. Ramond, Dual Theory for Free Fermions, Phys. Rev. **D3**, 2415 (1971).

[29] Y. A. Golfand and E. P. Likhtman, Extension of the Algebra of Poincare Group Generators and Violation of p Invariance, JETP Lett. **13**, 323 (1971), [Pisma Zh.Eksp.Teor.Fiz.13:452-455,1971].

[30] A. Neveu and J. H. Schwarz, Factorizable dual model of pions, Nucl. Phys. **B31**, 86 (1971).

[31] A. Neveu and J. H. Schwarz, Quark Model of Dual Pions, Phys. Rev. **D4**, 1109 (1971).

[32] J. Gervais and B. Sakita, Field theory interpretation of supergauges in dual models, Nucl. Phys. **B34**, 632 (1971).

[33] D. V. Volkov and V. P. Akulov, Is the Neutrino a Goldstone Particle?, Phys. Lett. **B46**, 109 (1973).

[34] J. Wess and B. Zumino, A Lagrangian Model Invariant Under Supergauge Transformations, Phys. Lett. **B49**, 52 (1974).

[35] J. Wess and B. Zumino, Supergauge Transformations in Four-Dimensions, Nucl. Phys. **B70**, 39 (1974).

[36] P. Fayet, Supersymmetry and Weak, Electromagnetic and Strong Interactions, Phys. Lett. **B64**, 159 (1976).

[37] P. Fayet, Spontaneously Broken Supersymmetric Theories of Weak, Electromagnetic and Strong Interactions, Phys. Lett. **B69**, 489 (1977).

[38] G. R. Farrar and P. Fayet, Phenomenology of the Production, Decay, and Detection of New Hadronic States Associated with Supersymmetry, Phys. Lett. **B76**, 575 (1978).

[39] P. Fayet, Relations Between the Masses of the Superpartners of Leptons and Quarks, the Goldstino Couplings and the Neutral Currents, Phys. Lett. **B84**, 416 (1979).

[40] S. Dimopoulos and H. Georgi, Softly Broken Supersymmetry and SU(5), Nucl. Phys. **B193**, 150 (1981).

[41] G. Giudice and R. Rattazzi, Theories with gauge mediated supersymmetry breaking, Phys.Rept. **322**, 419 (1999), Several minor changes; new appendix with complete analytical formulae for the mass spectrum in gauge mediation at the next-to-leading order, `hep-ph/9801271`.

[42] M. Dine and W. Fischler, A Phenomenological Model of Particle Physics Based on Supersymmetry, Phys. Lett. **B110**, 227 (1982).

[43] L. Alvarez-Gaume, M. Claudson, and M. B. Wise, Low-Energy Supersymmetry, Nucl. Phys. **B207**, 96 (1982).

[44] C. R. Nappi and B. A. Ovrut, Supersymmetric Extension of the SU(3) x SU(2) x U(1) Model, Phys. Lett. **B113**, 175 (1982).

[45] M. Dine and A. E. Nelson, Dynamical supersymmetry breaking at low-energies, Phys. Rev. **D48**, 1277 (1993), `hep-ph/9303230`.

[46] M. Dine, A. E. Nelson, and Y. Shirman, Low-energy dynamical supersymmetry breaking simplified, Phys. Rev. **D51**, 1362 (1995), `hep-ph/9408384`.

[47] M. Dine, A. E. Nelson, Y. Nir, and Y. Shirman, New tools for low-energy dynamical supersymmetry breaking, Phys. Rev. **D53**, 2658 (1996), `hep-ph/9507378`.

[48] ATLAS Collaboration, G. Aad *et al.*, Search for lepton flavour violation in the $e\mu$ continuum with the ATLAS detector in $\sqrt{s} = 7\,\text{TeV}$ pp collisions at the LHC, (2012), `1205.0725`.

[49] D. Kazakov, Supersymmetry in particle physics: the renormalization group viewpoint, Phys.Rept. **344**, 309 (2001), `hep-ph/0001257`.

[50] C. Giunti, C. W. Kim, and U. Lee, Running coupling constants and grand unification models, Mod. Phys. Lett. **A6**, 1745 (1991).

[51] J. Ellis, S. Kelley, and D. Nanopoulos, Probing the desert using gauge coupling unification, Phys. Lett. **B260**, 131 (1991).

[52] U. Amaldi, W. de Boer, and H. Furstenau, Comparison of grand unified theories with electroweak and strong coupling constants measured at LEP, Phys. Lett. **B260**, 447 (1991).

[53] P. Langacker and M.-X. Luo, Implications of precision electroweak experiments for M(t), rho(0), sin**2-Theta(W) and grand unification, Phys. Rev. **D44**, 817 (1991).

[54] E. Witten, Dynamical Breaking of Supersymmetry, Nucl. Phys. **B188**, 513 (1981).

[55] M. Dine, W. Fischler, and M. Srednicki, Supersymmetric Technicolor, Nucl. Phys. **B189**, 575 (1981).

[56] S. Dimopoulos and S. Raby, Supercolor, Nucl. Phys. **B192**, 353 (1981).

[57] N. Sakai, Naturalness in Supersymmetric Guts, Zeit. Phys. **C11**, 153 (1981).

[58] R. Kaul and P. Majumdar, CANCELLATION OF QUADRATICALLY DIVERGENT MASS CORRECTIONS IN GLOBALLY SUPERSYMMETRIC SPONTANEOUSLY BROKEN GAUGE THEORIES, Nucl. Phys. **B199**, 36 (1982).

[59] H. Goldberg, Constraint on the photino mass from cosmology, Phys. Rev. Lett. **50**, 1419 (1983).

[60] J. Ellis, J. Hagelin, D. Nanopoulos, K. Olive, and M. Srednicki, Supersymmetric relics from the big bang, Nucl. Phys. **B238**, 453 (1984).

[61] B. Allanach, M. Battaglia, and G. Blair, The snowmass points and slopes: benchmarks for susy searches, The European Physical Journal C - Particles and Fields **25**, 113 (2002), 10.1007/s10052-002-0949-3.

[62] K. Hamaguchi, E. Nakamura, and S. Shirai, A measurement of neutralino mass at the lhc in light gravitino scenarios, Physics Letters B **666**, 57 (2008).

[63] P. Meade, N. Seiberg, and D. Shih, General Gauge Mediation, Prog. Theor. Phys. Suppl. **177**, 143 (2009), 0801.3278.

[64] M. Buican, P. Meade, N. Seiberg, and D. Shih, Exploring General Gauge Mediation, JHEP **03**, 016 (2009), 0812.3668.

[65] L. M. Carpenter, M. Dine, G. Festuccia, and J. D. Mason, Implementing General Gauge Mediation, Phys. Rev. **D79**, 035002 (2009), 0805.2944.

[66] J. Jaeckel, V. V. Khoze, and C. Wymant, Mass Sum Rules and the Role of the Messenger Scale in General Gauge Mediation, JHEP **1104**, 126 (2011), 1102.1589.

[67] C. Macesanu, C. D. McMullen, and S. Nandi, New signal for universal extra dimensions, Phys. Lett. **B546**, 253 (2002), hep-ph/0207269.

[68] T. Appelquist, H.-C. Cheng, and B. A. Dobrescu, Bounds on universal extra dimensions, Phys. Rev. **D64**, 035002 (2001), hep-ph/0012100.

[69] T. Flacke, D. Hooper, and J. March-Russell, Improved bounds on universal extra dimensions and consequences for LKP dark matter, Phys. Rev. **D73**, 095002 (2006), hep-ph/0509352.

[70] T. Flacke, Improved bounds on universal extra dimensions, (2006), hep-ph/0605156.

[71] C. Macesanu, The Phenomenology of universal extra dimensions at hadron colliders, Int.J.Mod.Phys. **A21**, 2259 (2006), review article, 39 pages, 10 figures, uses IJMPA style files, hep-ph/0510418.

[72] M. ElKacimi, D. Goujdami, H. Przysiezniak, and P. Z. Skands, One Universal Extra Dimension in Pythia, Comput.Phys.Commun. **181**, 122 (2010), 0901.4087.

[73] D0 Collaboration, V. M. Abazov *et al.*, Search for diphoton events with large missing transverse energy in $6.3\,\mathrm{fb}^{-1}$ of $\mathbf{p\bar{p}}$ collisions at $\sqrt{s} = 1.96\,\mathrm{TeV}$, Phys. Rev. Lett. **105**, 221802 (2010), 1008.2133.

[74] CDF Collaboration, T. Aaltonen *et al.*, Search for Supersymmetry with Gauge-Mediated Breaking in Diphoton Events with Missing Transverse Energy at CDF II, Phys. Rev. Lett. **104**, 011801 (2010), 0910.3606.

[75] ATLAS Collaboration, G. Aad *et al.*, Search for diphoton events with large missing transverse momentum in 7 TeV proton-proton collision data with the ATLAS detector, (2012), submitted to Physics Letters B, 1209.0753.

[76] CMS Collaboration, Search for supersymmetry in events with photons and missing energy, (2012), CMS-PAS-SUS-12-001.

[77] CMS Collaboration, Search for supersymmetry in events with photons and missing energy, (2012), CMS-PAS-SUS-12-018.

[78] CMS Collaboration, Susy search in photon(s)+jets+$E_{\mathrm{T}}^{\mathrm{miss}}$ final state with the jet-gamma balance method, (2012), CMS-PAS-SUS-12-013.

[79] CMS Collaboration, S. Chatrchyan *et al.*, Search for supersymmetry in events with photons and low missing transverse energy in *pp* collisions at $\sqrt{\mathrm{s}} = 7\,\mathrm{TeV}$, (2012), 1210.2052.

[80] ATLAS Collaboration, G. Aad *et al.*, Search for Diphoton Events with Large Missing Transverse Momentum in $1\,\mathrm{fb}^{-1}$ of 7 TeV Proton-Proton Collision Data with the ATLAS Detector, Phys.Lett. **B710**, 519 (2012), 1111.4116.

[81] ATLAS Collaboration, G. Aad *et al.*, The ATLAS Experiment at the CERN Large Hadron Collider, JINST **3**, S08003 (2008).

[82] L. Evans and P. Bryant, LHC Machine, JINST **3**, S08001 (2008).

[83] ATLAS Collaboration, G. Aad *et al.*, Annual Charts of Luminosity - 2011 *pp* Collisions, https://twiki.cern.ch/twiki/bin/view/AtlasPublic/LuminosityPublicResults, April, 13th, 2012.

[84] Wikipedia, A. Horvath, LHC experiments and preaccelerators, December, 2011, http://upload.wikimedia.org/wikipedia/commons/7/74/LHC.svg.

[85] J. Stirling, MSTW PDFs : key plots, http://mstwpdf.hepforge.org/plots/plots.html, May, 16th, 2012.

[86] J. Pequenao, Computer generated image of the whole ATLAS detector, https://cdsweb.cern.ch/record/1095924, March, 2008.

[87] ATLAS Collaboration, ATLAS calorimeter performance: Technical Design Report, 1996.

[88] ATLAS Collaboration, ATLAS liquid-argon calorimeter: Technical Design Report, 1996.

[89] M. Aharrouche, J. Colas, and L. D. Ciaccio, Response uniformity of the ATLAS liquid argon electromagnetic calorimeter, Nuclear Instruments and Methods in Physics Research Section A: Accelerators, Spectrometers, Detectors and Associated Equipment **582**, 429 (2007).

[90] ATLAS Collaboration, ATLAS tile calorimeter: Technical Design Report, 1996.

[91] ATLAS Collaboration, ATLAS muon spectrometer: Technical Design Report, 1997.

[92] ATLAS Collaboration, ATLAS first-level trigger: Technical Design Report, CERN-LHCC-98-14.

[93] ATLAS Collaboration, G. Aad *et al.*, Performance of the ATLAS Trigger System in 2010, Eur.Phys.J. **C72**, 1849 (2012), 1110.1530.

[94] ATLAS Collaboration, ATLAS high-level trigger, data acquisition and controls: Technical Design Report, CERN-LHCC-2003-022.

[95] J. Boyd, The ATLAS trigger - commissioning with cosmic rays, Journal of Physics: Conference Series **119**, 022014 (2008).

[96] ATLAS Collaboration, Performance of the Electron and Photon Trigger in $p-p$ Collisions at $\sqrt{s} = 7\,\text{TeV}$, May, 2011, ATLAS-COM-CONF-2011-090.

[97] ATLAS Collaboration, G. Duckeck *et al.*, ATLAS computing: Technical Design Report, CERN-LHCC-2005-022.

[98] ATLAS Collaboration, G. Aad *et al.*, The ATLAS Simulation Infrastructure, Eur.Phys.J. **C70**, 823 (2010), Submitted to Eur. Phys. J. C, 1005.4568.

[99] ATLAS Collaboration, K. Cranmer, The ATLAS analysis architecture, Nucl.Phys.Proc.Suppl. **177-178**, 126 (2008).

[100] M. Dobbs *et al.*, Les Houches guidebook to Monte Carlo generators for hadron collider physics, p. 411 (2004), Compiled by the Working Group on Quantum Chromodynamics and the Standard Model, hep-ph/0403045.

[101] A. Buckley *et al.*, General-purpose event generators for LHC physics, Phys.Rept. **504**, 145 (2011), 1101.2599.

[102] T. Sjostrand, S. Mrenna, and P. Z. Skands, PYTHIA 6.4 Physics and Manual, JHEP **0605**, 026 (2006), hep-ph/0603175.

[103] W. Beenakker, R. Hopker, and M. Spira, PROSPINO: A Program for the production of supersymmetric particles in next-to-leading order QCD, (1996), hep-ph/9611232.

[104] B. Andersson, G. Gustafson, G. Ingelman, and T. Sjostrand, Parton Fragmentation and String Dynamics, Phys.Rept. **97**, 31 (1983).

[105] E. Bratkovskaya, W. Cassing, V. Konchakovski, and O. Linnyk, Parton-Hadron-String Dynamics at Relativistic Collider Energies, Nucl.Phys. **A856**, 162 (2011), 27 pages, 15 figures, 1101.5793.

[106] F. E. Paige, S. D. Protopopescu, H. Baer, and X. Tata, ISAJET 7.69: A Monte Carlo event generator for pp, $\bar{p}p$, and e^+e^- reactions, (2003), hep-ph/0312045.

[107] G. Corcella *et al.*, HERWIG 6.5: an event generator for Hadron Emission Reactions With Interfering Gluons (including supersymmetric processes), JHEP **01**, 010 (2001), hep-ph/0011363.

[108] G. Corcella *et al.*, HERWIG 6.5 release note, (2002), hep-ph/0210213.

[109] M. Bahr *et al.*, Herwig++ Physics and Manual, Eur. Phys. J. **C58**, 639 (2008), 0803.0883.

[110] S. Gieseke, A. Ribon, M. H. Seymour, P. Stephens, and B. Webber, Herwig++ 1.0: An Event generator for e^+e^- annihilation, JHEP **0402**, 005 (2004), hep-ph/0311208.

[111] J. M. Butterworth, J. R. Forshaw, and M. H. Seymour, Multiparton interactions in photoproduction at HERA, Z. Phys. **C72**, 637 (1996), hep-ph/9601371.

[112] B. Webber, A QCD Model for Jet Fragmentation Including Soft Gluon Interference, Nucl.Phys. **B238**, 492 (1984).

[113] M. L. Mangano, M. Moretti, F. Piccinini, R. Pittau, and A. D. Polosa, ALPGEN, a generator for hard multiparton processes in hadronic collisions, JHEP **0307**, 001 (2003), hep-ph/0206293.

[114] S. Frixione and B. R. Webber, Matching NLO QCD computations and parton shower simulations, JHEP **0206**, 029 (2002), hep-ph/0204244.

[115] J. Alwall *et al.*, MadGraph/MadEvent v4: The New Web Generation, JHEP **0709**, 028 (2007), 0706.2334.

[116] GEANT4, S. Agostinelli *et al.*, GEANT4: A Simulation toolkit, Nucl.Instrum.Meth. **A506**, 250 (2003).

[117] W. Lampl *et al.*, Calorimeter clustering algorithms: Description and performance, (2008).

[118] ATLAS Collaboration, G. Aad *et al.*, Electron performance measurements with the ATLAS detector using the 2010 LHC proton-proton collision data, Eur.Phys.J. **C72**, 1909 (2012), Long author list - awaiting processing, 1110.3174.

[119] ATLAS Collaboration, Expected electron performance in the ATLAS experiment, April, 2011, ATL-PHYS-PUB-2011-006.

[120] ATLAS Collaboration, G. Aad *et al.*, Expected Performance of the ATLAS Experiment - Detector, Trigger and Physics, (2009), 0901.0512.

[121] ATLAS Collaboration, Electron and photon reconstruction and identification in ATLAS: expected performance at high energy and results at 900 GeV, Jun, 2010, ATLAS-CONF-2010-005.

[122] ATLAS Collaboration, Expected photon performance in the ATLAS experiment, Apr, 2011, ATL-PHYS-PUB-2011-007.

[123] ATLAS Collaboration, G. Aad *et al.*, Measurement of the isolated di-photon cross-section in pp collisions at $\sqrt{s} = 7$ TeV with the ATLAS detector, Phys.Rev. **D85**, 012003 (2012), 1107.0581.

[124] ATLAS Collaboration, G. Aad *et al.*, Measurement of the inclusive isolated prompt photon cross section in pp collisions at $\sqrt{s} = 7\,\text{TeV}$ with the ATLAS detector, Phys.Rev. **D83**, 052005 (2011), 1012.4389.

[125] M. Cacciari, G. P. Salam, and G. Soyez, The Anti-k(t) jet clustering algorithm, JHEP **0804**, 063 (2008), 0802.1189.

[126] ATLAS Collaboration, G. Aad *et al.*, Measurement of inclusive jet and dijet cross sections in proton-proton collisions at 7 TeV centre-of-mass energy with the ATLAS detector, Eur.Phys.J. **C71**, 1512 (2011), 53 pages plus author list (67 pages total), 26 figures, 22 tables. Typo in abstract corrected, document unchanged. Submitted to EPJC, 1009.5908.

[127] W. Lampl *et al.*, CERN Report No. ATL-LARG-PUB-2008-002. ATL-COM-LARG-2008-003, 2008 (unpublished).

[128] ATLAS Collaboration, G. Aad *et al.*, Jet energy measurement with the ATLAS detector in proton-proton collisions at $\sqrt{s} = 7\,\text{TeV}$, (2011), 1112.6426.

[129] S. Hassani *et al.*, A muon identification and combined reconstruction procedure for the ATLAS detector at the LHC using the (MUONBOY, STACO, MuTag) reconstruction packages, Nucl.Instrum.Meth. **A572**, 77 (2007).

[130] R. Nicolaidou *et al.*, Muon identification procedure for the ATLAS detector at the LHC using Muonboy reconstruction package and tests of its performance using cosmic rays and single beam data, J.Phys.Conf.Ser. **219**, 032052 (2010).

[131] ATLAS Collaboration, Muon Reconstruction and Identification: Studies with Simulated Monte Carlo Samples., Mar, 2009, ATL-PHYS-PUB-2009-008. ATL-COM-PHYS-2009-151.

[132] T. Lagouri, Muon identification and reconstruction in ATLAS, (1999), Hardcopy at DESY.

[133] ATLAS Collaboration, M. Moreno Llacer, Muon performance and related ATLAS first physics, J.Phys.Conf.Ser. **259**, 012024 (2010).

[134] ATLAS Collaboration, Muon reconstruction efficiency in reprocessed 2010 LHC proton-proton collision data recorded with the ATLAS detector, April, 2011, ATLAS-CONF-2011-063.

[135] ATLAS Collaboration, Muon Momentum Resolution in First Pass Reconstruction of pp Collision Data Recorded by ATLAS in 2010, March, 2011, ATLAS-CONF-2011-046.

[136] ATLAS Collaboration, G. Aad *et al.*, Performance of Missing Transverse Momentum Reconstruction in Proton-Proton Collisions at 7 TeV with ATLAS, Eur.Phys.J. **C72**, 1844 (2012), 1108.5602.

[137] T. Barillari *et al.*, CERN Report No. ATL-LARG-PUB-2009-001-2. ATL-COM-LARG-2008-006. ATL-LARG-PUB-2009-001, 2008 (unpublished).

[138] ATLAS Collaboration, Performance of the missing transverse energy reconstruction in proton-proton collisions at center-of-mass energy of $\sqrt{s} = 7\,\text{TeV}$ with the ATLAS detector, July, 2010, ATLAS-CONF-2010-039.

[139] ATLAS Collaboration, ATLAS tunes of PYTHIA 6 and Pythia 8 for MC11, July, 2011, ATL-PHYS-PUB-2011-009.

[140] ATLAS Collaboration, New ATLAS event generator tunes to 2010 data, April, 2011, ATL-PHYS-PUB-2011-008.

[141] J. Pumplin *et al.*, New generation of parton distributions with uncertainties from global QCD analysis, JHEP **07**, 012 (2002), `hep-ph/0201195`.

[142] P. M. Nadolsky *et al.*, Implications of CTEQ global analysis for collider observables, Phys. Rev. **D78**, 013004 (2008), `0802.0007`.

[143] ATLAS Collaboration, F. Alonso *et al.*, Search for a diphoton and $E_{\text{T}}^{\text{miss}}$ final state in $\sqrt{s} = 7\,\text{TeV}$ pp collisions at the LHC using the ATLAS detector, April, 2012, ATL-COM-PHYS-2012-463.

[144] J. Butterworth *et al.*, CERN Report No. ATL-COM-PHYS-2010-695, 2010 (unpublished).

[145] A. Djouadi, J.-L. Kneur, and G. Moultaka, SuSpect: A Fortran code for the supersymmetric and Higgs particle spectrum in the MSSM, Comput.Phys.Commun. **176**, 426 (2007), `hep-ph/0211331`.

[146] M. Muhlleitner, A. Djouadi, and Y. Mambrini, SDECAY: A Fortran code for the decays of the supersymmetric particles in the MSSM, Comput.Phys.Commun. **168**, 46 (2005), `hep-ph/0311167`.

[147] A. Sherstnev and R. Thorne, Parton Distributions for LO Generators, Eur.Phys.J. **C55**, 553 (2008), 40 pages, 29 figures as .ps or .eps files, `0711.2473`.

[148] T. Plehn, Prospino2, `http://www.thphys.uni-heidelberg.de/~plehn/index.php?show=prospino&visible=tools`, February, 2012.

[149] W. Beenakker, R. Hopker, M. Spira, and P. Zerwas, Squark and gluino production at hadron colliders, Nucl.Phys. **B492**, 51 (1997), `hep-ph/9610490`.

[150] A. Kulesza and L. Motyka, Threshold resummation for squark-antisquark and gluino-pair production at the LHC, Phys.Rev.Lett. **102**, 111802 (2009), `0807.2405`.

[151] W. Beenakker *et al.*, Squark and gluino hadroproduction, Int.J.Mod.Phys. **A26**, 2637 (2011), `1105.1110`.

[152] A. Kulesza and L. Motyka, Soft gluon resummation for the production of gluino-gluino and squark-antisquark pairs at the LHC, Phys.Rev. **D80**, 095004 (2009), 0905.4749.

[153] W. Beenakker *et al.*, Soft-gluon resummation for squark and gluino hadroproduction, JHEP **0912**, 041 (2009), 0909.4418.

[154] W. Beenakker *et al.*, NLO+NLL SUSY-QCD, http://web.physik.rwth-aachen.de/service/wiki/bin/view/Kraemer/SquarksandGluinos, February, 2012.

[155] ATLAS Collaboration, ExtendedPileupReweighting, https://twiki.cern.ch/twiki/bin/viewauth/AtlasProtected/ExtendedPileupReweighting, October, 2012.

[156] ATLAS Collaboration, G. Aad *et al.*, Luminosity Determination in *pp* Collisions at $\sqrt{s} = 7\,\text{TeV}$ Using the ATLAS Detector at the LHC, Eur. Phys. J. **C71**, 1630 (2011), 1101.2185.

[157] ATLAS Collaboration, Luminosity Determination in *pp* Collisions at $\sqrt{s} = 7\,\text{TeV}$ using the ATLAS Detector in 2011, Aug, 2011, ATLAS-CONF-2011-116.

[158] V. Cindro *et al.*, The ATLAS beam conditions monitor, JINST **3**, P02004 (2008).

[159] P. Jenni and M. Nessi, ATLAS Forward Detectors for Luminosity Measurement and Monitoring, Mar, 2004, CERN-LHCC-2004-010. LHCC-I-014.

[160] H. Burkhardt and P. Grafstrom, Absolute luminosity from machine parameters, (2007).

[161] W. Kozanecki *et al.*, Interaction-Point Phase-Space Characterization using Single-Beam and Luminous-Region Measurements at PEP-II, Nucl.Instrum.Meth. **A607**, 293 (2009).

[162] S. van der Meer, CALIBRATION OF THE EFFECTIVE BEAM HEIGHT IN THE ISR, (1968).

[163] ATLAS Collaboration, G. Aad *et al.*, Data Quality Information for 2010 and 2011 Data, https://twiki.cern.ch/twiki/bin/view/AtlasPublic/RunStatsPublicResults2010, February, 28th, 2012.

[164] ATLAS Collaboration, ATLAS Luminosity Calculator, February, 2012, https://atlas-lumicalc.cern.ch/.

[165] ATLAS Collaboration, SusyObjectDefinitionsr17, https://twiki.cern.ch/twiki/bin/viewauth/AtlasProtected/SusyObjectDefinitionsr17, January, 2012.

[166] ATLAS Collaboration, Data/MC correction factors (a.k.a. fudge factors) for photons, https://twiki.cern.ch/twiki/bin/viewauth/AtlasProtected/PhotonFudgeFactors, September, 2012.

[167] ATLAS Collaboration, PhotonIDTool, https://twiki.cern.ch/twiki/bin/viewauth/AtlasProtected/PhotonIDTool, September, 2012.

[168] ATLAS Collaboration, LArCleaningAndObjectQuality, https://twiki.cern.ch/twiki/bin/viewauth/AtlasProtected/LArCleaningAndObjectQuality, July, 2012.

[169] Q. Buat, J. Leveque, N. Lorenzo Martinez, F. Polci, and B. Trocme, CERN Report No. ATL-COM-PHYS-2012-134, 2012 (unpublished).

[170] ATLAS Collaboration, EnergyScaleResolutionRecommendations, https://twiki.cern.ch/twiki/bin/viewauth/AtlasProtected/EnergyScaleResolutionRecommendations, October, 2012.

[171] D. Banfi *et al.*, CERN Report No. ATL-PHYS-INT-2010-038, 2010 (unpublished).

[172] ATLAS Collaboration, ElectronsEnergyDirection , https://twiki.cern.ch/twiki/bin/viewauth/AtlasProtected/ElectronsEnergyDirection, January, 2012.

[173] ATLAS Collaboration, Data-Quality Requirements and Event Cleaning for Jets and Missing Transverse Energy Reconstruction with the ATLAS Detector in Proton-Proton Collisions at a Center-of-Mass Energy of $\sqrt{s} = 7\,\text{TeV}$, July, 2010, ATLAS-CONF-2010-038.

[174] ATLAS Collaboration, Recommendations for jet cleaning for data 2011 , https://twiki.cern.ch/twiki/bin/view/AtlasProtected/HowToCleanJets2011, April, 2012.

[175] ATLAS Collaboration, Performance of primary vertex reconstruction in proton-proton collisions at $\sqrt{s} = 7\,\text{TeV}$ in the ATLAS experiment, July, 2010, ATLAS-CONF-2010-069.

[176] ATLAS Collaboration, LArEventVetoRel17, https://twiki.cern.ch/twiki/bin/viewauth/Atlas/LArEventVetoRel17, May, 2012.

[177] ATLAS Collaboration, FakeMetEstimator, https://twiki.cern.ch/twiki/bin/viewauth/AtlasProtected/FakeMetEstimator, January, 2012.

[178] ATLAS Collaboration, Evidence for prompt photon production in pp collisions at $\sqrt{s} = 7\,\text{TeV}$ with the ATLAS detector, July, 2010, ATLAS-CONF-2010-077.

[179] ATLAS Collaboration, J. Alasia *et al.*, Search for a diphoton and $E_{\text{T}}^{\text{miss}}$ final state in $\sqrt{s} = 7\,\text{TeV}$ TeV pp collisions at the LHC using the ATLAS detector, November, 2011, ATL-PHYS-INT-2011-095.

[180] G. Bozzi, F. Campanario, M. Rauch, and D. Zeppenfeld, $Z\gamma\gamma$ production with leptonic decays and triple photon production at NLO QCD, Phys.Rev. **D84**, 074028 (2011), 1107.3149.

[181] G. Bozzi, F. Campanario, M. Rauch, and D. Zeppenfeld, $W^{\pm}\gamma\gamma$ production with leptonic decays at NLO QCD, Phys.Rev. **D83**, 114035 (2011), 1103.4613.

[182] K. Arnold *et al.*, VBFNLO: A Parton level Monte Carlo for processes with electroweak bosons, Comput.Phys.Commun. **180**, 1661 (2009), 0811.4559.

[183] A. Bocci *et al.*, CERN Report No. ATL-COM-PHYS-2011-1629, 2011 (unpublished).

[184] A. Martin, W. Stirling, R. Thorne, and G. Watt, Parton distributions for the LHC, Eur.Phys.J. **C63**, 189 (2009), 0901.0002.

[185] A. L. Read, Presentation of search results: The CL(s) technique, J.Phys.G **G28**, 2693 (2002).

[186] G. Cowan, K. Cranmer, E. Gross, and O. Vitells, Asymptotic formulae for likelihood-based tests of new physics, Eur.Phys.J. **C71**, 1554 (2011), 1007.1727.

[187] ATLAS Collaboration, G. Aad *et al.*, Search for squarks and gluinos using final states with jets and missing transverse momentum with the ATLAS detector in $\sqrt{s} = 7\,\text{TeV}$ proton-proton collisions, Phys.Lett. **B710**, 67 (2012), 1109.6572.

[188] W. A. Rolke, A. M. Lopez, and J. Conrad, Limits and confidence intervals in the presence of nuisance parameters, Nuclear Instruments and Methods in Physics Research Section A: Accelerators, Spectrometers, Detectors and Associated Equipment **551**, 493 (2005).

[189] J. T. Linnemann, Measures of significance in HEP and astrophysics, eConf **C030908**, MOBT001 (2003), physics/0312059.

[190] ATLAS Collaboration, M. Baak *et al.*, Combination package, https://svnweb.cern.ch/trac/atlasgrp/browser/Physics/SUSY/Analyses/Combination/tags/Combination-00-00-22/, 2012.

Danksagung

Ich möchte mich bei allen, die mich während dieser Arbeit unterstützt haben, bedanken:

- Bei Prof. Johannes Haller für die Betreuung und Unterstützung bei der Durchführung dieser Arbeit, sowie für die nützlichen Anregungen und Diskussionen.
- Prof. Peter Schleper für die Erstellung des Zweitgutachtens zu dieser Arbeit und Dr. Kerstin Tackmann als Zweitgutachterin der Disputation.
- Dr. Wolfgang Ehrenfeld danke ich für die Betreuung und die gute Zusammenarbeit.
- I also like to thank the photons + $E_{\mathrm{T}}^{\mathrm{miss}}$ analysis team for the good collaboration from which I benefited a lot.
- Meinen Kollegen, insbesondere Cécile, Darío, Dörthe, Janet, Kristin, Mareike, Mark, Martin, Michael, Sebastian, Tiago, danke ich für die angenehme Atmosphäre, die hilfreichen Diskussionen und die gute Zeit. Außerdem danke ich allen Korrekturlesern, wobei ein besonderer Dank an Dörthe geht.
- Ganz herzlich danke ich meiner Familie, die mich immer unterstützt hat und mir alles ermöglicht hat.